Contribution of Post-critical Reflections to Ground Motions from Mega-thrust Events in the Cascadia Subduction Zone

By

Andrew Floyd McNeill
B.Sc., University of British Columbia, 2002

A Thesis Submitted in Partial Fulfillment of the Requirements for the Degree of

MASTER OF SCIENCE

in the School of Earth and Ocean Sciences

Contribution of Post-critical Reflections to Ground Motions from Mega-thrust Events in the Cascadia Subduction zone

By

Andrew Floyd McNeill
B.Sc., University of British Columbia, 2002

Supervisory Committee

Dr. G.D. Spence (School of Earth and Ocean Sciences)

Co-Supervisor

Dr. G.C. Rogers (Geological Survey of Canada, Pacific Geoscience Centre and School of Earth and Ocean Sciences)

Co-Supervisor

Dr. J.F. Cassidy (Geological Survey of Canada, Pacific Geoscience Centre and School of Earth and Ocean Sciences)

Departmental Member

Supervisory Committee

Dr. G.D. Spence (School of Earth and Ocean Sciences)

Co-Supervisor

Dr. G.C. Rogers (Geological Survey of Canada, Pacific Geoscience Centre and School of Earth and Ocean Sciences)

Co-Supervisor

Dr. J.F. Cassidy (Geological Survey of Canada, Pacific Geoscience Centre and School of Earth and Ocean Sciences)

Departmental Member

ABSTRACT

In this study the contribution of post-critical reflections at the oceanic Moho to ground motions from mega-thrust events in the Cascadia subduction zone is examined. The hypothesis to be tested is that the Moho post-critical reflection is a primary component of the S-wave-field at large epicentral distances from a subduction zone thrust earthquake. Pseudo 3-D modeling using P-SV pseudo-spectral synthetic seismograms and ray tracing amplitude calculations are employed. Double couple line sources are initiated within a structural model for the Cascadia subduction zone that incorporates an updated Juan de Fuca slab geometry. Areas in which the oceanic Moho post-critical reflection is a primary component of the seismic wave-field are defined as a function of landward extent of rupture for the next mega-thrust event. For rupture extending landward of the down-dip limit of the seismogenic zone, Moho post-critical reflections create a broad maximum in peak ground motions at locations that fall within the Pacific Northwest urban corridor [Portland, Seattle, Vancouver, Victoria]. At these locations, ground motions from sources with dominant frequencies between 1 Hz and 3 Hz can be a factor up to 1.5 greater than those modeled in the absence of the oceanic Moho post-critical reflection. A second maximum is associated with the presence of forearc mantle serpentinization, which affords a route for post-critical reflections at the oceanic Moho to escape upwards toward the Earth's surface rather than being trapped in the oceanic crust wave-guide. The forearc mantle wedge acts to concentrate seismic energy within a narrow region at locations, just landward of major population centers.

TABLE OF CONTENTS

LIST OF TABLES

LIST OF FIGURES

AKNOWLEDGEMENTS

I wish to extend my gratitude to George Spence for entertaining my countless questions. I would like to express my appreciation to Garry Rogers for guiding this thesis project. Finally, I would like to thank John Cassidy for his valuable insight.

I wish to thank my understanding wife Leah. She was a constant source of support and encouragement. I could not of finished this project without her. Finally, I would like to thank my little girl Kate. She could also make me smile at the end of the day.

For Kate

Trust in the Lord with all your heart
And do not lean on your own understanding.
In all your ways acknowledge Him,
And He will make your paths straight.
Proverbs 3:5 – 6

CHAPTER 1
INTRODUCTION

Unlike comparable subduction zones around the Pacific where young, less than 20 Ma, lithosphere is being subducted, the Cascadia subduction zone has not experienced a major thrust earthquake on the subduction interface in historic time, the last 150 – 200 years [Heaton & Kanamori, 1984; Rogers, 1988]. However, there is extensive paleoseismic evidence from sites along the coast of southern Vancouver Island, Washington, Oregon and California indicating past mega-thrust events prior to the first historical records [summarized by Atwater et al., 1995]. It is now generally accepted that Cascadia subduction zone thrust fault is locked and that the accumulated strain across the margin may be released in a future mega-thrust earthquake [Hyndman & Wang 1995]. Rogers [1988] estimated the maximum magnitude of a mega-thrust earthquake to be 9.1 based on the potential area of rupture.

Numerical modeling of strong ground motions from a mega-thrust event in the Cascadia subduction zone is required to estimate seismic hazard within the Pacific Northwest urban corridor, particularly because no thrust events have been observed historically. Previous studies have indicated that coherent seismic arrivals associated with particular classes of propagation paths are responsible for strong ground shaking within specific epicentral ranges. Burger et al. [1987] found that peak ground motion amplitudes at distances beyond approximately 100 km from an earthquake source are controlled by critical reflections, which cause a flat trend in the attenuation relation in the distance range 100 to 200 km. Analysis of accelerograms from the Loma Prieta earthquake recorded in the San Francisco and Oakland areas suggest that elevated ground motion amplitudes in the distance range 40 to 100 km were due to critical reflections from the base of the crust [Somerville & Yoshimura, 1990]. 2-D finite difference wave simulations for a hypothetical mega-thrust earthquake in the Puget Sound-Portland region indicated the direct S and the oceanic Moho post-critical reflection as the primary component of the S wave-field in the distance range 0 km to 150 km. [Cohee et al., 1991]. A further study found that maximum ground motions at large epicentral distances from a mega-thrust event resulted from post-critical reflections at the oceanic Moho or the continental Moho [McNeill et al., 2004]. In light of previous studies, this thesis examines the contribution of post-critical reflections at the oceanic Moho to ground motions from mega-thrust events in the Cascadia subduction zone.

1.1 Purpose

The aim of this thesis is to define and examine the character of the geographical region in which post-critical reflections at the oceanic Moho are a primary component of the seismic wave-field from a mega-thrust event in the Cascadia subduction zone. Furthermore, within this region the contribution of post-

critical reflections at the oceanic Moho to strong ground motions is quantified. Finally, the impact of oceanic Moho post-critical reflections on seismic hazard in the Pacific Northwest is assessed.

1.2 Outline

In Chapter Two, a review of the tectonic setting of the Cascadia subduction zone is presented. This is accomplished through reviewing the literature concerning the past and present plate motions as well as the regional geology. The Chapter concludes with a description of the current seismicity in the region followed by a discussion on the constraints to the seismogenic zone.

Chapter Three describes the numerical methods employed to model ground motions from a mega-thrust event in the Cascadia Subduction zone. In this chapter, a detailed description of the 3-D seismic velocity and attenuation model for the region is presented. The algorithms applied to calculate amplitudes and attenuation are outlined. The Chapter concludes with a discussion on the limitations of applying this method to model ground motions.

In Chapter Four, results of the numerical modeling are presented in terms of the geographical distribution of peak ground motions where post-critical reflections at the oceanic Moho are the primary component of the seismic wave-field. Within this region the contribution of post-critical reflections at the oceanic Moho to peak ground motions is quantified. The effect of seismic attenuation on the results is examined. The results are compared to empirical estimates of peak ground acceleration from a mega-thrust event. The Chapter concludes with a discussion on the implications of the results on seismic hazard in the Pacific Northwest.

In Chapter Five, the distribution of strong ground motions from the 2003 Tokachi-oki earthquake are examined using the National Research Institute for Earth Science and Disaster Prevention (NEID) strong ground motion network. Using the synthetic seismogram methodology developed in Chapter Three, variations in peak ground acceleration with distance are modeled. Specifically, an explanation for the observed maximum in peak ground acceleration is proposed.

Chapter Six summarizes the main conclusions of the thesis.

CHAPTER 2
BACKGROUND

2.1 Tectonic Setting

The Cascadia subduction zone is positioned adjacent to the western margin of North American extending from the Queen Charlotte fault offshore northern British Columbia, Canada to Cape Mendocino offshore northern California, USA (figure 2.1). The subduction zone is composed of three distinct oceanic plates, the Explorer, Juan de Fuca and Gorda, which converge towards the continental North American Plate. Spreading between the Pacific Plate and the Juan de Fuca Plate system occurs along a series of spreading ridges. From north to south, the spreading ridges are: the Explorer Ridge, at the northwestern boundary of the Explorer Plate; the Juan de Fuca Ridge, the western boundary of the Juan de Fuca Plate; and the Gorda Ridge marking the western boundary of the Gorda Plate. The ocean ridge system is offset by a series of faults. From north to south, the faults are: the Revere-Dellwood-Wilson faults, marking the southwestern boundary of the Dellwood/Winona Block, part of the Explorer Plate; the Sovanco Fault Zone, marking the southwestern boundary of the Explorer Plate; the Blanco Fault Zone, the southwest boundary of the Juan de Fuca Plate and the Mendocino Fault Zone, to the south of the Gorda Plate. As well, the Nootka Fault Zone is a transform fault between the Explorer and Juan de Fuca Plates.

2.2 Continental Plate Geological Structure

Southern British Columbia is comprised of five linear morphogeological belts, which extend parallel to the north – northwest strike of the Canadian Cordillera. From west to east the belts are: the Insular, Coast, Intermontane, Omineca and Foreland belts (figure 2.2). Vancouver Island and its adjacent continental shelf are located within the westernmost orogen. Within this region, the Insular belt is divisible into three accreted terranes: Wrangellia, Pacific Rim and Crescent (figure 2.3).

The Wrangellia terrane, one of the largest terranes in the Cordillera, includes rocks of Devonian to Jurassic age and underlies approximately 90% of Vancouver Island [Johnston & Acton, 2003]. Jurassic – Mid Cretaceous deformation indicates the accretion of Wrangellia to the autochthon in the mid – Cretaceous. The southern coastal regions of Vancouver Island are underlain by two smaller terranes. The Pacific Rim terrane, adjacent to the southwestern edge of the Wrangellia terrane, consists of Triassic – Jurassic arc volcanics, marine sedimentary rocks, pillow basalts and amphibolites [Johnston & Acton, 2003]. Outboard of the Pacific Rim terrane lies the Crescent terrane; a Paleocene – Eocene assemblage of oceanic basalt flows, breccias, tuff and volcanic sandstones. This landward-dipping terrane provides a backstop to the large accretionary prism that has accumulated since the Eocene [Hyndman et al., 1990].

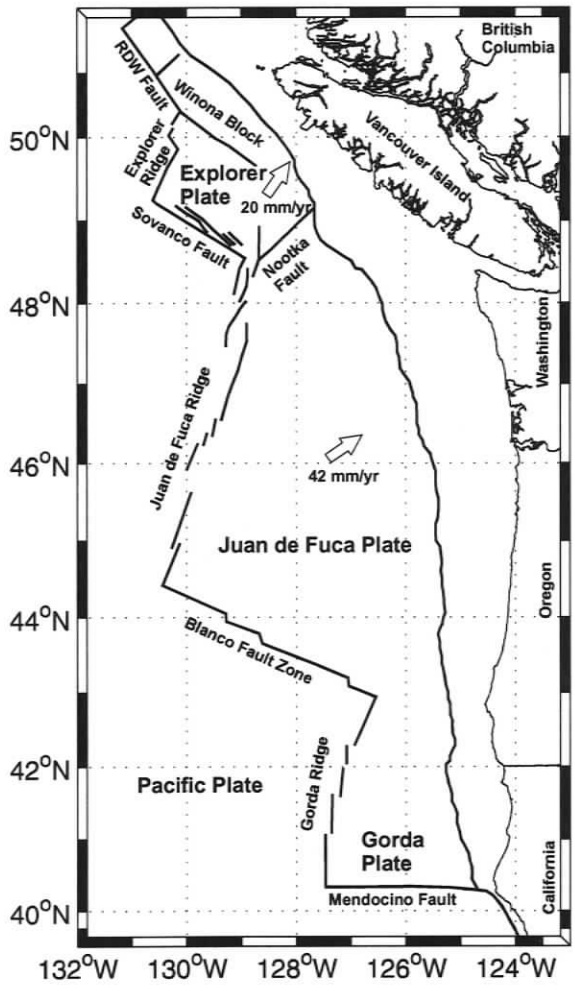

Figure 2.1. Plate boundaries in the Cascadia subduction zone, for the North America, Pacific, Juan de Fuca, Explorer and Gorda plates. RDW designates the RevereDellwood and DellwoodWilson faults [adapted from Willoughby & Hyndman, 2005].

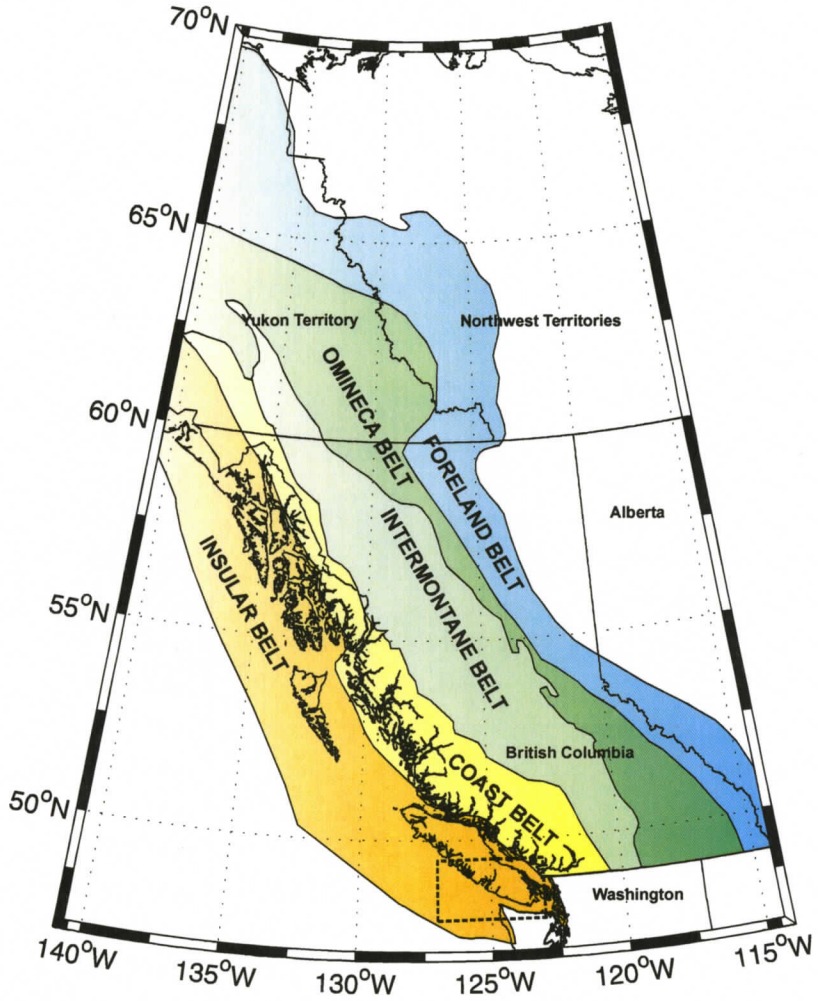

Figure 2.2. Five belt framework of the Canadian Cordillera [adapted from Wheeler & McFeely, 1991, Geological Survey of Canada Map 1712a]. Location of regional geological structure as in figure 2.3 is outlined.

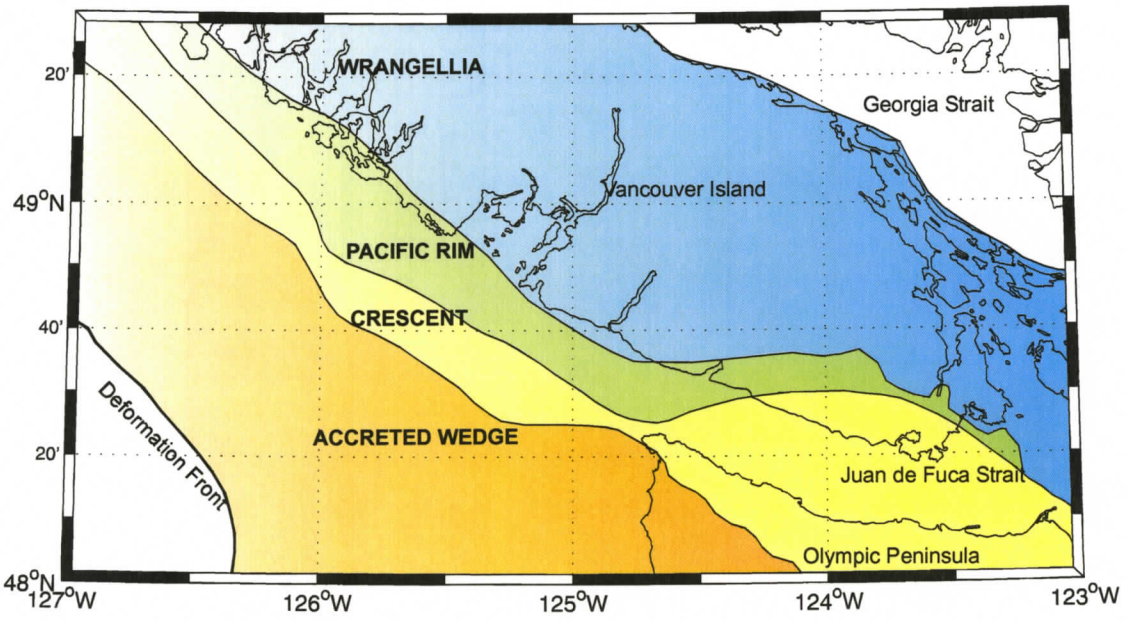

Figure 2.3. Simplified geological structure of the southern Vancouver Island continental margin and adjacent areas [adapted from Hyndman et al., 1990].

Subduction along the margin of southwestern British Columbia was initiated in the early Eocene [Engelbretson et al., 1985]. During this time the Pacific Rim terrane was emplaced against the Wrangellia terrane, which defined the western edge of North America [Hyndman, 1995]. Concurrently, the Crescent terrane was thrust adjacent and under the Pacific terrane [Calvert, 1996]. As a result, the locus of subduction stepped seaward, to the present zone of subduction, initiating the seaward growth of a large accretionary prism against the Crescent terrane.

2.3 Past Plate Motions

The predominantly convergent nature of the western Canadian continental margin since the Mesozoic has largely consumed oceanic plates in its vicinity. Inferences about size, motion and nature of these oceanic plates have been constructed by the study of sea floor magnetic anomalies [Atwater, 1970]. The subsequent subduction and fragmentation of these oceanic plates define the plate tectonic history along the western Canadian margin.

During the Mesozoic era in the vicinity of the western margin of North America, there were three principal oceanic plates, the Pacific, Kula and Farallon, [Riddihough, 1982]. The Pacific plate moved generally northward, whereas the North American plate progressed steadily westward as it spread away from the Eurasian Plate. Both the Kula and Farallon oceanic plates were subducted faster than they were created. Consequently, the area of these plates diminished. During the Oligocene the Farallon plate became progressively narrower, such that a section of the spreading ridge reached the convergent margin of North America at ~25 Ma. This split the plate into two distinct parts separated by a Pacific – North American transform, the proto-San Andreas fault. During the subsequent 25 Ma the northern Farallon plate remnant, the Juan de Fuca plate, continued to diminish in size. By the Miocene, the western margin of North America had completely consumed the Kula plate [Atwater, 1970]. This is because the southern triple junction currently at Cape Mendocino, migrates to the north faster than the northern triple junction, currently just south of the Queen Charlotte Islands [Atwater, 1989]. The last 10 Ma has seen the fragmentation of the Juan de Fuca plate into the Explorer and South Gorda plates near the northern and southern triple junctions, respectively [Riddihough, 1984].

2.4 Present Plate Motions

Contemporary plate motions are inferred from recent magnetic anomaly patterns, current seismicity and GPS measurements. Over the past three decades various studies have interpreted these forms of data to define the present motion of the plates comprising the Cascadia subduction zone (figure 2.1). Pacific – Juan de Fuca motion is well defined by the orientation of the most linear segments of the Juan de Fuca ridge and the width of the Brunhes magnetic chron, which yields a full spreading rate of 58mm/yr [Atwater,

1970, Davis & Currie, 1993]. However, Pacific – Explorer motion is much less resolved. Estimates of a full spreading rate vary from 42 mm/yr [Riddihough, 1977] to a northward increasing rate from 30 – 40 mm/yr [Botros & Johnson, 1988].

Plate motions can be defined with respect to the North American Plate. The current maximum Explorer – North American motion rate is about 20 mm/yr and the Explorer plate moves in a northeasterly direction relative to the North American plate. Convergence increases from negligible to about 20 mm/yr from the northwest to southeast along the Explorer – North American boundary [Braunmiller & Nabelek, 2002]. In particular, the Winona Block converges with a rate of approximately 10mm/yr [Davis & Riddihough, 1982]. In contrast, the Juan de Fuca plate motion is estimated at 42 mm/yr in a northeasterly direction [DeMets et al., 1990, Riddihough, 1984]. The difference in rate motions between the Explorer and the Juan de Fuca plate are accommodated by the left lateral Nootka fault, which exhibits motion of approximately 20 mm/yr [Riddihough, 1984]. Furthermore, if the southern part of the Gorda plate is treated as rigid, this plate moves to the northwest at approximately 40 mm/yr with respect to North America [Riddihough, 1984].

2.5 Seismicity

Southwestern British Columbia represents one of the most seismically active regions in Canada (figure 2.4). Within this area, earthquakes are subdivided into three distinct source regions: continental crustal earthquakes, in-slab earthquakes within the subducting Juan de Fuca oceanic crust and mega-thrust earthquakes. Crustal earthquakes within the North American plate dominate the seismicity pattern of southwestern British Columbia [Rogers, 1998]. In historical time, there have been three notable crustal earthquakes: the 1918 magnitude 7 earthquake on Vancouver Island, the 1946 magnitude 7.3 central Vancouver Island earthquake [Rogers & Hasegawa, 1978] and the 1872 magnitude 6.5 – 7.0 earthquake in northern Washington state [Bakun et al., 2002]. Beneath the western and eastern coastlines of Vancouver Island, earthquakes within the subducting oceanic crust concentrate in two distinctive bands approximately 50 km wide. These geographic bands merge on the south between 48^0 N and 47^0 N where the subducting oceanic crust is arched [Crosson & Owens, 1987]. The intraslab earthquakes have been attributed to an increase in the dip of the oceanic crust, dehydration embrittlement of the oceanic mantle and the gradual transformation of basalt to eclogite [Rogers, 1998, Calvert, 2004, Hacker et al., 2003, Preston et al., 2003]. The most damaging earthquakes in western Washington have occurred within this area and include the 1949 Olympia earthquake, 1965 Seattle-Tacoma Puget Sound earthquake and the recent 2001 Nisqually earthquake.

Mega-thrust earthquakes occur on the subduction interface between the Juan de Fuca Plate and the continental North American Plate. A mega-thrust event on the Cascadia subduction zone interface has not

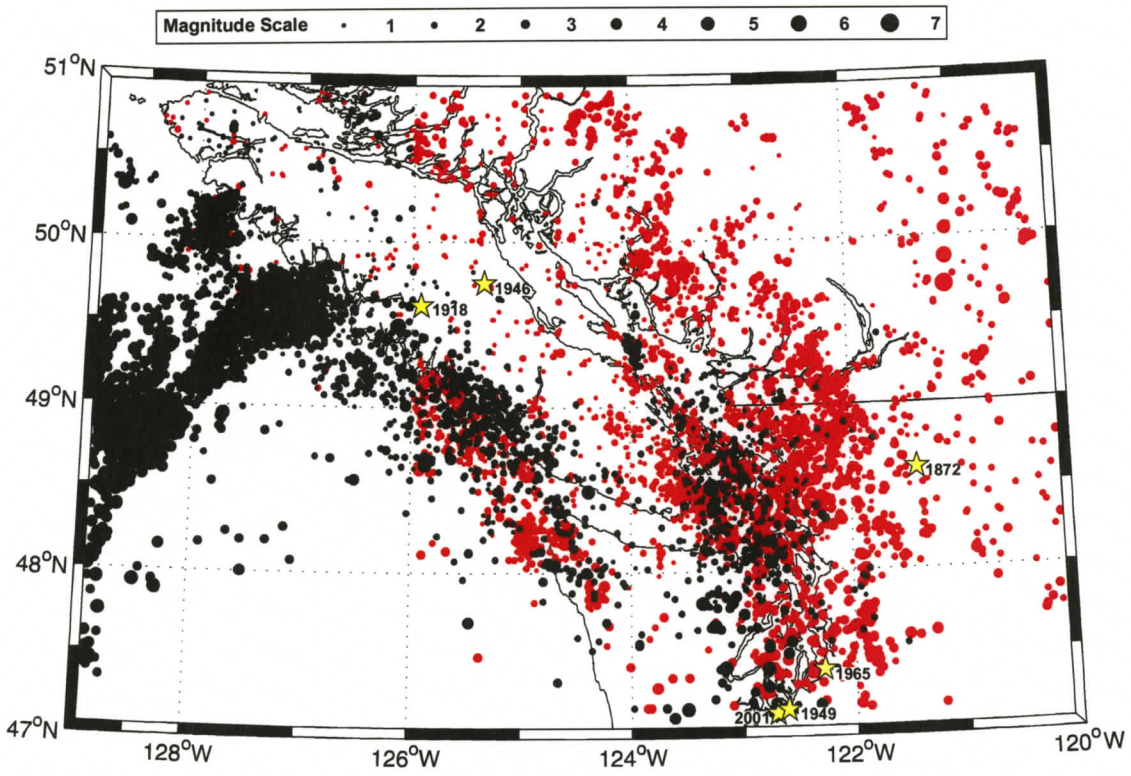

Figure 2.4. Seismicity of southwestern British Columbia [1985 - 2004]. Juan de Fuca Plate seismicity indicated by black, North American Plate seismicity indicated by red. Notable historical earthquakes indicated by star.

been observed within the short written history of the west coast of Canada, the last 150 – 200 years. However, there is extensive evidence for past mega-thrust events prior to the first historical records. In tidal marshes and estuaries along the coast of southern Vancouver Island to northern California, a repeating sedimentary sequence of peat overlain by mud, often with an intervening sand layer, indicate abrupt subsidence and tsunamis associated with a mega-thrust event [summarized by Atwater et al., 1995]. Deep-sea turbidite layers originating from continental slope landslides indicate periodic strong continental margin shaking [Adams, 1990]. In Washington State, dating of annual growth rings from western red cedar killed by salt-water influx related to abrupt coastal subsidence indicates that a mega-thrust event occurred in approximately 1700 [Yamaguchi et al., 1997]. This date corresponds to a widespread tsunami of remote origin, which struck the Pacific coast of Japan. Satake et al., [1996] concluded that this tsunami originated at the Cascadia subduction zone and estimated a mega- thrust earthquake origin time as 9:00pm, January 27, 1700 (PST). Paleoseismic studies have established that mega-thrust events have repeatedly occurred along the Cascadia subduction zone with irregular intervals averaging 500 years [summarized by Atwater et al., 1995].

2.6 Thermal Constraints to the Seismogenic Zone

Theoretical models for the extent of rupture on the Cascadia subduction thrust are required to estimate seismic hazard associated with a mega-thrust event, particularly because no thrust events have been observed historically. The down-dip limit of rupture along the thrust defines the landward limit of the seismogenic zone. This limit is important in assessing seismic hazard since it determines whether or not the seismogenic zone is located beneath or close to population centers.

Several authors have suggested that the thermal regime may be the primary constraint on defining the width of the seismogenic portion of the subduction thrust, the locked zone [Hyndman & Wang, 1993; Hyndman & Wang, 1995; Savage et al., 1991; Oleskevich et al., 1999]. This hypothesis is consistent with the change in rock behavior with respect to temperature and pressure or depth, brittle at low temperatures and pressures and ductile or plastic at high temperatures and pressures. The critical transition is from seismogenic velocity-weakening to stable sliding velocity-strengthening behavior [Scholtz, 1990].

Along the subduction thrust, the thermally driven dehydration of smectite to illite at temperatures of 120-150^{0}C is thought to be the key mineralogical change controlling the up-dip limit of the locked zone [Hyndman & Wang, 1993]. However, other thermally or depth-dependent processes may be important in the controlling the onset of frictional velocity weakening. These processes include: shear localization, porosity reduction, increasing effective stress due to overburden, and pressure solution [Saffer & Marone, 2003].

Hyndman & Wang, [1993] estimated that the critical temperature for the transition between velocity-weakening to velocity-strengthening behavior in crustal rocks as approximately 350^0C. The down-dip limit of the locked zone is predicted to extend to this temperature isotherm. For colder subduction zones, this limit is hypothesized at the intersection of the subducting slab with the forearc mantle wedge [Peacock & Hyndman, 1999]. However, in some areas it has been suggested that the down-dip limit extends into the mantle. Along the Sumatra subduction zone it has been found that this limit extends below the 30 km deep forearc mantle, to a depth of ~46 km where the temperature is estimated at 260 ± 100^0C [Simoes et al., 2004]. An abrupt discontinuity at the down-dip limit of the locked zone is physically unrealistic; therefore, a transition zone is defined between inter-seismic completely locked and free slip portions of the subduction thrust. The down-dip limit of the transition zone is taken at 450^0C isotherm, marking the maximum depth to where the rupture of a large earthquake may extend [Oleskevich et al., 1999].

Apart from thermal constraints, the down-dip extent of the Cascadia locked seismogenic zone has been estimated by dislocation modeling of current deformation data [Dragert et al., 1994; Dragert & Hyndman, 1995; Hyndman & Wang, 1993, 1995; Fluck et al., 1997; Wang et al., 2003]. In elastic dislocation modeling, a shallow portion of the fault is assumed to be locked, whereas the fault is assumed to slip at the full convergence rate at a certain depth down-dip from this zone. The slip deficit of the locked zone is recovered in a future mega-thrust event. Given the fault geometry and convergence rate, the deformation is dependent upon the size and position of the locked and transition zones. Fluck et al. (1997) and Wang et al. (2003) conclude that the down-dip limit of the seismogenic zone is thermally controlled, that is, the limit depends on fault depth.

The locked portion of the Cascadia subduction thrust, as defined by the thermal and deformation constraints, is located offshore where the subduction thrust is less than 20 km depth (figure 2.5). This coincides with the region where the contact is between the oceanic crust and the accretionary wedge, the deformation front. The narrow locked zone is a consequence of the unusually hot Cascadia margin due to the young plate age and the insulating thick sediment section on the incoming plate [Hyndman & Wang, 1993]. The locked zone is wider off the Olympic peninsula compared to the rest of the margin because of the much shallower dip angle and the slightly older age of the plate. The transition zone extends down-dip of the locked zone to the coastline.

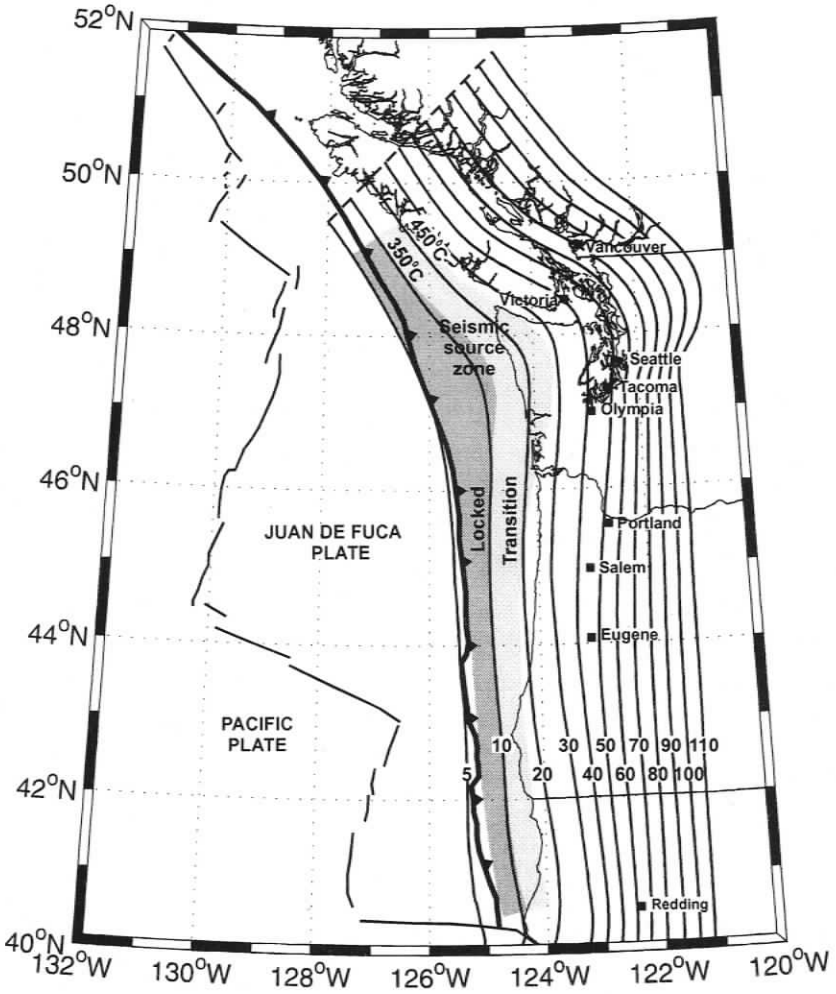

Figure 2.5. Locked and transition zones on the subduction thrust fault. The down-dip limits of the locked and transition zone correspond to the 350°C and 450°C isotherm respectively [adapted from Hyndman & Wang, 1995].

CHAPTER 3
METHOD

3.1 Introduction

Recorded strong ground motions from significant earthquakes are greatly affected by variations in crustal structure through which seismic energy propagates [Kennett & Furumura, 2002]. In structurally complex regions coherent seismic arrivals associated with particular classes of propagation paths are responsible for strong ground shaking within specific epicentral ranges [Furumura & Kennett, 1998]. Numerical modeling of P- and S-waves in a 3-D heterogeneous velocity model can provide direct insight into the nature of seismic phases responsible for strong ground motions. The contribution of specific seismic phases can be quantified through the examination of synthetic seismograms generated by numerical modeling.

In this chapter, the numerical methods employed to determine seismic waveforms and hence the contribution of post-critical reflections at the oceanic Moho boundary to ground motions from mega-thrust events in the Cascadia subduction zone will be presented. A detailed description of the numerical velocity model and attenuation model used for the Cascadia subduction zone will be provided. The numerical model is based upon velocity and attenuation models developed previously. The presence of many phases on the synthetic seismograms can make picking-phase specific amplitudes difficult. Therefore, an algorithm to accomplish this is developed. Seismic attenuation is not modeled explicitly in the synthetic seismograms; therefore, an approximate attenuation scheme, based on ray-tracing of specific phases, will be outlined.

3.2 Psuedo-spectral Method

To simulate the characteristics of the regional seismic wave-field a 2-D pseudo-spectral method for P – SV waves is applied. The pseudo-spectral method provides a direct solution of the equations of momentum conservation combined with the stress – strain relation for an isotropic elastic solid undergoing infinitesimal deformation. In the pseudo-spectral method, field quantities are expanded in terms of Fourier interpolation polynomials. Spatial differentiation of the equations is analytically performed in the wave-number domain; therefore, two grid-points per wavelength are theoretically sufficient to model wave propagation [Kosloff & Baysal, 1982]. This offers an attractive alternative method to finite difference and finite element schemes in which ten grid-points (elements) are required to resolve a particular wavelength [Alford et al., 1974]. Therefore, the pseudo-spectral method offers high-accuracy results with a reduction of several orders of magnitude in both computational time and memory requirements and is very efficient

for large-scale modeling.

In the pseudo-spectral method, the geological structure is specified through the density and seismic wave velocity at the grid points. The method allows for both continuous and discontinuous variation of model parameters. For spatial frequencies less than two grid points in wavelength, spatial derivatives are infinitely accurate [Kosloff & Baysal, 1982]. When the frequency band of the source is appropriately chosen, errors in the numerical solution only arise from the second order finite-difference approximation of the time derivative. Therefore, dispersion and instability of the numerical solution can be avoided by applying the appropriate grid size, time step interval and source frequency. Kosloff et al. [1984] determine appropriate values for these parameters in terms of two relations:

$$dt = (0.2 * MIN\{dx.dy\}/MAX\{V\}, \tag{3.1}$$

$$F=MIN\{V\}/(2*MAX\{dx,dy\}), \tag{3.2}$$

where dt is the minimum time step interval, {dx,dy} is the cell dimension, V is the seismic velocity and F is the maximum source frequency. These stability constraints combined with computational limitations define the maximum source frequencies and model dimensions.

The pseudo-spectral method allows for three types of sources: localized directional body force, pressure source and shear source. The source is introduced over a small region of the computational mesh with a specified distribution. The source time history is defined in terms of a wavelet with a set peak frequency and high-cut frequency. Hudson [1980] showed that cylindrically symmetric solutions to the wave equation maybe constructed by the superposition of point sources arranged on an infinite line. Cylindrically symmetric solutions to the wave equation correspond to the solutions of the wave equation in two-dimensional space. Therefore, a point source initiated in two-dimensional space corresponds to a line source initiated in three-dimensional space assuming an isotropic velocity model with lateral homogeneity in a direction normal to the plane of the model.

The pseudo-spectral method propagates the solution to the isotropic elastic wave equation in time by means of a second-order finite-differencing scheme. Given the initial conditions, the material properties and the source-time histories, the wave equation is solved in terms of acceleration components for a particular time step. The solution of the current time step carries forward to the initial conditions for the following time step. In this sense, the solution is propagated time step by time step to the stopping criterion. The pseudo-spectral method wave-field snapshots and synthetic seismic sections include surface waves, multiples and

mode conversions. A detailed description of the algorithm for the pseudo-spectral method of solution is presented in Appendix A.

Although the pseudo-spectral method is highly accurate and provides direct insight into the nature of the propagation process, it has several limitations. Foremost, there is a limitation on describing complex velocity models in terms of a computational mesh with a defined grid size. The method as defined by solving the isotropic elastic wave equation does not incorporate the effect of attenuation on amplitudes, apart from geometric spreading. The presence of many phases on the time sections and snapshots from the pseudo-spectral method can make interpretation prohibitively complicated [Reshef & Kosloff, 1985].

3.3 Ray Tracing Method

A number of algorithms based on asymptotic ray theory [Cerveny et al., 1977] have been developed to calculate the theoretical traveltime and amplitude response of a laterally inhomogeneous medium. The Zelt & Ellis [1988] routine allows for S- and P-wave propagation including converted phases, multiple and surface reflections, head waves and approximate attenuation. The routine can be applied to identify particular phases responsible for peak ground motions for an earthquake source.

The complex amplitudes of turning, reflected, multiply reflected and converted rays are calculated by zero-order asymptotic ray theory. The effect of attenuation on amplitudes is simplified by assuming that attenuation is frequency independent. For each ray, the attenuation is calculated at a specific dominant frequency and is applied equally at all frequencies [Zelt & Ellis, 1988]. This approximation is expected to be as good as a more accurate frequency-dependent calculation assuming that the source energy is concentrated within a narrow frequency band or attenuation is small. P-wave and S-wave attenuation values are specified for each model block. For a detailed description of the amplitude calculation see Zelt & Ellis [1988].

Ray tracing is particularly useful in interpreting the time section from the pseudo-spectral method, which can become excessively complicated. Furthermore, ray tracing provides an efficient means of calculating the effect of attenuation on specific seismic phases. In section 3.7, an approximate attenuation scheme developed from ray-tracing modeling will be combined with the pseudo-spectral method to account for attenuation.

3.4 Numerical Model

A numerical model for the geographical region of the Cascadia subduction zone is required to simulate the regional seismic wave-field. In the following sections, the specific attributes and origin of the numerical model are discussed in detail. Furthermore, the earthquake source model used in the simulations is defined.

3.4.1 Juan de Fuca Slab Geometry

The geometry of the subducting Juan de Fuca oceanic plate is a crucial element in developing a structural model of the Cascadia subduction zone (figure 3.1). The oceanic plate geometry incorporates data from several studies.

Thrust plane constraints were compiled by Hyndman & Wang [1995]. The dips of the seaward portions of the thrust were estimated from multi-channel seismic refraction data. For the deeper portions of the thrust, the dip was estimated from Benioff-Wadati seismicity (assumed to be in the uppermost mantle about 5 km below the top of the subducting slab), from seismic refraction data and from seismic tomography. The dip profile is well defined for southern British Columbia and Washington, but it is poorly known for Oregon where Benioff-Wadati seismicity is absent.

In 1997, Fluck et al. updated the thrust plane constraints of Hyndman & Wang [1995] with additional data. Benioff-Wadati earthquake hypocenters were restricted to a thin core within the young subducting slab and the assumption that the center of seismicity is 10 km deeper than the top of the plate was applied.

McCrory et al. [2004] presented an updated model of the Juan de Fuca slab beneath southern British Columbia, Washington, Oregon and northern California. The model incorporates the results of several wide-angle seismic reflection and refraction transects that have been completed along the continental margin of Washington, Oregon and northern California since Fluck et al. [1997]. The most significant improvements include: continuation of the slab surface to its full northern and southern edges, extension of the slab surface to 110 km depth and revision of the slab shape based on new seismic-reflection and seismic refraction studies. The slab geometry is revised beneath Puget Sound, where the pronounced arch of the slab is reduced. However, the slab geometry is poorly constrained beneath 50 km depth. This is due to the sparse Benioff-Wadati seismicity within the Cascadia subduction zone system. Slab geometry to depths of 90-110 km has been extrapolated assuming a constant dip on deeper profiles

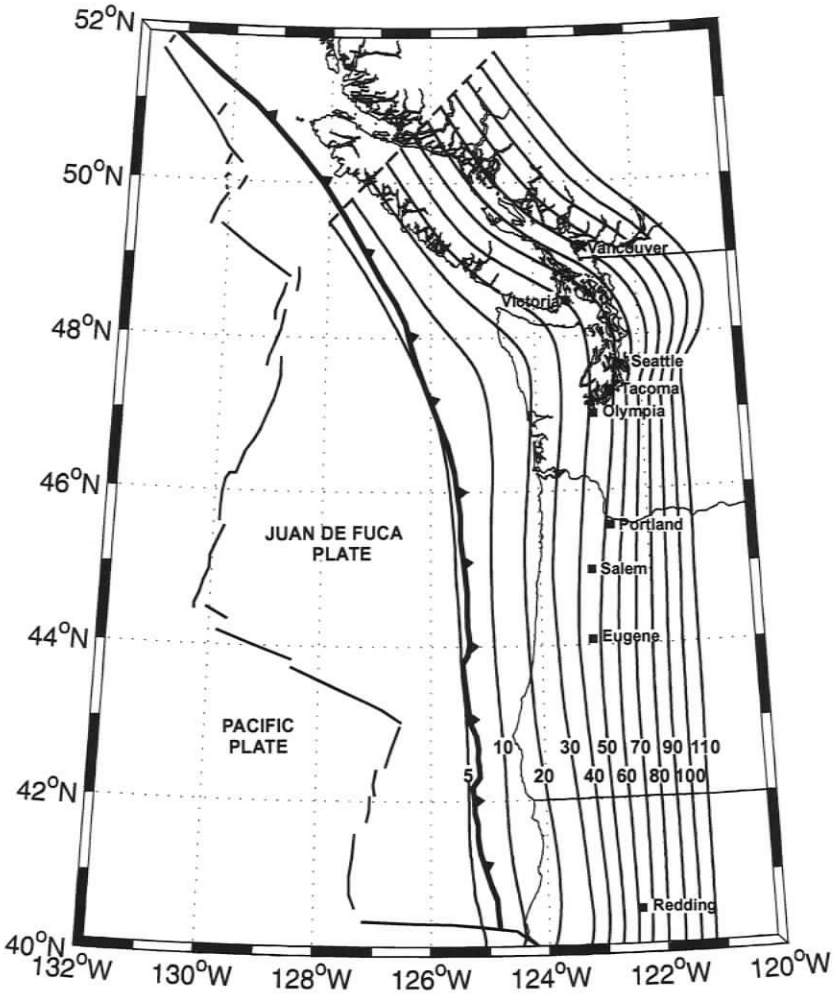

FIGURE 3.1. Configuration of Juan de Fuca slab beneath the western margin of North America [adapted from McCrory at al., 2004].

Considerable controversy centers on the position of the subducting oceanic crust in relation to a zone of unusually prominent seismic reflectors known as the E-reflectors (or E-layer) originally identified in the LITHOPROBE studies. In the first studies of the LITHOPROBE profiles from southernmost Vancouver Island, the base of the E-layer is interpreted as the top of the subducting oceanic crust [Clowes et al., 1987; Green et al., 1986]. However, beneath Vancouver Island the top of the oceanic crust is now commonly proposed to correlate with weak reflection know as the F-reflector imaged on the LITHOPROBE profiles [Drew & Clowes, 1990; Calvert, 2004]. This places the top of the oceanic crust 5 – 8 km beneath the E-layer. A new interpretation associates the top of the oceanic crust with the bottom of the E-reflector, based on analysis of reflection data, tomographic velocities and seismicity [Nedimovic et al., 2003]. Furthermore, a new teleseismic study across southern British Columbia and northwestern Washington interprets the E-reflector as representing the dehydrating oceanic crust of the Juan de Fuca Plate [Nicholson et al., 2005]. The geometry of the subducting Juan de Fuca Plate proposed by McCrory et al. [2004] is consistent with interpreting the F-reflector as the top of the oceanic crust.

3.4.2 Cascadia velocity model

The development of a 3-D velocity model for the geographical region of the Cascadia subduction zone is required to numerically simulate ground motions. The structural model consists of continental mantle, oceanic mantle, continental crust and oceanic crust. Two "layers" further define the seismic structure of the igneous oceanic crust. Seismic layer 2 is characterized by a high vertical velocity gradient (~1 s^{-1}), with velocities commonly increasing from 3 - 4 km/s at the top of the crust to ~ 6.5 km/s at an average depth of 2 km. The lower oceanic crust (seismic layer 3) is distinguished from layer 2 by both a higher P-wave velocity (6.7 - 7.0 km/s) and a much smaller vertical velocity gradient (~0.1 s^{-1}) [Spudich & Orcutt, 1980; White et al., 1992; Detrick et al., 1994]. Recent interpretations of seismic refraction data have correlated the seismic layer 2/3 boundary with gradual downward changes in crustal porosity and alteration, not a lithological transition from sheeted dykes to gabbro [Detrick et al., 1994].

The geometry of the down-going oceanic crust is adopted from McCrory et al. [2004]. Velocity values for the structural units are derived from a number of seismic transects collected across the western margin of North America (see table 3.1 for references) (figure 3.2). It is important to include the general characteristics of published velocity models without introducing traits specific to any one model that may not be representative of the region in an average sense

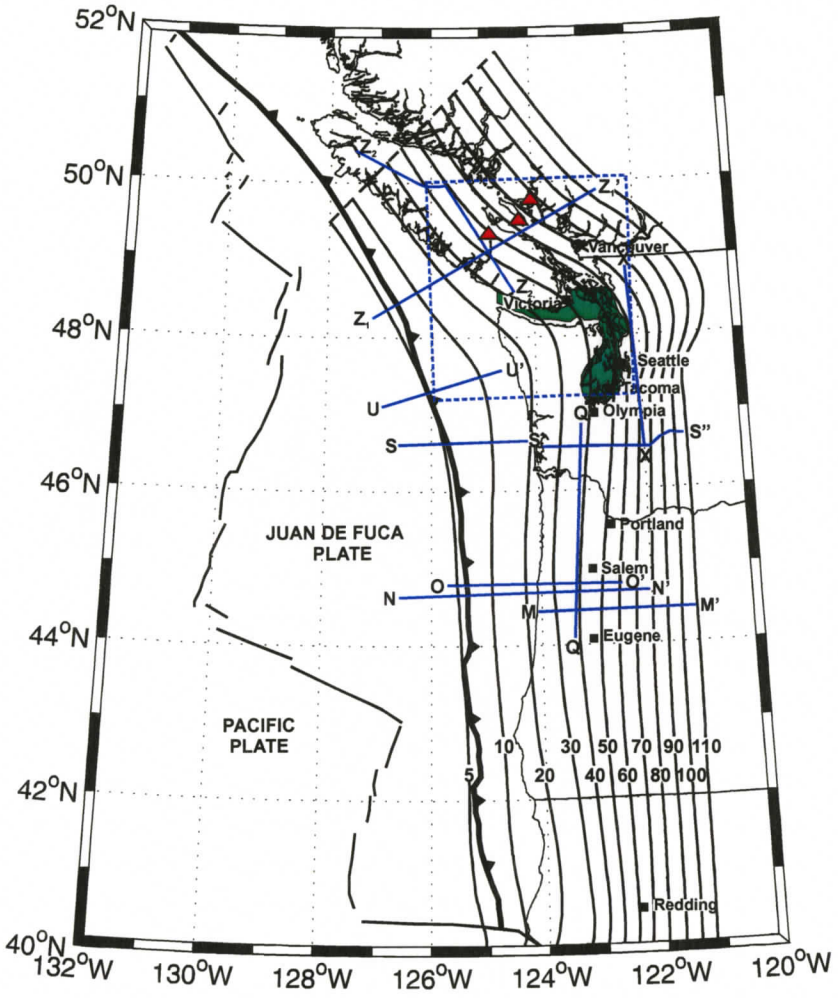

FIGURE 3.2. Map shows location of wide-angle transects used to construct velocity model of the Cascadia Subduction zone. Survey lines are labeled according to table 3.1. Triangles indicate location of teleseismic receiver function studies. Shaded area and dashed box indicate location of tomographic velocity models [adapted from McCrory et al., 2004].

TABLE 3.1 List of published references used to construct velocity model of the Cascadia Subduction zone (see figure 3.2 for location of transects and profiles).

WIDE-ANGLE (ACTIVE SOURCE) TRANSECTS

Transect Z_1Z_1'	Spence et al., 1985; Drew & Clowes, 1990
Transect Z_2Z_2'	McMechan & Spence, 1983
Transect OO'	Trehu et al., 1994
Transect QQ'	Trehu et al., 1994
Transect NN'	Gerdom et al., 2000
Transect SS'S''	Parsons et al., 1998
Transect SS' and UU'	Flueh et al., 1998
Tansect XX'	Miller et al., 1997

TELESEISMIC (PASSIVE SOURCE) TRANSECTS

Transect MM'	Bostock et al., 2002

TELESEISMIC RECEIVER FUNCTION STUDIES

Triangle	Cassidy & Ellis, 1991; 1993

TOMOGRAPHIC VELOCITY MODELS

Shaded area	Brocher et al., 2001
Dashed box	Ramachandran et al., 2005

The Vancouver Island region of the Cascadia subduction zone has been the site of numerous seismic reflection, seismic refraction and receiver function studies. The interpretation of the 1980 Vancouver Island Seismic Project (VISP80) data yielded a P-wave seismic velocity structure along the length of Vancouver Island as well as across the margin [McMechan & Spence, 1983; Spence et al., 1985; Drew & Clowes, 1990]. The upper crust in this region consists of a simple gradually increasing velocity from ~5.3 km/s at the surface to ~6.4 km/s at 3 km depth. The structure below 3 km is complicated, but in an average sense can be represented with a gradually increasing velocity from ~6.4 km/s to ~6.95 km/s at continental Moho depth. The continental Moho is defined at approximately 37 km depth beneath western Vancouver

Island with mantle velocities 7.95 – 8.20 km/s. The oceanic crust consist of a ~2 km thick layer with depth dependent velocities 6.00 – 6.82 km overlying a ~4 km thick layer with depth dependent velocities 6.85 – 7.28 km/s. Oceanic upper mantle velocities range from 8.10 – 8.33 km/s. Receiver function studies on Vancouver Island support velocity values and continental Moho depths derived from seismic studies [Cassidy & Ellis, 1991; 1993, Cassidy et al., 1998]. A recent three-dimensional tomographic velocity model for the crust and upper mantle beneath southwestern British Columbia is in agreement with the previous studies [Ramachandran et al., 2005].

Several controlled source seismic experiments have been conducted in northwestern and central Washington to determine the velocity structure across the convergent margin. In western Washington, continental crustal velocities increase from ~6.0 km/s at 10 km depth to ~7.2 km/s at the continental Moho at 37 km depth [Miller et al., 1997]. Brocher et al. [2001] imaged velocities of 6.3 – 6.6 km/s at 6 km depth along the Olympia Peninsula. Parsons et al. [1998] developed a cross-section velocity model for an east-west transect across southern Washington. Continental crustal velocities range from 4.5 km/s at the surface to 7.0 km/s at the continental Moho below which upper mantle velocities are defined as 7.8 km/s. Offshore northwestern Washington, Flueh et al. [1998] determined an oceanic crust composed of three layers each approximately 2 km thick with depth dependent velocities 4.9 – 6.2 km/s, 6.2 – 6.8 km/s and 6.8 – 7.0 km/s, respectively. In southern Washington the oceanic crust was imaged with a thickness of approximately 6 km/s and velocities from 6.5 – 7.0 km/s [Parsons et al., 1998]. Oceanic upper mantle velocities of 7.9 – 8.2 km/s were estimated [Flueh et al., 1998]. Velocity values derived in Washington are comparable to those in the vicinity of Vancouver Island.

A number of seismic studies have been performed across the central Oregon margin. In this region, upper crustal velocities gradually increase from ~5.0 km/s at the surface to ~6.0 km/s at ~7 km depth [Trehu et al., 1994; Gerdom et al., 2000]. Lower crustal velocities range from 6.5 – 7.2 km/s. The continental Moho is evident as a boundary near 37 km depth [Bostock et al., 2002]. The oceanic crust is defined as 5 – 6 km thick. Velocities within the subducting slab increase with depth ranging from 6.50 – 7.10 km/s [Trehu et al., 1994, Gerdom et al., 2000]. Velocity values within Oregon are comparable to those derived along the extent of the Cascadia subduction zone.

Velocity models derived from a number of seismic transects across the Cascadia subduction zone illustrate common structures and velocities. The oceanic crust is defined with a thickness of approximately 6 km along the entire margin. The continental Moho is consistently evident at 37 km. Figure 3.3b displays a profile through the 3-D velocity model illustrating the average P-wave velocity model as derived from the above seismic studies. The specific velocity structure within the forearc mantle wedge incorporates the

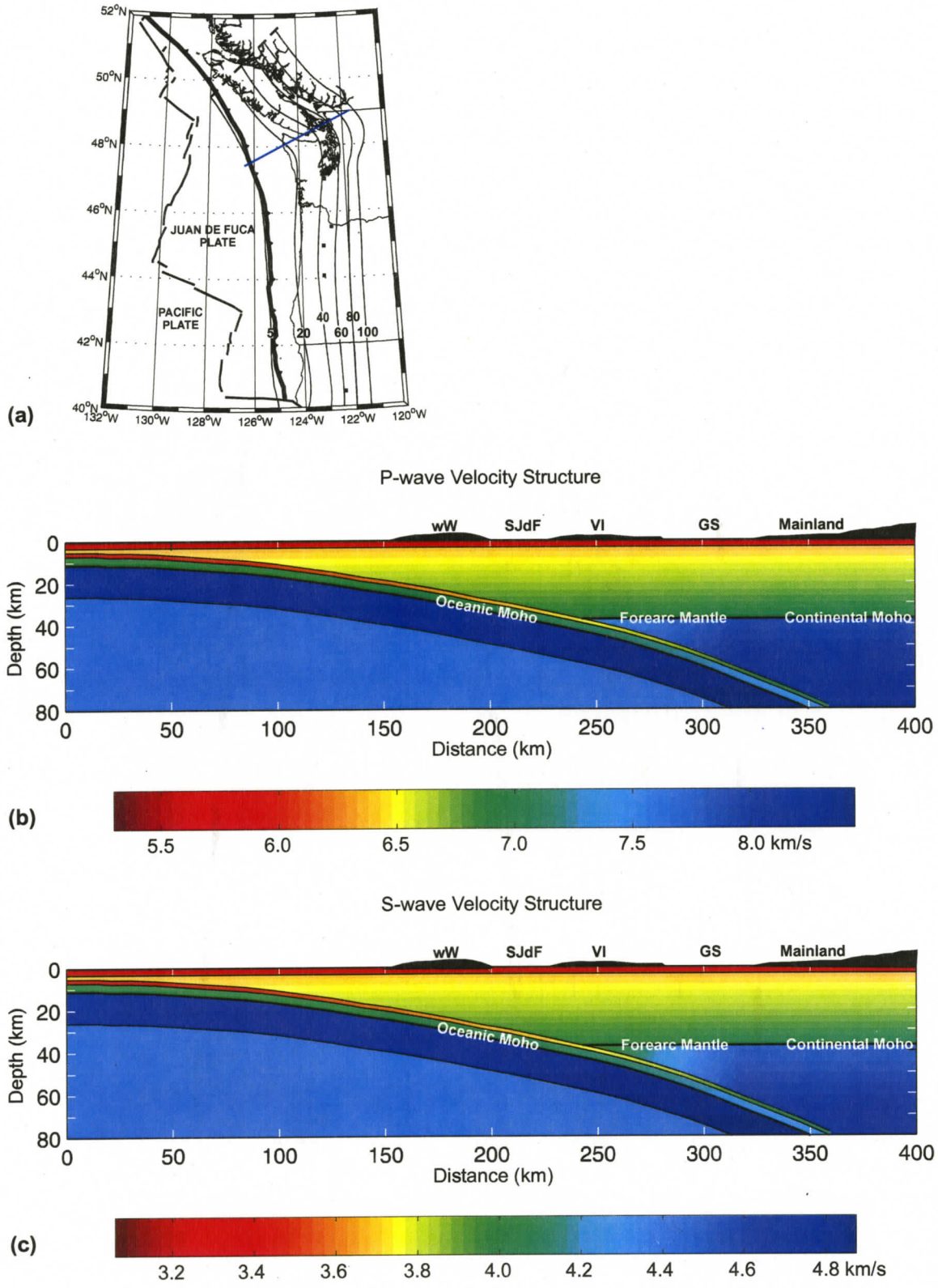

Figure 3.3. (a) Map indicating location of profile line. (b) P-wave velocity model and (c) S-wave velocity model for the Cascadia subduction zone. Abbreviations: wW-western Washington; SJdF-Strait of Juan de Fuca; VI-Vancouver Island; GS-Georgia Strait.

effect of serpentinization on mantle velocities. The origin of serpentinization within this region and its impact on seismic velocities is elaborated in the next section.

By applying appropriate Poisson's ratio to the structural units an S-wave velocity model can be derived (figure 3.3c). The average Poisson's ratio for typical continental and oceanic crust is in the range of 0.24 – 0.27 [Braile et al., 1989; Holbrook et al., 1992; Clarke & Silver; 1993; Zandt & Ammon, 1995]. A value of 0.25 is applied to the oceanic and continental crust. For the mantle a Poisson's ration of 0.26 is applied which corresponds to that of unaltered ultramafic rocks [Christensen, 1996]. A variable Poisson's ratio is applied in the forearc mantle region to account for serpentinization. Approximately 30% serpentinization in this region yields a Poisson's ratio of 0.31 [Hyndman & Peacock, 2003]. This value reverts back to a normal upper mantle Poisson's ratio landward of Puget Sound and the Strait of Georgia.

The S-wave velocity model is a smoothly varying derivative of a P-wave velocity model that is consistent with a number of studies. However, it does not include the prominent low S-wave velocity zones evident beneath southern Vancouver Island dipping eastwards through the Georgia Strait/Puget Sound, the C and E layers documented by Cassidy and Ellis (1991, 1993) using receiver function analysis. These low S-wave velocity zones have not been documented in northern Washington State; therefore these zones are not incorporated into the velocity model. Recently, during the course of this thesis study, an alternate interpretation of these S-wave velocity structures has been proposed [Nicholson et al., 2005] suggesting that the E layer defines the position of the oceanic crust. Discussions on the implication of the more complex S-wave velocity structure and of the recent alternate interpretation are included in Chapter 4.

In order to perform wave simulations in a complex model, compromises are necessary, particularly for the representation of shallow structure. The water layer is excluded from the model; however, this does not have a significant influence on the character of the wave propagation [Furumura & Furumura, 2001]. For most of the region the water depth is less than 2 km. The surface topography (less that 2 km across the region) and the details of sedimentary basins are excluded from the calculations, so that the simulations are for a level competent surface.

3.4.3 Forearc Mantle Serpentinization

In 2002, Bostock et al. imaged the structure of the mantle wedge in the southern Cascadia subduction zone using scattered teleseismic waves recorded on a dense array of portable seismometers across central Oregon. In this region, low shear-wave velocities in the cold forearc mantle wedge indicated the occurrence of a negative velocity contrast across the continental Moho, an inverted continental Moho.

Seaward of the Cascade arc, the Moho reverts to normal polarity. This observation provided evidence for a highly hydrated and serpentinized forearc mantle, consistent with thermal and petrological models.

As the subducting oceanic lithosphere encounters increasing pressure and temperature conditions, significant volumes of aqueous fluids are expelled upward by dehydration reactions in the oceanic crust and sediments [Hyndman & Peacock, 2003] (figure 3.4). This acts to cool the overlying mantle wedge. Upon hydration at low temperatures within the forearc mantle, depleted peridotite, the dominant mantle rock type, will stabilize as hydrous serpentine minerals [Bostock et al., 2002]. Serpentinite exhibits low elastic wave velocities and high Poisson's ratio. Therefore, the degree of serpentinization will drastically reduce the seismic velocity and density of the mantle wedge while increasing the Poisson's ratio [Hyndman & Peacock, 2003]. Bostock et al. [2002] suggested that the level of serpentinization near the mantle wedge corner could be as high as 50-60%.

The weak or inverted continental Moho seismic velocity contrast in the forearc region can significantly reduce the amplitude of both wide-angle and near vertical Moho reflections. Brocher et al. [2003] compiled upper mantle (Pn) velocities, near-vertical-incidence reflection images and wide-angle reflection amplitudes from the top of the upper mantle (PmP) along the Cascadia subduction zone from Vancouver Island to California. Weak or missing PmP reflections and low upper mantle velocities characterize a narrow region along the continental margin (figure 3.5). These features were interpreted as the effects of widespread hydration and serpentinization of the forearc mantle wedge along the entire Cascadia margin.

The low S-wave velocities within the serpentinized forearc mantle and the small velocity contrast between the subducting oceanic crust and mantle will alter the nature of seismic waves propagating in the forearc region [McNeill et al., 2004].

The velocity model of the Cascadia subduction zone incorporates these forearc mantle features. Seismic reflection, refraction and tomography observations indicate upper mantle P-wave velocities of 7.2 – 7.6 km/s in the forearc [Brocher, et al., 2003]. This is indicative of 15 – 30% serpentinization, which yields an S-wave velocity of 3.8 – 4.2 km/s and a Poisson's ratio of approximately 0.31 [Hyndman & Peacock, 2003]. These velocities revert to normal upper mantle values landward of Puget Sound and the Strait of Georgia

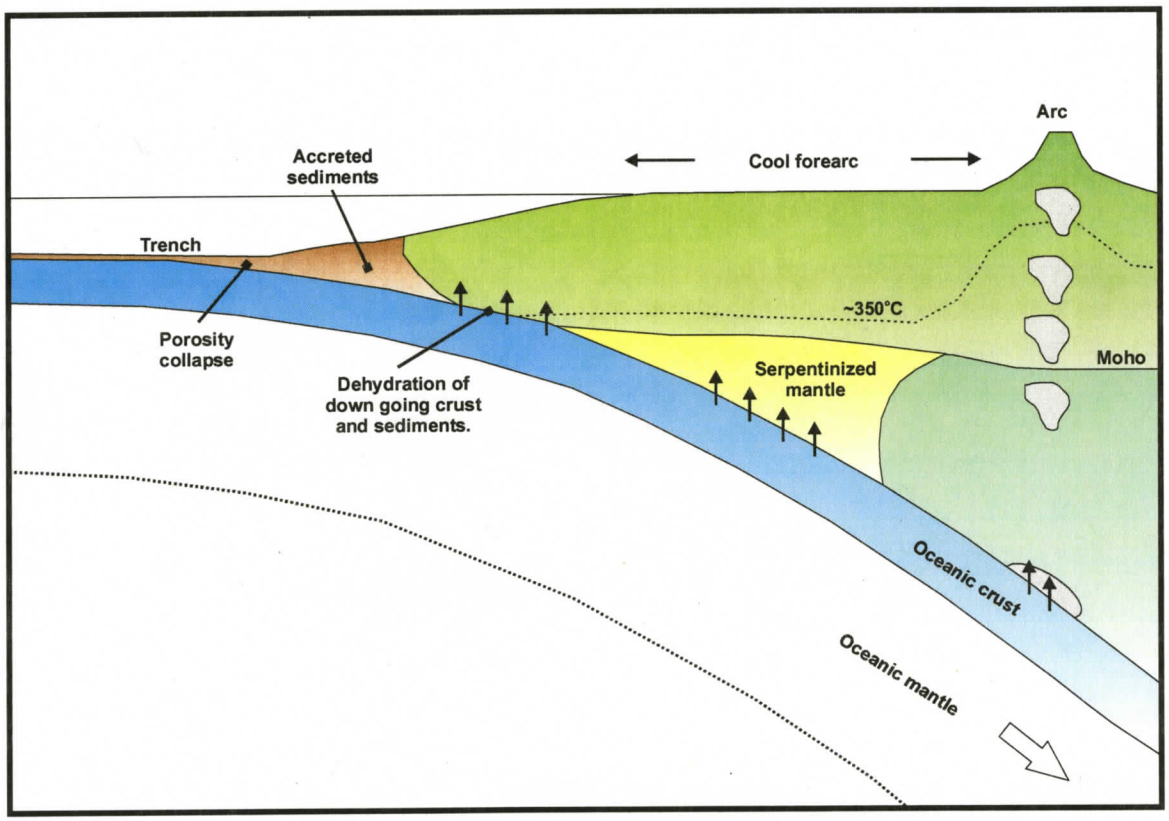

FIGURE 3.4. Schematic cross section illustrating fluid expulsion from subducting oceanic crust and sediments, and serpentinization of the overlying mantle [Hyndman & Peacock, 2003].

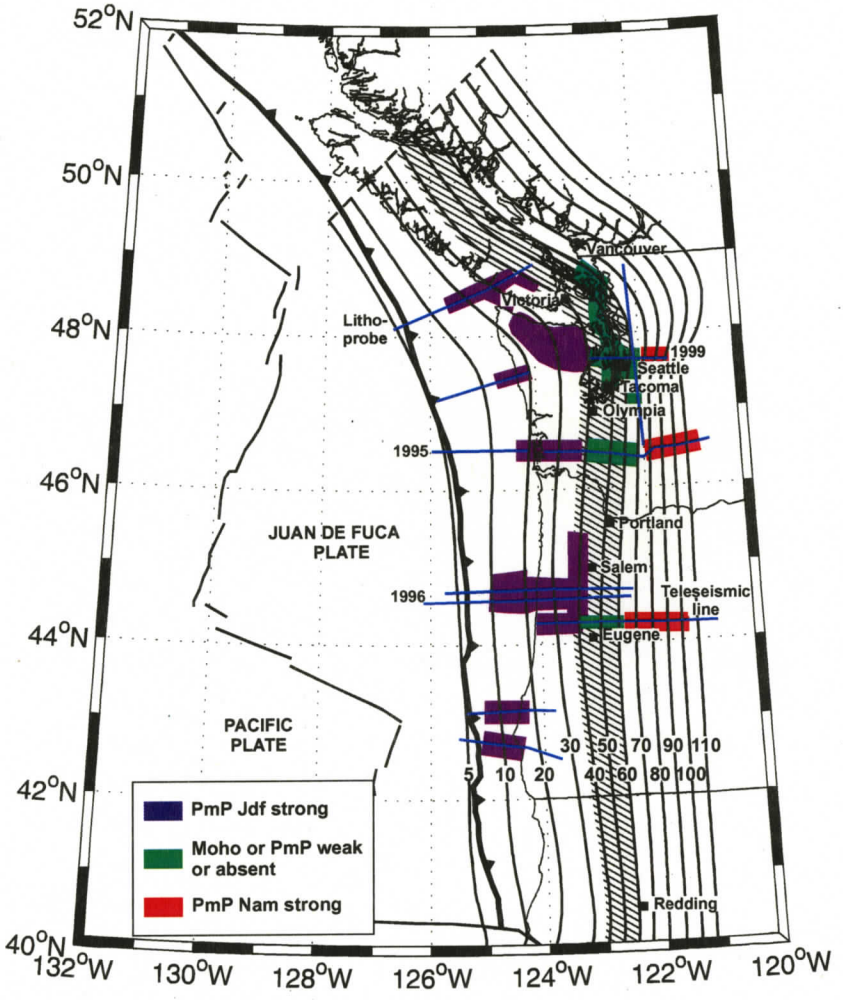

FIGURE 3.5. Location of teleseismic line and seismic surveys providing upper mantle observations in Cascadia. Observations are color coded as explained in the key. Stippled area indicates region above the 37 - 60 km Juan de Fuca slab contours [adapted from Brocher et al., 2003]. Abbreviations: PmP JdF-Juan de Fuca Plate Moho reflections; PmP NAm-North American Plate Moho reflections.

3.4.4 Attenuation model

Energy loss due to anelastic processes or internal friction during wave propagation affects seismic wave amplitude. The strength of intrinsic attenuation, or the strength of a combination of intrinsic and scattering attenuation is given in terms of a dimensionless quantity Q, the quality factor. The attenuation of P- and S-waves is specifically proportional to Q_p^{-1} and Q_s^{-1}, respectively. Pseudo-spectral method results indicate that peak ground displacements are derived from S-wave phases. Therefore, an attenuation model of the Cascadia subduction zone in terms of Q_s is required to calculate numerical the effect of seismic attenuation on peak ground displacements.

The attenuation structure of the Cascadia subduction zone is poorly known. Nevertheless, a model can be developed based upon attenuation structures present in comparable subduction zones. Furthermore, the known temperature and compositional structure of the Cascadia subduction zone can provide additional constraints on the attenuation model. S-wave attenuation values are assigned to the continental crust, the oceanic crust, the upper oceanic mantle, the upper continental mantle and the forearc mantle wedge.

The Q_s structure imaged in the upper mantle beneath central Alaska, an active subduction zone, provides the basis for the Cascadia attenuation model [Stachnik & Abers, 2004]. Attenuation estimates are defined at a frequency of 1 Hz. Inversion results show $Q_s > 400$ for the continental crust. This value is significantly higher than $Q_s = 250$ employed by Ristau [2004] in the northern Cascadia subduction zone. The oceanic crust below 75 km depth shows low attenuation ($Q_s > 1000$). Unexpectedly, the oceanic crust shows relatively high attenuation at depths less than 80 km, $Q_s = 200 - 400$. This is likely due to dehydration of the oceanic crust. Low Q_s values ($Q_s < 150$) exist in the mantle wedge, above the slab at depths greater than 80 km. The forearc mantle wedge, at depths shallower than 80 km, shows moderate Q_s values of ~ 500. The spatial pattern of Q_s beneath Alaska is qualitatively similar to other subduction zones. A similar pattern has been observed in northern Japan [Tsumura et al., 2000; Takanami et al., 2000].

The simplest explanation for the attenuation structure in the mantle is that low Q_s indicates hot and less viscous mantle, while high Q_s indicates the mantle is cold. This explanation agrees with numerical viscous flow modeling of subduction zones by Conder [2004], which indicates a sharp vertical transition between the hot mantle beneath the arc and cold mantle beneath the forearc. Q predictions, based upon Q dependence on temperature and pressure, show that various parameterizations develop vertical transitions of varying quality between the cold mantle wedge corner and the mantle beneath the arc. However, Q beneath the forearc is probably reduced relative to the slab due to the presence of fluids and

serpentinization.

Laboratory results indicate a Q_s value in the range of 80 – 130 for serpentinite at 600MPa [Kern et al., 1997]. However, within the serpentinized forearc mantle wedge, no anomalous attenuation has been observed. Coda Q values derived for a range of sampling volumes in southwestern British Columbia do not indicate an increase in attenuation when sampling the forearc mantle wedge [Zelt et al., 1999].

In figure 3.6 the attenuation model applied to the Cascadia subduction zone is illustrated. The model values are indicative of an attenuation structure comparable to that beneath central Alaska.

3.4.5 Source Characterization

Earthquakes can be idealized as movement across a planar fault of arbitrary orientation. It can be shown that a distribution of body forces can produce the same displacement field as a slip on a planar fault [Shearer, 1999]. Therefore, a fault model can be represented in terms of the equivalent body forces. Specifically, the seismic energy radiating from a fault can be modeled with a double-couple source, the equivalent body-force representation of the displacement field. Therefore, a force double couple oriented to represent displacement on the subduction thrust fault can model the source of a mega-thrust event. This configuration of body forces is implemented in the pseudo-spectral method to forward model a mega-thrust event.

3.5 Amplitude calculations

Numerical modeling of P- and S-seismic waves in a 2-D heterogeneous model using the pseudo-spectral method provides the full waveforms of seismic phases arriving at the surface. However, specific seismic phases on the synthetic seismograms need to be distinguished in order to define the amplitudes associated with these seismic phases. In this section, the algorithm applied to distinguish the peak amplitudes associated with post-critical reflections from the oceanic Moho is outlined.

For a specific numerical model configuration the pseudo-spectral method outputs a synthetic seismic section. Peak amplitude as a function of model distance can be derived from the peak amplitude associated with each synthetic trace comprising the section. Comparing travel-times of seismic phases calculated by the ray-tracing method with the synthetic seismic section helps identify the seismic phases on the section. In particular, the peak amplitudes associated with the arrival of post-critical reflections from the ocean Moho can be distinguished. Figure 3.7 illustrates the complete processes of distinguishing amplitudes

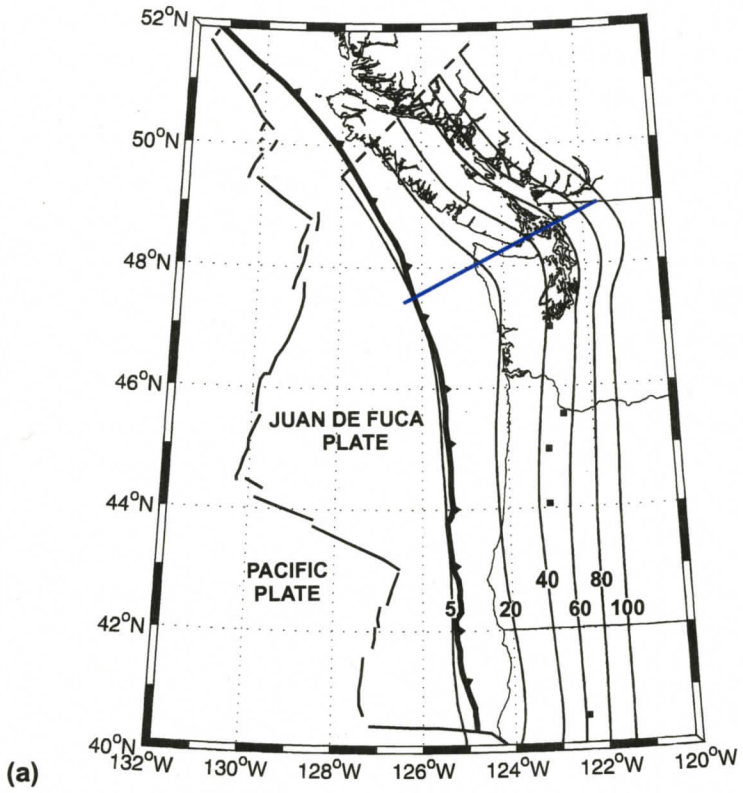

(a)

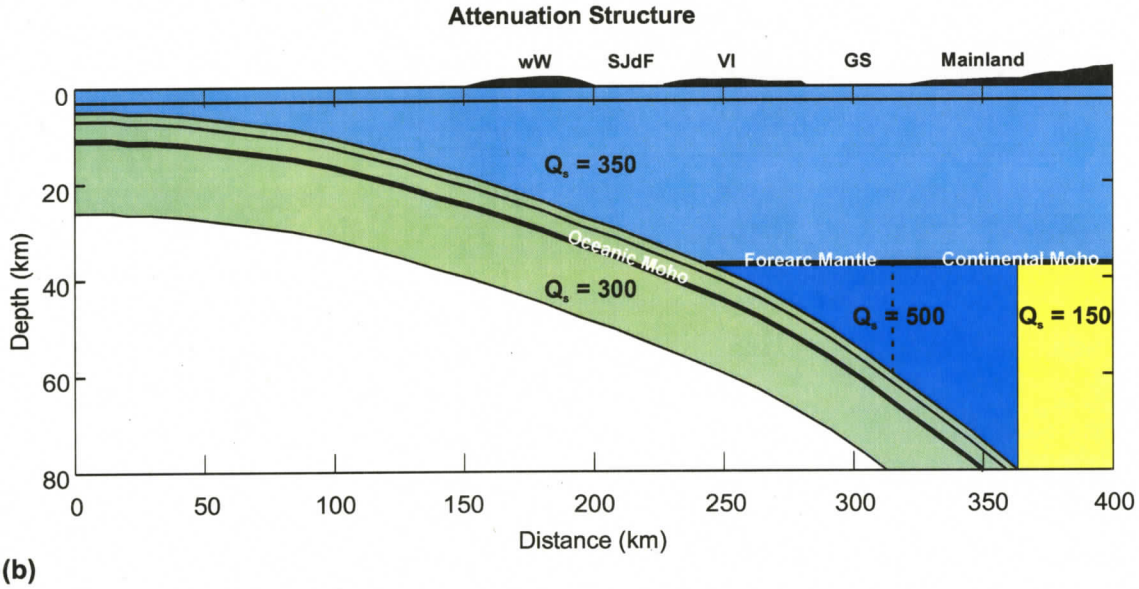

(b)

FIGURE 3.6. (a) Map indicating location of profile line. (b) Attenuation model for the Cascadia subduction zone. Abbreviations: wW-western Washington; SJdF-Strait of Juan de Fuca; VI-Vancouver Island; GS-Georgia Strait.

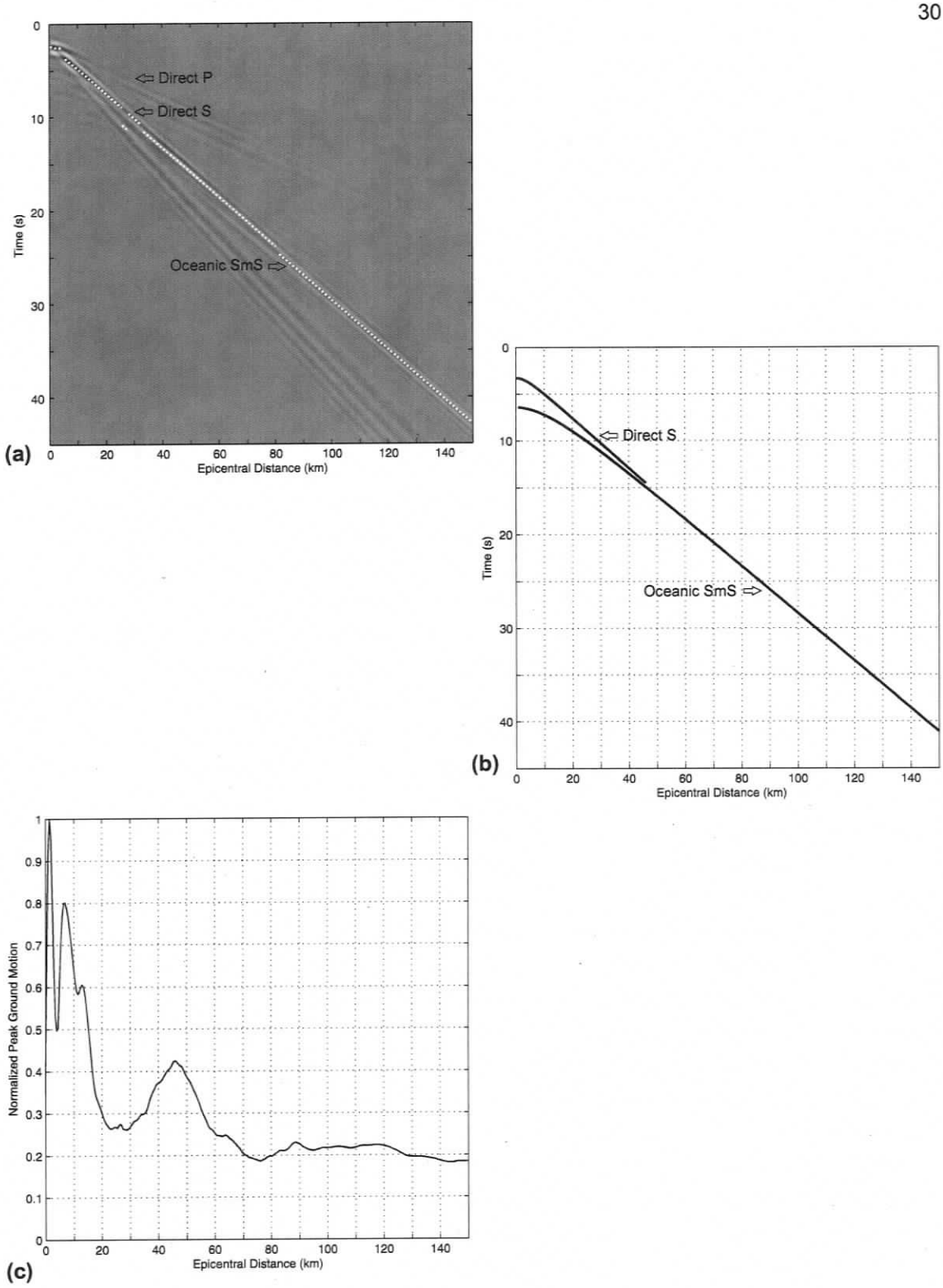

Figure 3.7 Algorithm to pick phase specific amplitudes. (a) Vertical component pseudo-spectral synthetic seismic section (dashed line indicates peak amplitudes). (b) Travel-times calculated by ray-tracing method. (c) Vertical component peak ground motion as a function of epicentral distance. Peak amplitudes associated with the arrival of post-critical reflections at the ocean Moho are highlighted.

associated with a specific seismic phase.

3.6 Pseudo 3-D Modeling

The pseudo-spectral method offers a solution to the P-SV seismic wave-field in two-dimensions. The ray tracing method calculates traveltimes and amplitudes in two-dimensional media. However, the regional seismic wave-field along the Cascadia subduction zone from a mega-thrust event in three-dimensions is required. In order to accomplish this, a pseudo 3-D forward modeling method is employed. That is, a three-dimensional model is decomposed into a series of two-dimensional models. Forward modeling is performed for the series of two-dimensional models and the results are combined to obtain a three-dimensional result. In this section, the method by which a three-dimensional velocity model of the Cascadia subduction zone is decomposed into a series of two-dimensional velocity model will be outlined. Furthermore, the method of combining the results from these two-dimensional models will be discussed.

In some instances, a two-dimensional model is a valid representation of a three-dimensional model. A two-dimensional velocity model corresponds to a three-dimensional velocity model assuming lateral homogeneity in a direction normal to the plane of the model. A two-dimensional assumption for the source is a reasonable approximation considering a rupture area extending 100s of kilometers laterally and displacements from a mega-thrust event oriented predominantly along the dip of the oceanic slab [McNeill et al., 2004]. Therefore, a source initiated in two-dimensional space corresponds to a mega-thrust event in three-dimensional space assuming lateral homogeneity in the strike direction.

The Cascadia subduction zone exhibits a degree of lateral homogeneity parallel to the margin. This is evident by the contours of the subducting Juan de Fuca Plate (figure 3.1). Therefore, the three-dimensional velocity model of the Cascadia subduction zone can be decomposed into a series of two-dimensional velocity models perpendicular to the margin. The orientation of the two-dimensional profile is defined with respect to the direction of the steepest decent of the slab in the vicinity of the source. In order to define this direction, the slab contours are projected into a Universal Transverse Mercator (UTM) coordinate system. In this coordinate system the gradient of the slab dip in the vicinity of the source is calculated, which provides the direction of steepest decent. By specifying the profile line in this way, the lateral homogeneity about the profile line in the three-dimensional model is maximized. Figure 3.8 illustrates the profile lines used to decompose the three-dimensional model for sources located at specific slab depths.

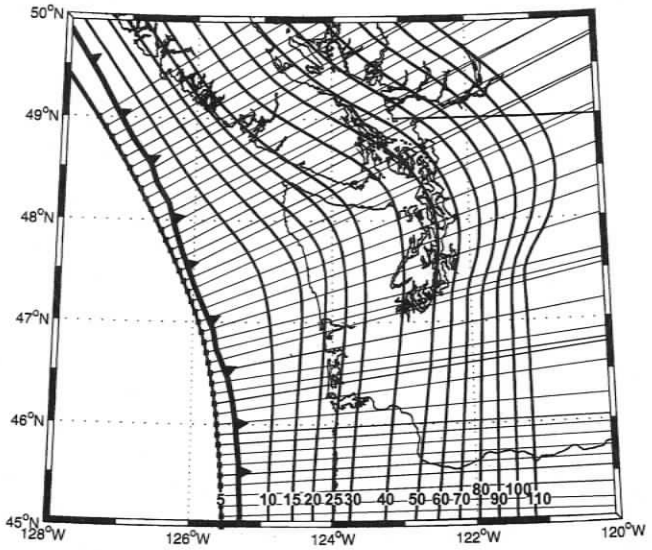

(a)

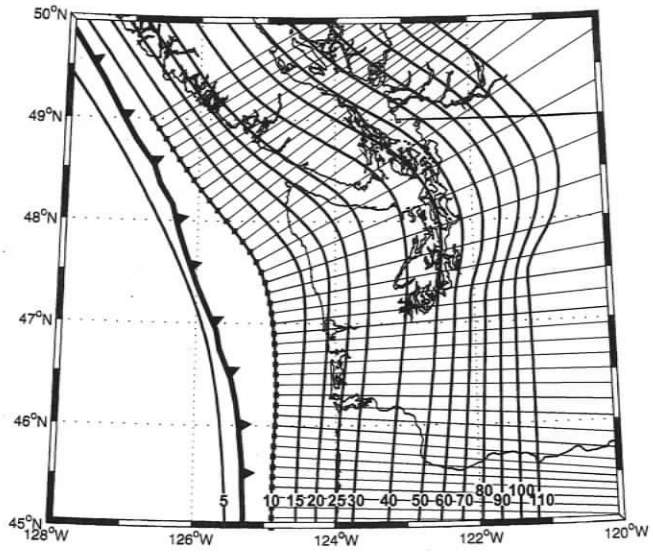

(b)

Figure 3.8 Profile lines applied to decompose the three-dimensional velocity model of the Cascadia subduction zone. Source depths of (a) 5 km, (b) 10 km, (c) 15 km, (d) 20 km, (e) 25 km and (f) 30 km.

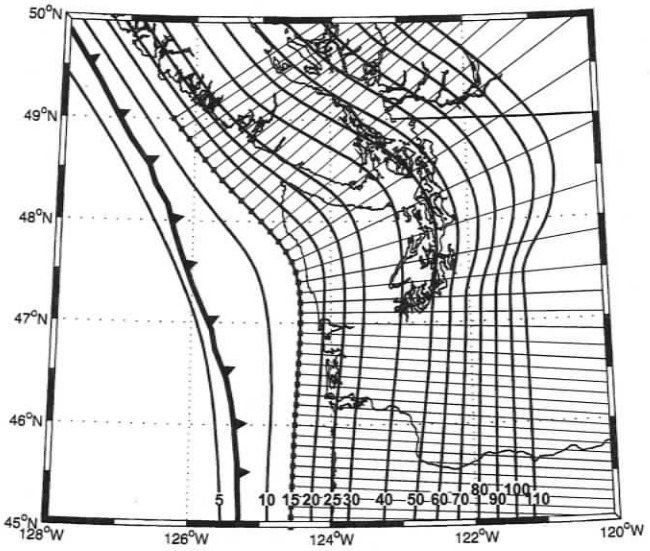

(c)

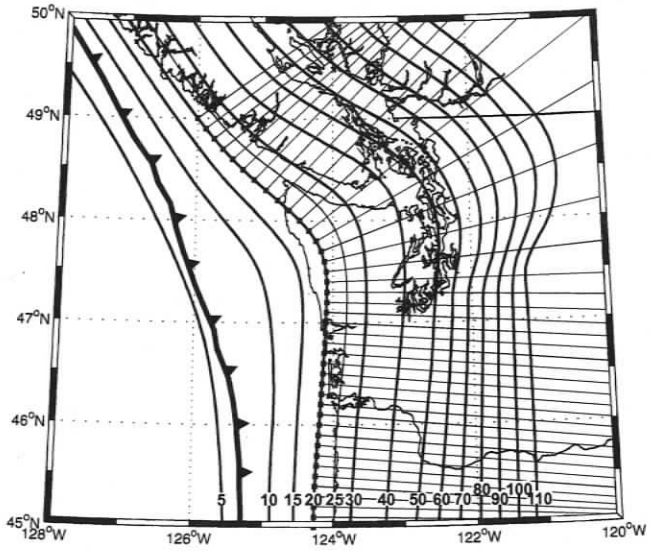

(d)

Figure 3.8 continued...

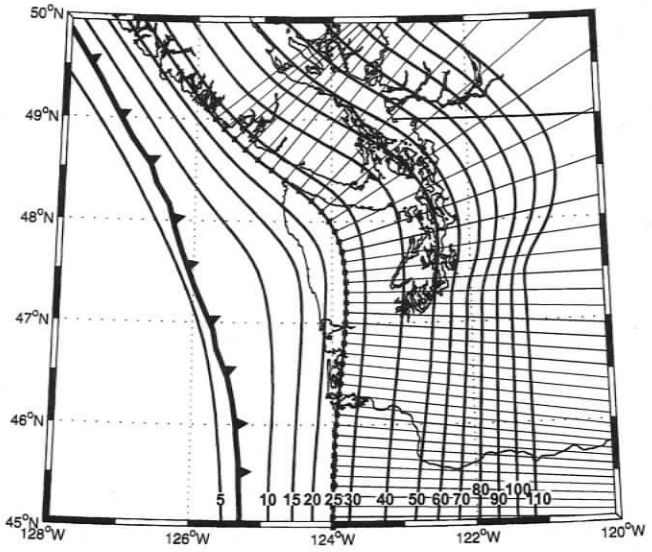

(e)

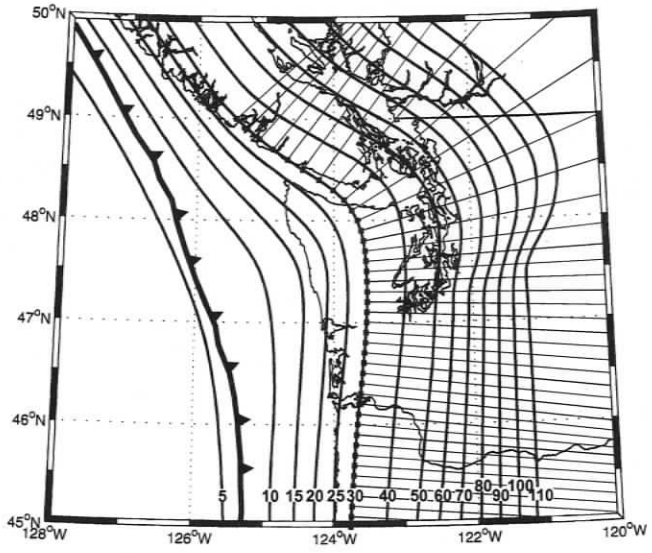

(f)

Figure 3.8 continued...

For each profile line a two-dimensional velocity model is derived from the velocity model for the Cascadia subduction zone. A source at the slab interface at a specific depth is initiated within the two-dimensional velocity model. The pseudo-spectral method produces a synthetic seismic section along the profile. Peak amplitudes are measured from the synthetic seismic section. The amplitudes calculated for the profiles with a common source depth are then combined using a triangle based linear interpolation. The result gives amplitudes in terms of geographic location for a mega-thrust event occurring at a specific depth.

3.7 Attenuation Calculations

The pseudo-spectral method provides a direct solution for an isotropic elastic solid undergoing infinitesimal deformation. However, this formulation does not account for the affect of seismic attenuation on P- and S-waves. To apply attenuation to the pseudo-spectral method results, the effect of seismic attenuation with respect to the amplitude of individual seismic phases needs to be quantified. This is accomplished by a comparison of seismic phase amplitudes from a model with no attenuation to a model that incorporates attenuation. Specific seismic phase amplitudes are numerically calculated by a ray-tracing algorithm.

The examination of the pseudo-spectral synthetic seismic section identifies two seismic phases responsible for vertical peak ground displacements, namely, the direct S-wave and the S-wave reflected from the oceanic Moho (oceanic SmS) (figure 3.9a). The travel-time curve associated with the direct S-wave phase is very simple (figure 3.9b). However, the traveltime curve of the oceanic SmS phase is complicated with several branches. These travel-time branches are associated with propagation paths through the complicated velocity structure of the forearc mantle wedge. Based upon traveltime branches, there are three possible propagation paths for the oceanic SmS phase. The first path propagates through the continental crust, the second path propagates through the mantle wedge and the third path propagates through the mantle wedge and continental upper mantle. Amplitude calculations are performed for the seismic phases and travel-time branches for a model without attenuation and a model with attenuation. A comparison of the amplitudes yields scaling factors as a function of epicentral distance, which quantifies the effect of seismic attenuation on a specific seismic phase (figure 3.9c). An overall scaling factor is derived from the attenuation effect of phases responsible for peak ground motions (figure 3.9d). The overall scaling factor is then applied to the peak ground motions from the pseudo-spectral method (figure 3.9e). Figure 3.9 displays the process of developing an attenuation scheme and the resultant application to the pseudo-spectral results

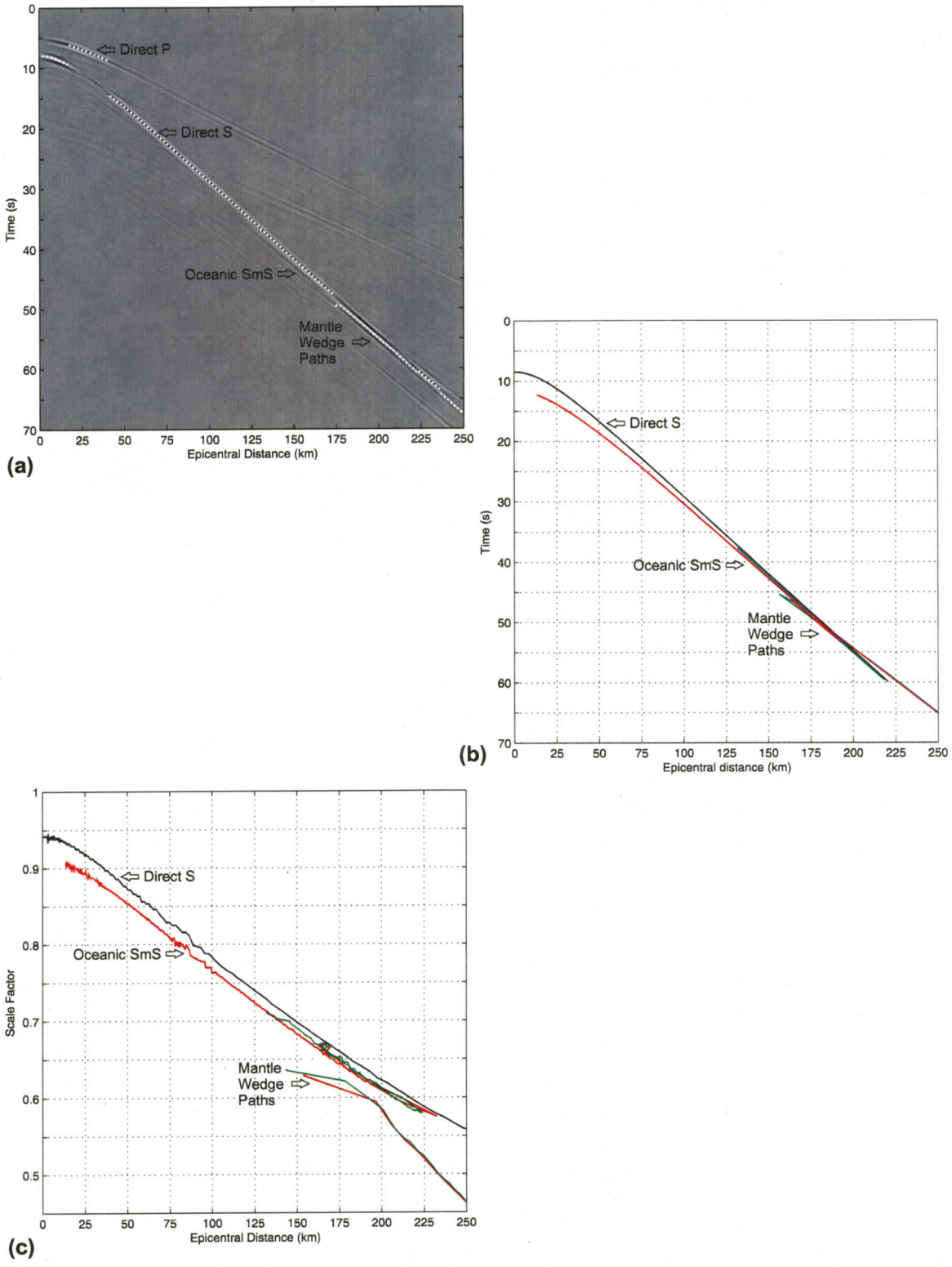

Figure 3.9 Algorithm to pick phase specific amplitudes. (a) Vertical component pseudo-spectral synthetic seismic section (dashed line indicates peak amplitudes). (b) Travel-times for the Direct S (black), the oceanic SmS (red) and refraction in the oceanic crust (green) calculated by the ray-tracing method. (c) Vertical component peak ground motion as a function of epicentral distance. Peak amplitudes associated with the arrival of post-critical reflections at the ocean Moho are

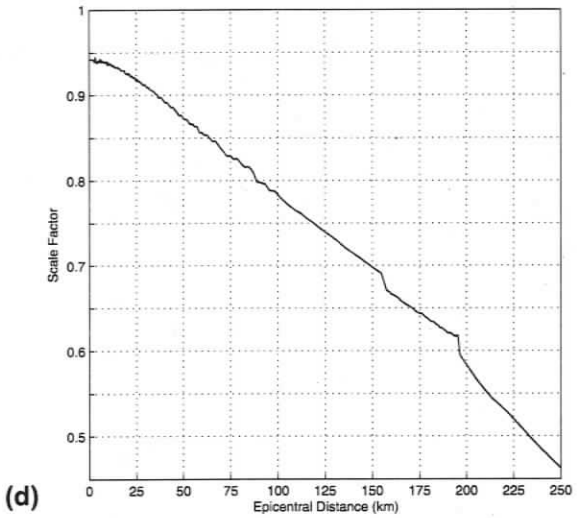

(d)

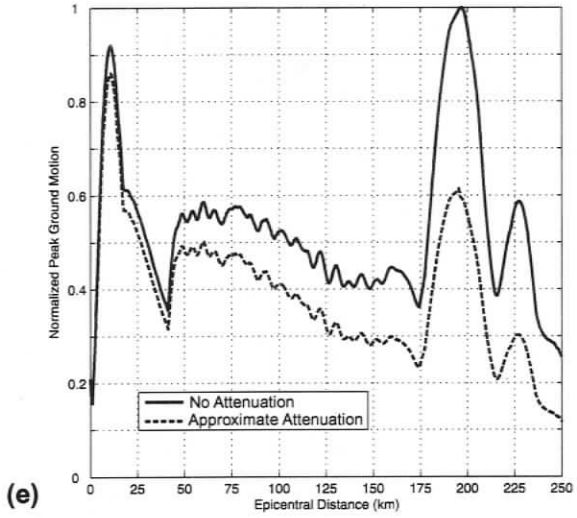

(e)

Figure 3.9 Attenuation scheme continued. (d) Overall scaling factor accounting for approximate attenuation. (e) Peak ground motions from the pseudo-spectral method with attenuation (dashed line) and without (solid line).

3.8 Limitations

In order to numerically simulate ground motions from a mega-thrust event in the Cascadia subduction zone, several approximations were applied to simplify the complex rupture processes as well as the structural model. These approximations impose limitations on the results.

The simulations have involved relatively simple structural models, as the objective is to isolate and characterize the effect of post-critical reflections at the oceanic Moho to ground motions observed on the surface. Previous finite difference simulations have indicated that additional complexities in the velocity model do not produce significant secondary arrivals; direct waves, refractions within the oceanic crust and post-critical reflections at the oceanic Moho control peak amplitudes [Cohee et al., 1991]. The incorporation of bathometry, topography and complexities in upper crustal velocities will not substantially influence the character of wave propagation in the simple structural model.

The transverse invariance of structure is a reasonable approximation where the strike of the subduction zone remains relatively constant. Beneath western Washington the subducting Juan de Fuca Plate exhibits arched slab geometry and the 2-D approximation may be less appropriate in this region. However, the qualitative behavior of wave propagation should be adequately represented.

Simulated results employ a Ricker source time-function with a specified dominant frequency to demonstrate the influence of post-critical reflections while excluding the influence of complex source processes. However, mega-thrust events exhibit diverse rupture behavior from very simple rupture histories to very complex multiple events [Bilek et al., 2004]. Furumura & Furumura [2001] suggest that the actual wave-field from a mega-thrust event could be evaluated by convolution of the time-history of the source process with the simulated waveform.

In the previous analysis of ground motions from mega-thrust events, individual 2-D double-couple line sources orientated to represent slip on the subduction thrust were located at specific depth contours of the oceanic slab. Clearly, localization of the source to a line in space (2-D) is not entirely appropriate as the extent of rupture parallel to the dip could exceed 100 km if the entire fault is ruptured [Rogers, 1988]. However, the use of a line source simplifies the analysis of the influence of post-critical reflections at the oceanic Moho to peak ground motions. Realistic rupture geometries can be modeled by linearly superimposing a distribution of delayed sequence of sources [McNeill et al., 2004].

In the previous numerical simulations, peak ground motions were examined for a variety of source locations. All sources were assigned the same magnitude and hence represent equivalent slip on the subduction thrust fault. Clearly, this is not entirely realistic as there is significant evidence that earthquake rupture varies both laterally and down-dip in shallow subduction zones [Bilek et al., 2004]. Nevertheless, the use of equivalent slip sources should adequately represent the relative behavior of peak ground motions. Realistic earthquake rupture can be modeled by linearly superimposing a distribution of magnitude scaled and delayed sequence of sources on the subduction fault thrust interface.

CHAPTER 4
RESULTS

4.1 Introduction

For a realistic 3-D structural model of the Cascadia subduction zone, pseudo 3-D P-SV wave simulations for a hypothetical mega-thrust event with dominant source frequencies of 1 Hz, 2 Hz and 3Hz are performed to investigate the pattern of ground motions. Pseudo-spectral synthetic seismograms are examined in order to define the geographical region in which post-critical reflections at the oceanic Moho are a primary component of the seismic wave-field. Within this region, the contribution of post-critical reflections at the oceanic Moho to the seismic wave-field is quantified in terms of an increase in peak ground motions. Attenuation is not modeled explicitly in the pseudo-spectral synthetics. However, an approximate attenuation scheme, based on ray tracing of specific phases, is applied.

4.2 Peak Ground Motions on Synthetic Seismograms

To identify the geographical region in which post-critical reflections at the oceanic Moho are a primary component of the seismic wave-field (post-critically enhanced regions), 2-D P-SV pseudo-spectral synthetic seismograms were examined. A series of 2-D profiles were selected to approximate a 3-D model of ground motions from a mega-thrust event.

In the pseudo-spectral synthetic seismograms, the strongest ground motions are found in the vertical component and are caused by the S-wave-field. The peak ground motions in the vertical component of the synthetic seismograms, in the absence of a low velocity surface layer, can be considered analogous to the peak ground motions in the radial horizontal component. A low velocity surface layer is excluded from the simulation model due to computational limitations. The addition of a low velocity surface layer will partition the strong amplitudes of the S-wave-field into the horizontal component due to near vertical incidences of up-going SV-waves on the free surface.

The direct S and oceanic Moho post-critical reflection (oceanic SmS) are the primary components of the S-wave-field. The arrivals of these phases are mainly responsible for the pattern of peak ground motions (figure 4.1). For near source distances (0 – 65 km), the pseudo-spectral synthetic seismograms are dominated by the direct S-wave arrival. At greater distances the S-wave reflection off the oceanic Moho turns post-critical, producing an arrival that is comparatively larger than the direct S arrival, thereby increasing peak ground motion amplitudes.

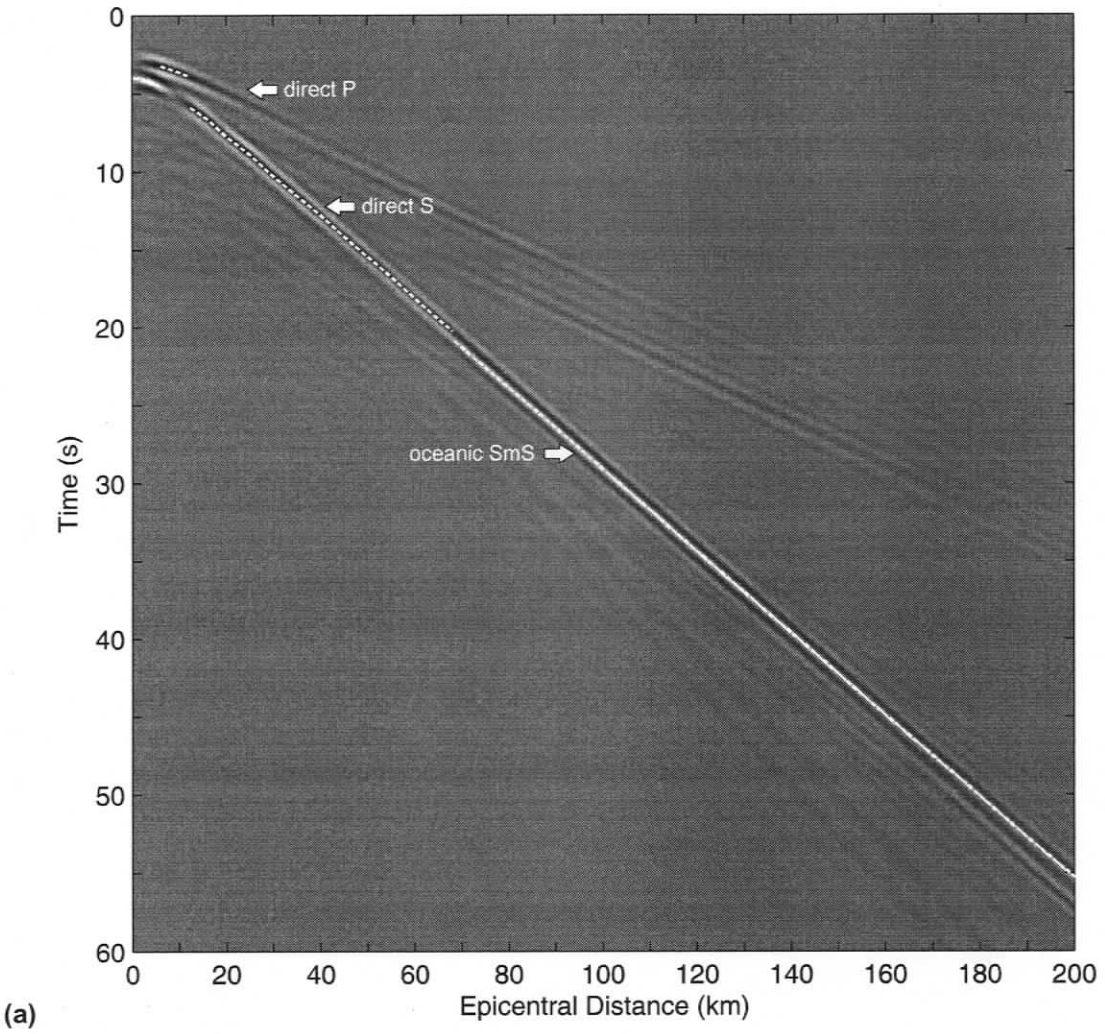

(a)

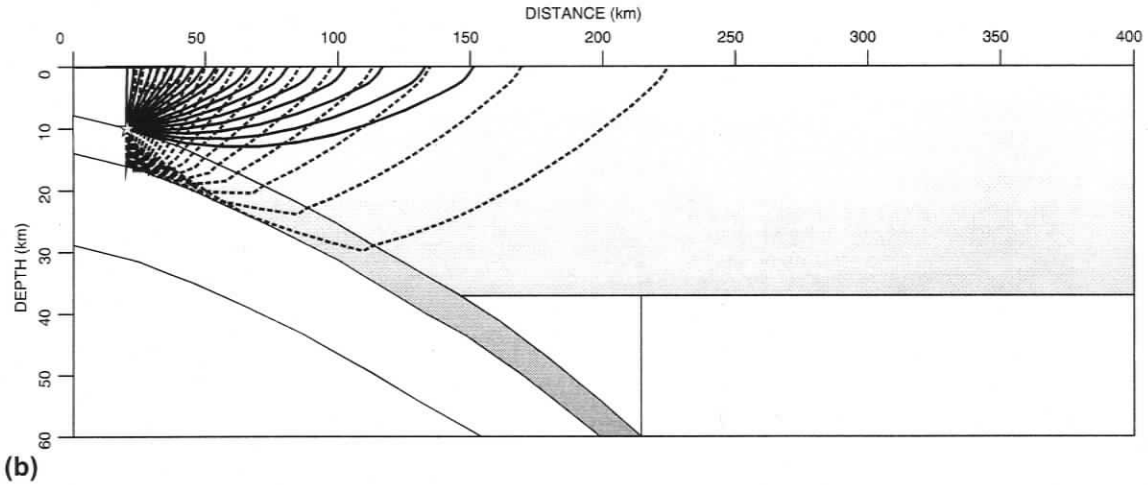

(b)

Figure 4.1 (a) Vertical component synthetic seismogram for a 1 Hz source at the down-dip limit of the locked zone (dashed line indicates peak amplitudes). (b) Ray tracing diagram indicating propagation paths of direct waves (solid line) and reflections at the oceanic Moho (dashed line).

A suite of later arrivals may also cause an increase in peak ground motion amplitudes (figure 4.2). These arrivals represent a sequence of strong amplitude multiples of post-critical reflections between the base of oceanic layer 2 and the top of the oceanic crust. These arrivals are notably absent for lower source frequencies where wavelengths are much greater than the ~2 km thick oceanic layer 2.

The presence of a low velocity forearc mantle wedge causes a narrow region on the surface to receive simultaneously, arrivals that have propagated along different paths (figure 4.3). In particular, the post-critical reflection at the oceanic Moho may follow several different propagation paths through this region. The complex interaction of these arrivals produces the observed peak ground motions.

4.3 Simulations

Numerical simulations were run for a variety of source locations and source frequencies to provide insight into the character of the post-critically enhanced regions for a mega-thrust event. For mega-thrust events, the width of the seismogenic zone is defined by the up-dip limit and down-dip limit of the locked zone. However, rupture may extend beyond the seismogenic or locked zone. The up-dip or seaward limit of rupture could be the seafloor at the deformation front. A conceptual model for the stress accumulating across the Cascadia subduction zone interface implies that the down-dip or landward extent of rupture for the next mega-thrust earthquake is marked by the down-dip limit of the transition zone [Dragert et al., 1994]. As identified in figure 2.5, the up-dip limit of the locked zone, the down-dip limit of the locked zone and the down-dip limit of the transition zone for Cascadia correspond approximately to the 5 km, 10 km and 25 km depth contours of the subducting oceanic crust, respectively. In the following, sources along the subducting oceanic crust interface at those depths, as well as at 15 km, 20 km and 30 km are considered.

In the following analysis of ground motions from mega-thrust events, individual 2-D double couple line sources represent slip on the subduction thrust. The seismic source has a Ricker time history function that imparts seismic waves with a specified dominant frequency. Dominant source frequencies of 1 Hz, 2 Hz and 3 Hz are considered. For a 1 Hz source, numerical simulations were conducted on a 675 x 120 grid with a node spacing of 500 m for a series of profiles. Wave propagation was simulated over a 75 second duration after source initiation using a temporal sampling of 0.01 seconds, allowing frequencies between 0 Hz and 3 Hz to be accurately modeled. For a 2 Hz source, numerical simulations were conducted on a 1000 x 200 grid with a node spacing of 300 m. Wave propagation was simulated over a 70 second duration using a temporal sampling of 0.007 seconds, allowing frequencies less than 5 Hz to be accurately modeled. Finally, for a 3 Hz source, numerical simulations were conducted on a 1200 x 240 grid with a node spacing of 250 m. Wave propagation was simulated over a 60 second duration using a temporal sampling of 0.006

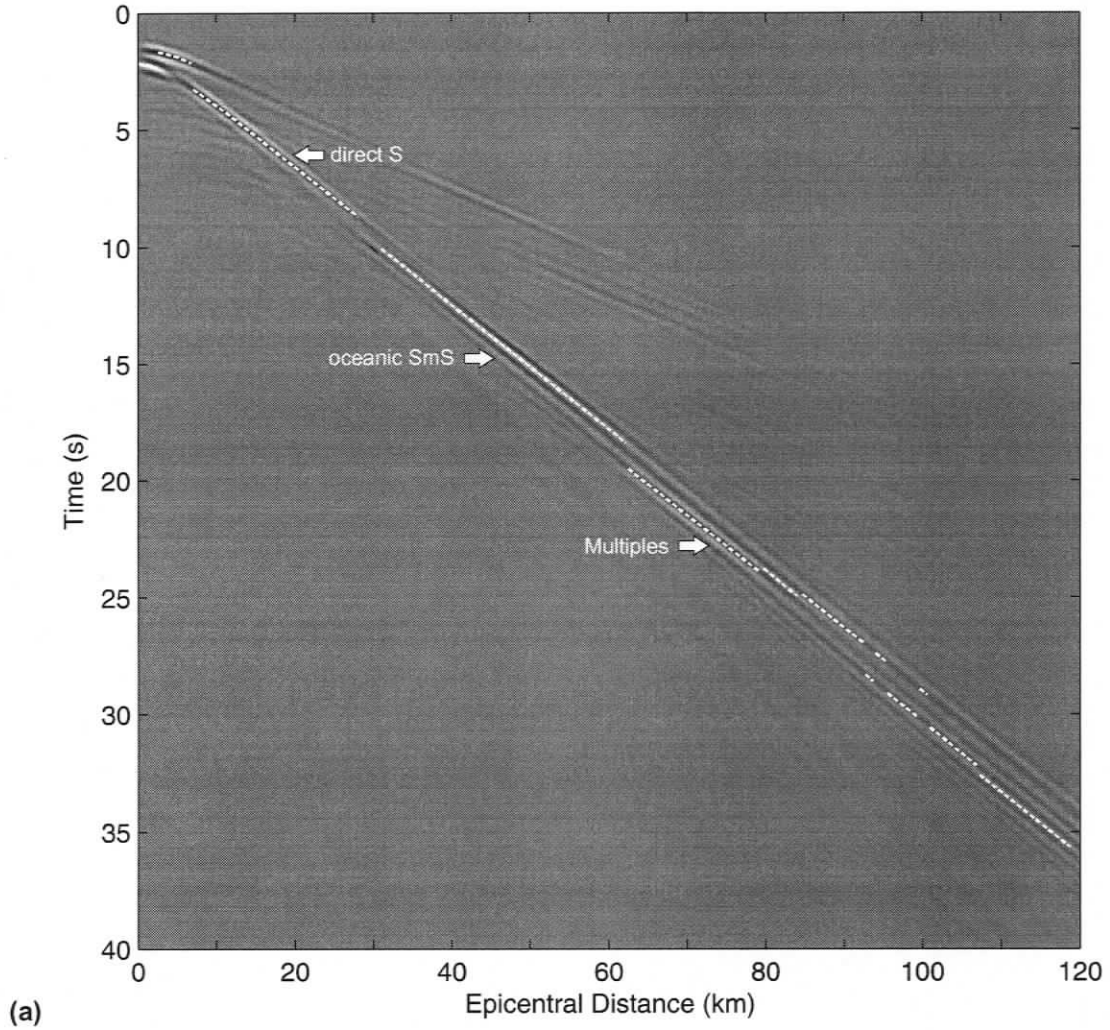

(a)

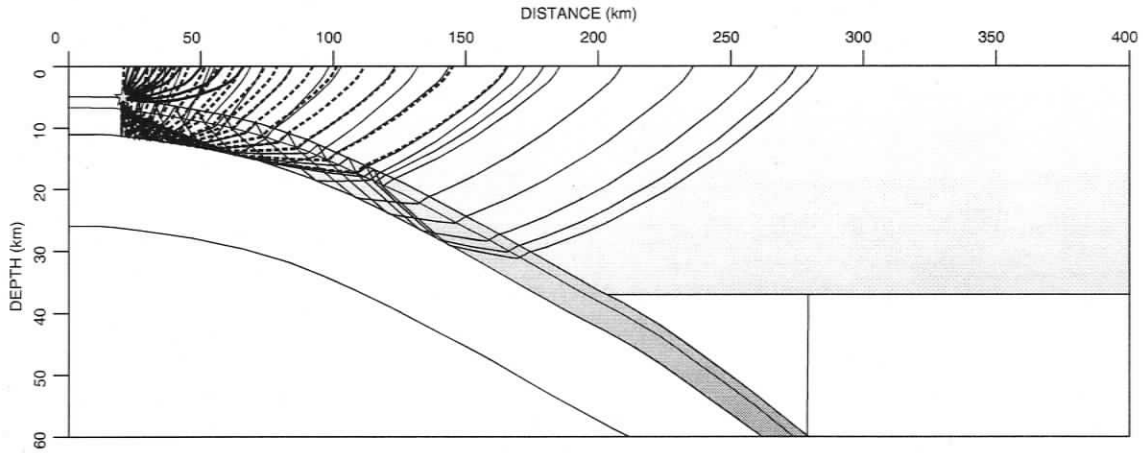

(b)

Figure 4.2 (a) Vertical component synthetic seismogram for a 2 Hz source at the up-dip limit of the locked zone (dashed line indicates peak amplitudes). (b) Ray tracing diagram indicating propagation paths of direct waves (thick solid line), reflections at the oceanic Moho (dashed line) and multiples (thin solid line).

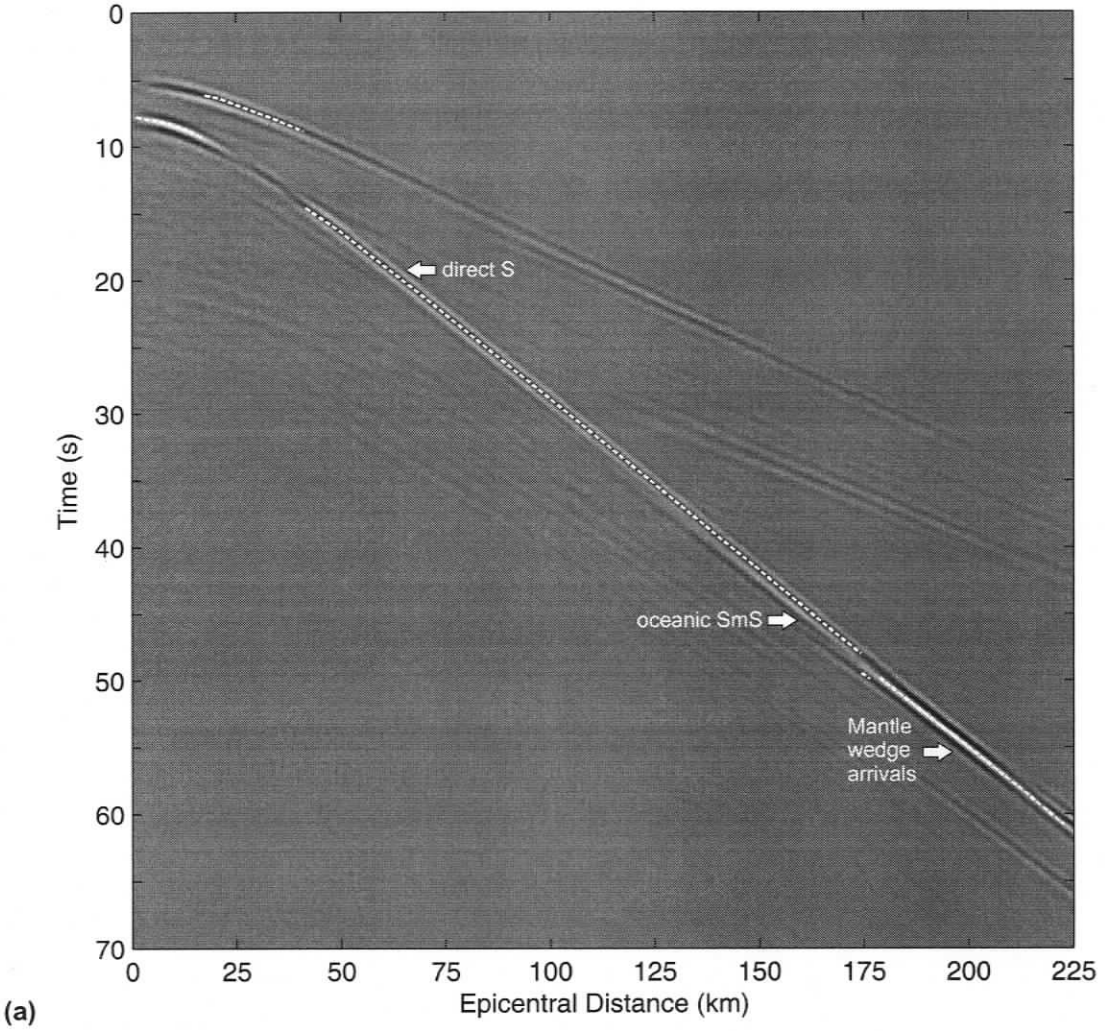

(a)

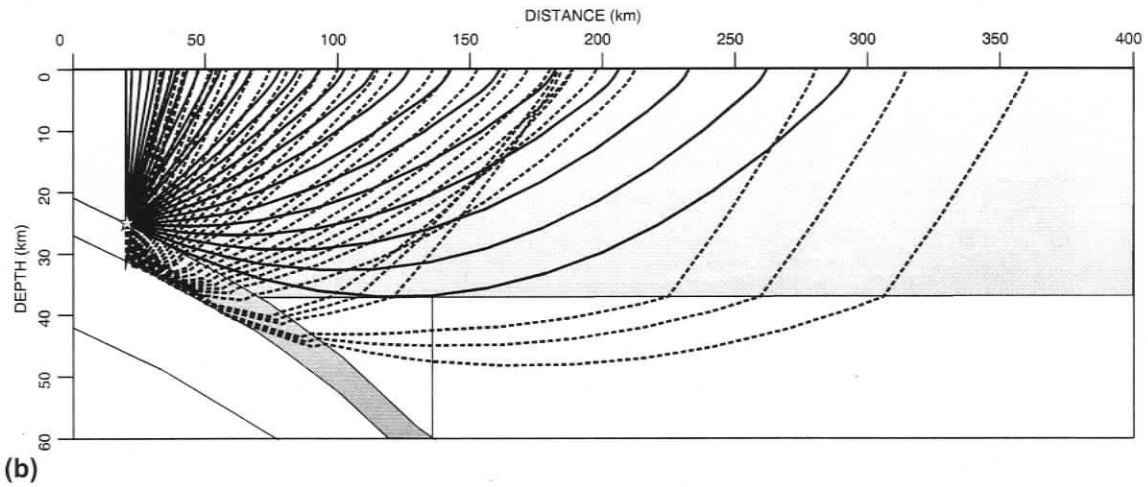

(b)

Figure 4.3 (a) Vertical component synthetic seismogram for a 1 Hz source at the down-dip limit of the transition zone (dashed line indicates peak amplitudes). (b) Ray tracing diagram indicating propagation paths of direct waves (solid line) and reflections at the oceanic Moho (dashed line).

seconds, allowing frequencies less than 6 Hz to be accurately modeled

4.4 Geographic Distribution of Post-critically Enhanced Peak Ground Motions

Figures 4.4 – 4.19 display the vertical component of peak ground motions (PGM) for the geographical region in which oceanic Moho post-critical reflections are a primary component of the seismic wave-field for the respective source frequency and down-dip extent of rupture. Normalization of the PGM is with respect to the peak amplitude on the vertical component synthetic seismograms from a source located at the up-dip limit of the locked zone. This normalization is defined independently for each source frequency.

4.4.1 1 Hz Source

In this section, the geographical region in which post-critical reflections at the oceanic Moho are a primary component of the seismic wave-field is examined as a function of the down-dip extent of rupture for a mega-thrust event with a dominant frequency of 1 Hz.

Figure 4.4 maps the normalized PGM of the post-critically enhanced region for rupture at the up-dip limit of the locked zone. PGM amplitudes decay with distance within 30 km of the source. Beyond 30 km, as strong post-critical reflections arrive, PGM amplitudes initially increase with distance. Maximum PGM amplitudes are located approximately 45 km from the source and decrease only slightly out to 70 km. Beyond 70 km, PGM amplitudes decay, corresponding approximately to geometric spreading in two dimensions. The post-critically enhanced region lies approximately parallel to the source location, beneath the ocean. The narrow offset between the source location and the post-critically enhanced region can be attributed to the shallow source depth and the shallow apparent dip of the oceanic slab in the vicinity of the source. The apparent dip in the vicinity of the source is approximately 3 degrees.

Figure 4.5 illustrates the post-critically enhanced region for rupture at the down-dip limit of the locked zone. The enhanced region is located between 60 km and 160 km from the source location, encroaching upon the urban corridor, with maximum PGM amplitudes occurring at approximately 80 km. Offsets between the source location and the enhanced region increase away from the arch in the subducting plate. This is due to an increase in the apparent dip of the subducting slab from ~7 degrees at the peak of the arch to ~10 degrees north and south. The magnitudes of the PGM amplitudes within the enhanced region have decreased with respect to the previous source location. This is a consequence of increased source depth and increased offset between the source location and the enhanced region

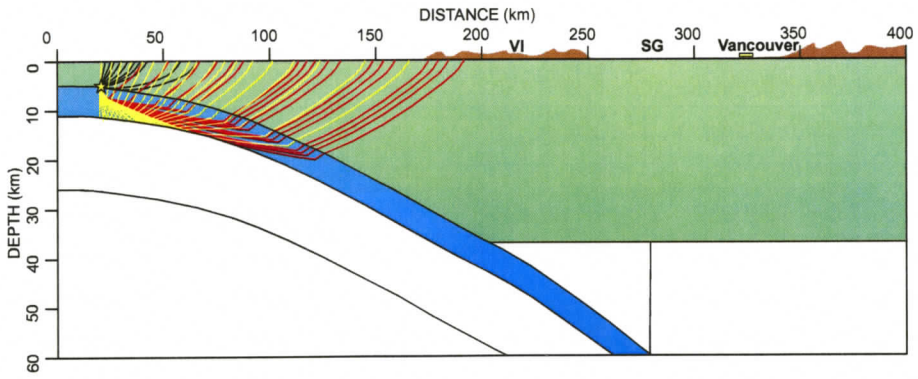

(a)

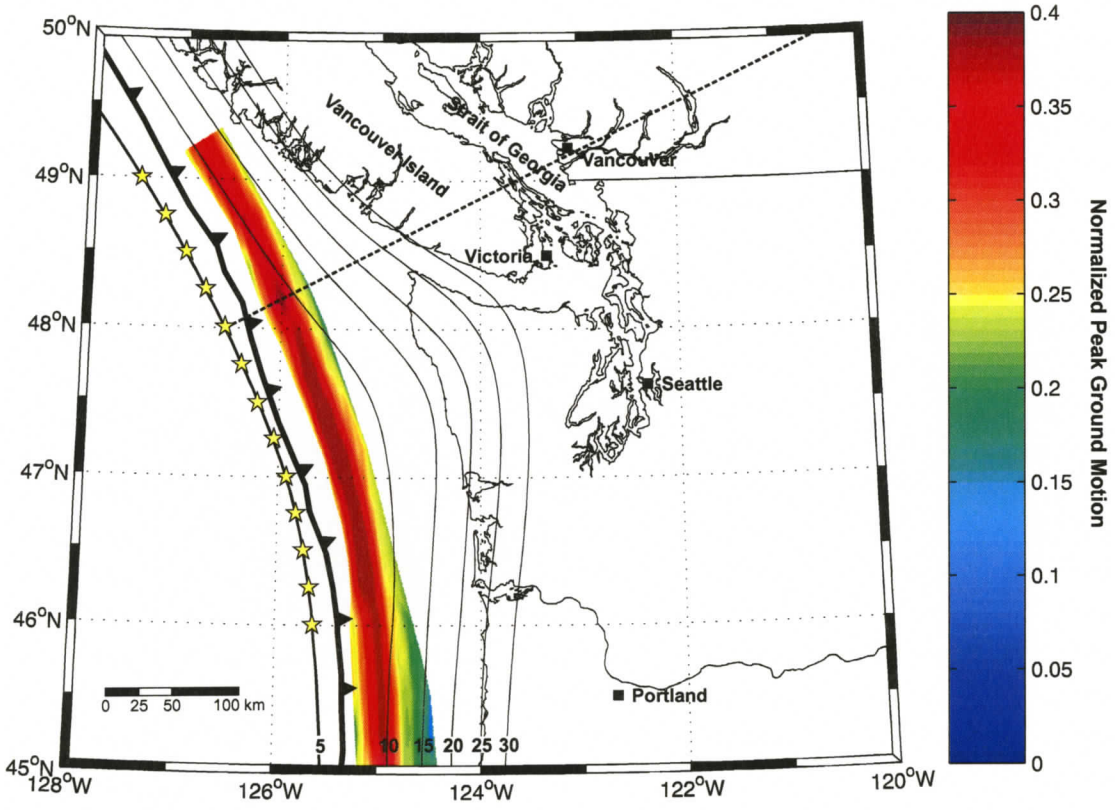

(b)

Figure 4.4 Post-critically enhanced region for a 1 Hz source (yellow stars) at the up-dip limit of the locked zone. (a) Ray tracing diagram indicating propagation paths of direct waves (green), refractions in the oceanic crust (red) and reflections at the oceanic Moho (yellow). (b) Normalized peak ground motions within the post-critically enhanced region. Ray tracing profile indicated by dashed line. Abbreviations: VI-Vancouver Island; SG-Strait of Georgia.

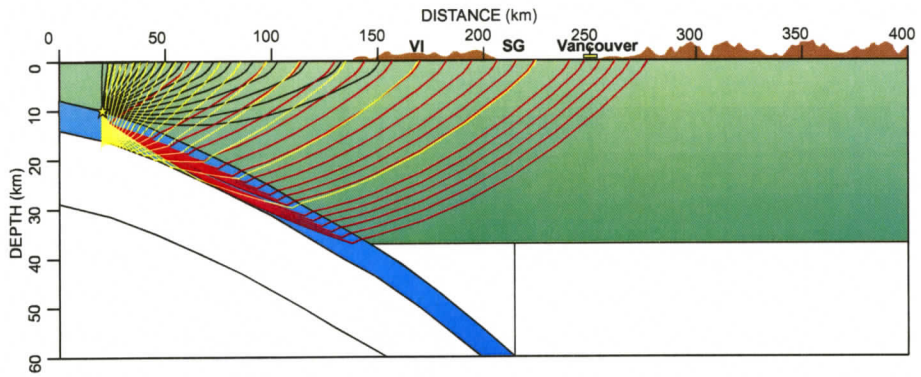

(a)

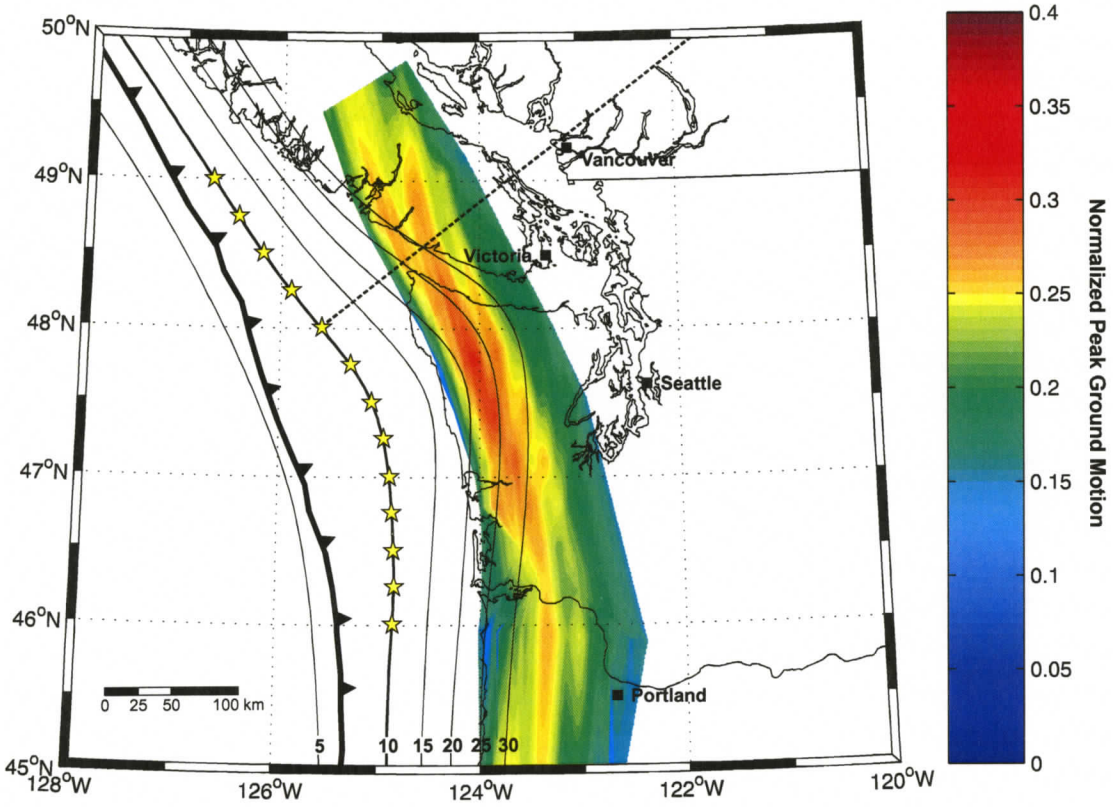

(b)

Figure 4.5 Post-critically enhanced region for a 1 Hz source (yellow stars) at the down-dip limit of the locked zone. (a) Ray tracing diagram indicating propagation paths of direct waves (green), refractions in the oceanic crust (red) and reflections at the oceanic Moho (yellow). (b) Normalized peak ground motions within the post-critically enhanced region. Ray tracing profile indicated by dashed line. Abbreviations: VI-Vancouver Island; SG-Strait of Georgia.

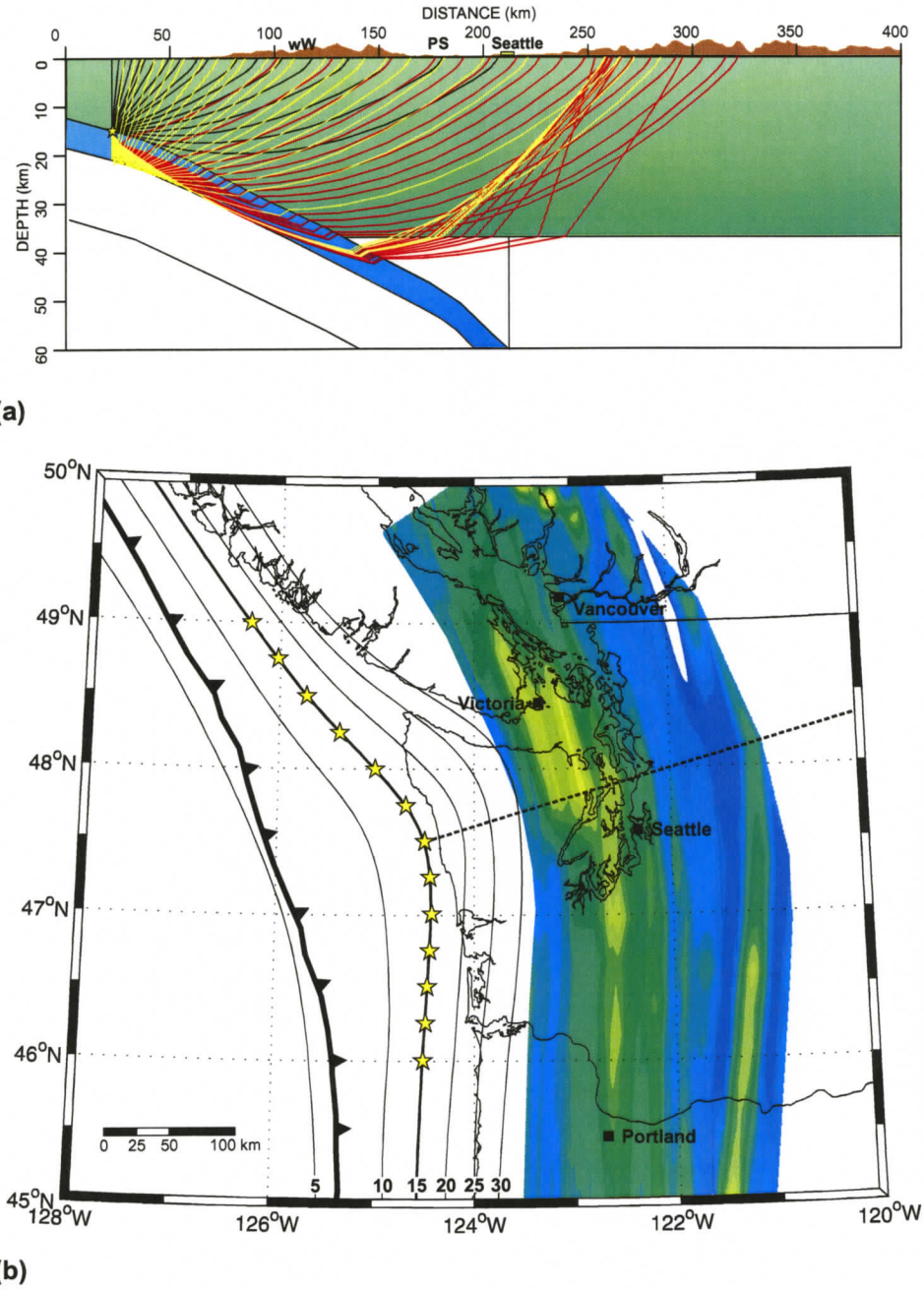

Figure 4.6 Post-critically enhanced region for a 1 Hz source (yellow stars) located at the 15 km depth contour of the oceanic slab. (a) Ray tracing diagram indicating propagation paths of direct waves (green), refractions in the oceanic crust (red) and reflections at the oceanic Moho (yellow). (b) Normalized peak ground motions within the post-critically enhanced region. Ray tracing profile indicated by dashed line. Abbreviations: wW-Western Washington; PS-Puget Sound.

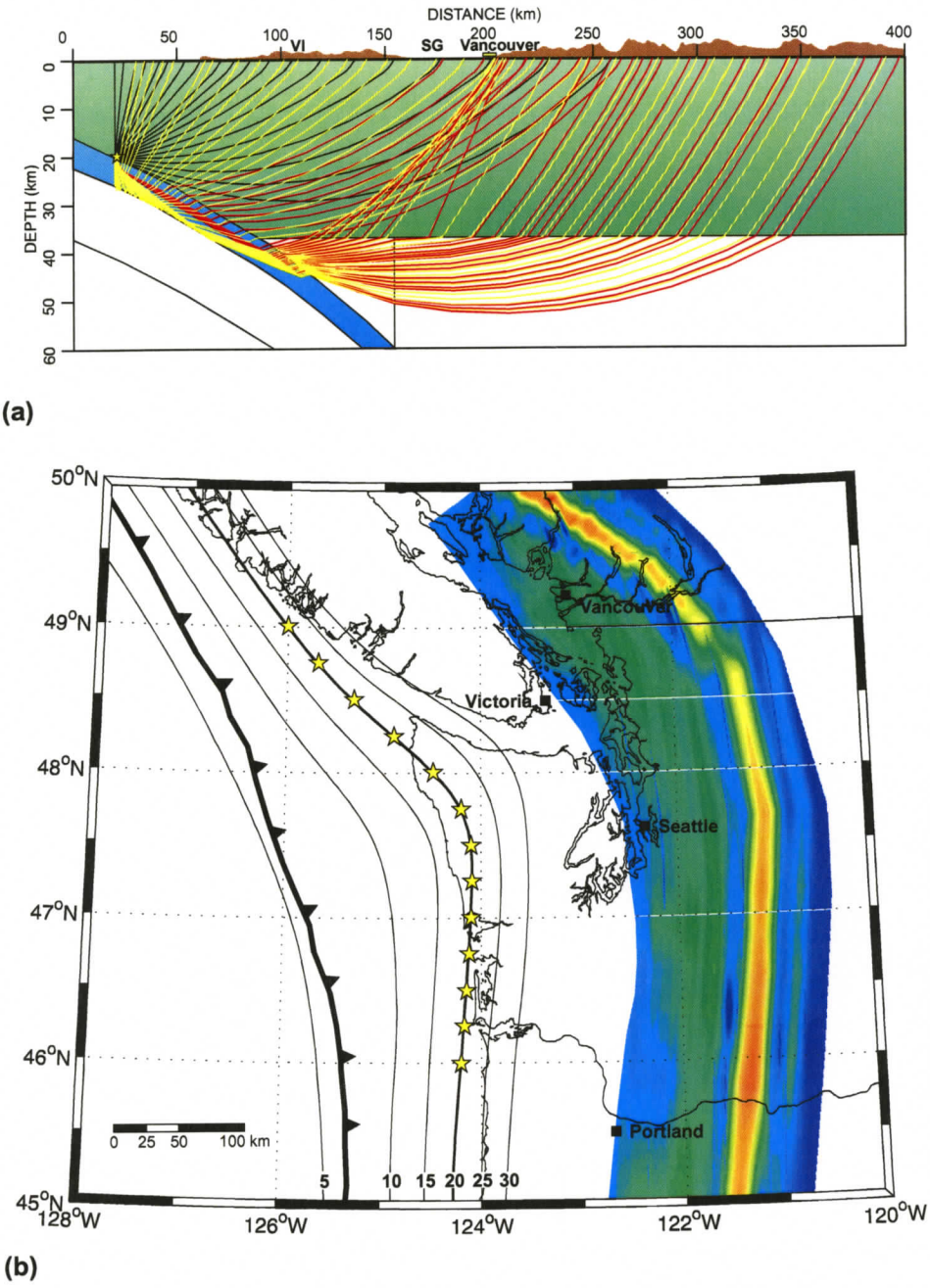

Figure 4.7 Post-critically enhanced region for a 1 Hz source (yellow stars) located at the 20 km depth contour of the oceanic slab. (a) Ray tracing diagram indicating propagation paths of direct waves (green), refractions in the oceanic crust (red) and reflections at the oceanic Moho (yellow). (b) Normalized peak ground motions within the post-critically enhanced region. Ray tracing profile indicated by dashed line. Abbreviations: VI-Vancouver Island; SG-Strait of Georgia.

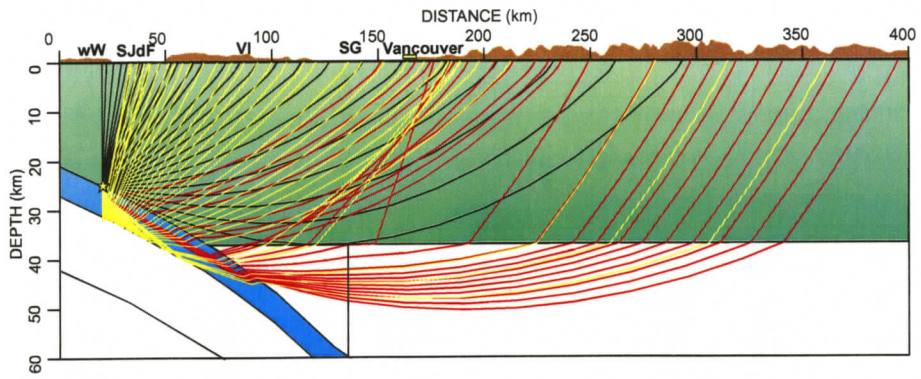

(a)

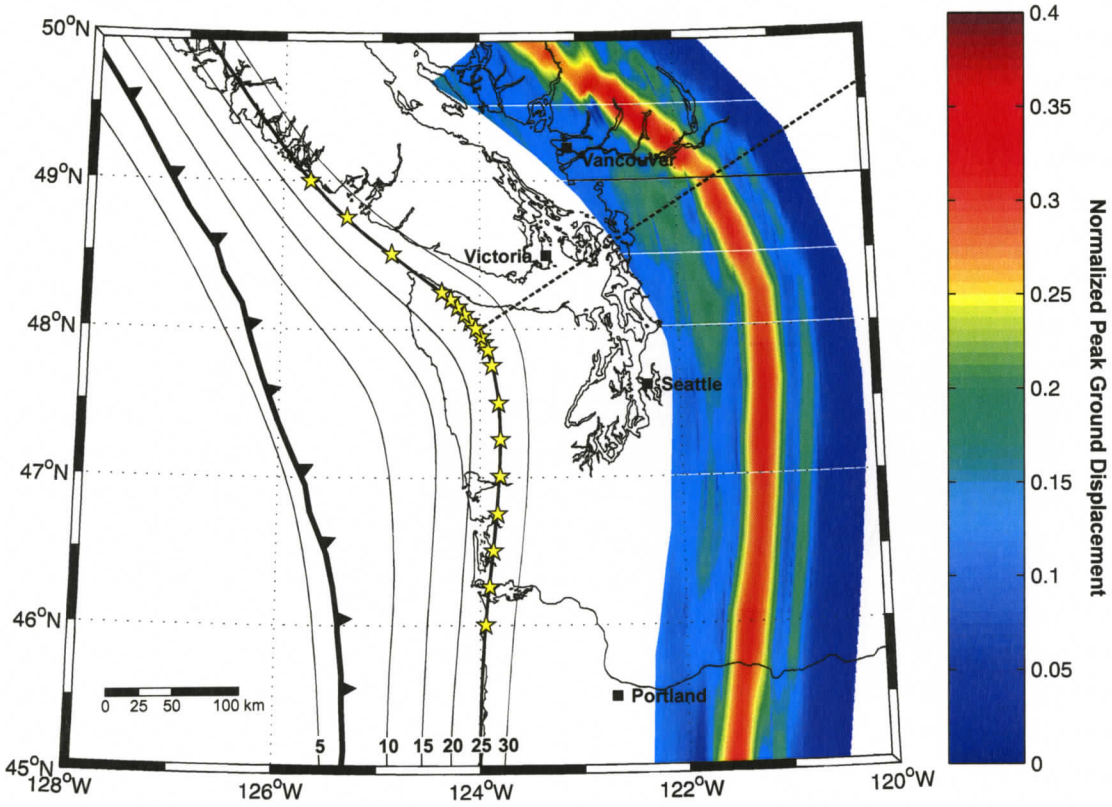

(b)

Figure 4.8 Post-critically enhanced region for a 1 Hz source (yellow stars) at the down-dip limit of the transition zone. (a) Ray tracing diagram indicating propagation paths of direct waves (green), refractions in the oceanic crust (red) and reflections at the oceanic Moho (yellow). (b) Normalized peak ground motions within the post-critically enhanced region. Ray tracing profile indicated by dashed line. Abbreviations: wW-western Washington; SJdF-Strait of Juan de Fuca; VI-Vancouver Island; SG-Strait of Georgia.

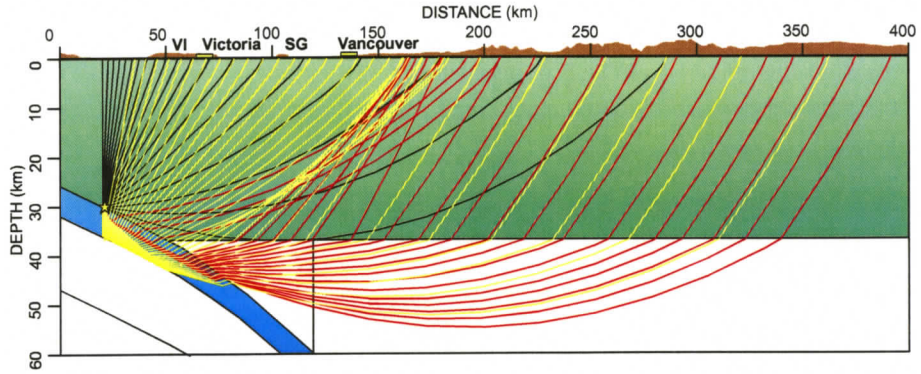

(a)

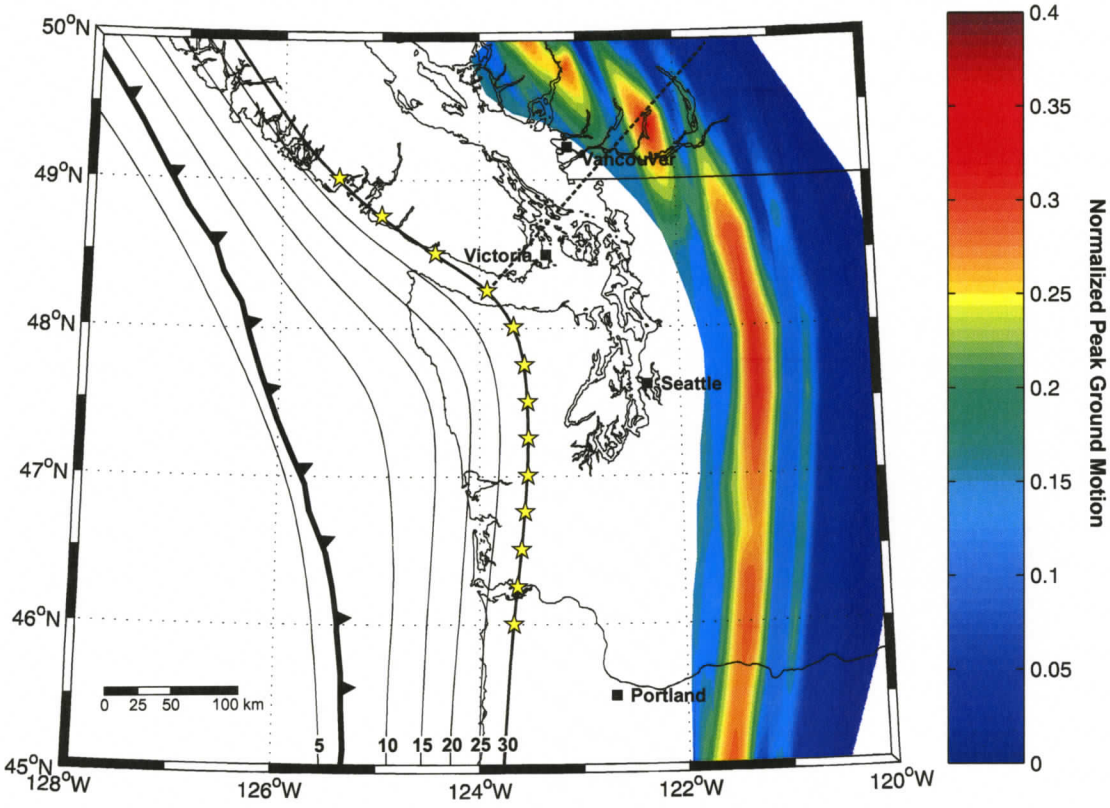

(b)

Figure 4.9 Post-critically enhanced region for a 1 Hz source (yellow stars) located at the 30 km depth contour of the oceanic slab. (a) Ray tracing diagram indicating propagation paths of direct waves (green), refractions in the oceanic crust (red) and reflections at the oceanic Moho (yellow). (b) Normalized peak ground motions within the post-critically enhanced region. Ray tracing profile indicated by dashed line. Abbreviations: VI-Vancouver Island; SG-Strait of Georgia.

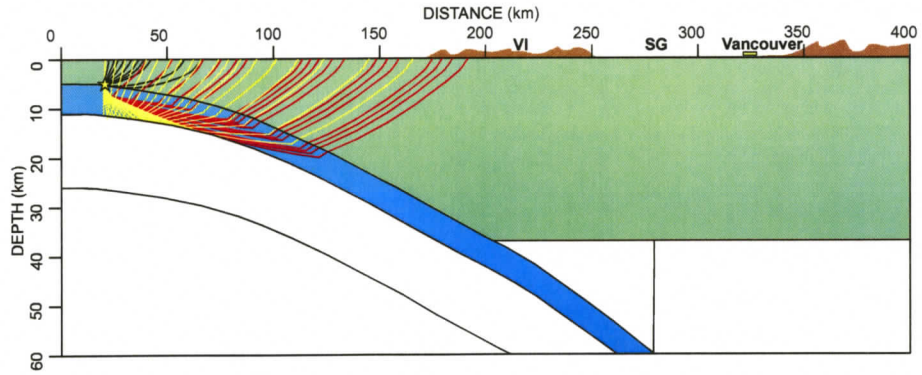

(a)

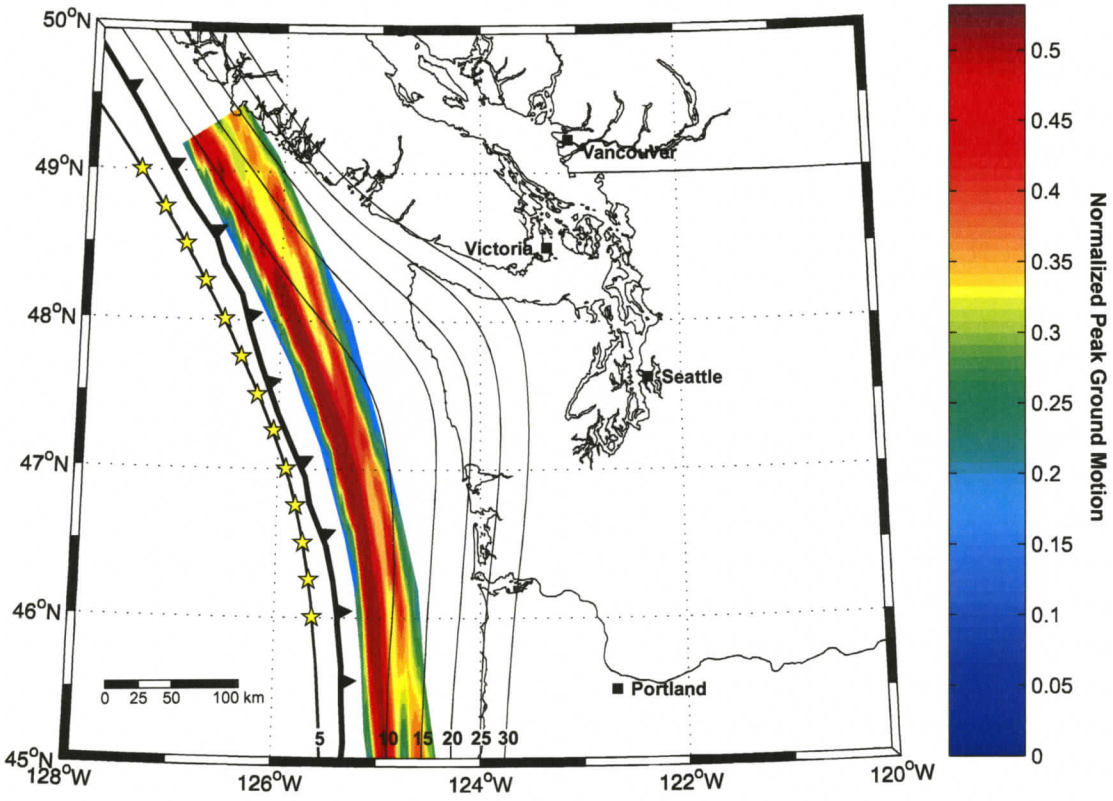

(b)

Figure 4.10 Post-critically enhanced region for a 2 Hz source (yellow stars) at the up-dip limit of the locked zone. (a) Ray tracing diagram indicating propagation paths of direct waves (green), refractions in the oceanic crust (red) and reflections at the oceanic Moho (yellow). (b) Normalized peak ground motions within the post-critically enhanced region. Abbreviations: VI-Vancouver Island; SG-Strait of Georgia.

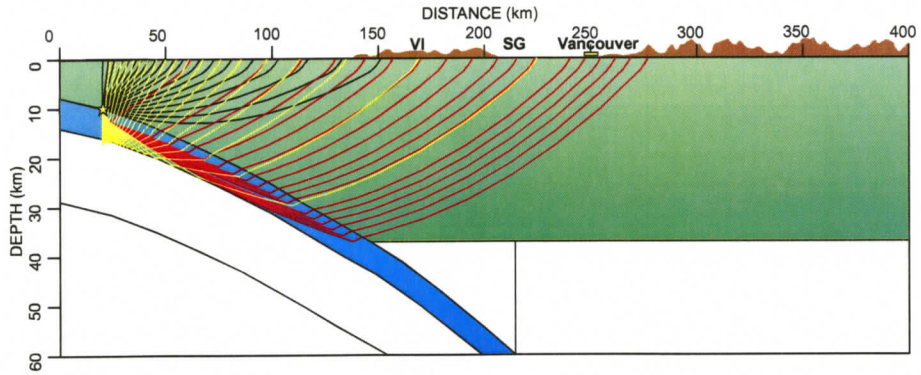

(a)

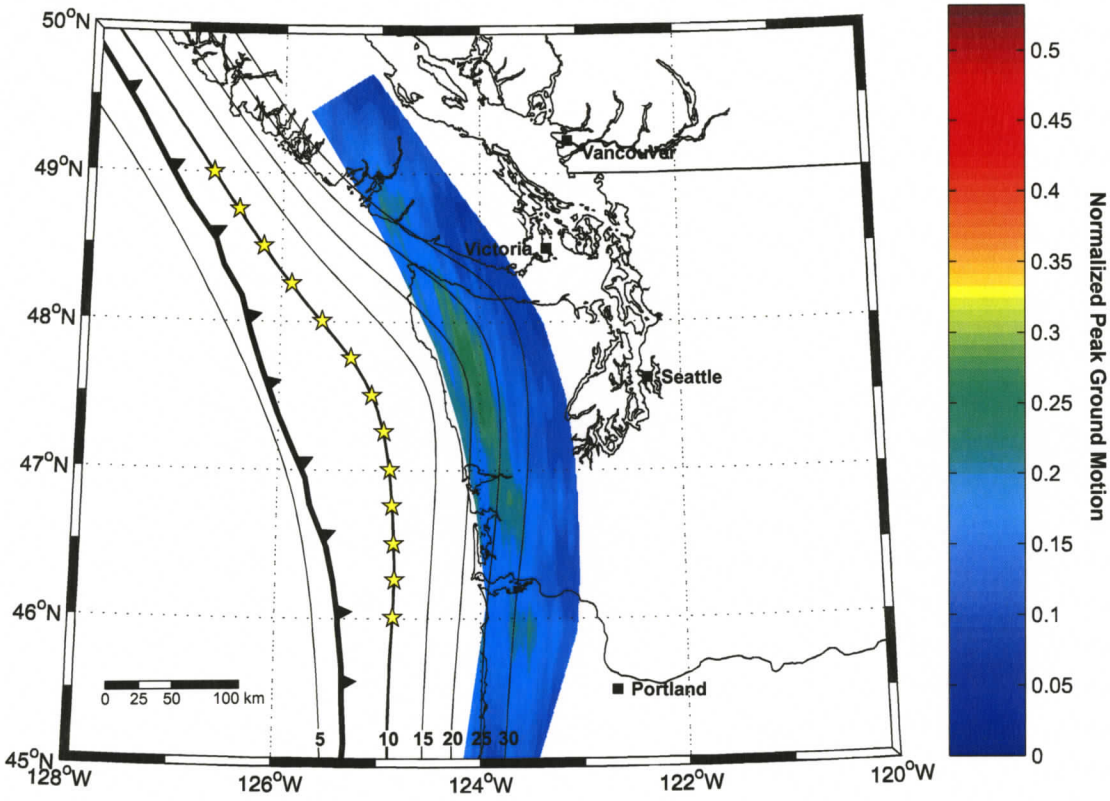

(b)

Figure 4.11 Post-critically enhanced region for a 2 Hz source (yellow stars) at the down-dip limit of the locked zone. (a) Ray tracing diagram indicating propagation paths of direct waves (green), refractions in the oceanic crust (red) and reflections at the oceanic Moho (yellow). (b) Normalized peak ground motions within the post-critically enhanced region. Abbreviations: VI-Vancouver Island; SG-Strait of Georgia.

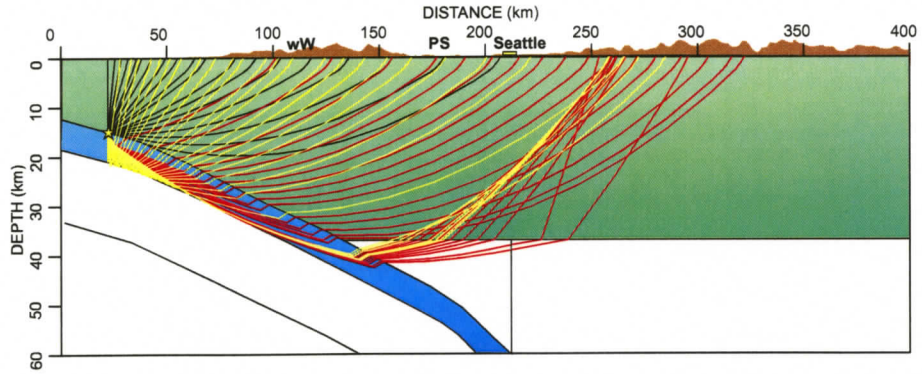

(a)

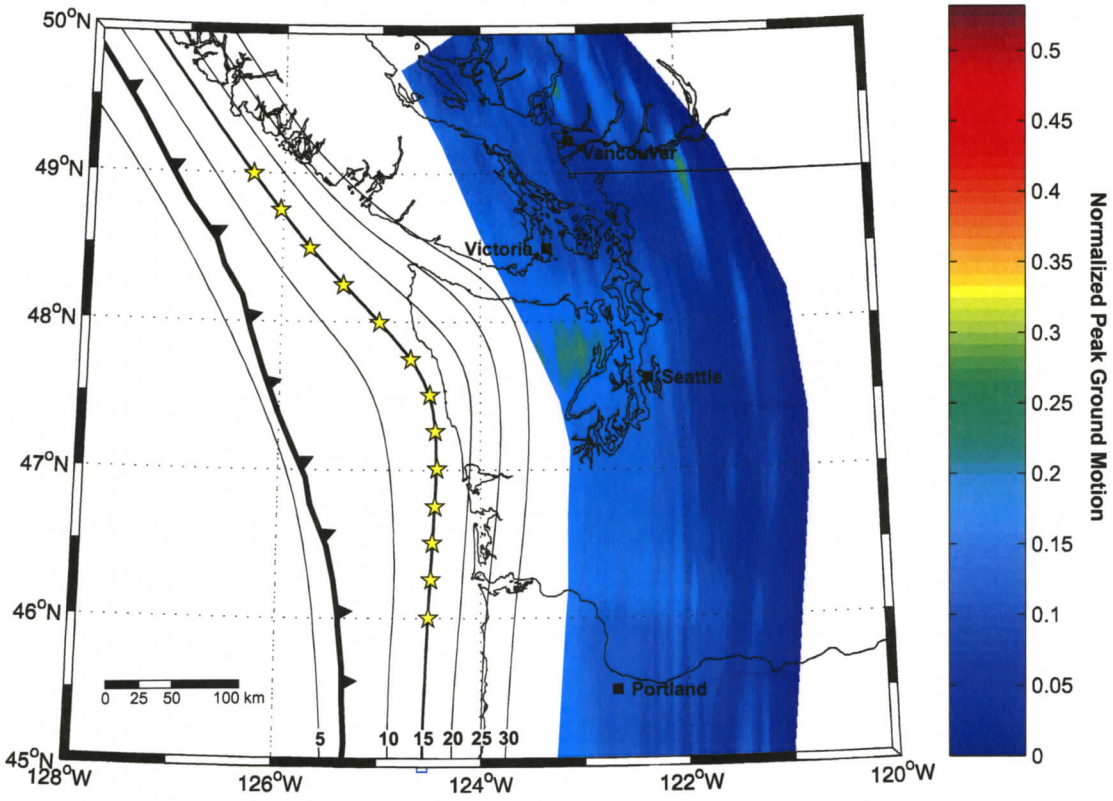

(b)

Figure 4.12 Post-critically enhanced region for a 2 Hz source (yellow stars) located at the 15 km depth contour of the oceanic slab. (a) Ray tracing diagram indicating propagation paths of direct waves (green), refractions in the oceanic crust (red) and reflections at the oceanic Moho (yellow). (b) Normalized peak ground motions within the post-critically enhanced region. Abbreviations: wW-Western Washington; PS-Puget Sound.

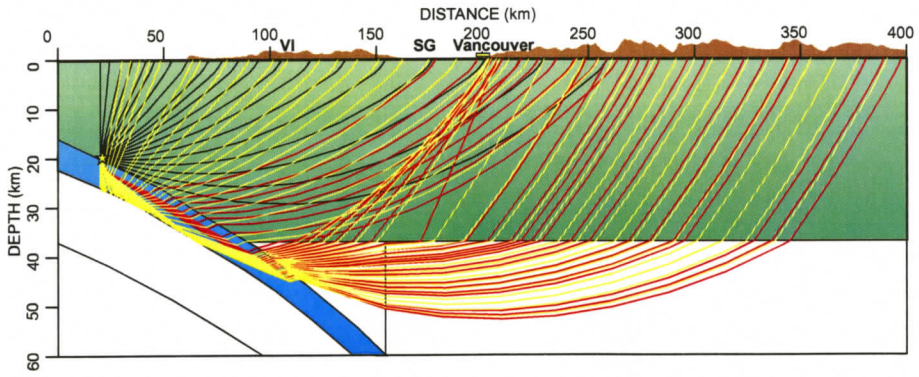

(a)

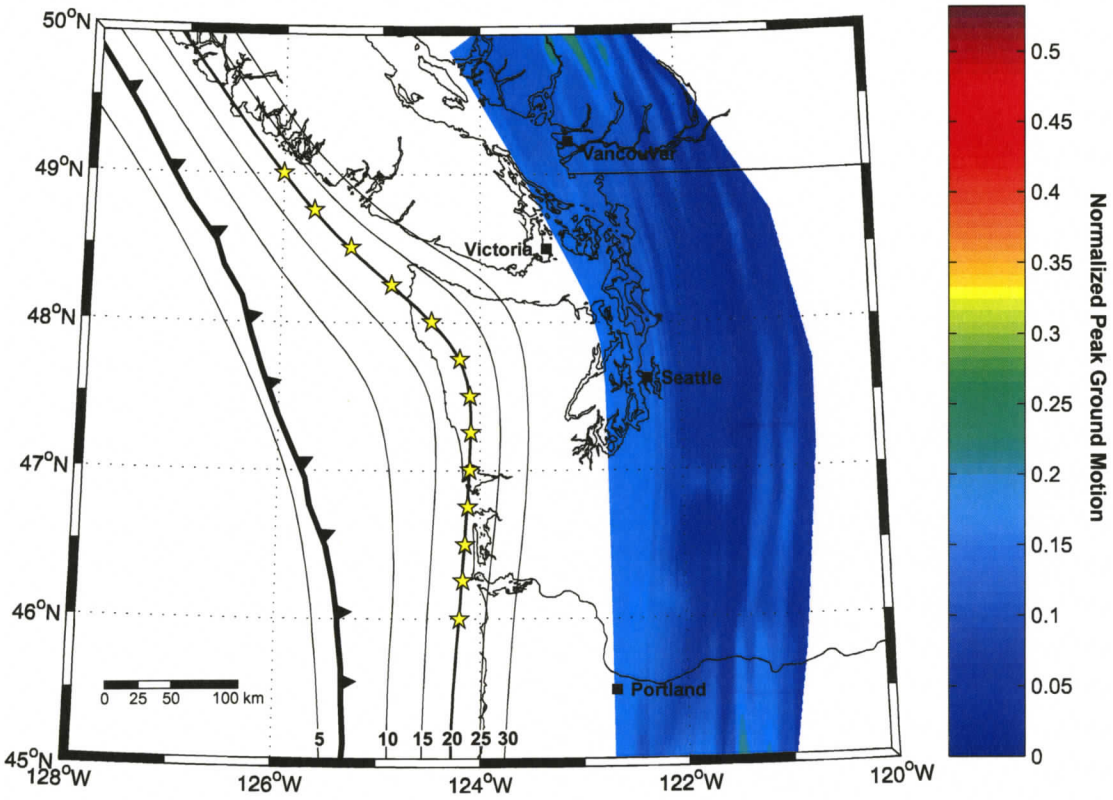

(b)

Figure 4.13 Post-critically enhanced region for a 2 Hz source (yellow stars) located at the 20 km depth contour of the oceanic slab. (a) Ray tracing diagram indicating propagation paths of direct waves (green), refractions in the oceanic crust (red) and reflections at the oceanic Moho (yellow). (b) Normalized peak ground motions within the post-critically enhanced region. Abbreviations: VI-Vancouver Island; SG-Strait of Georgia.

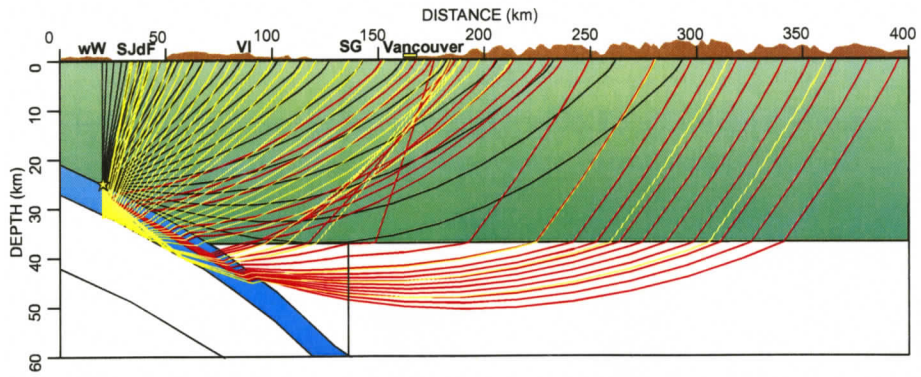

(a)

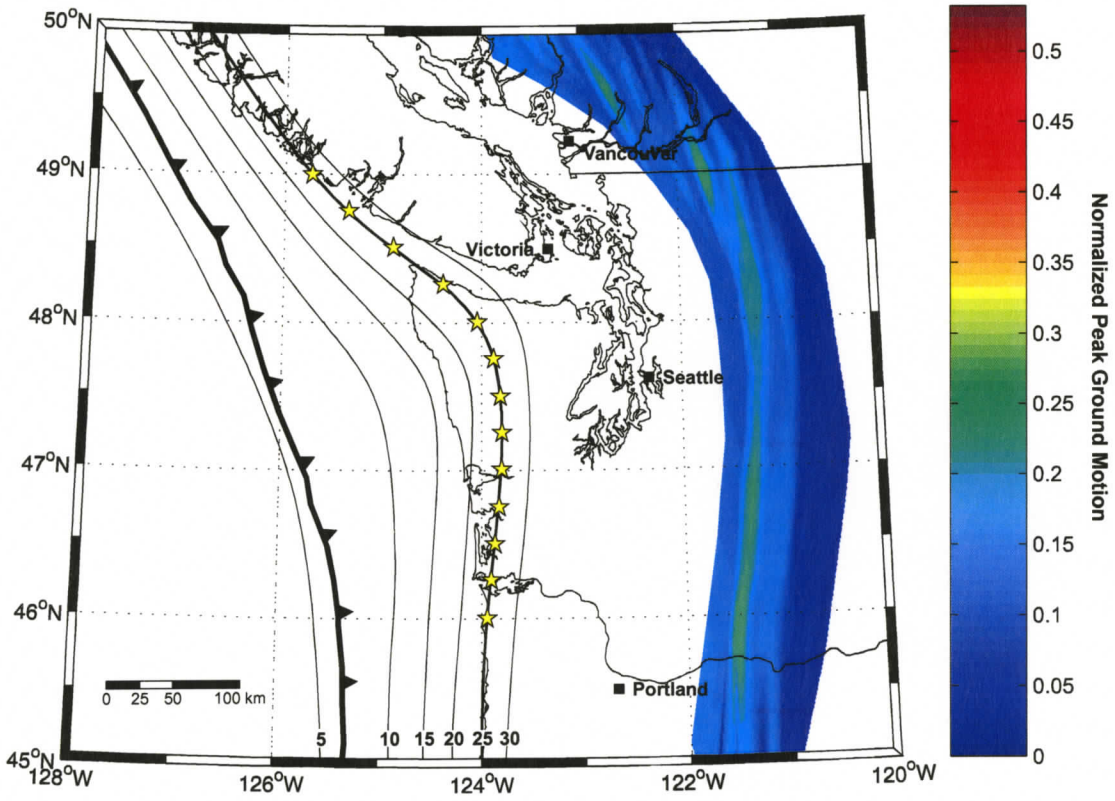

(b)

Figure 4.14 Post-critically enhanced region for a 2 Hz source (yellow stars) at the down-dip limit of the transition zone. (a) Ray tracing diagram indicating propagation paths of direct waves (green), refractions in the oceanic crust (red) and reflections at the oceanic Moho (yellow). (b) Normalized peak ground motions within the post-critically enhanced region. Abbreviations: wW-western Washington; SJdF-Strait of Juan de Fuca; VI-Vancouver Island; SG-Strait of Georgia.

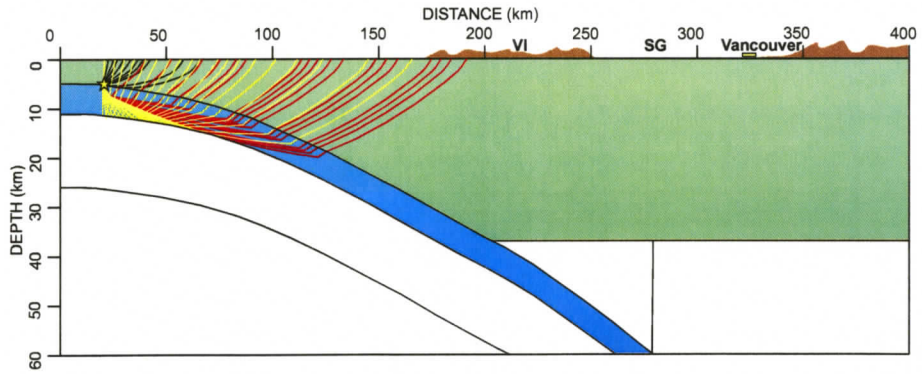

(a)

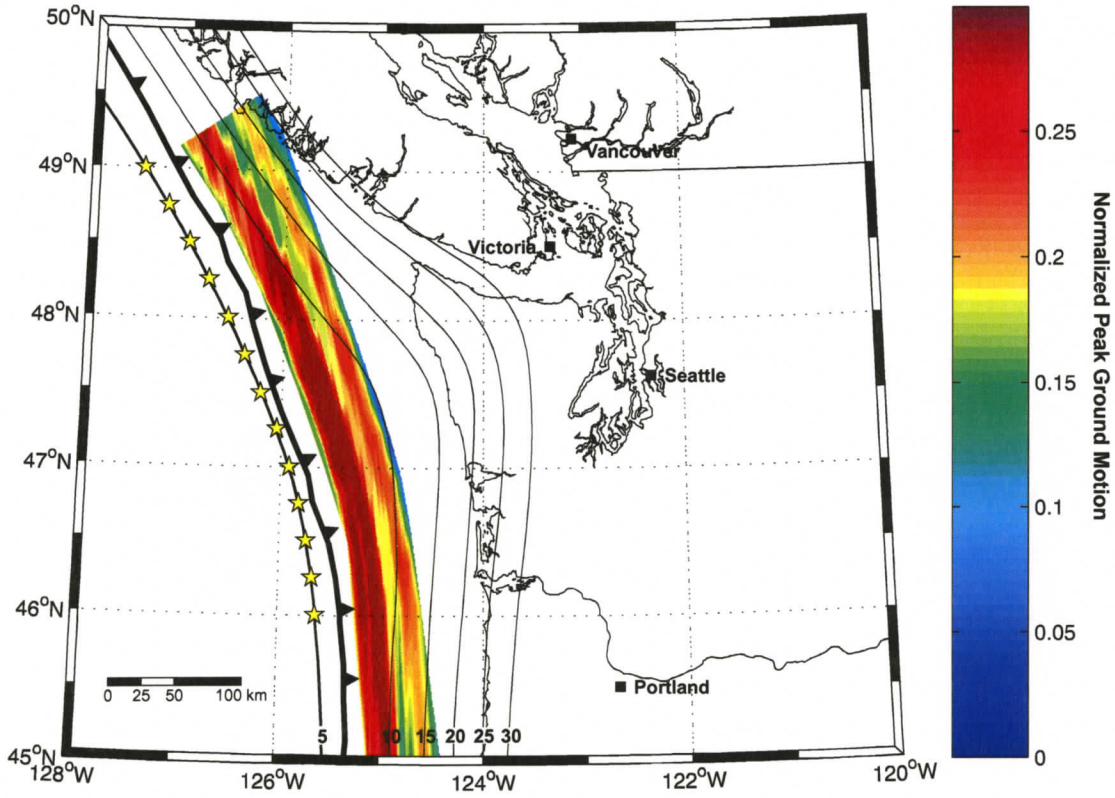

(b)

Figure 4.15 Post-critically enhanced region for a 3 Hz source (yellow stars) at the up-dip limit of the locked zone. (a) Ray tracing diagram indicating propagation paths of direct waves (green), refractions in the oceanic crust (red) and reflections at the oceanic Moho (yellow). (b) Normalized peak ground motions within the post-critically enhanced region. Abbreviations: VI-Vancouver Island; SG-Strait of Georgia.

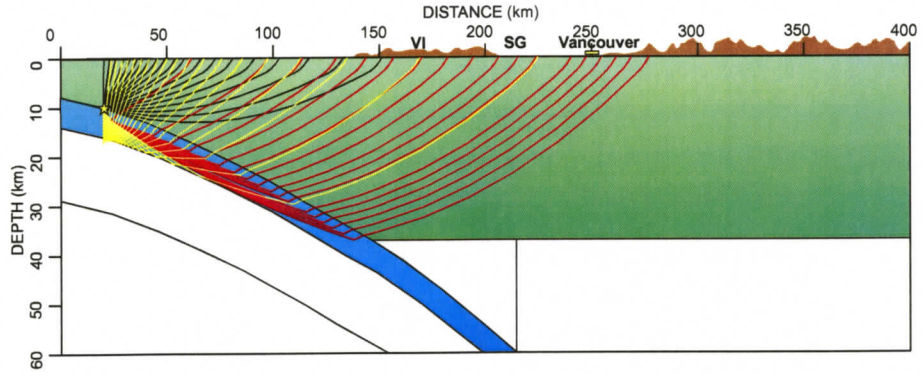

(a)

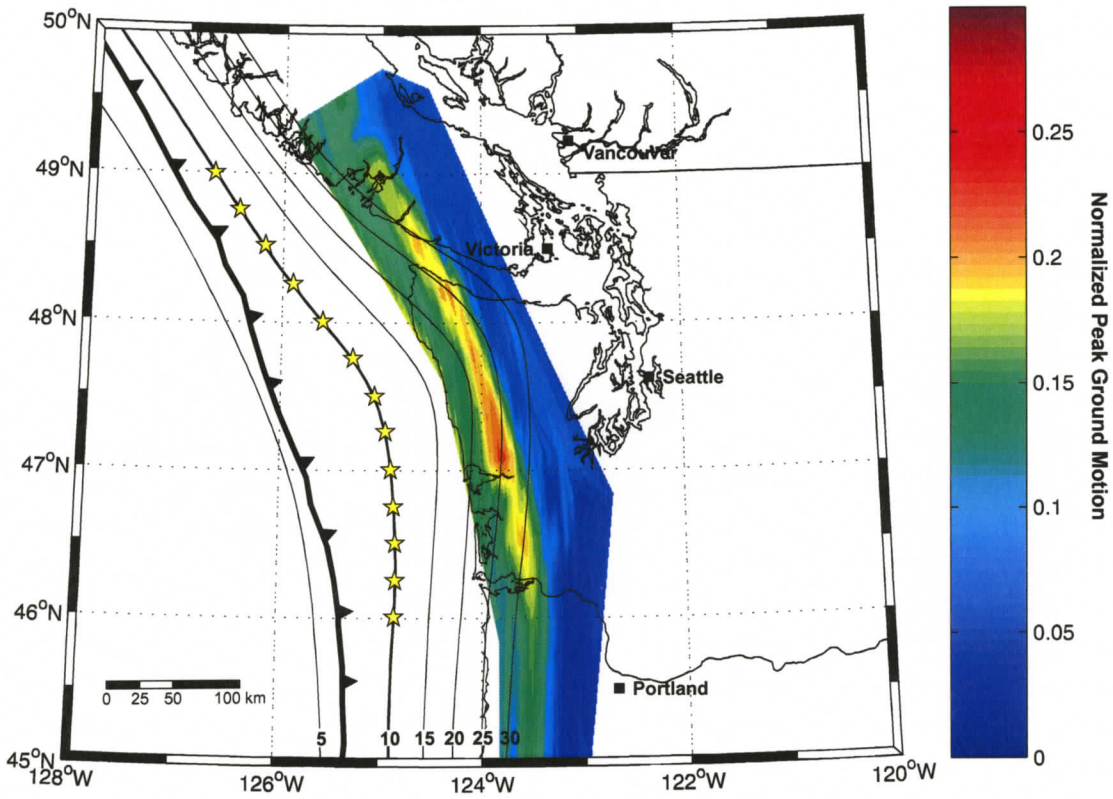

(b)

Figure 4.16 Post-critically enhanced region for a 3 Hz source (yellow stars) at the down-dip limit of the locked zone. (a) Ray tracing diagram indicating propagation paths of direct waves (green), refractions in the oceanic crust (red) and reflections at the oceanic Moho (yellow). (b) Normalized peak ground motions within the post-critically enhanced region. Abbreviations: VI-Vancouver Island; SG-Strait of Georgia.

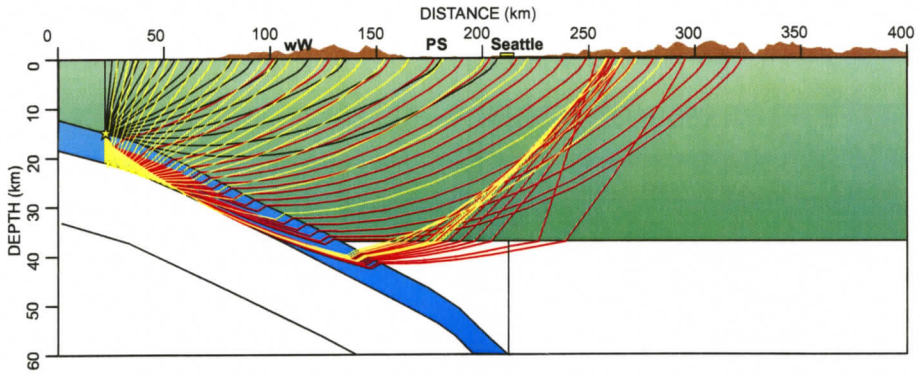

(a)

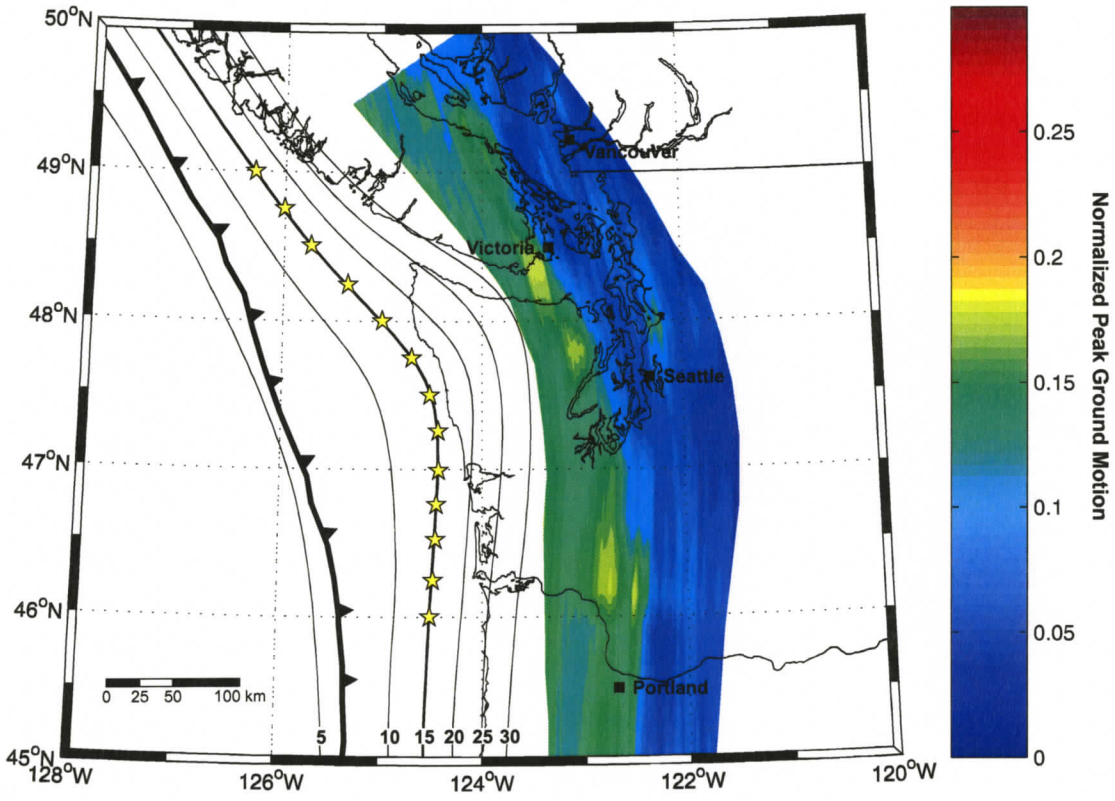

(b)

Figure 4.17 Post-critically enhanced region for a 3 Hz source (yellow stars) located at the 15 km depth contour of the oceanic slab. (a) Ray tracing diagram indicating propagation paths of direct waves (green), refractions in the oceanic crust (red) and reflections at the oceanic Moho (yellow). (b) Normalized peak ground motions within the post-critically enhanced region. Abbreviations: wW-Western Washington; PS-Puget Sound.

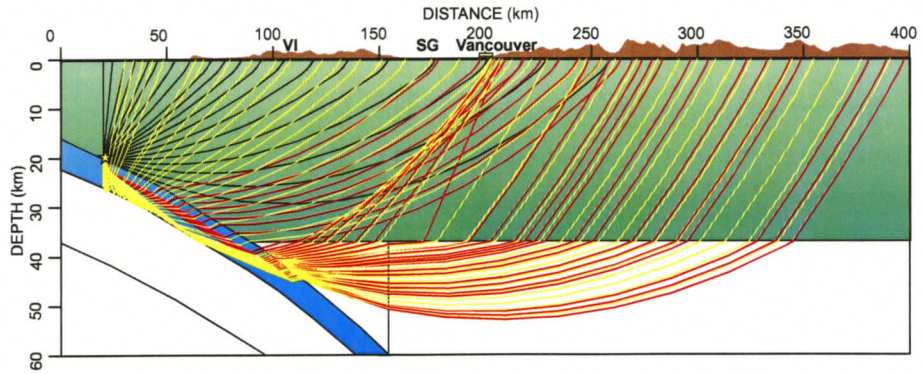

(a)

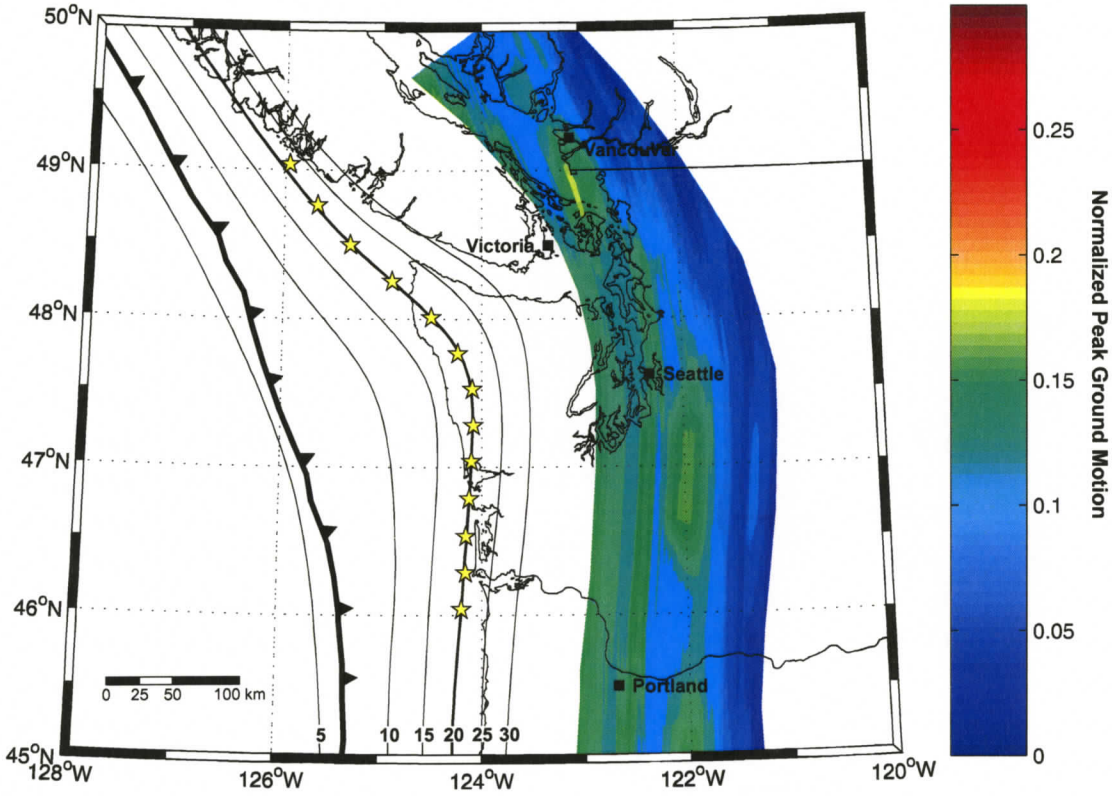

(b)

Figure 4.18 Post-critically enhanced region for a 3 Hz source (yellow stars) located at the 20 km depth contour of the oceanic slab. (a) Ray tracing diagram indicating propagation paths of direct waves (green), refractions in the oceanic crust (red) and reflections at the oceanic Moho (yellow). (b) Normalized peak ground motions within the post-critically enhanced region. Abbreviations: VI-Vancouver Island; SG-Strait of Georgia.

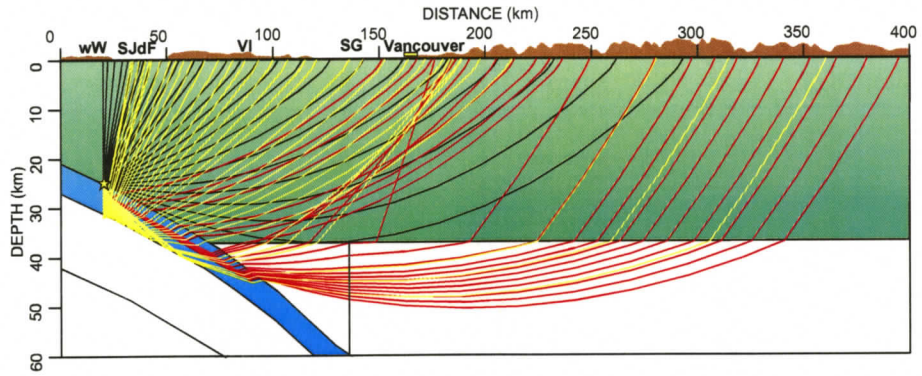

(a)

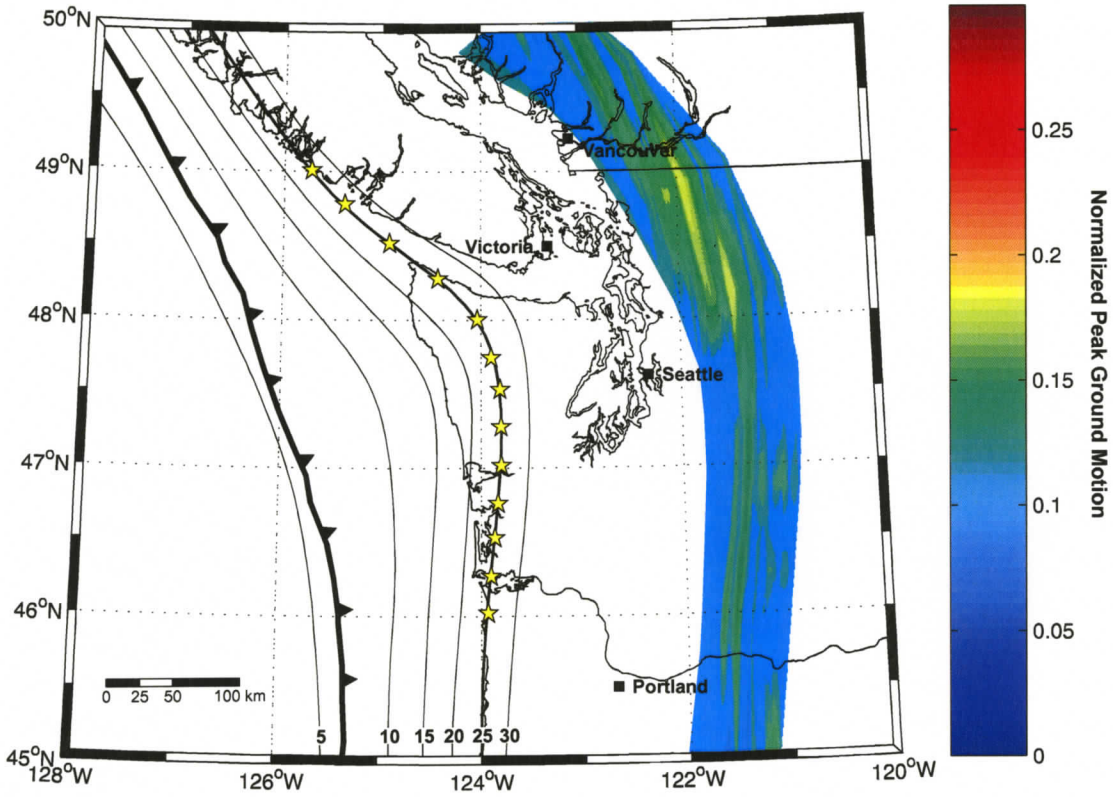

(b)

Figure 4.19 Post-critically enhanced region for a 3 Hz source (yellow stars) at the down-dip limit of the transition zone. (a) Ray tracing diagram indicating propagation paths of direct waves (green), refractions in the oceanic crust (red) and reflections at the oceanic Moho (yellow). (b) Normalized peak ground motions within the post-critically enhanced region. Abbreviations: wW-western Washington; SJdF-Strait of Juan de Fuca; VI-Vancouver Island; SG-Strait of Georgia.

For rupture at the 15 km depth contour of the oceanic slab, the post-critically enhanced region maps within the Pacific Northwest urban corridor [Portland, Seattle, Vancouver, Victoria] (figure 4.6). The main portion of the enhanced region is located in the range 90 – 200 km. Maximum PGM amplitudes within this region occur in the vicinity of Victoria, Seattle and Portland at approximately 140 km. The character of the main portion of the enhanced region is comparable in all respects to that of the previous source location. However, a second distinctive band of increased PGM amplitudes is evident in the range 225 – 250 km. Ray tracing indicates that post-critical reflections at the oceanic Moho are focused through the serpentinized forearc mantle wedge into the region of this distinctive band (figure 4.6a).

For a source located at the 20 km depth contour of the oceanic slab, the post-critically enhanced region has shifted landward and extends over the offset range from 125 km to 275 km (figure 4.7). Maximum PGM amplitudes within this region are present in a distinctive band between 210 km and 235 km. This band occurs landward of the major population centers of Vancouver, Seattle and Portland. The magnitude of the PGM amplitudes within the enhanced region has increased with respect to the previous source location. This is due to more post-critical reflections propagating through the serpentinized forearc mantle wedge and consequently being focused within this narrow region (figure 4.7a).

In figure 4.8 the post-critically enhanced region maps between 125 km and 250 km from a source located at the down-dip limit of the transition zone. Beyond 250 km PGM amplitudes decay, corresponding approximately to geometric spreading in two dimensions. The prominent feature is the elevated PGM amplitudes in the distance range 175 – 210 km. The location of this narrow region is consistent with that observed for the previous two source depths, although more prominent.

Finally, the enhanced region for rupture on the oceanic slab interface at a depth of 30 km is evident in the distance range 140 – 225 km (figure 4.9). Similar to previous source locations, a distinctive band of increased PGM amplitudes is present between 155 km and 185 km.

4.4.2 2 Hz Source

In a similar fashion, the geographical range of post-critically enhanced regions for a source with a dominant frequency of 2 Hz is examined. Figure 4.10 maps the post-critically enhanced region for rupture at the up-dip limit of the locked zone. The behavior of PGM within this region has changed when the source frequency is increased to 2 Hz. The enhanced region is evident between 35 km and 80 km with maximum PGM amplitudes at approximately 50 km. A second local maximum in PGM is evident in the range 60 – 80 km. Synthetic seismograms indicate that the first local maximum is cause by the arrival of post-critical

reflections at the oceanic Moho. A suite of later arrivals causes the second peak in PGM amplitudes. These arrivals represent strong amplitude multiples between the base of oceanic layer 2 and the top of the oceanic crust.

For a source initiated at the down-dip limit of the locked zone, the post-critically enhanced region maps on the coastal regions of the Pacific Northwest (figure 4.11). The enhanced region is between 60 km and 120 km from the source. Maximum PGM amplitudes are located approximately 80 km from the source between 48^0N and 47^0N. The enhanced region displays similar features to that for a 1 Hz source, although the region is approximately 40 km narrower in extent.

For a source located at the 15 km depth contour along the slab interface, the enhanced region maps within the Pacific Northwest urban corridor (figure 4.12). Maximum PGM amplitudes encroach upon the Puget Sound area 100 km from the source. Within this region, PGM amplitudes decay less rapidly than expected for geometric spreading in two dimensions. This is in contrast to the previous source frequency, where a dramatic increase in PGM was observed. Between 230 km and 245 km a band of slightly increased PGM amplitudes is evident. This band corresponds to that observed for a 1 Hz source; however, the band is much less prominent and narrower in width.

In figure 4.13, the post-critically enhanced region for a source located at the 20 km depth contour of the oceanic slab is shown. The enhanced region remains within the Pacific Northwest urban corridor. Elevated PGM amplitudes are present in a narrow region in the range 220 – 245 km. However, this feature is not very distinct.

For a source initiated at the down-dip limit of the transition zone, the maximum amplitudes in the post-critically enhanced region map landward of the major population centers (figure 4.14). Maximum PGM amplitudes are located between 175 km and 230 km. The region is narrower in extent compared to that for a 1 Hz source

The post-critically enhanced region for a 2 Hz source at a depth of 30 km on the slab interface is not modeled. It is evident from the previous source frequency that the enhanced region will be in the vicinity of the distinct band of increased PGM amplitudes observed for sources at 15, 20 and 25 km depth.

4.4.3 3 Hz Source

In the final model, the enhanced regions from a source with a dominant frequency of 3 Hz is considered. For sources initiated at the up-dip and the down-dip limit of the locked zone, the post-critically enhanced regions are comparable to those observed for a 2 Hz source (figure 4.15 & 4.16).

Figure 4.17 maps the post-critically enhanced region within the urban corridor for a source located on the slab interface at 15 km depth. Similar to the previous source frequencies, maximum PGM amplitudes are observed approximately 100 km from the source in the vicinity of Victoria, Seattle and Portland. However, the distinctive band of increased PGM amplitudes approximately 225 km from the source is not apparent.

The post-critically enhanced region for a source located at 20 km depth on the subduction interface is shown in figure 4.18. An increase in PGM amplitudes is observed within the urban corridor between 125 km and 235 km, with maximum amplitudes in the vicinity of Vancouver. No distinctive band of increased PGM amplitudes is present, as compared with the previous source frequencies.

Finally, the post-critically enhanced region for a source located at the down-dip limit of the transition zone is illustrated in figure 4.19. PGM amplitudes within this region form a distinctive band between 175 km and 205 km. This band corresponds to that observed for source frequencies of 1 Hz and 2 Hz.

4.5 Contribution of Moho Reflections to Peak Ground Motions

To quantify the contribution of post-critical reflections at the oceanic Moho, 2-D P-SV pseudo-spectral synthetic seismograms from two models of the Cascadia subduction zone, one with a strong oceanic Moho the other without, are examined. The focus will be to understand the effect that post-critical reflections at the oceanic Moho have on observed ground motion amplitudes.

Throughout the examples that follow, seismic wave propagation in two distinct velocity models of the Cascadia subduction zone will be compared, hereafter referred to as the "base" model and the "perturbed" model. The base model is the velocity model already mentioned in chapter 3 (figure 3.3). In contrast, the perturbed model exhibits no oceanic Moho velocity boundary. This is accomplished by ensuring that there is no velocity contrast across the oceanic Moho. Velocities at a given depth in the oceanic crust are modeled to increase landwards as the subducting plate descends to greater depths and mantle velocities beneath the Moho are also modeled in a similar manner to increase landward. As well, the vertical velocity gradient in the oceanic mantle is assigned a value of zero (figure 4.20). By doing this, no oceanic Moho

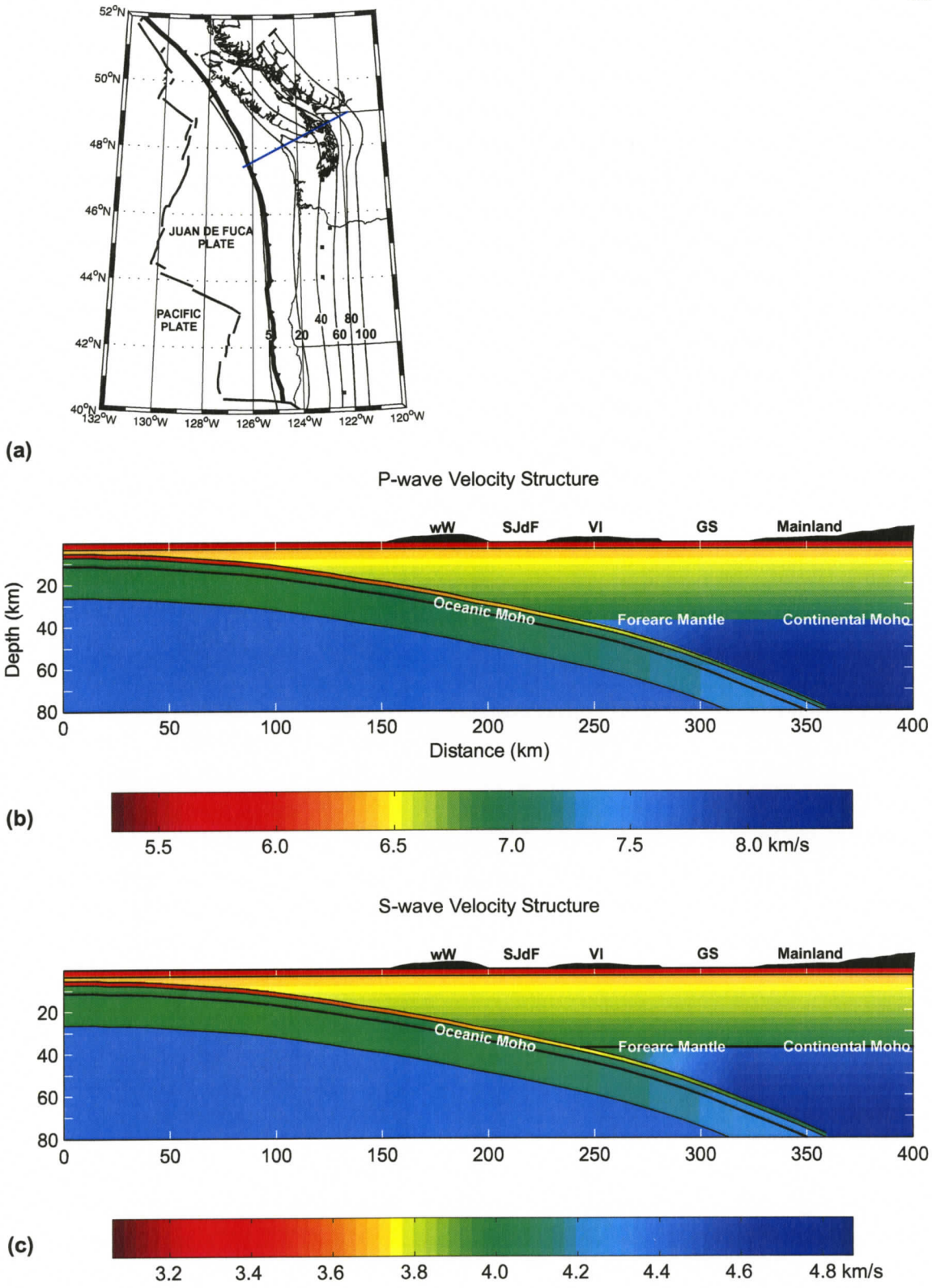

Figure 4.20 (a) Map indicating location of profile line. (b) P-wave velocity model and (c) S-wave velocity model for the Cascadia subduction zone with no velocity contrast across the Moho. Abbreviations: wW-western Washington; SJdF-Strait of Juan de Fuca; VI-Vancouver Island; GS-Georgia Strait.

reflections and no additional refractions in the oceanic mantle will be present in the synthetic seismograms. Therefore, any differences between the base model and perturbed model synthetic seismograms can be attributed to the influence of oceanic Moho reflections. Attenuation is not modeled in the synthetics; however, its implications on the results will be discussed in a later section.

In the following analysis of ground motions from mega-thrust events, individual 2-D double-couple line sources orientated to represent slip on the subduction thrust located at the up-dip and down-dip limit of the locked zone as well as the down-dip limit of the transition zone are considered. Dominant source frequencies of 1 Hz, 2 Hz and 3 Hz are applied. 2-D forward modeling of ground motions for the previously defined source locations and source frequencies were performed for profiles in the vicinity of the major population centers of the Pacific Northwest (Vancouver, Victoria, Seattle and Portland) (figure 4.21). The following analysis focuses on those profiles that display unique characteristics. For completeness, all results not displayed in this section are provided in Appendix B.

The following figures (4.22 – 4.40) display the vertical component of PGM as a function of epicentral distance. Normalization of the PGM is with respect to the peak amplitude on the vertical component synthetic seismograms for a source located at the up-dip limit of the locked zone. This normalization is defined independently for each source frequency. Furthermore, the ratio between PGM of the base and perturbed models is quantified by a multiplication factor with respect to the perturbed model results.

4.5.1 Up-dip Limit of the Locked Zone

In this section, the contribution of post-critical reflections at the oceanic Moho to ground motions are examined for a source at the up-dip limit of the locked zone of both the base and perturbed models. Source frequencies of 1 Hz, 2 Hz and 3 Hz are applied to understand the effect of source frequency on the contribution of post-critical reflections to ground motions.

Figure 4.22 displays the PGM as a function of distance from a 1 Hz source for both models along a profile in the vicinity of Vancouver. It indicates that ground motions from the base model and the perturbed model differ at distances between 30 km and 80 km. Amplitudes in the base model exceed those in the perturbed model by a factor of up to 1.5 between 30 km – 60 km through the arrival of strong post-critical reflections at the oceanic Moho. In contrast, amplitudes in the perturbed model exceed those in the base model between 60 km and 80 km. Base model amplitudes decrease by a factor of 0.8 with respect to the perturbed model. Synthetic seismograms from the perturbed model indicate that within this range peak ground motions are caused by the arrival of refractions in the oceanic crust. The interactions of post-

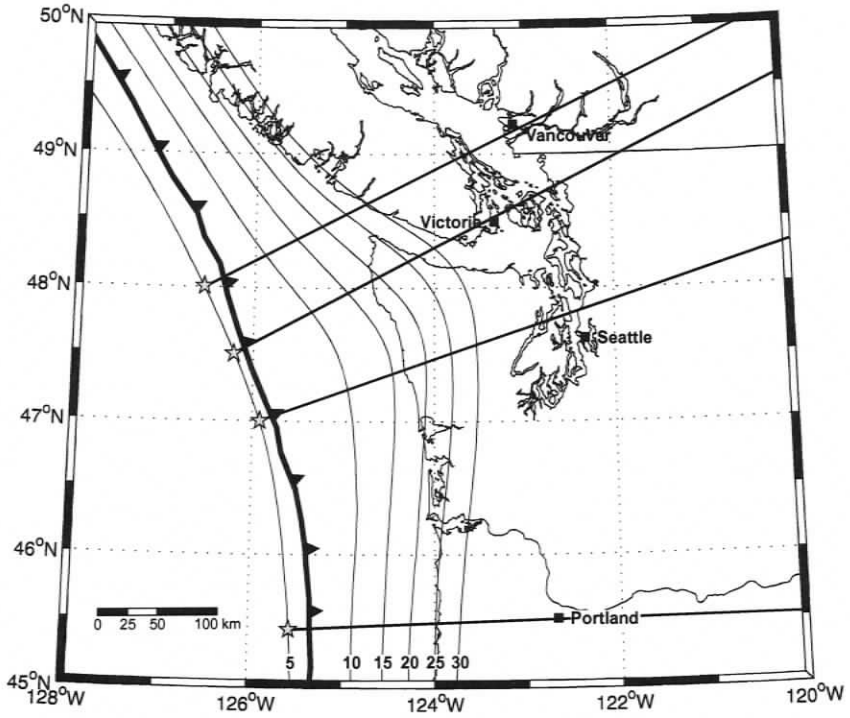

(a)

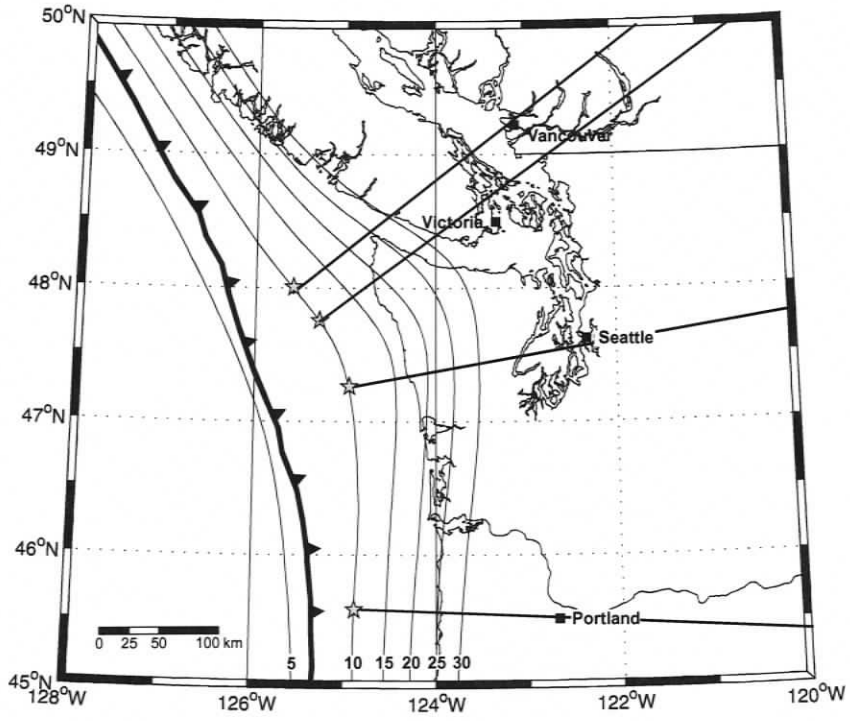

(b)

Figure 4.21 Profile lines in the vicinity of the major population centers of the Pacific Northwest. (a) Profiles for a source at the up-dip limit of the locked zone. (b) Profiles for a source at the down-dip limit of the locked zone. (c) Profiles for a source at the down-dip limit of the transition zone.

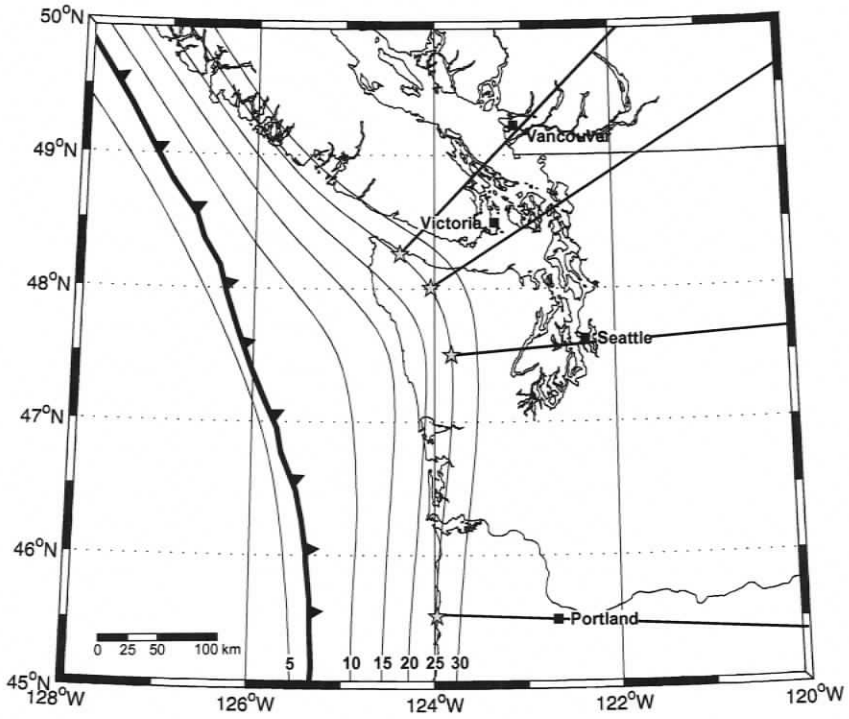

(c)

Figure 4.21 continued...

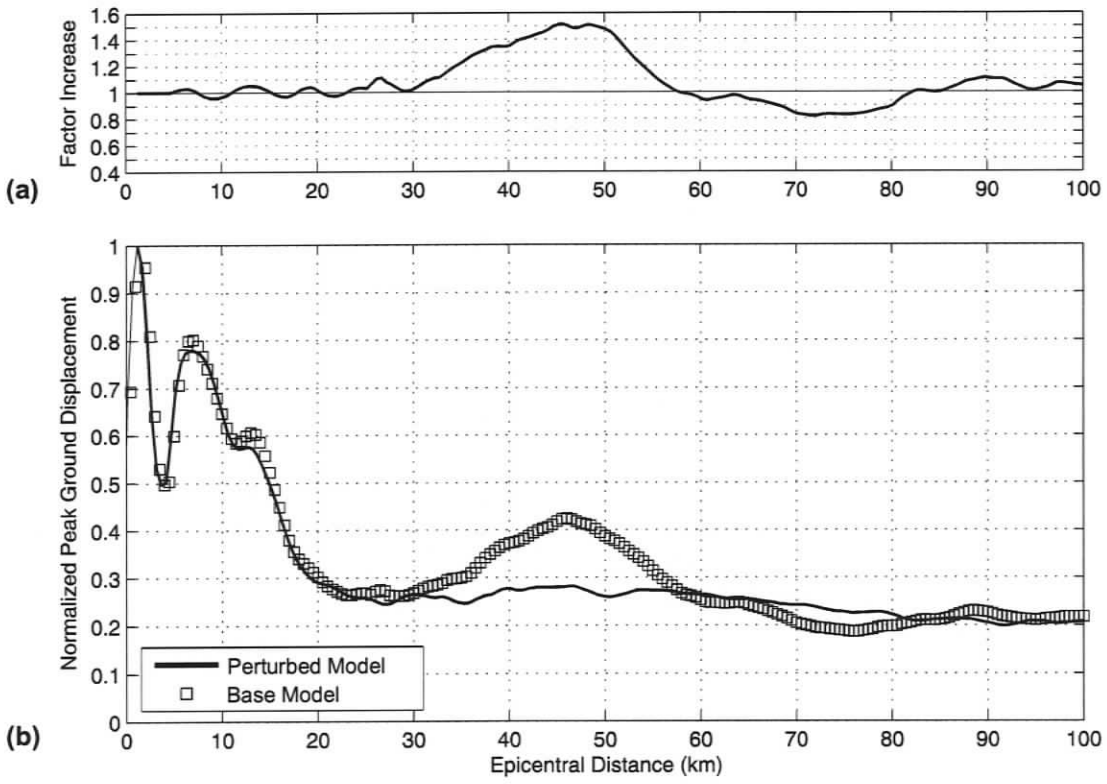

Figure 4.22 Quantitative comparison for a 1 Hz source at the up-dip limit of the locked zone along a profile in the vicinity of Vancouver. (a) Ratio between the base (square data points) and perturbed model results (solid line). (b) Peak ground motions for a 1 Hz source located at the up-dip limit of the locked zone for the base and perturbed models. Vancouver is located at ~325 km epicentral distance.

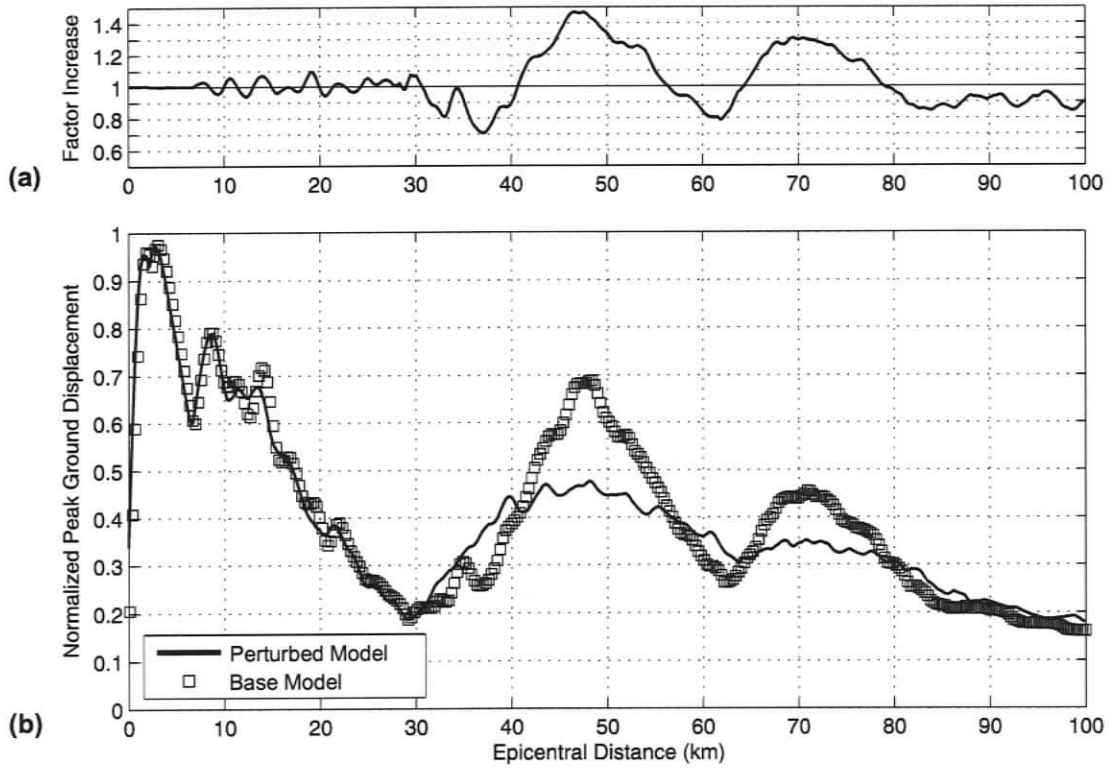

Figure 4.23 Quantitative comparison for a 2 Hz source at the up-dip limit of the locked zone along a profile in the vicinity of Vancouver. (a) Ratio between the base (square data points) and perturbed model results (solid line). (b) Peak ground motions for a 2 Hz source located at the up-dip limit of the locked zone for the base and perturbed models. Vancouver is located at ~325 km epicentral distance.

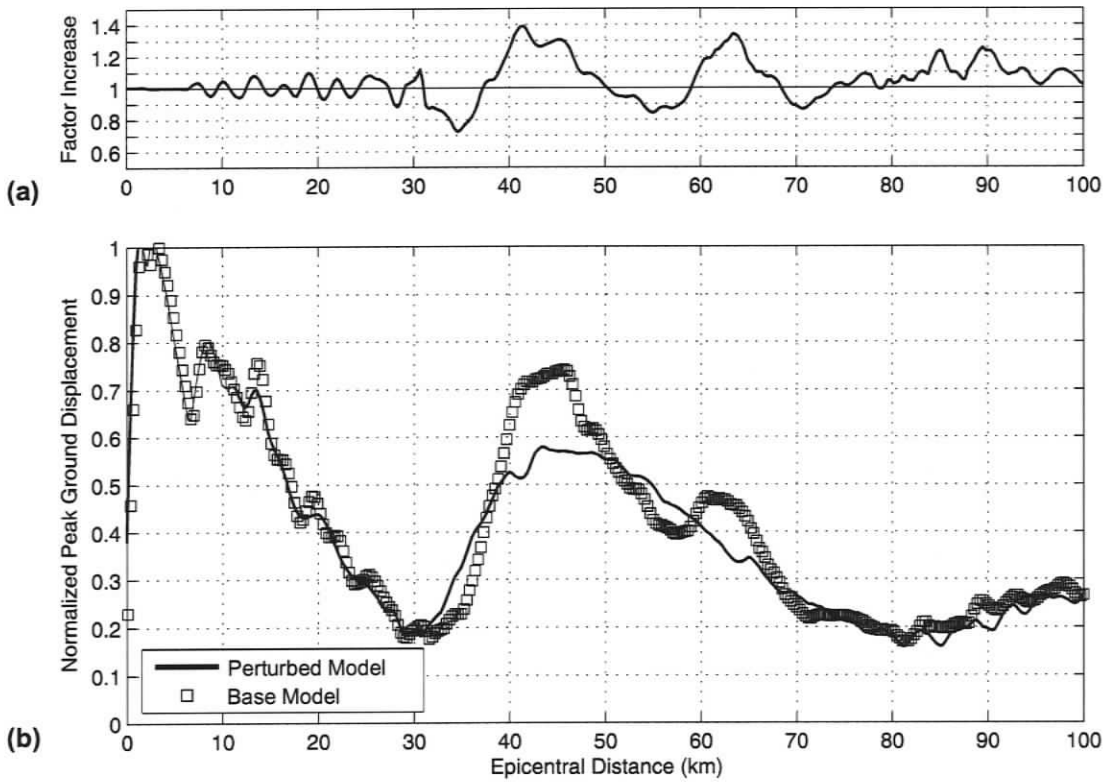

Figure 4.24 Quantitative comparison for a 2 Hz source at the up-dip limit of the locked zone along a profile in the vicinity of Seattle. (a) Ratio between the base (square data points) and perturbed model results (solid line). (b) Peak ground motions for a 2 Hz source located at the up-dip limit of the locked zone for the base and perturbed models. Seattle is located at ~285 km epicentral distance.

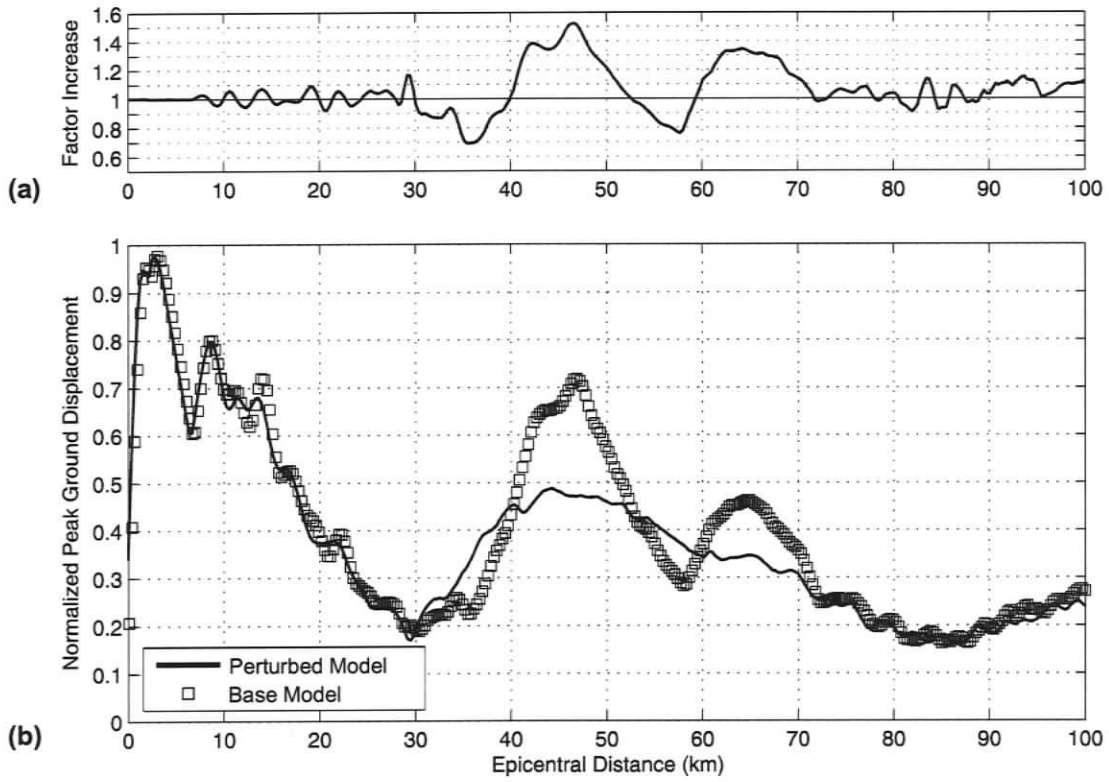

Figure 4.25 Quantitative comparison for a 2 Hz source at the up-dip limit of the locked zone along a profile in the vicinity of Victoria. (a) Ratio between the base (square data points) and perturbed model results (solid line). (b) Peak ground motions for a 2 Hz source located at the up-dip limit of the locked zone for the base and perturbed models. Victoria is located at ~240 km epicentral distance.

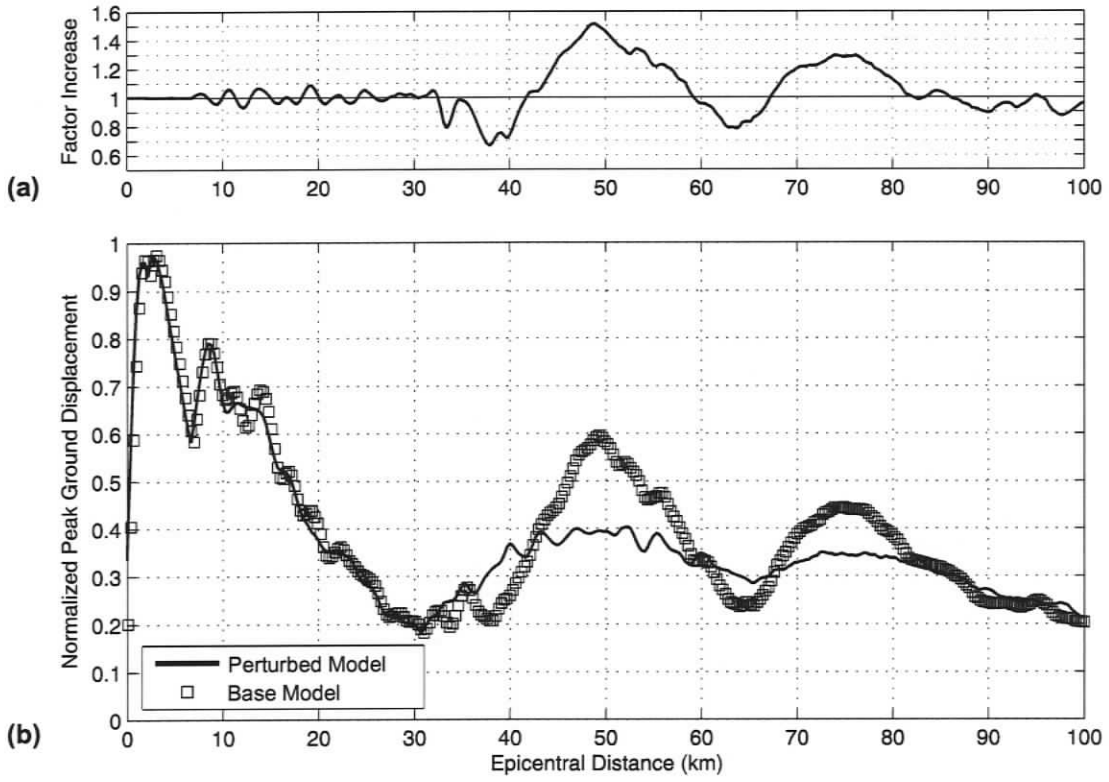

Figure 4.26 Quantitative comparison for a 2 Hz source at the up-dip limit of the locked zone along a profile in the vicinity of Portland. (a) Ratio between the base (square data points) and perturbed model results (solid line). (b) Peak ground motions for a 2 Hz source located at the up-dip limit of the locked zone for the base and perturbed models. Portland is located at ~230 km epicentral distance.

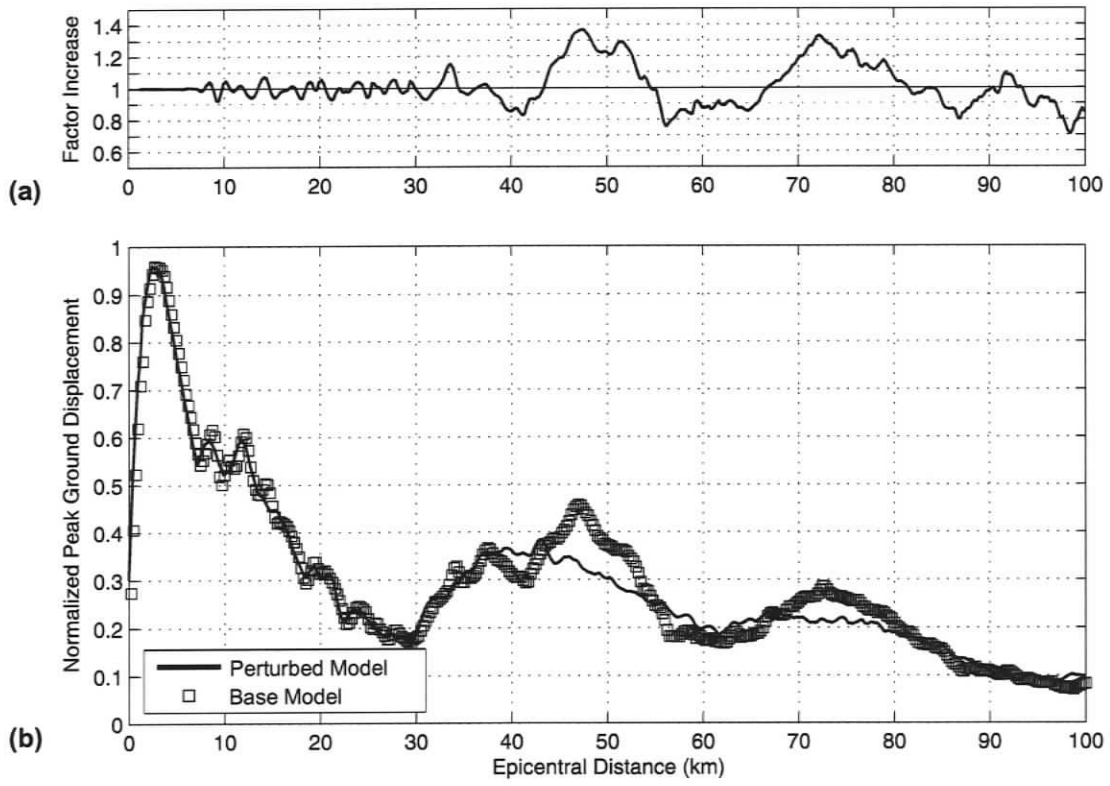

Figure 4.27 Quantitative comparison for a 3 Hz source at the up-dip limit of the locked zone along a profile in the vicinity of Vancouver. (a) Ratio between the base (square data points) and perturbed model results (solid line). (b) Peak ground motions for a 3 Hz source located at the up-dip limit of the locked zone for the base and perturbed models. Vancouver is located at 325 km epicentral distance.

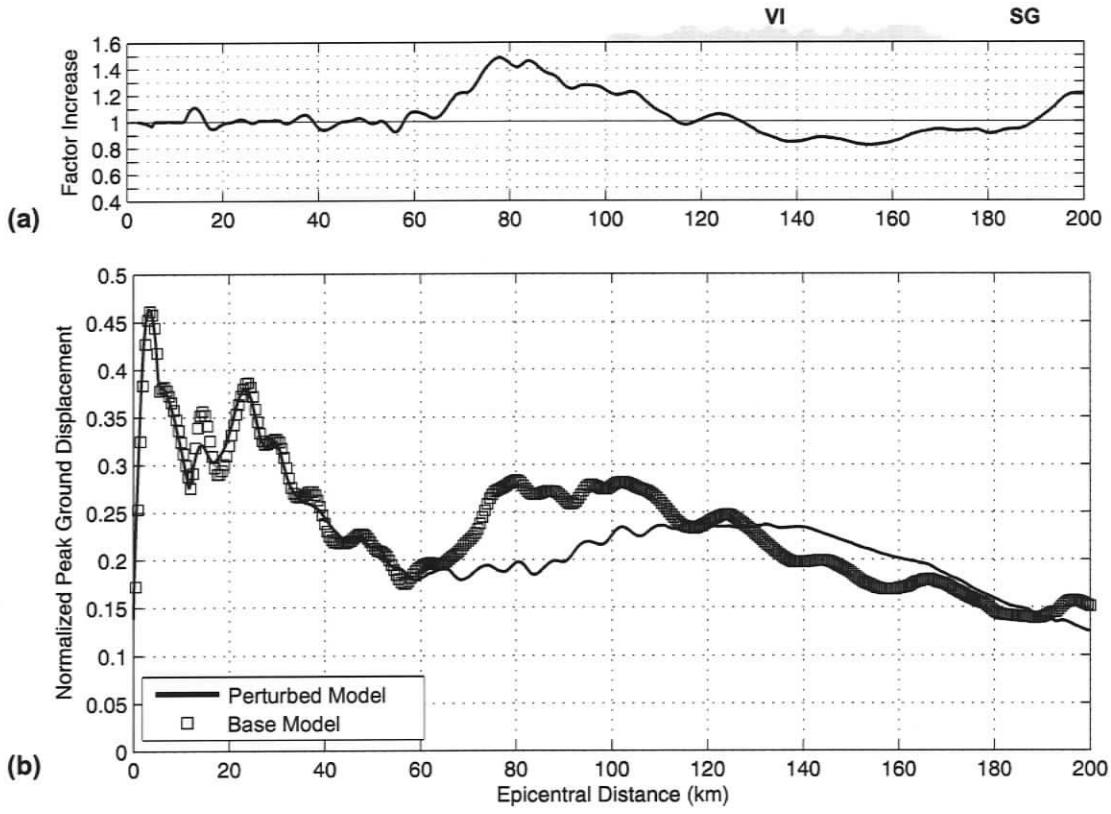

Figure 4.28 Quantitative comparison for a 1 Hz source at the down-dip limit of the locked zone along a profile in the vicinity of Vancouver. (a) Ratio between the base (square data points) and perturbed model results (solid line). (b) Peak ground motions for a 1 Hz source located at the up-dip limit of the locked zone for the base and perturbed models. Vancouver is located at ~250 km epicentral distance. Abbreviations: VI-Vancouver Island; SG-Strait of Georgia.

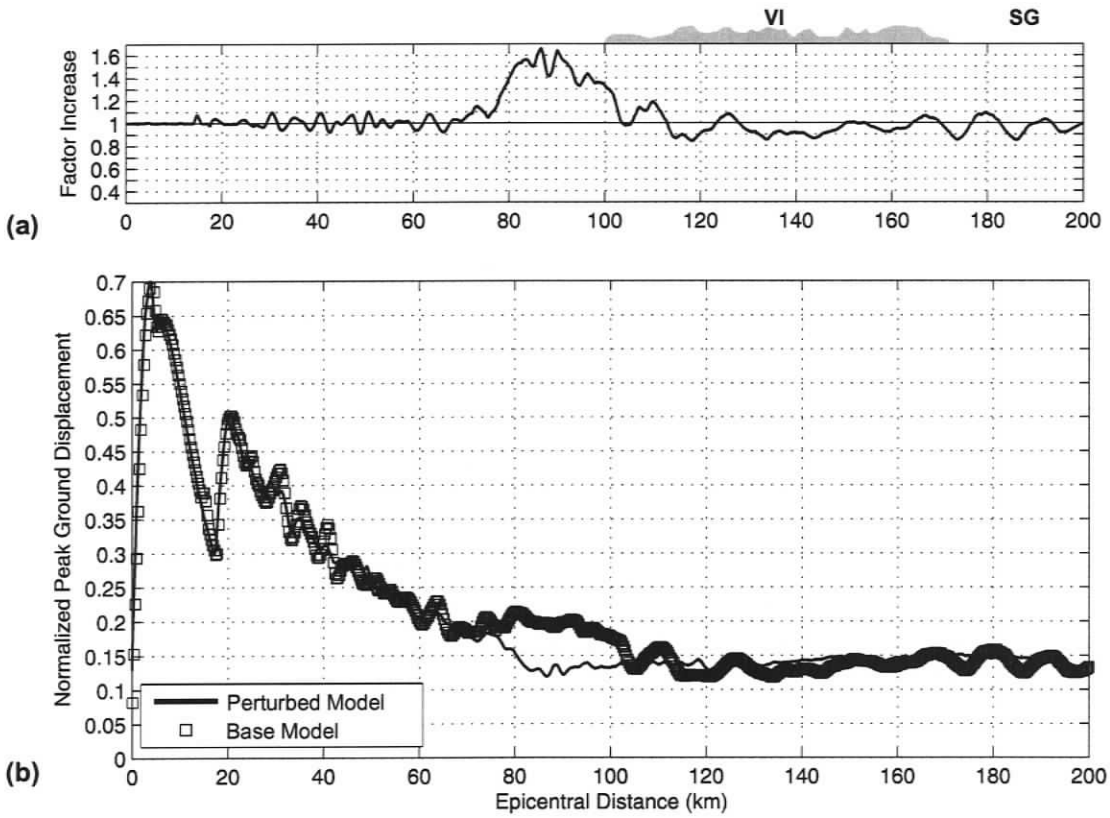

Figure 4.29 Quantitative comparison for a 2 Hz source at the down-dip limit of the locked zone along a profile in the vicinity of Vancouver. (a) Ratio between the base (square data points) and perturbed model results (solid line). (b) Peak ground motions for a 2 Hz source located at the up-dip limit of the locked zone for the base and perturbed models. Vancouver is located at ~250 km epicentral distance. Abbreviations: VI-Vancouver Island; SG-Strait of Georgia.

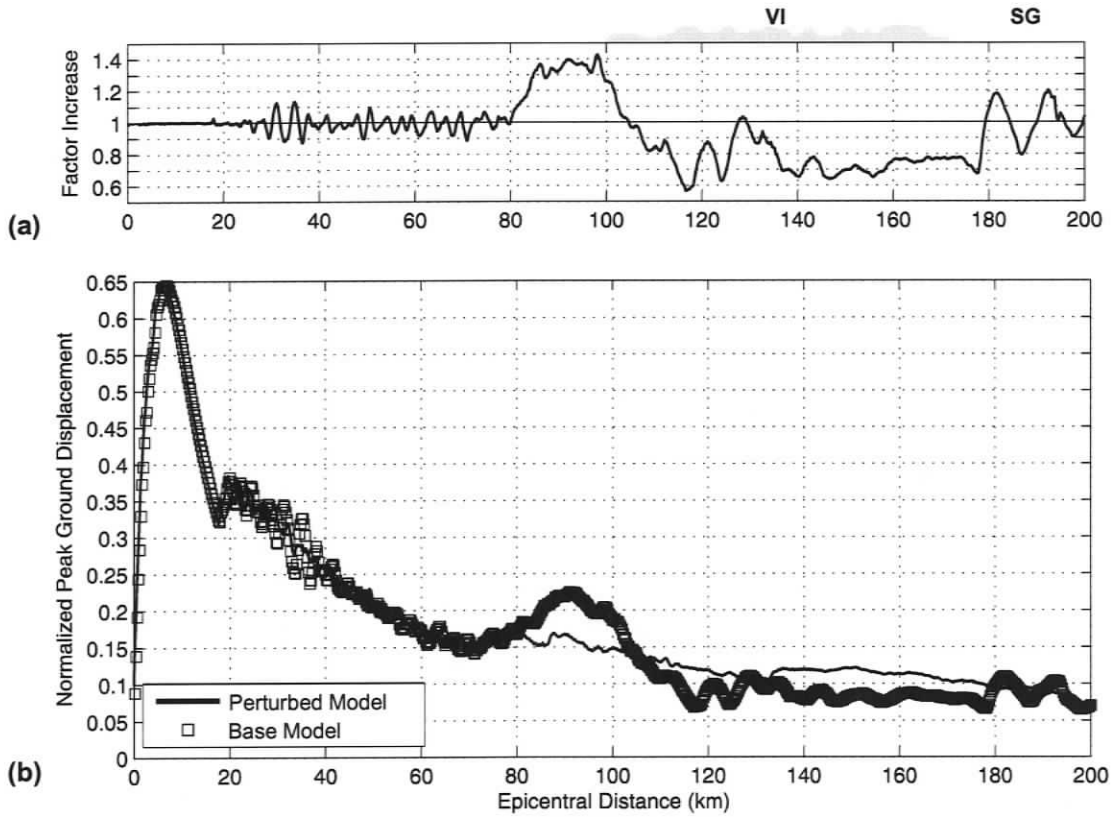

Figure 4.30 Quantitative comparison for a 3 Hz source at the down-dip limit of the locked zone along a profile in the vicinity of Vancouver. (a) Ratio between the base (square data points) and perturbed model results (solid line). (b) Peak ground motions for a 3 Hz source located at the up-dip limit of the locked zone for the base and perturbed models. Vancouver is located at ~250 km epicentral distance. Abbreviations: VI-Vancouver Island; SG-Strait of Georgia.

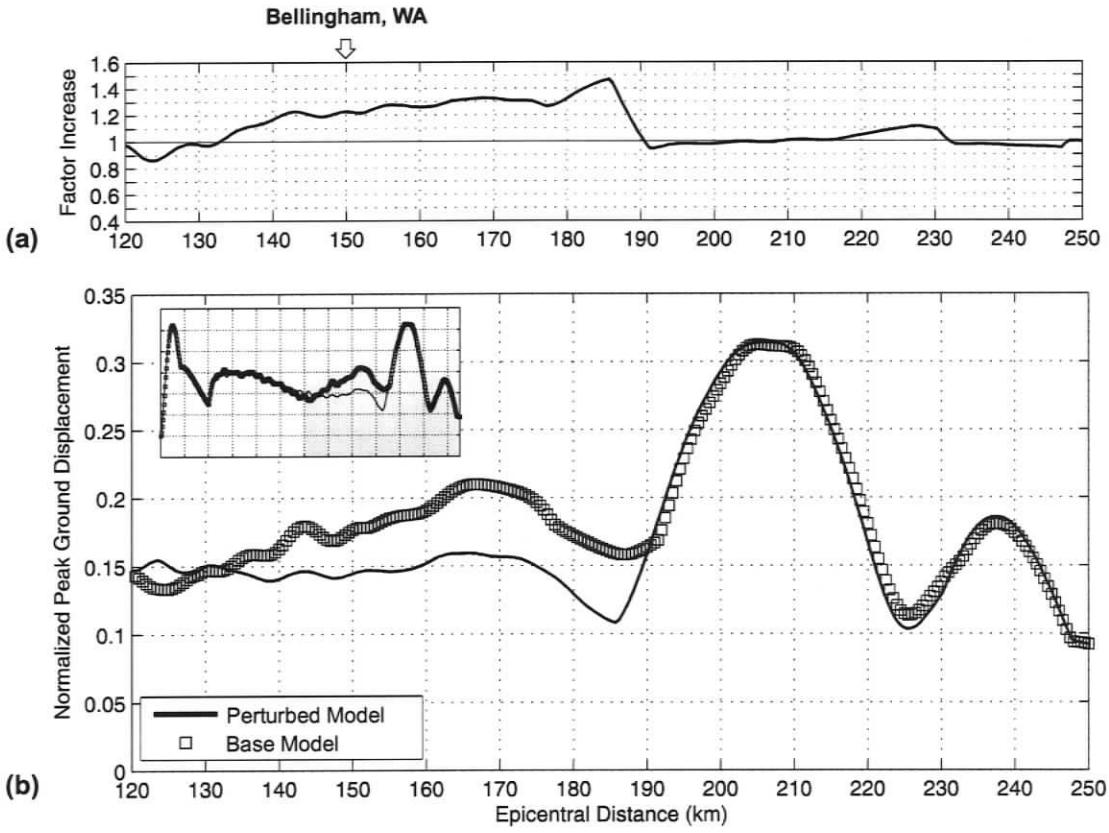

Figure 4.31 Quantitative comparison for a 1 Hz source at the down-dip limit of the transition zone along a profile in the vicinity of Victoria. (a) Ratio between the base (square data points) and perturbed model results (solid line). (b) Peak ground motions for a 1 Hz source located at the down-dip limit of the transition zone for the base and perturbed models. The inset shows peak ground motions in the range 0 - 250 km. Victoria is located at ~100 km epicentral distance.

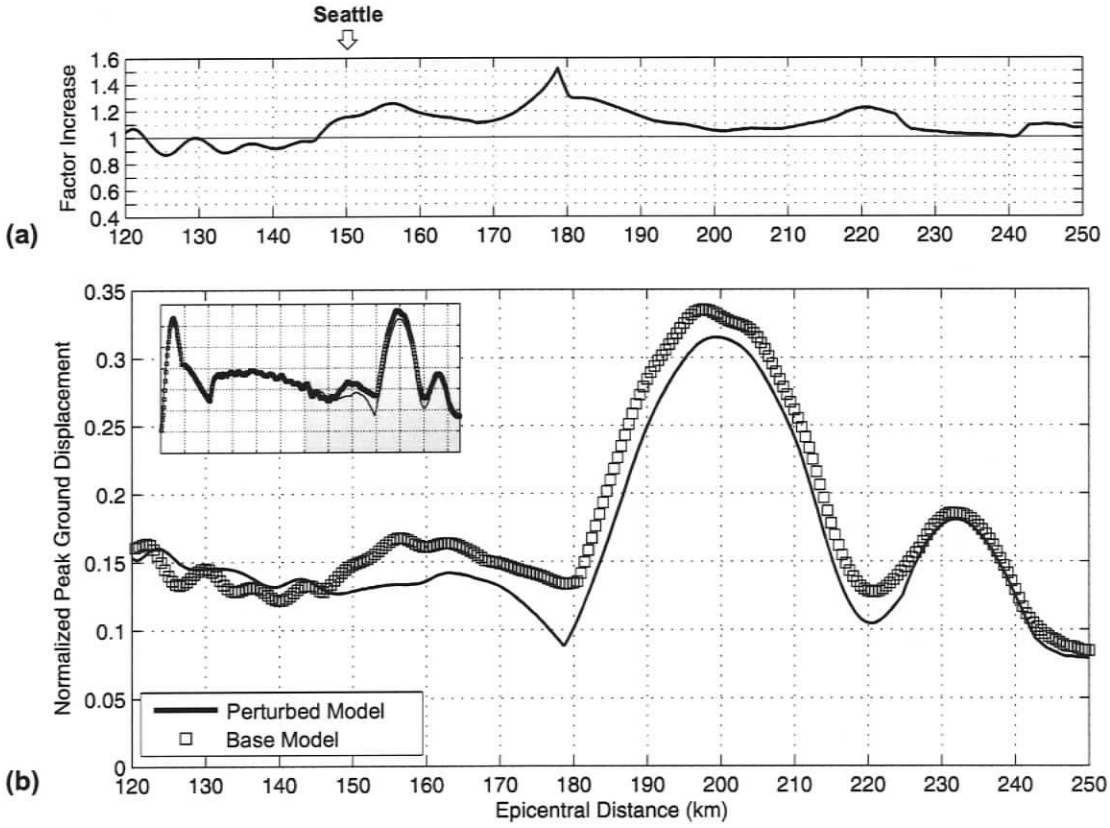

Figure 4.32 Quantitative comparison for a 1 Hz source at the down-dip limit of the transition zone along a profile in the vicinity of Seattle. (a) Ratio between the base (square data points) and perturbed model results (solid line). (b) Peak ground motions for a 1 Hz source located at the down-dip limit of the transition zone for the base and perturbed models. The inset shows peak ground motions in the range 0 - 250 km.

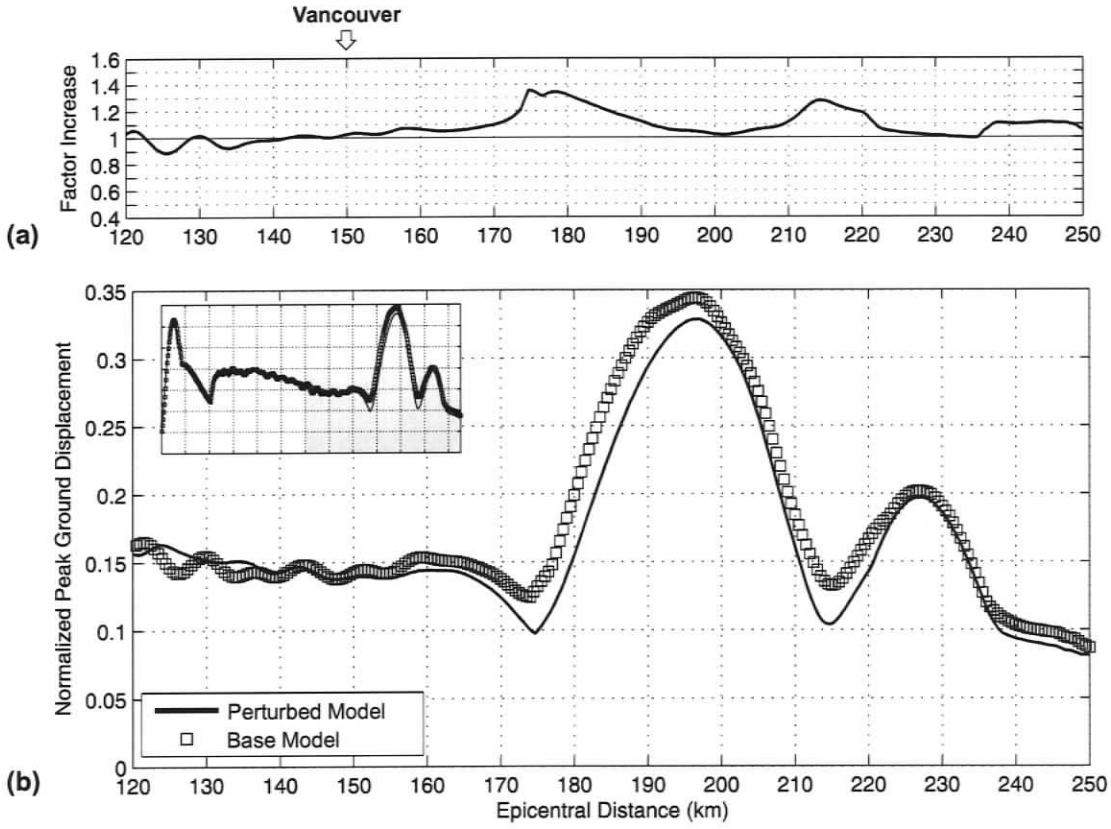

Figure 4.33 Quantitative comparison for a 1 Hz source at the down-dip limit of the transition zone along a profile in the vicinity of Vancouver. (a) Ratio between the base (square data points) and perturbed model results (solid line). (b) Peak ground motions for a 1 Hz source located at the down-dip limit of the transition zone for the base and perturbed models. The inset shows peak ground motions in the range 0 - 250 km.

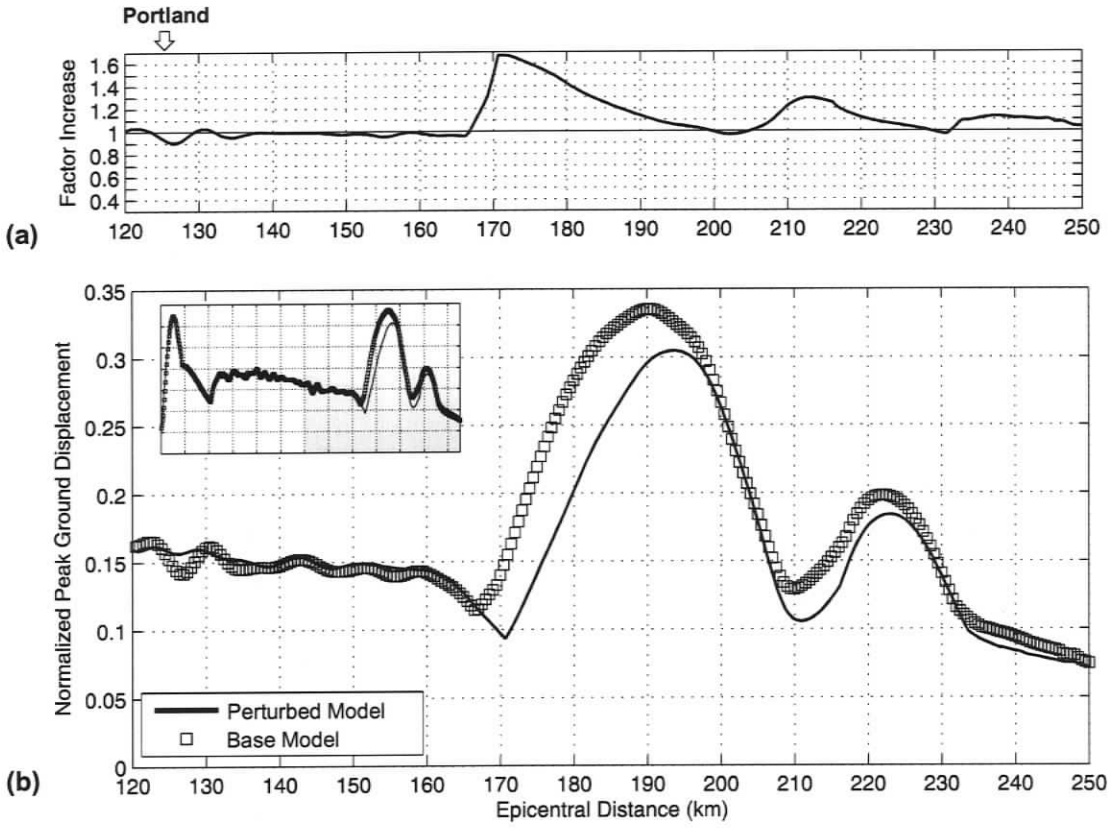

Figure 4.34 Quantitative comparison for a 1 Hz source at the down-dip limit of the transition zone along a profile in the vicinity of Portland. (a) Ratio between the base (square data points) and perturbed model results (solid line). (b) Peak ground motions for a 1 Hz source located at the down-dip limit of the transition zone for the base and perturbed models. The inset shows peak ground motions in the range 0 - 250 km.

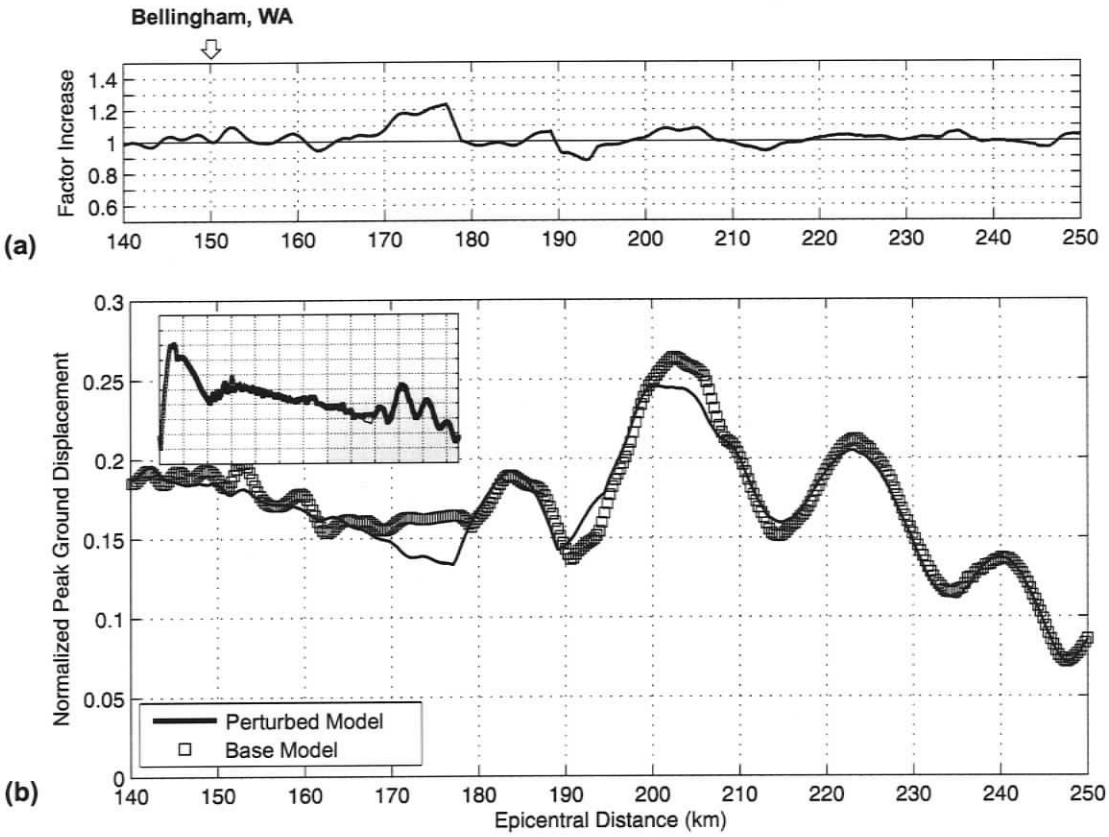

Figure 4.35 Quantitative comparison for a 2 Hz source at the down-dip limit of the transition zone along a profile in the vicinity of Victoria. (a) Ratio between the base (square data points) and perturbed model results (solid line). (b) Peak ground motions for a 2 Hz source located at the down-dip limit of the transition zone for the base and perturbed models. The inset shows peak ground motions in the range 0 - 250 km. Victoria is located at ~100 km epicentral distance.

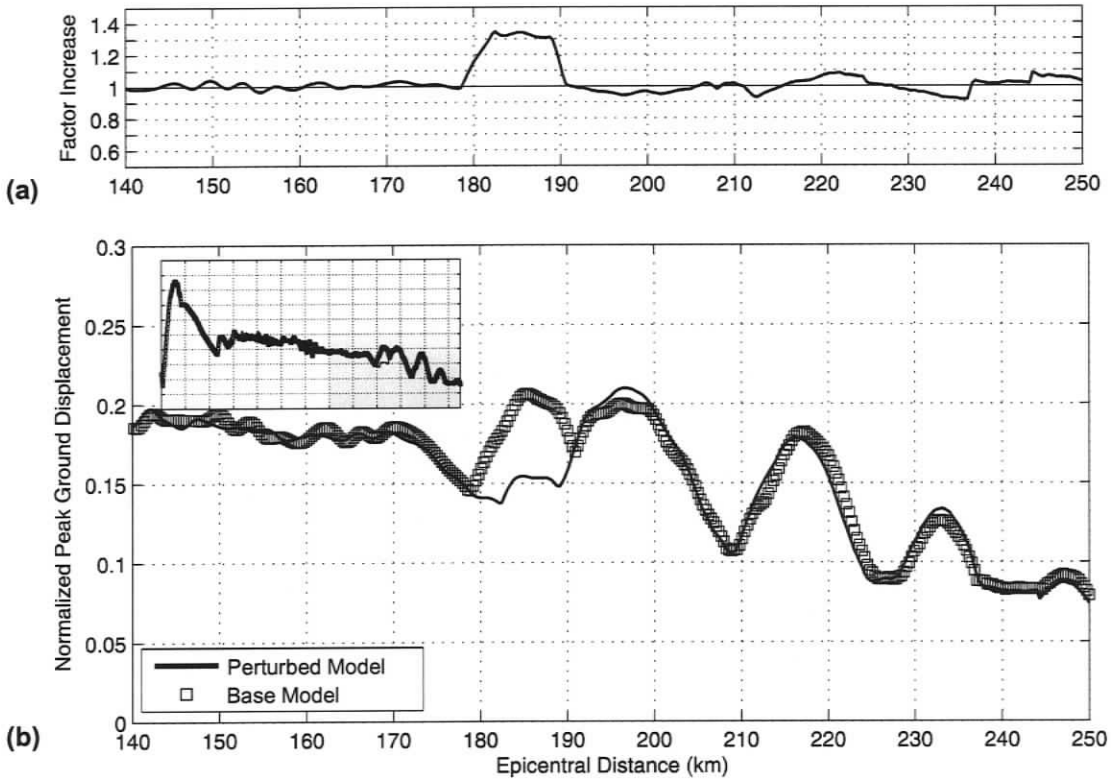

Figure 4.36 Quantitative comparison for a 2 Hz source at the down-dip limit of the transition zone along a profile in the vicinity of Portland. (a) Ratio between the base (square data points) and perturbed model results (solid line). (b) Peak ground motions for a 2 Hz source located at the down-dip limit of the transition zone for the base and perturbed models. The inset shows peak ground motions in the range 0 - 250 km. Portland is located at ~125 km epicentral distance.

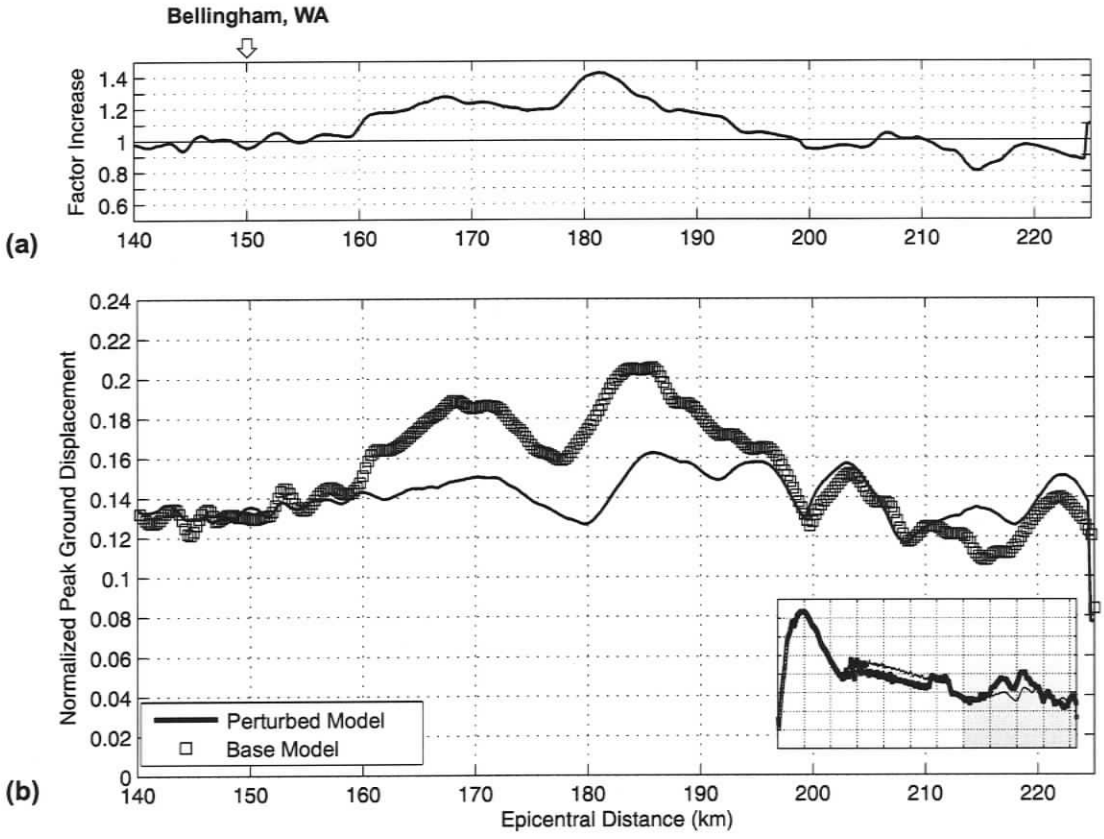

Figure 4.37 Quantitative comparison for a 3 Hz source at the down-dip limit of the transition zone along a profile in the vicinity of Victoria. (a) Ratio between the base (square data points) and perturbed model results (solid line). (b) Peak ground motions for a 3 Hz source located at the down-dip limit of the transition zone for the base and perturbed models. The inset shows peak ground motions in the range 0 - 230 km. Victoria is located at ~100 km epicentral distance.

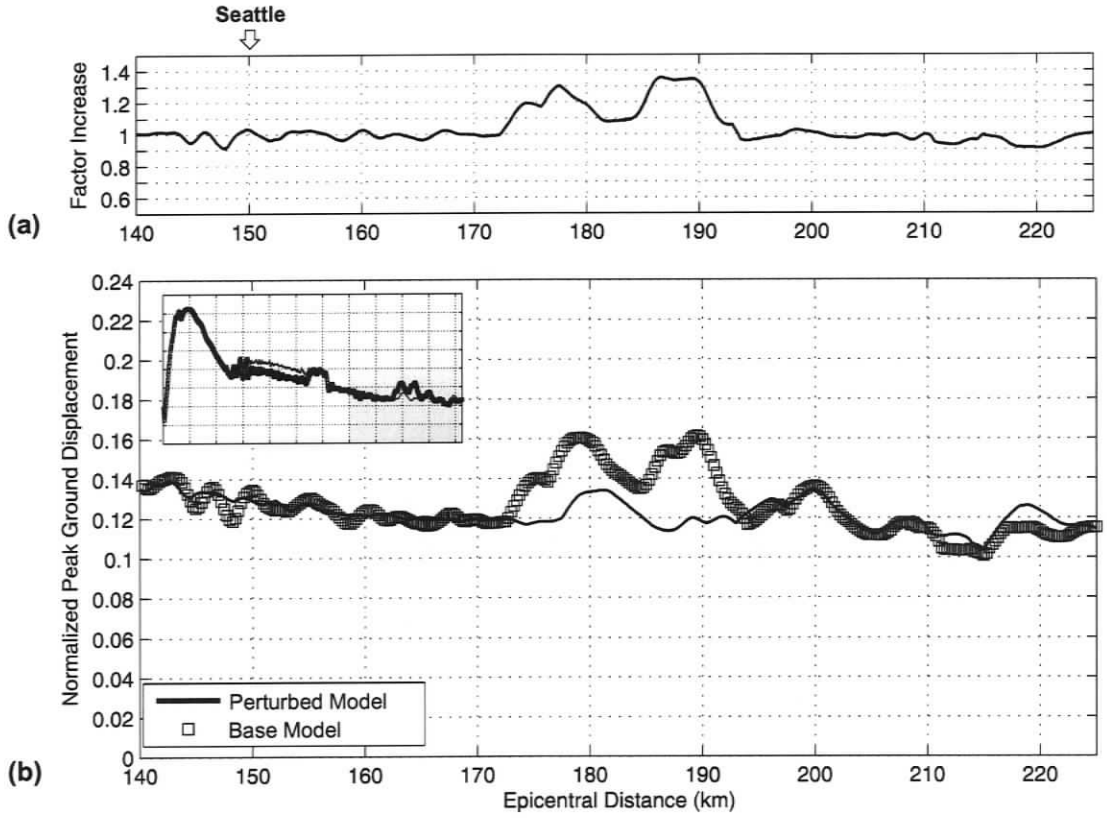

Figure 4.38 Quantitative comparison for a 3 Hz source at the down-dip limit of the transition zone along a profile in the vicinity of Seattle. (a) Ratio between the base (square data points) and perturbed model results (solid line). (b) Peak ground motions for a 3 Hz source located at the down-dip limit of the transition zone for the base and perturbed models. The inset shows peak ground motions in the range 0 - 230 km.

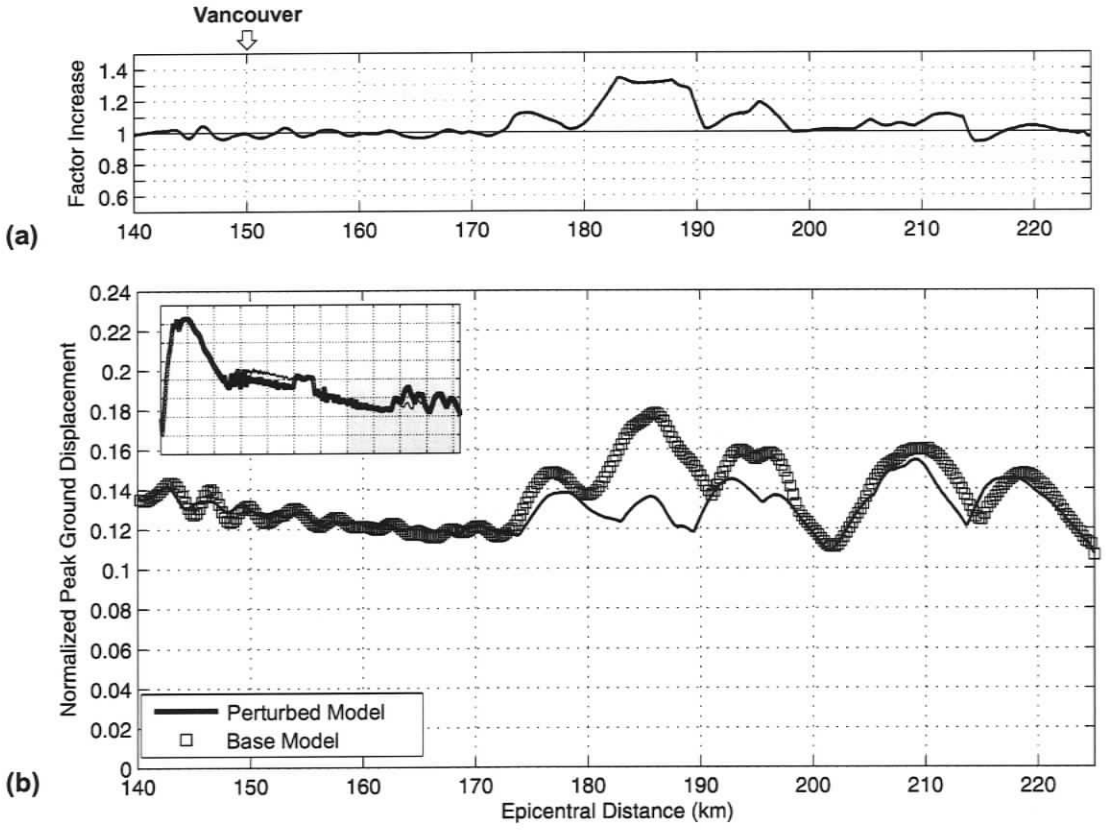

Figure 4.39 Quantitative comparison for a 3 Hz source at the down-dip limit of the transition zone along a profile in the vicinity of Vancouver. (a) Ratio between the base (square data points) and perturbed model results (solid line). (b) Peak ground motions for a 3 Hz source located at the down-dip limit of the transition zone for the base and perturbed models. The inset shows peak ground motions in the range 0 - 230 km.

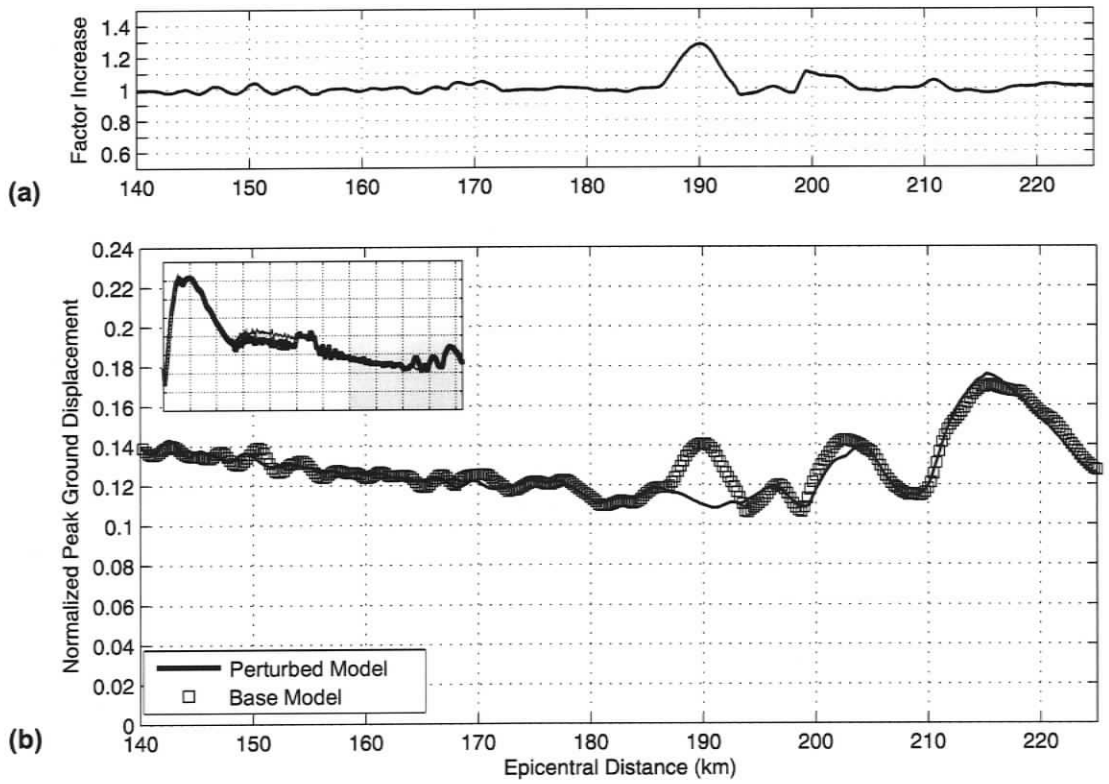

Figure 4.40 Quantitative comparison for a 3 Hz source at the down-dip limit of the transition zone along a profile in the vicinity of Portland. (a) Ratio between the base (square data points) and perturbed model results (solid line). (b) Peak ground motions for a 3 Hz source located at the down-dip limit of the transition zone for the base and perturbed models. The inset shows peak ground motions in the range 0 - 230 km. Portland is located at ~125 km epicentral distance.

critical reflection arrivals with arrivals from refractions in the oceanic crust decrease PGM in the base model. The remaining profiles for a 1 Hz source display similar results.

The behavior of peak ground motions change for a 2 Hz source along the same profile (figure 4.23). Amplitudes in the base model exceed those in the perturbed model in the 30 – 60 km range by a factor of up to 1.45. A second peak in which the base model exceeds the perturbed model by a factor of up to 1.3 is evident in the range 65 – 80 km. The first peak is due to the arrival of post-critical reflections at the oceanic Moho. The second peak is due to a suite of later arrivals, which represent strong amplitude multiples between the base of oceanic layer 2 and the top of the oceanic crust. In other profiles where the dip of the subducting oceanic crust is shallower, this pattern is less distinct. For a profile in the vicinity of Seattle, where the dip of the subducting slab is shallowest, the second peak has shifted seaward combining with the first peak (figure 4.24). For a profile in the vicinity of Victoria, where the dip of the oceanic slab is slightly steeper, the two-peak pattern is evident, but not as developed as that observed for the Vancouver profile (figure 4.25). Finally, a similar pattern of peak ground motions is evident for the Portland profile, where the oceanic slab has a similar dip to that along the Vancouver profile (figure 4.26). The change in the pattern of PGM is due to the effect of the apparent dip of the oceanic slab on the arrival times of multiples. This change will affect the manner in which arrivals from multiples interact. The behavior of PGM for a 3 Hz source is similar to that observed for a 2 Hz source, as a profile in the vicinity of Vancouver indicates (figure 4.27). However, the second peak is less distinct.

4.5.2 Down-dip Limit of the Locked Zone

The behavior of maximum ground motions does not change dramatically when the 1 Hz source is moved to the estimated down-dip limit of the locked zone, as is evident in a plot of PGM with distance for a profile in the vicinity of Vancouver (figure 4.28). Amplitudes in the base model exceed those in the perturbed model by a factor of up to 1.45 between 60 km and 130 km. Between 130 km and 190 km, base model amplitudes decrease by a factor of 0.8 with respect to the perturbed model. The remaining profiles for a 1Hz source display similar results.

The behavior of peak ground motions has changed slightly when the dominant source frequency is increased to 2 Hz. Figure 4.29 displays the PGM as a function of distance from a 2 Hz source for both models along a profile in the vicinity of Vancouver. In the range 70 – 120 km, amplitudes in the base model exceed those in the perturbed model by a factor up to 1.5. Beyond this range, oceanic post-critical reflections have little effect on observed peak ground motions. Profiles in the vicinity of Victoria, Seattle and Portland display a similar pattern.

The pattern of peak ground motions for a 3 Hz source is similar to that observed for a 1.0 Hz source (figure 4.30). The base model exceeds the perturbed model by a maximum factor of up to 1.4 in the range 80 – 110 km. In contrast, the perturbed model exceeds the base model between 110 and 180 km. Base model amplitudes decrease by a factor of up to 0.6 with respect to the perturbed model. This pattern of PGM is observed for other profiles with the same source frequency.

4.5.3 Down-dip limit of the Transition Zone

In the final models, the contribution of post-critical reflections at the oceanic Moho to ground motions is examined for a source at the down-dip limit of the transition zone of both the base and perturbed models. The pattern of peak ground motions for this source location is complicated by seismic energy propagating through the velocity structure of the serpentinized forearc mantle wedge. Based upon travel-time branches, there are three possible propagation paths for reflections at the oceanic Moho. The first path propagates through the continental crust, the second path propagates through the forearc mantle wedge and the third path propagates through the forearc mantle wedge and the upper continental mantle. As well, refractions within the oceanic crust may have these propagation paths. The interaction of arrivals from these phases and multiple propagation paths define the pattern of PGM.

Figure 4.31 displays the maximum ground motions for a profile in the vicinity of Victoria from a 1 Hz source. Amplitudes in the base model exceed those in the perturbed model by a factor of up to 1.45 between 130 km and 190 km. In this range, arrivals from strong oceanic Moho post-critical reflections propagating through the continental crust increase ground motions. Beyond 190 km, amplitudes in the base model and those in the perturbed model are similar. This indicates that oceanic Moho reflections do not increase PGM in this region.

In other profiles where the dip of the subducting oceanic crust is steeper, the pattern of PGM changes. For a profile in the vicinity of Seattle, where the dip of the subducting slab is slightly steeper, the increase in peak ground motions between 120 km and 190 km is less distinct (figure 4.32). Furthermore, an increase in peak ground motion is evident in the range 180 – 250 km. For a profile in the vicinity of Vancouver, where the dip of the oceanic slab is even steeper, amplitudes of the base model in the range 170 – 250 km have increased (figure 4.33). Finally, for a profile in the vicinity of Portland, where the dip of the oceanic slab is steepest, base model amplitudes in the range 170 – 250 km have continued to increase (figure 4.34). This change in the contribution of post-critical reflections at the oceanic Moho to peak ground motions as a function of the apparent dip of the oceanic slab can be explained in terms of the interaction of propagation paths. For a shallow oceanic slab dip, a significant portion of post-critical reflections at the oceanic Moho

propagates exclusively through the continental crust. In the range 120 – 180 km, PGM amplitudes increase with the arrival of strong post-critical reflections propagating through the continental crust. As the dip of the oceanic slab increases, the portion of post-critical reflections propagating through the continental crust reduces while the portion propagating through the forearc mantle wedge increases. This causes a decrease in base model amplitudes in the range 120 – 180 km, while increasing amplitudes in the range 180– 250 km. Finally, for the Portland profile amplitudes of the base model exceed the perturbed model by a factor of up to 1.65 between 170 km and 250 km.

The behavior of PGM is more complicated when the dominant source frequency is increased to 2 Hz. This is due to the interaction of more impulsive arrivals as compared to the previous source frequency. However, many of the same patterns of PGM described above are evident, although less distinct.

Figure 4.35 displays the PGM for a profile in the vicinity of Victoria. Amplitudes in the base model exceed those in the perturbed model by a factor of up to 1.25 between 165 km and 180 km. Beyond this range, base model results and perturbed models are similar. As the apparent dip of the oceanic slab increases, the contribution of post-critical reflections in the range 160 – 180 km decreases while beyond this range the contribution increases. This is evident in the profiles for Seattle, Vancouver and Portland. Specifically, for a profile in the vicinity of Portland amplitudes of the base model exceed those in the perturbed model by a factor of up to 1.32 in the range 180 – 190 km (figure 4.36).

The behavior of PGM becomes more complicated when the source frequency is increased to 3 Hz. For a profile in the vicinity of Victoria, amplitudes in the base model exceed the perturbed model by a factor of up to 1.4 between 160 km and 200 km (figure 4.37). The region in which the base model exceeds the perturbed model becomes narrower for a profile in the vicinity of Seattle (figure 4.38). For a profile in the vicinity of Vancouver, this region becomes broader being evident in the range 170 – 200 km (figure 4.39). Finally, for a profile in the vicinity of Portland the amplitudes of the base model exceed the perturbed model by a factor of up to 1.3 between 185 km and 195 km (figure 4.40). This region is significantly narrow than those present in the previous profiles. A clear dependence of peak ground motions on the dip of the oceanic slab is not evident in the profiles for a 3 Hz source.

4.6 Lower Source Frequency

In this section, a lower source frequency of 0.5 Hz is modeled. Lower frequencies will influence larger structures. Nominally, the resonant period for a structure is 1/10 of a second per floor. For example, a 10-

story building will be influenced by 1 Hz energy, whereas 0.5 Hz data will influence 20-story structures. Figures pertaining to the 0.5 Hz results are included in Appendix C.

Figure C.1 maps the normalized PGM of the post-critically enhanced region for rupture at the up-dip limit of the locked zone for a source with a dominant frequency of 0.5 Hz. Similar to the 1 Hz results, amplitudes initially increase with distance beyond 30 km. Maximum PGM amplitudes are located at approximately 40 km and decay only slightly to 80 km (figure C.7 – C.9).

For source depths at 10 km and greater, amplitudes within the post-critically enhanced region are less peaked for the 0.5 Hz source compared to higher source frequencies (figures C.2 – C.5). Amplitudes within the enhanced region exhibit a flat trend with localized variations in amplitudes with widths on the order of 10 – 20 km (figures C.10 – C.17). For frequencies less than 0.5 Hz (periods greater than 2 seconds), amplitudes within the post-critically enhanced region for source depths greater than 10 km also tend to be flattened. Localized variations in amplitudes within the region also exist.

For a source frequency of 0.5 Hz, the dominant period of arrivals is 2 seconds. The maximum separation of arrivals is approximately 2 seconds. Therefore, a lower source frequency will cause a greater interaction between arrivals. The effect of interference between several arrivals will diminish the weight of post-critical reflections on peak ground motions. Lower frequencies will tend to average amplitudes thereby flattening PGM within the enhanced region. Localized variations within the post-critically enhanced region are likely due to the interaction of later arriving phases. Hence, for structures of about 20 stories or higher, post-critical reflections do not contribute significantly to ground motions from great thrust earthquakes.

4.7 Effect of Seismic Attenuation

To quantify the influence of attenuation on the numerical simulation results, PGM from two models of the Cascadia subduction zone, one with approximate attenuation the other without, are examined. The focus will be to understand the effect of attenuation on the relative amplitudes of PGM.

In the following analysis, the effect of attenuation on ground motions from sources located at the up-dip and down-dip limits of the locked zone as well as the down-dip limit of the transition zone is considered. In addition, the effect of attenuation on ground motions for source frequencies of 1 Hz, 2 Hz and 3 Hz will be examined. An attenuation model for the Cascadia subduction zone as outlined in section 3.4.4 is applied. The influence of attenuation is accounted for by applying an approximate attenuation scheme

outlined in section 3.7. In the following figures (4.41 – 4.43), PGM along a profile in the vicinity of Vancouver will be compared to attenuated values.

Figure 4.41a displays the PGM as a function of distance for a 1 Hz at the up-dip limit of the locked zone. PGM are reduced by a maximum of 25% at 100 km. Attenuation has a minimal affect on the relative amplitudes of PGM. A distinctive increase in PGM is still visible in the range 30 – 60 km. For source frequencies 2 Hz and 3 Hz, ground motions are reduced by up to 35% and 50%, respectively (figure 4.41b & 4.41c). However, the relative increase in PGM is still apparent between 30 km and 90 km.

When the source location is moved to the down-dip limit of the locked zone, ground motions are reduced by up to 40%, 60% and 80% for source frequencies of 1 Hz, 2 Hz and 3 Hz, respectively (figure 4.42). The effect of attenuation is more significant for higher frequencies. The qualitative behavior of PGM remains relatively unchanged.

In the final model, the effect of attenuation is considered for a source located at the down-dip limit of the transition zone (figure 4.43). For a 1 Hz source, peak ground motions are reduced by up to 50%. However, the qualitative behavior of PGM is unchanged. For a 2.0 Hz source, ground motions are reduced by up to 80%. Beyond 215 km, the effect of attenuation is strongest due to propagation paths through the more highly attenuating portion of the continental mantle. The overall pattern of PGM becomes less distinct. Finally, for a 3 Hz source, amplitudes are reduced by up to 85%. The pattern of PGM is difficult to distinguish. Attenuation has significantly affected the qualitative behavior of PGM.

Figure 4.44 illustrates the effect of attenuation on the pattern of peak ground motions within the post-critically enhanced region for rupture at the down-dip limit of the locked zone. For a source frequency of 1 Hz the pattern of peak ground motions is relatively unchanged. However, amplitudes within the region have decreased with respect to figure 4.5 due to attenuation. For a source frequency of 3 Hz, an increase in peak ground motions within the enhanced area is barely evident. The effect of attenuation dramatically reduces amplitudes within the region compared to figure 4.16.

It is evident from the above observations that attenuation does not significantly alter the qualitative pattern of PGM for source depths less than 25 km and source frequencies less than 3 Hz. In conclusion, a significant increase in the observed PGM due to the influence of strong post-critical reflections at the oceanic Moho remains valid over the modeled frequency range, although the effect is less important at higher frequencies

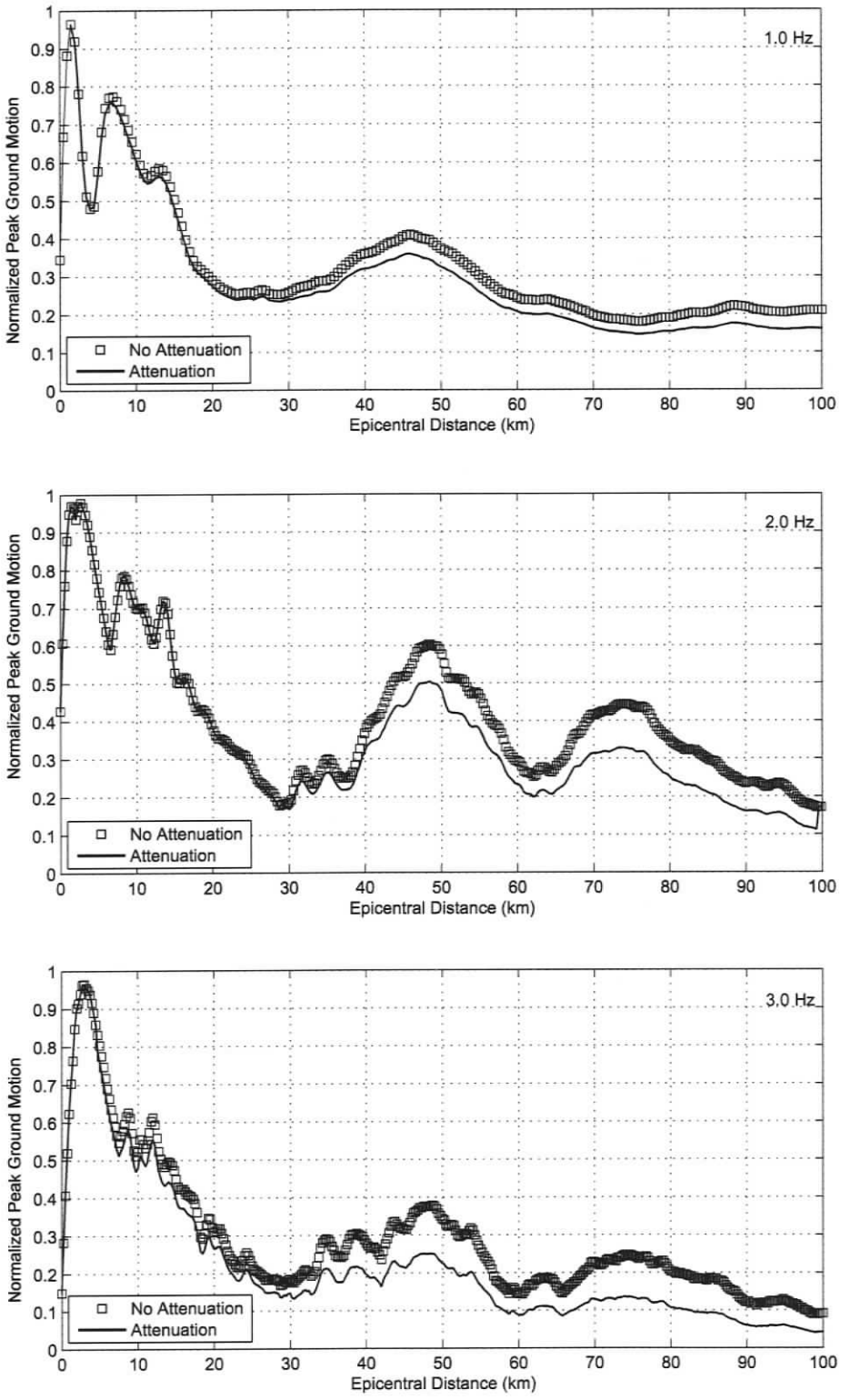

Figure 4.41 Normalized peak ground motion as a function of distance for a source at the up-dip limit of the locked zone for a model with attenuation (solid line) and without (square data points). Dominant source frequencies of (a) 1.0 Hz, (b) 2.0 Hz and (c) 3.0 Hz.

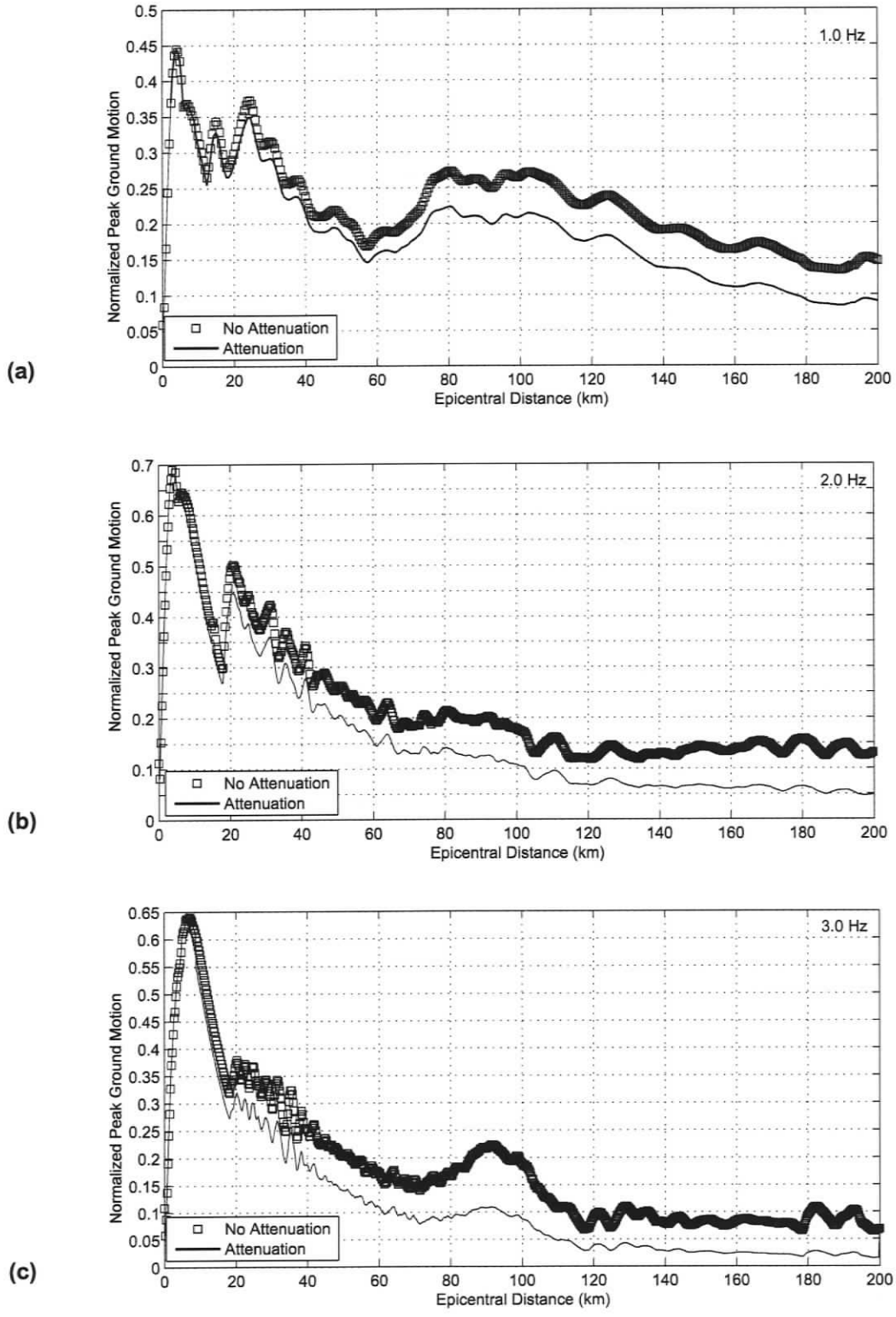

Figure 4.42 Normalized peak ground motion as a function of distance for a source at the down-dip limit of the locked zone for a model with attenuation (solid line) and without (square data points). Dominant source frequencies of (a) 1.0 Hz, (b) 2.0 Hz and (c) 3.0 Hz.

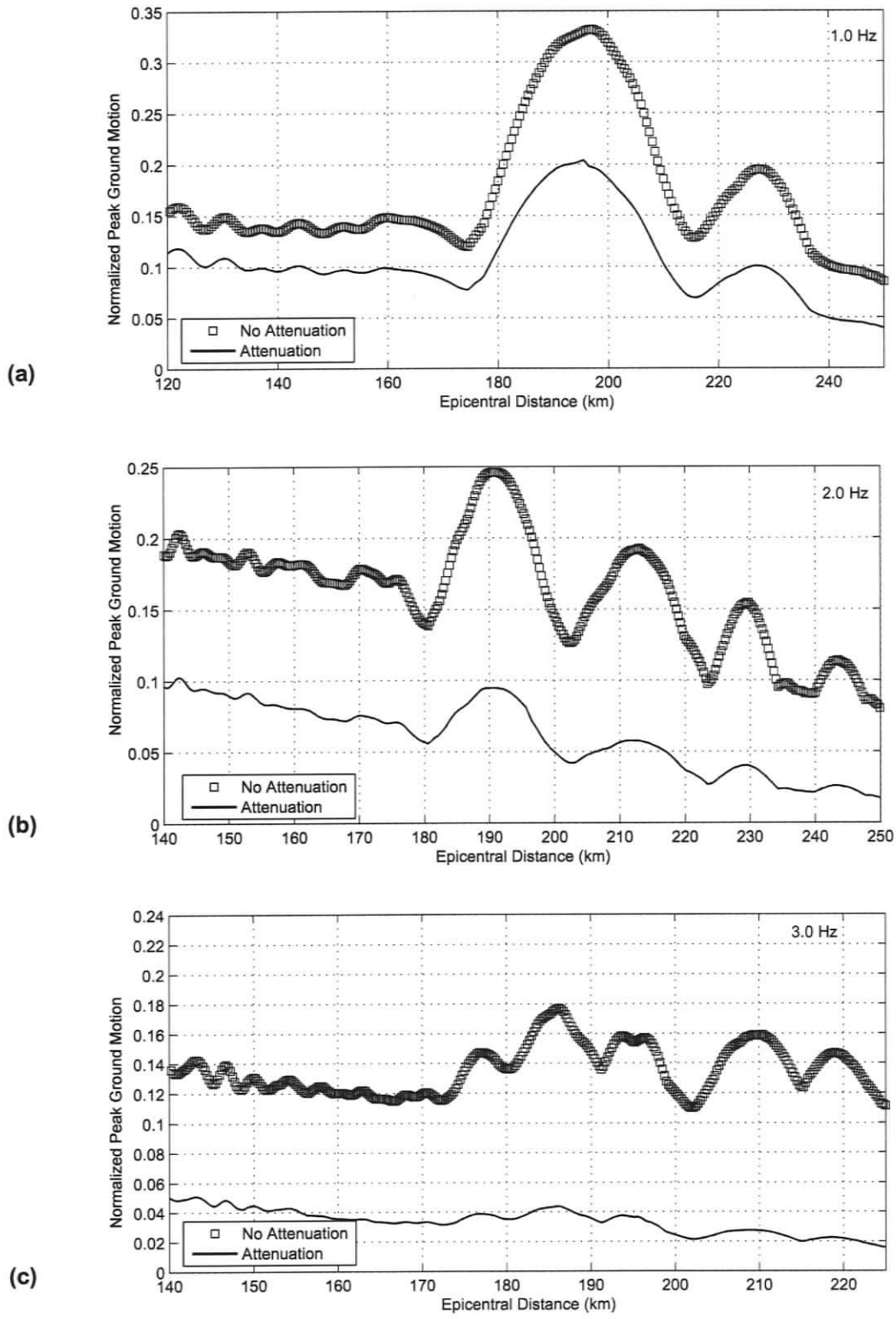

Figure 4.43 Normalized peak ground motion as a function of distance for a source at the down-dip limit of the transition zone for a model with attenuation (solid line) and without (square data points). Dominant source frequencies of (a) 1.0 Hz, (b) 2.0 Hz and (c) 3.0 Hz.

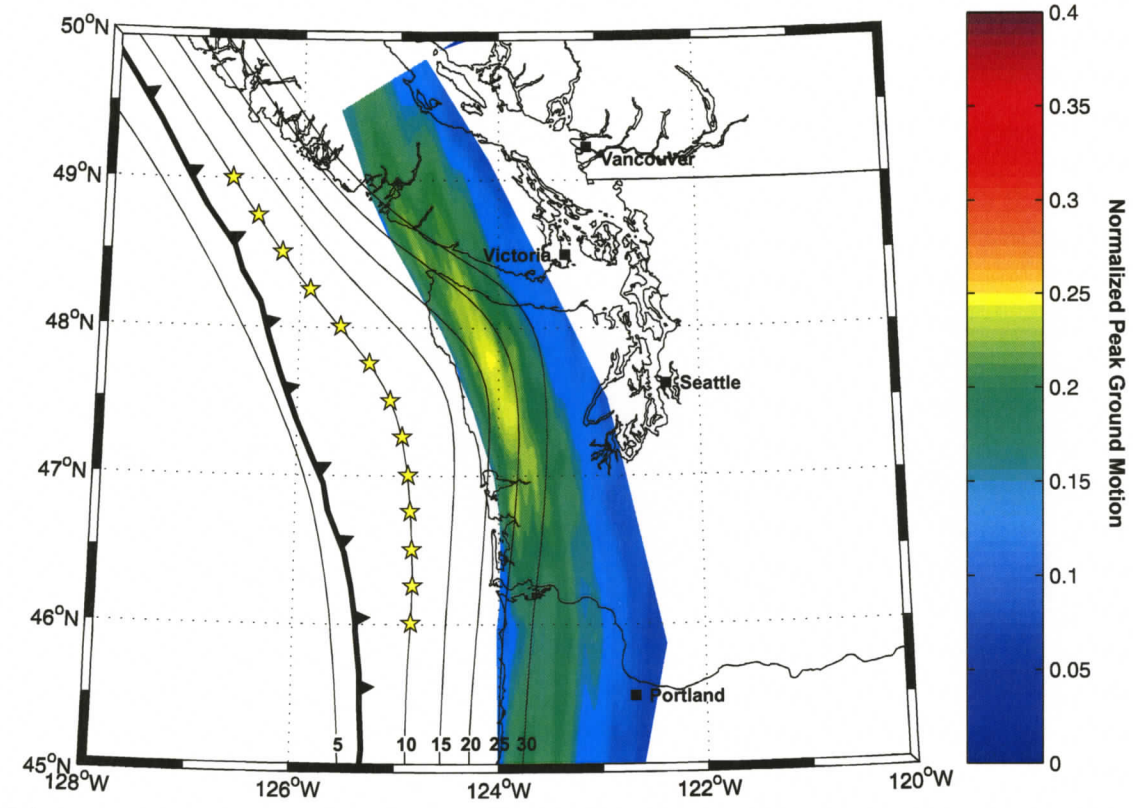

(a)

Figure 4.44 (a) Post-critically enhanced region for a 1 Hz source (yellow stars) at the down-dip limit of the locked zone with approximate attenuation applied. (b) Post-critically enhanced region for a 3 Hz source (yellow stars) at the down-dip limit of the locked zone with approximate attenuation applied.

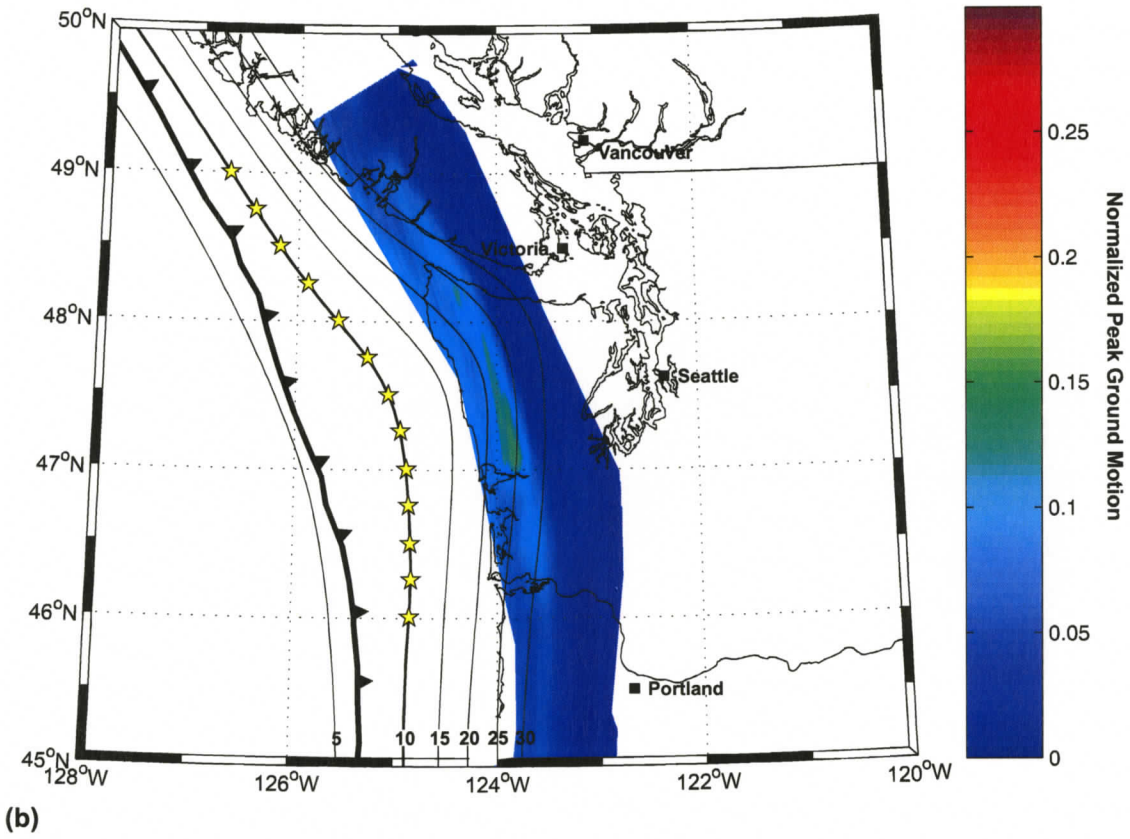

(b)

Figure 4.44 Continued...

4.8 Discussion

In the preceding analysis, the influence of post-critical reflections at the oceanic Moho on the spatial distribution of peak ground motions from a mega-thrust event was examined. Furthermore, the relative contribution of post-critical reflections to observed peak ground motions was quantified. These analyses have led to several interesting observations.

The change in dip of the oceanic slab directly influences the critical distance for the oceanic Moho reflections. The reflection off the oceanic Moho becomes post-critical at greater distances from the source as the apparent dip of the oceanic slab increases. This increases the offset between the post-critically enhanced region and the source location. Furthermore, increasing the source depth will have a similar effect due to geometric implications. Consequently, as rupture propagates down-dip, the offset between the source region and the post-critically enhanced region increases.

A sequence of strong amplitude multiples of post-critical reflections between the base of oceanic layer 2 and the top of the oceanic crust may cause a second distinct increase in peak ground motions at larger offsets. Due to geometric implications, this second peak occurs landward of the initial increase in peak ground motions attributed to the primary post-critical reflections. This causes the region in which post-critical reflections influence peak ground motions to broaden. However, the influence of multiples is only significant for source frequencies of 2 Hz and greater, located at the up-dip of the locked zone. For a source frequency of 1 Hz the wavelengths (~6km) are much larger than the ~2 km thick oceanic layer 2 and so constructive interference with the primary reflection will not occur.

The presence of the low-velocity forearc mantle wedge will affect the pattern of ground motions. It affords a route by which post-critical reflections at the oceanic Moho and refractions within the oceanic crust can escape upwards toward the Earth's surface rather than being trapped in the oceanic crust wave-guide [McNeill et al., 2004]. It acts to concentrate seismic energy by allowing different propagation paths to focus energy within a narrow band at approximately $122^{0}30$'W (figures 4.6 – 4.9).

The contribution of post-critical reflections at the ocean Moho to peak ground motions in the band at approximately $122^{0}30$'W is dependent on the portion of propagation paths through the forearc mantle wedge. For rupture at the down-dip limit of the transition zone, the portion of post-critical reflections propagating through the wedge increases as the apparent dip of the oceanic slab becomes steeper. This causes post-critical reflections to contribute more to observed PGM in this region. Alternatively, for a

shallower dipping oceanic slab, the contribution of post-critical reflections is more significant in the region seaward of this band.

In the analysis of ground motions from mega-thrust events, dominant source frequencies of 1 Hz, 2 Hz and 3 Hz were applied to examine the effect of source frequency on the contribution of post-critical reflections to peak ground motions. The geographical region in which post-critical reflections at the oceanic Moho influence peak ground motions is similar for different source frequencies. However, the behavior of peak ground motions within these regions did exhibit some source frequency dependence. For rupture extending down-dip of the locked zone, higher source frequencies did not exhibit a dramatic increase in peak ground motions within the post-critically enhanced region. Within this region, PGM amplitudes decay less rapidly than expected for geometric spreading in two dimensions. This observation combined with the effect of attenuation on the results indicates that the influence of post-critical reflections to peak ground motions is progressively less significant at higher frequencies.

4.8.1 Implications of Alternate Velocity Models

Analysis of teleseismic receiver functions recorded in the northern Cascadia subduction zone indicates a prominent low velocity zone beneath central Vancouver Island [Cassidy & Ellis, 1991; 1993]. This feature correlates with the E-reflectors observed in LITHOPROBE reflection data. This complex S-wave velocity structure is not incorporated into the large-scale velocity model for the Cascadia subduction zone outline in Chapter 3. The addition of this embedded layer will not significantly alter the geographic distribution of post-critically enhanced peak ground motions. The location where rays emerge at the surface from paths propagating through the E-layer will not be significantly changed due to the parallel boundaries of the E-layer. However, the absolute amplitudes of peak ground motions in this region will decrease due to additional energy -partitioning of propagation paths through the low-velocity layer. Relative amplitudes within this region will not be strongly affected.

Several competing interpretations exist for the position of the subducting oceanic crust. The structural model employed for the Cascadia subduction zone adopts the traditional view that the F-reflector marks the top of the oceanic crust. Alternate interpretations imply that the oceanic crust is 6 – 8 km shallower beneath Vancouver Island. A shallower subducting oceanic crust will shift the post-critically enhanced region seaward due to geometric implications.

4.8.2 Comparison to Empirical Estimates of Peak Ground Acceleration

Estimates of ground motions for earthquakes that occur in subduction zones are an important input into seismic hazard analysis. However, there are rarely a sufficient number of strong-ground motion recordings in the vicinity of a site to develop a direct empirical estimation of the motions expected for an earthquake. It is necessary to develop relations in the form of attenuation curves for estimating peak ground acceleration in terms of magnitude, distance, site conditions, and other variables from strong ground motion data from a large region or particular tectonic setting [Boore et al., 1997]. This is particularly applicable to the Cascadia region (British Columbia, Washington, Oregon and northern California) where there is little ground motion data from which to develop attenuation relations [Atkinson & Boore, 2003]. Therefore, an empirical ground motion relation based on a global database of subduction zone earthquakes is applied in the seismic hazards analysis in this region. Current seismic hazard maps of the Cascadia region estimate the ground motions from in-slab and interface earthquakes based on a global subduction database using attenuation relations developed by Youngs et al. (1997).

Attenuation relationships for horizontal peak ground acceleration from subduction zone earthquakes are developed by performing regression analyses on the global subduction dataset. The functional form of the regression model incorporates specific features of the data, such as magnitude dependence, source-to-site distance, focal depth and geometric spreading. Additional coefficients in the functional form are determined by regression analysis, but do not have a physical analogy.

Like any empirical regression, attenuation relations model the database, which they claim to represent, in a mean sense. Variability of peak ground accelerations of individual recordings about the median attenuation relationship exists [Youngs et al., 1997]. Attenuation relations will not accurately estimate region specific increases in peak ground acceleration, as those imposed by the arrival of post-critical reflections at the oceanic Moho. In this section, peak ground accelerations from the synthetic seismograms are compared to the attenuation curve from an interface earthquake in a subduction zone developed by Youngs et al. (1997).

In order to appropriately compare synthetic peak ground accelerations to the attenuation relation values, several fundamental differences between the two methodologies need to be addressed. Seismic attenuation is not modeled in the pseudo-spectral synthetics; therefore approximate seismic attenuation is applied to the synthetic seismograms. Peak ground acceleration values are measured from the vertical component of the synthetic accelerograms. The vertical component of peak ground acceleration from the synthetic seismograms, in the absence of a low velocity surface layer in the structural model, can be considered

analogous to the peak ground acceleration in the horizontal component. Therefore, vertical peak ground acceleration from the synthetic accelograms is compared to the horizontal peak ground acceleration estimates from the attenuation relation. The geometric attenuation for the 2-D numerical model is slightly weaker than that for an actual 3-D wave-field. To account for this, the square root of the empirical value is applied to obtain a reference attenuation curve for the 2-D wave-field [Furumura & Kennett, 1998]. Simulated peak ground accelerations are from an instantaneous rupture along a line whereas the attenuation values are from rupture propagating on the subduction interface. In order to compare the relative amplitudes, simulated peak ground acceleration amplitudes are scaled by a multiplier, which is defined by minimizing a least-squares fit to the empirical values in the range 10 – 200 km.

In figure 4.45a, the simulated peak ground accelerations values from a 1 Hz source at the down-dip limit of the locked zone are compared to the peak ground acceleration values on a rock site predicted from a **M** 9 interface earthquake with a focal depth of 10 km using the attenuation relation developed by Youngs et al. (1997). Simulated peak ground acceleration values exhibit considerable variability about the median attenuation relation. In the range 60 – 150 km, simulated results display a local increase in amplitudes due to the influence of post-critical reflections at the oceanic Moho. In this region, simulated amplitudes exceed the attenuation curve between 70 km and 110 km. In contrast, simulated amplitudes are significantly less than the attenuation curve in the ranges 25 – 70 km and 110 – 200 km.

The behavior of the simulated peak ground acceleration values compared to the attenuation curve do not change dramatically when the focal depth is increased to 15 km, as is evident in figure 4.45b. Simulated results display an increase in amplitudes due to the influence of post-critical reflections between 80 km and 180 km, exceeding the attenuation curve in the range 100 – 160 km. Alternatively, the attenuation curve exceeds simulated amplitudes in the range 35 – 70 km and 110 – 200 km.

In the final comparison, the source location is moved to the down-dip limit of the transition zone at a focal depth of 25 km (figure 4.45c). A dramatic increase in simulated peak ground acceleration values is evident between 150 km and 240 km. In this range, the low velocity serpentinized forearc mantle wedge focuses post-critical reflections at the oceanic Moho and refractions within the oceanic crust upward to the surface.

In a similar fashion, simulated peak ground acceleration for dominant source frequencies of 2 Hz and 3 Hz can be compared to the attenuation relation developed by Youngs et al. (1997) (figure 4.46 & 4.47). For both frequencies the simulated amplitudes are significantly less than the attenuation curve beyond 50 km epicentral range. This is due to the increased effect of seismic attenuation on higher frequencies.

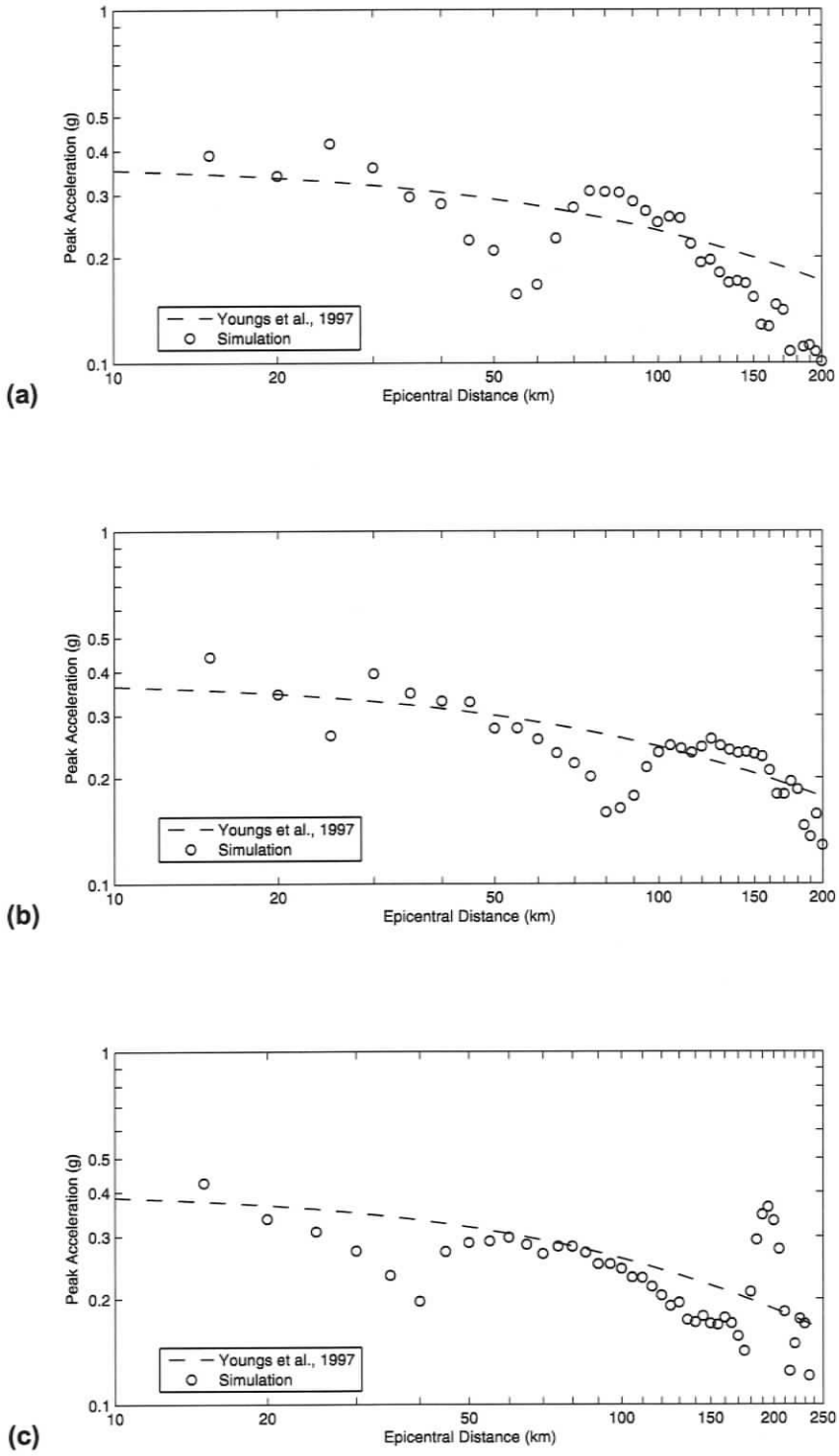

Figure 4.45 Comparison of the simulated peak ground accelerations values (circle data points) from a 1 Hz source for focal depths of (a) 10 km, (b) 15 km and (c) 25 km to the peak ground acceleration values on a rock site predicted from a **M** 9 interface earthquake using the attenuation relation (dashed line) developed by Youngs et al. (1997).

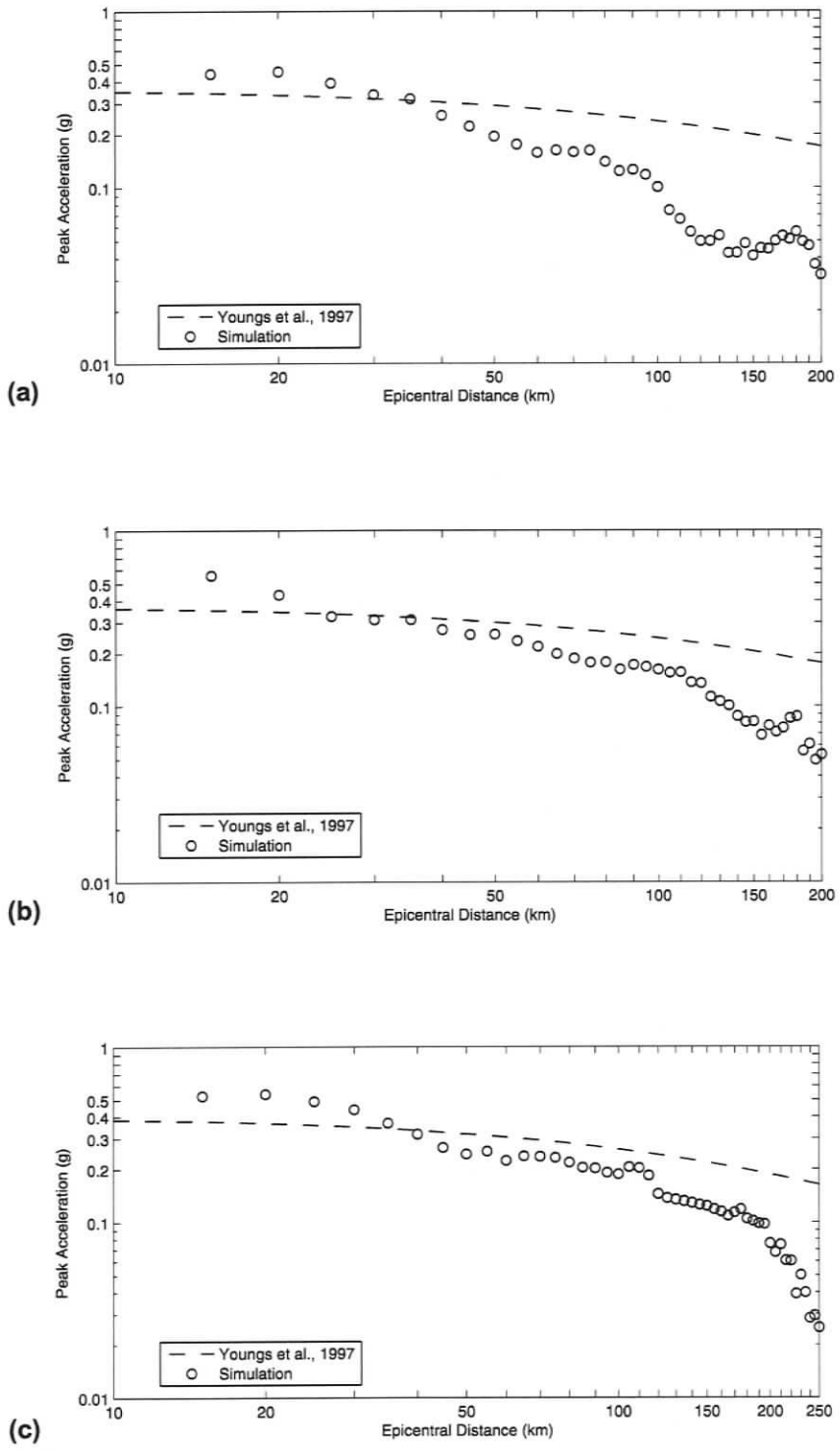

Figure 4.46 Comparison of the simulated peak ground accelerations values (circle data points) from a 2 Hz source for focal depths of (a) 10 km, (b) 15 km and (c) 25 km to the peak ground acceleration values on a rock site predicted from a **M** 9 interface earthquake using the attenuation relation (dashed line) developed by Youngs et al. (1997).

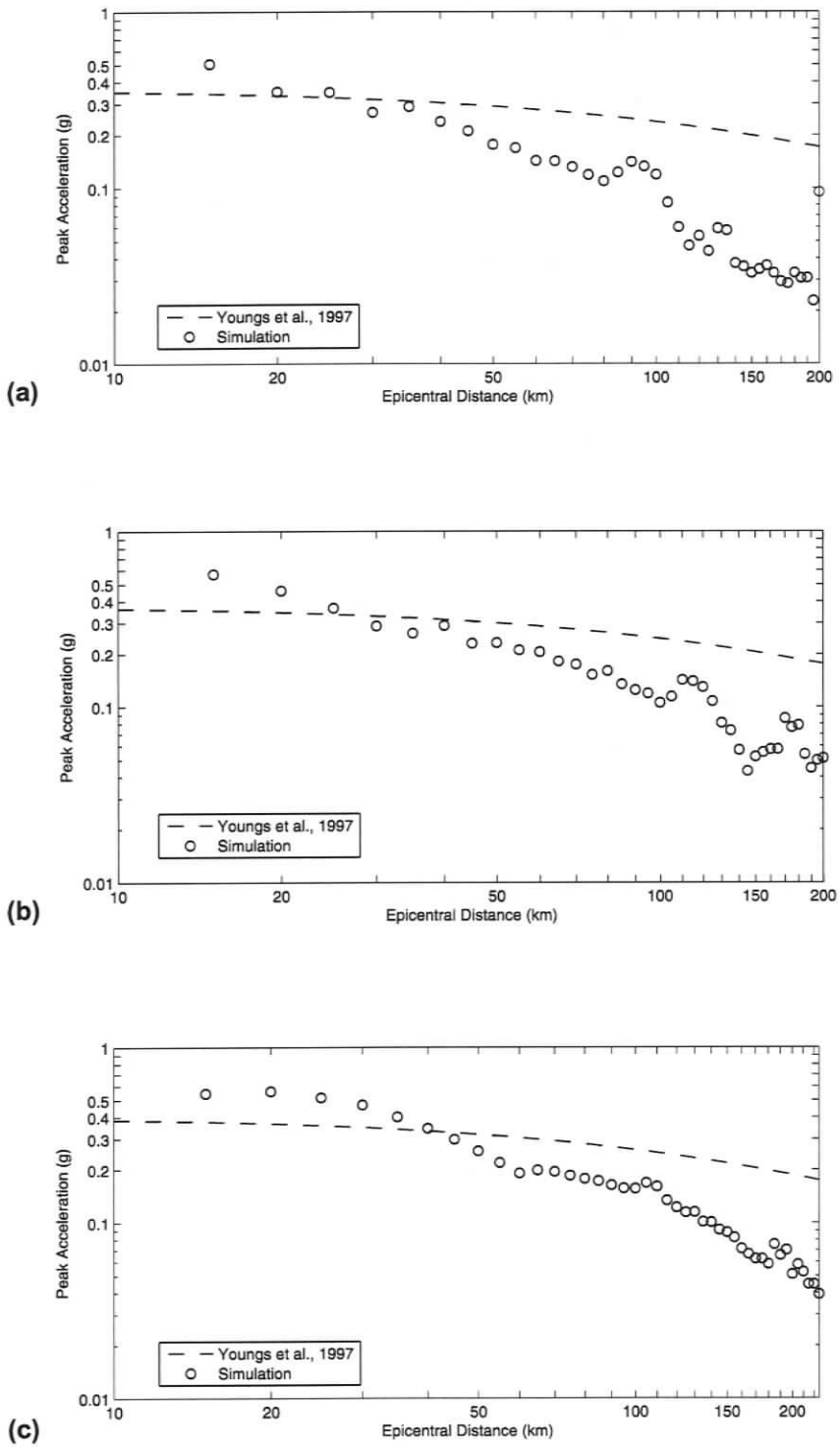

Figure 4.47 Comparison of the simulated peak ground accelerations values (circle data points) from a 3 Hz source for focal depths of (a) 10 km, (b) 15 km and (c) 25 km to the peak ground acceleration values on a rock site predicted from a **M** 9 interface earthquake using the attenuation relation (dashed line) developed by Youngs et al. (1997).

The above comparison indicates that the attenuation curve provides an estimate of the median peak ground acceleration, but it does not estimate localized variations. For a source frequency of 1 Hz and focal depths of 10 km and 15 km, peak ground acceleration amplitudes within the post-critically enhanced region did not significantly exceed the attenuation curve. However, for a focal depth of 25 km the focusing effect of the serpentinized forearc mantle wedge produced significantly elevated peak ground acceleration amplitudes in the range 180 – 210 km. At source frequencies higher than 1 Hz, the simulated amplitudes are significantly less than the attenuation curve.

4.8.3 Implications of Results on Seismic Hazard in the Pacific Northwest

The landward limit to the seismogenic zone, which extends little if at all beneath the coast, limits the ground motions from a mega-thrust event at the larger Cascadia cities located 100 – 200 km inland [Hyndman & Wang, 1995]. However, the influence of post-critical reflections at the oceanic Moho may locally increase peak ground motions in the vicinity of these populated areas. The geographic region in which post-critical reflections enhance peak ground motions is primarily dependent on the down-dip extent of rupture. For rupture extending to the down-dip limit of the locked zone, the enhanced region is located on the coast, between 60 km and 160 km from the source (figure 4.2, 4.8, 4.13). Peak ground motions are a factor of up to 1.45 greater than amplitudes calculated for a model without oceanic Moho post-critical reflections. A local increase in peak ground motions is clearly visible in the range 60 – 120 km for a profile in the vicinity of Vancouver (figure 4.25). For rupture extending to the 15 km depth contour of the subducting oceanic crust, the post-critically enhanced region maps within the Pacific Northwest urban corridor (figure 4.3, 4.9, 4.14). Profiles of peak ground motions in the vicinity of the major population centers of Vancouver, Victoria, Seattle and Portland illustrate a local increase in amplitudes. Although the maximum extent of rupture to a mega-thrust event may be offshore, a localized increase in peak ground motions may occur within the Pacific Northwest urban corridor. For rupture extending to the 15 km depth contour of the oceanic slab, peak ground motion amplitudes at distances beyond 100 km are controlled by post-critical reflections at the oceanic Moho.

For rupture extending down-dip of the 15 km depth contour of the oceanic slab, post-critical reflections propagate through the serpentinized forearc mantle wedge. This region acts to focus post-critical reflections at the oceanic Moho and refraction within the oceanic crust into a narrow band causing an increased peak ground motions. For a range of source depths, the geographic location of this band does not change (figure 4.3 – 4.6). The primary control on the location of this region is the forearc mantle structure. A current model for the structure of the serpentinized forearc mantle wedge focuses energy landward of the major population centers. However, these results indicate the importance of an accurate structural model

for the serpentinized forearc mantle wedge to predict ground motions from a mega-thrust event.

CHAPTER 5
APPLICATION

5.1 Introduction

On September 25, 2003 at 19:50 (GMT) the Tokachi-oki mega-thrust earthquake occurred ~80 km offshore Tokachi, Hokkaido, Northern Japan [Japanese Meteorological Agency, JMA]. Two people went missing and over 800 people were injured in the event. The M_{JMA} 8.0 earthquake was the largest event to occur since the installation of the high-density digital strong-motion seismograph network throughout Japan.

The Tokachi-oki region is situated on the northwestern Pacific margin approximately 200 km northwest of the junction of the Kuril and Japan trenches (figure 5.1). At the Kuril trench, the Pacific Plate subducts beneath Hokkaido at a rate of ~80 mm/yr and a direction $N60^0$ W [DeMets et al., 1990]. The northeast Japan arc and the Kuril arc form the arc-arc type Hidaka collision zone in southeastern Hokkaido. This collision has been occurring since the Miocene resulting in the Hidaka mountain range [Arita et al., 1998]. The tectonic motions in this region have produced a number of large inter-plate earthquakes as well as intra-plate earthquakes.

In this chapter, we examine the distribution of strong ground motions using the National Research Institute for Earth Science and Disaster Prevention (NEID) strong ground motion seismic network. The waveforms from the 2003 Tokachi-oki earthquake are used to investigate the characteristic features of seismic wave propagation within the crust and upper mantle and to measure the arrival times and amplitudes of prominent phases, specifically those phases responsible for maximum peak ground acceleration (PGA). Using the synthetic seismogram methodology developed in chapter 3, variations of PGA with epicentral distance are modeled. Specifically, an explanation for the observed maximum in PGA is proposed.

5.2 Observations of Strong Ground Motion

The 2003 Tokachi-oki earthquake was observed on the NEID digital strong-motion seismograph networks, KiK-NET and K-NET, across all of Japan. Each station is equipped with a three-component, force-balanced accelerometer (K-net95) with an 18-bit resolution and 108 dB dynamic range. KiK-NET and K-NET station instruments have a full-scale of 2000 gals and sampling frequencies of 200 Hz and 100 Hz, respectively. The instrument response is flat from DC to 20 Hz with a cut-off frequency of 30 Hz. The recording system is initiated by a triggering signal of 0.1 – 10 gals and has a 15 second pre-triggering memory.

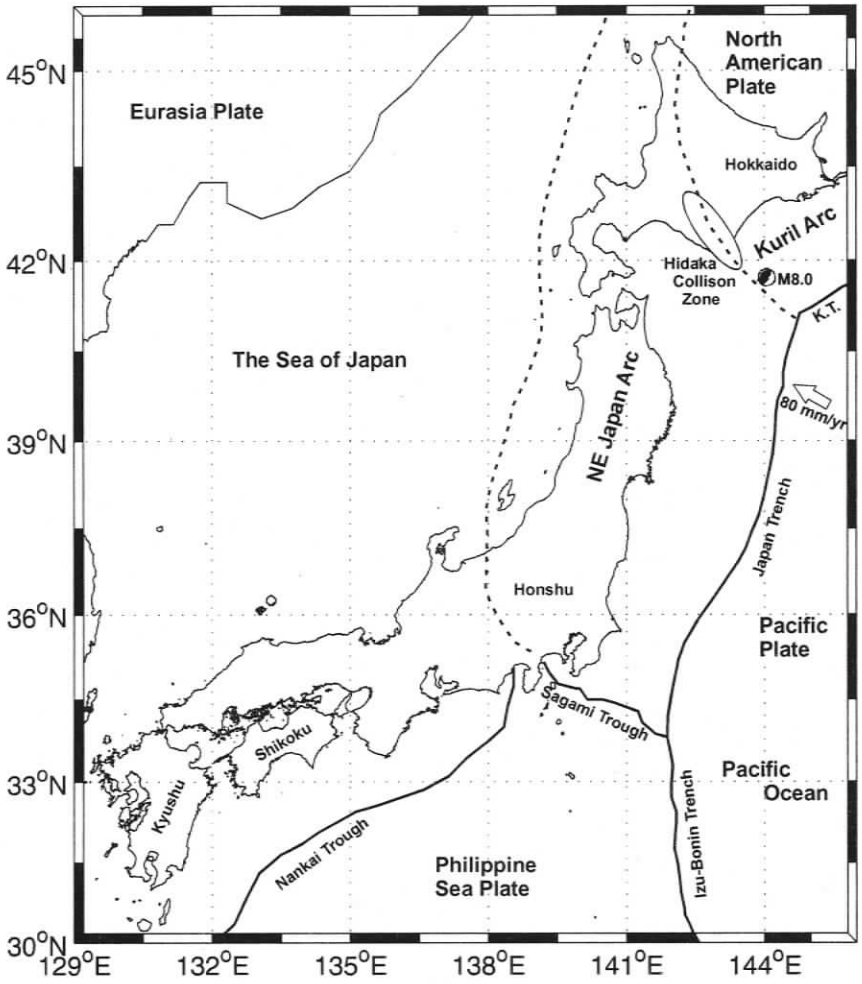

Figure 5.1 Tectonic map of Japan. Hokkaido is located 200 km northwest of the junction between the Kuril trench (K.T.) and the Japan Trench. Epicenter and focal mechanism of the 2003 Tokachi-oki earthquake determined by JMA.

Specific site conditions have the potential to amplify seismic shaking. Therefore, a stringent site condition classification is important for comparing peak ground acceleration (PGA) between distinct stations. The average shear-wave velocity of the uppermost 30 m ($\overline{V}_S$ (30)) and the corresponding National Earthquake Hazard Reduction Program (NEHRP) site class are widely used parameters for classifying sites to predict their potential to amplify seismic shaking (Table 5.1). KiK-NET and K-NET station site conditions are defined in terms of soil conditions and near-surface P-wave and S-wave velocities [data source: www.k-net.bosai.go.jp/ and www.kik.bosai.go.jp/]. With few exceptions, the shear–wave velocities at KiK-NET and K-NET stations are defined at depths 10 – 20 m. In order to calculate $\overline{V}_S$ (30) some method of extrapolating shear-wave velocities to 30 m must be applied. The simplest method (method 1) extrapolates shear-wave velocities to 30 m assuming that the lowermost velocity of the model extends to 30 m. This method will generally result in a lower value of $\overline{V}_S$ (30) and thereby yield a more conservative estimate of ground motion, which generally increases as $\overline{V}_S$ (30) decreases. Another method (method 2) uses the correlation between $\overline{V}_S$ (30) and the time-averaged velocity $\overline{V}_S$ (d) to a depth d to extrapolate shear-wave velocities [Boore, 2004]. In Appendix D, table D.1 lists the calculated value of $\overline{V}_S$ (30) using the two above methods as well as the corresponding NEHRP site class for all K-NET stations on Hokkaido. Unfortunately, site conditions for KiK-NET stations on Hokkaido are not available. KiK-NET stations on Hokkaido are assigned a NEHRP site class based on the nearest K-NET station (table D.2). Method 2 does a better job of classifying sites on average and is therefore used to classify KiK-NET and K-NET stations on Hokkaido [Boore, 2004]. Figures 5.2 and 5.3 present the NEHRP site classifications for KiK-NET and K-NET stations on Hokkaido, respectively.

Table 5.1 Definition of NEHRP site classes in terms of $\overline{V}_S$ (30), the average shear-wave velocity to 30 m.

Site class	Range of $\overline{V}_S$ (30), (m/s)	Description
A	$1500 < \overline{V}_S$ (30),	Hard Rock
B	$760 < \overline{V}_S$ (30), ≤ 1500	Rock
C	$360 < \overline{V}_S$ (30), ≤ 760	Soft Rock
D	$180 \leq \overline{V}_S$ (30), ≤ 360	Stiff Soil
E	$\overline{V}_S$ (30), <180	Soft Soil

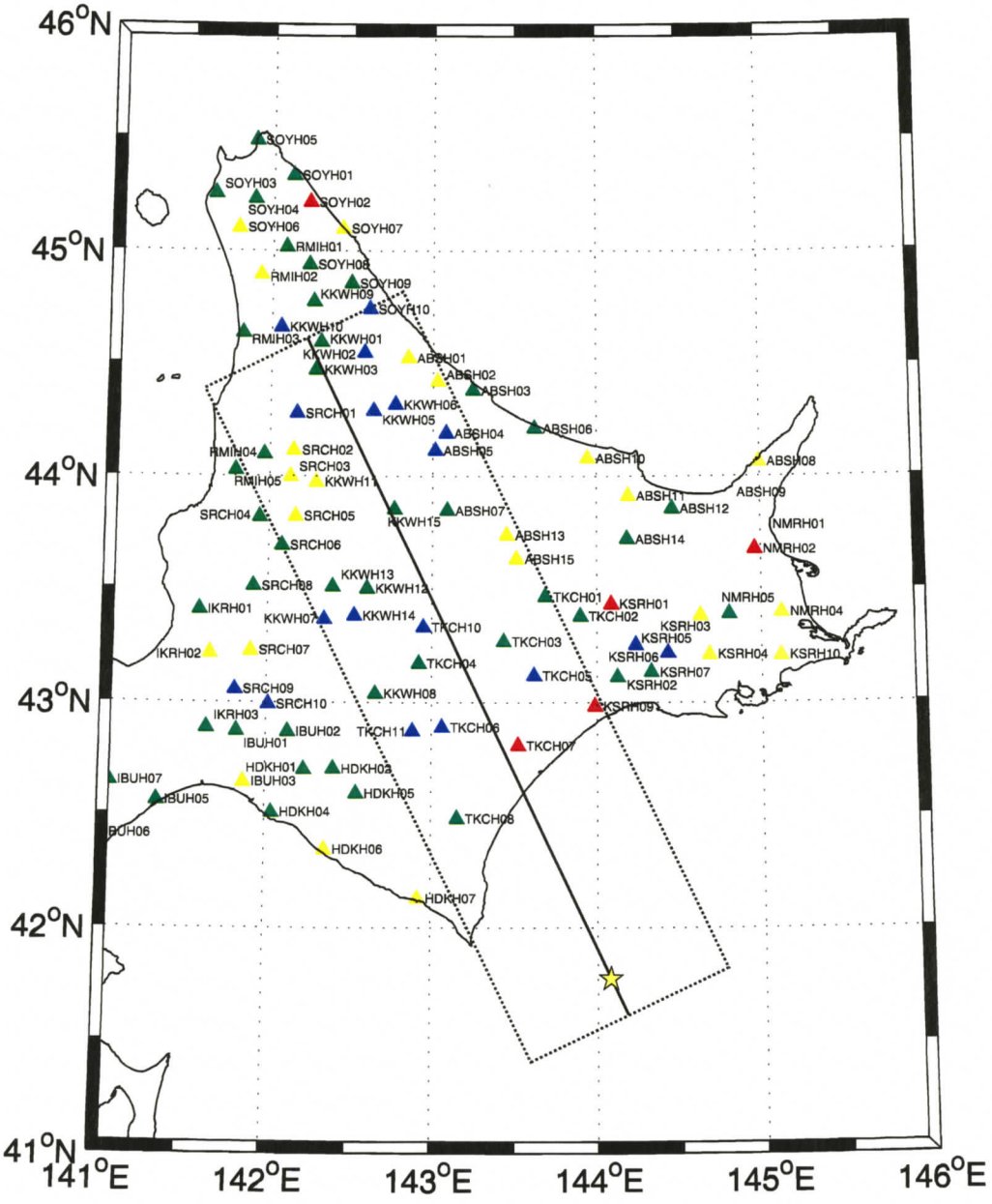

Figure 5.2 The KiK-NET (NEID) stations used in the present analysis. NEHRP Site class is indicated by color: NEHRP B (blue), NEHRP C (green), NEHRP D (yellow) and NEHRP E (red). Epicenter location (yellow star) of 2003 Tokachi-oki earthquake is indicated. Solid line defines profile associated with numerical simulations. Dashed box indicates stations used in model comparison.

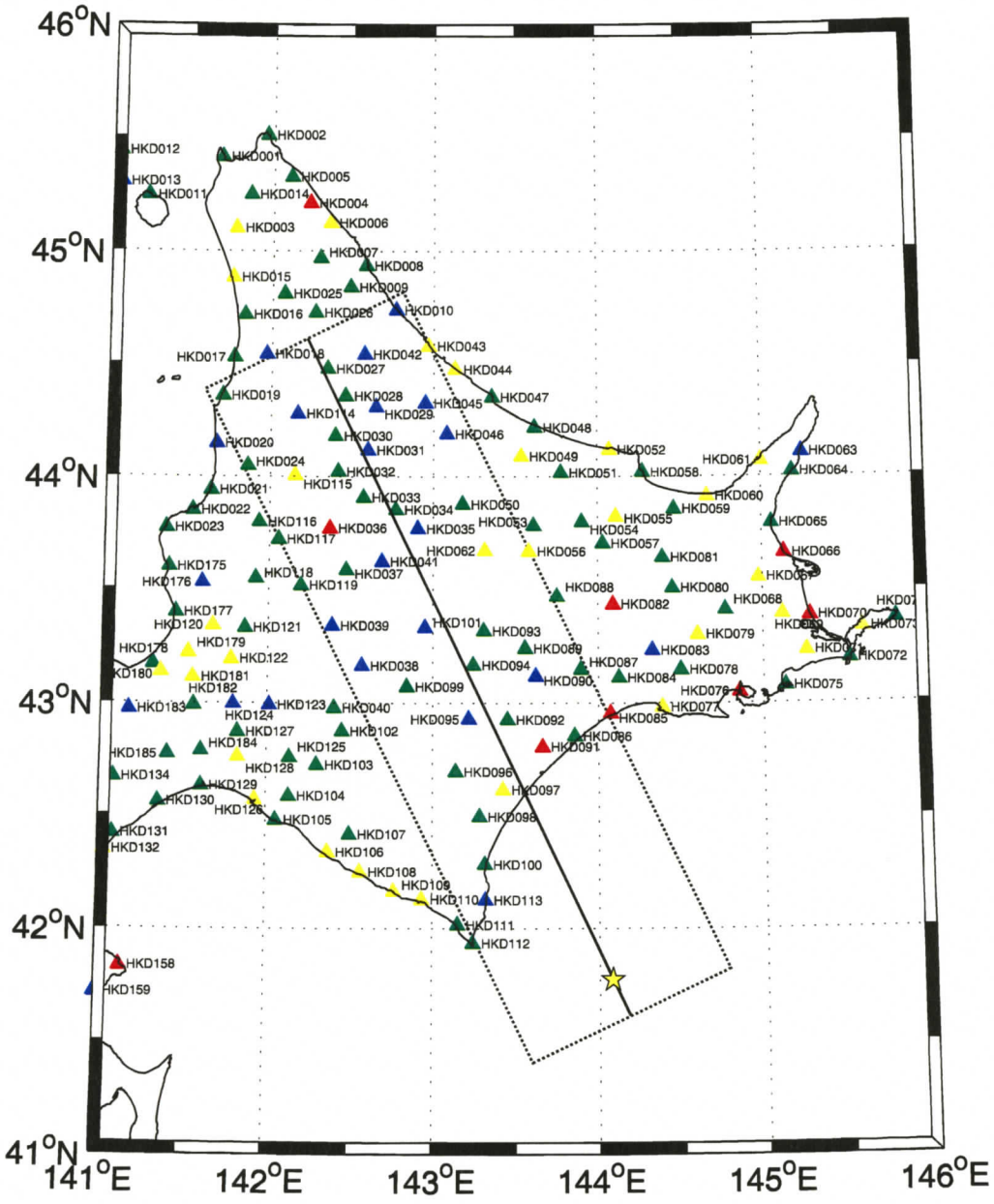

Figure 5.3 The K-NET (NEID) stations used in the present analysis. NEHRP Site class is indicated by color: NEHRP B (blue), NEHRP C (green), NEHRP D (yellow) and NEHRP E (red). Epicenter location (yellow star) of 2003 Tokachi-oki earthquake is indicated. Solid line defines profile associated with numerical simulations. Dashed box indicates stations used in model comparison.

Figure 5.4 displays a contour map of the PGA for the radial, transverse and vertical components derived from KiK-NET and K-NET stations on Hokkaido. PGA values were measured from the strong ground motion data [data source: www.k-net.bosai.go.jp/k-net/quake/index_en.html and www.kik.bosai.go.jp/kik/quake/index_en.html]. The data were band-passed between 0.01 Hz and 20 Hz, a frequency band that encompasses the frequencies observable in the data. PGA values on Hokkaido vary by a factor of approximately 7 as compared to PGA values in the epicentral range 50 – 70 km. The distribution of PGA extends with a northeastern strike orientation. Values increase from the southern coastal stations to the eastern coastal stations. The distribution of PGA values in the radial and transverse components exhibit the same characteristics. The maximum PGA values on the radial, transverse and vertical components form a distinctive band parallel to the coast at epicentral distances 100 – 160 km, beyond which values decrease gradually. The maximum PGA values within this band occur within the Tokachi sedimentary basin. However, the basin geometry alone cannot adequately explain the PGA pattern. Examining PGA values for all KiK-NET and K-NET stations on Hokkaido as a function of epicentral distance further clarifies the epicentral range of maximum PGA values, with the exception of few outlying PGA values (figure 5.5). Although varying site conditions cause local variations in PGA and frequency content, it is not apparent that they can explain the increase in PGA at epicentral distances 100 – 160 km.

5.3 Numerical Simulation

In order to determine the phase type responsible for the generation of the maximum PGA, numerical simulations are conducted for a transect perpendicular to the strike of the subducting oceanic crust in the vicinity of the 2003 Tokachi-oki epicenter (figure 5.2 & 5.3). The simulations are applied to a 275 km by 60 km model space discretized by a uniform grid spacing of 500 m. An efficient 2-D pseudo-spectral method [Kosloff & Baysal, 1982] is employed, which is capable of accurately resolving frequencies less than 2.5 Hz.

5.4 Velocity model

The velocity model for the applicable transect is derived from a 3-D velocity model of crust and upper mantle structure developed for the Hokkaido region (figure 5.6). The crustal velocity model is based upon recent reflection and refraction profiles in the complex Hidaka collision zone [Iwasaki et al., 2002; 1998, Arita et al., 1998]. The uppermost mantle in this region is characterized by low Pn velocities of 7.4 – 7.9 km/s [Iwasaki et al., 2002]. Observation of weak PmP phase indicates that the Moho is not a sharp boundary, but forms a transition zone from the upper mantle to the lower crust. Furthermore, tomographic studies indicate upper mantle P-wave velocities of ~7.7 km at 60 km depth [Miyamchi et al., 1994]. Due to

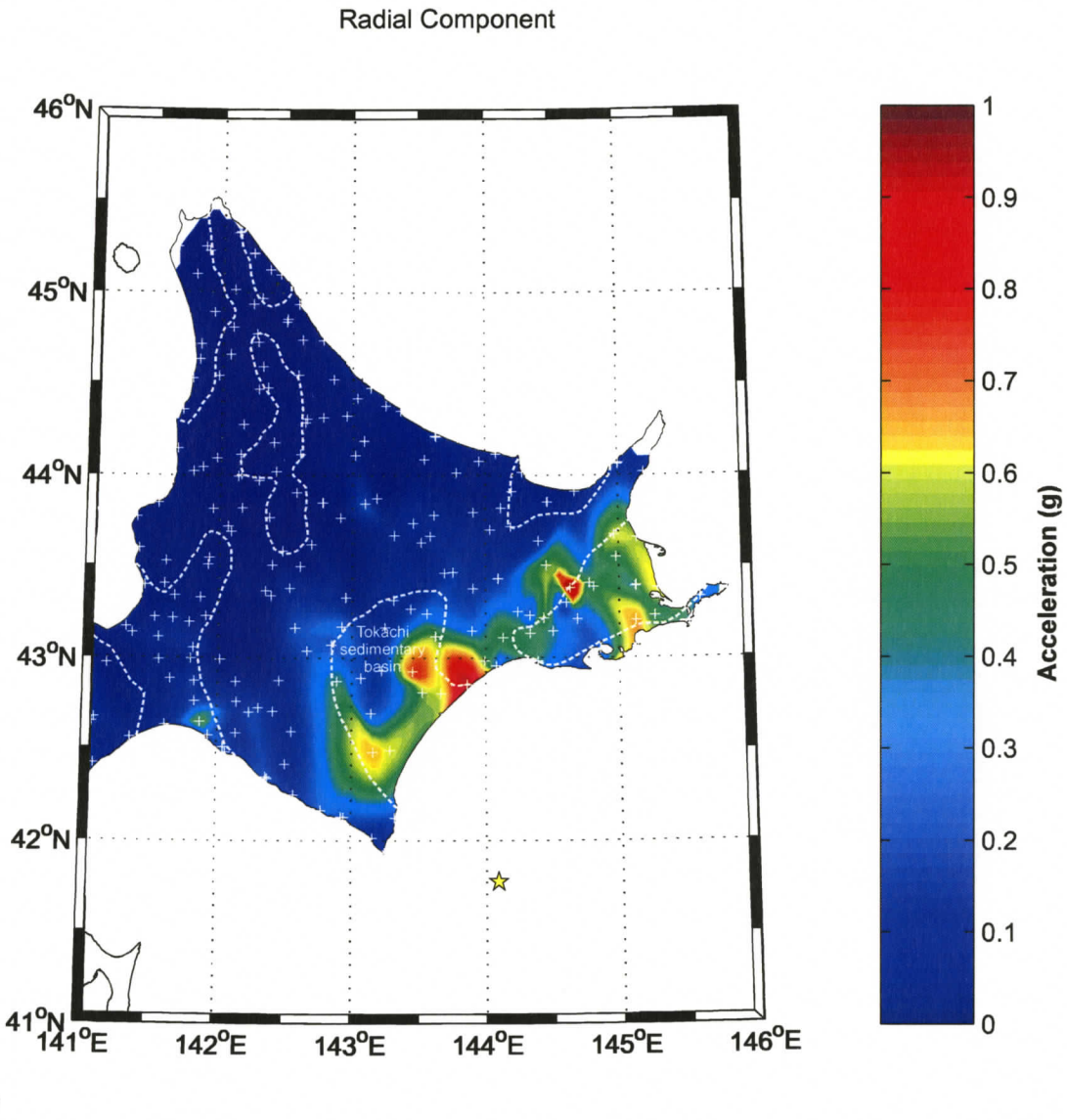

Figure 5.4 The PGA contour map of the (a) radial, (b) transverse and (c) vertical components on Hokkaido for the 2003 Tokachi-oki earthquake. Dashed lines indicate the location of sedimentary basins in the region. The epicenter is represented by a star. Station locations indicated by (+).

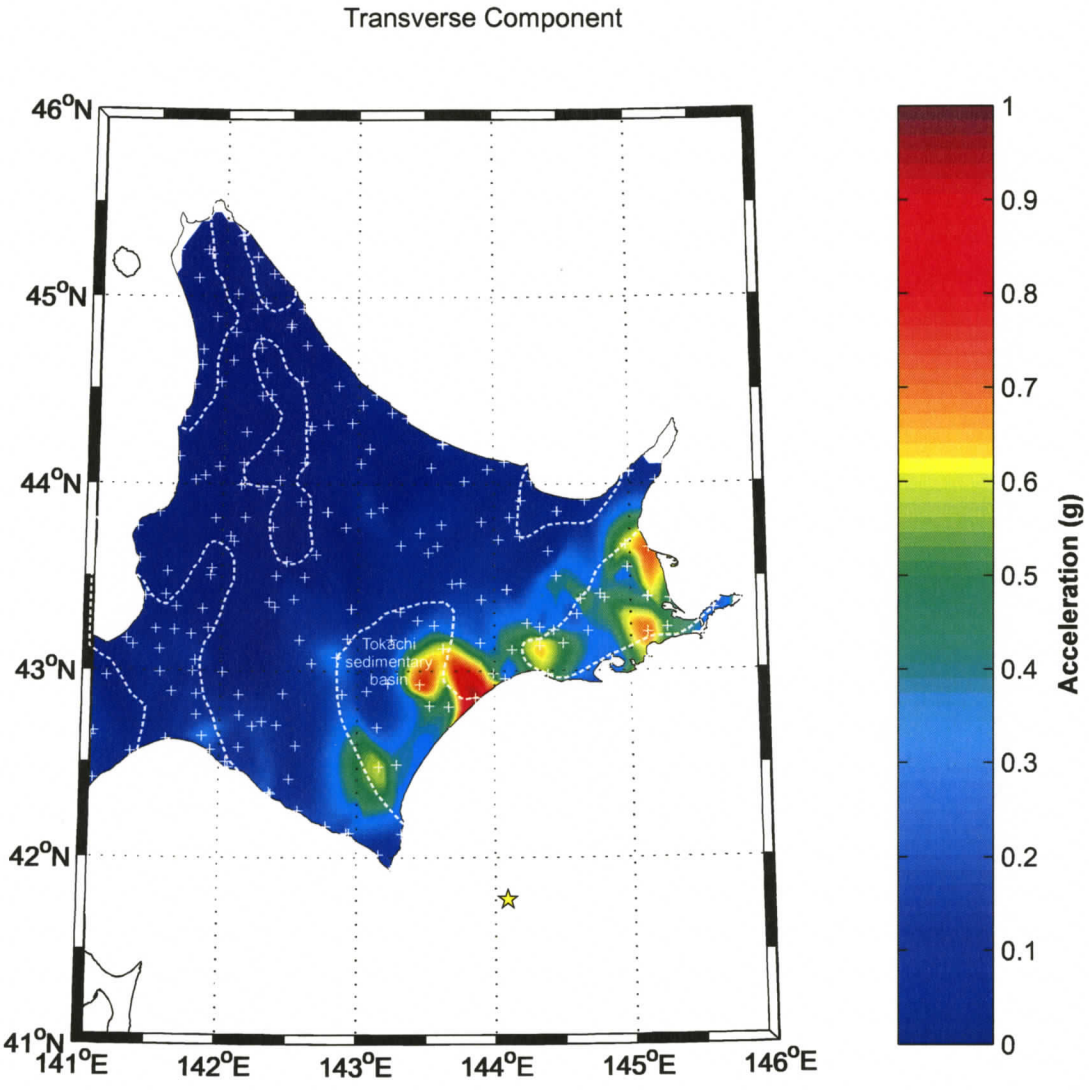

(b)

Figure 5.4 continued...

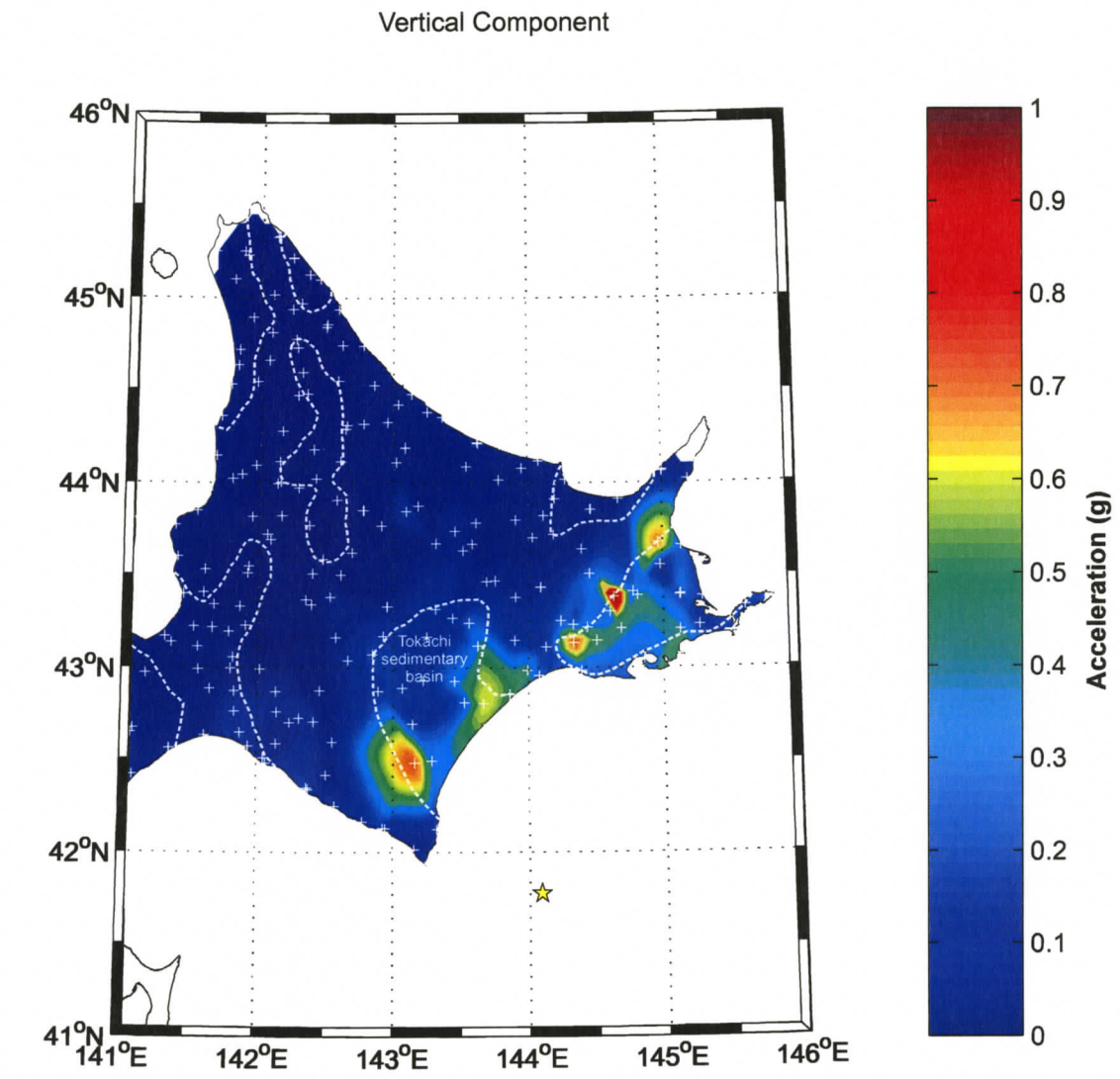

(c)

Figure 5.4 continued...

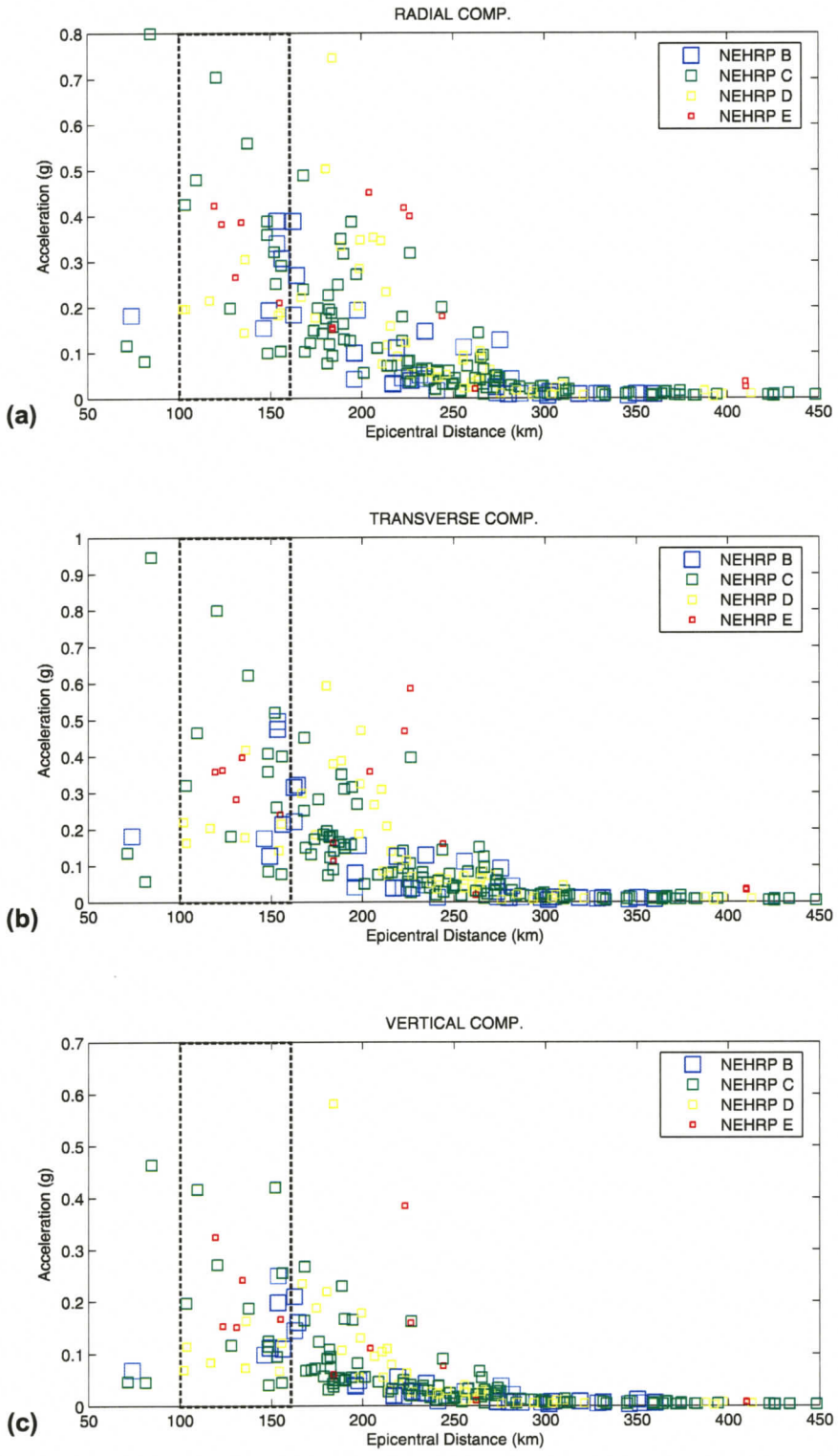

Figure 5.5 PGA versus epicentral distance for all Hokkaido stations. (a) Radial component, (b) transverse component and (c) vertical component. Symbols denote NEHRP site class. A increase in PGA as a function of distance is visible between 100 - 160 km.

the greater age for the oceanic crust (~129 Ma) and consequently the cooler temperatures, smaller volumes of aqueous fluids are released into the forearc mantle wedge relative to a warm subduction zone such as Cascadia. The mantle wedge is likely weakly serpentinized compared to a warm continental subduction zone explaining why its P-wave velocity is only slightly reduced compared to a normal mantle velocity of 8 km/s. The depth distribution of the continental Moho discontinuity under eastern Hokkaido is constrained by an arrival time study of Miyamachi et al. [1994], which is more reliable than previous studies [Zhao et al. 1992a; 1992b]. The depth contour of the upper boundary of the Pacific Plate compiled from Nakanishi et al. [2001], Hasegawa et al. [1994] and Katsumata [2003] by Earthquake Research Committee [2003] is applied. An oceanic crustal thickness of ~6 –7 km as derived by Nakanishi et al. [2004] offshore northeastern Hokkaido is accepted. Depth-dependent oceanic crustal velocities from Furumura & Furumura [2001], consistent with velocities derived from wide-angle refraction studies offshore Hokkaido, are adopted. Furthermore, the model optionally includes the sedimentary-basin structure of Furumura & Furumura [2001], derived from a number of refraction experiments and micro tremor surveys, supplemented with surface geology and gravity anomaly data. The topography and water layer are excluded from the velocity model, but this does not significantly influence the propagation of seismic waves in the structure beneath Hokkaido. In particular, two distinct models are applied: (1) a base model neglecting sedimentary basin structure, but incorporating a 1 km thick low velocity surface layer with sedimentary basin velocities, and (2) a complete model composed of all the above structures.

5.5 Source model

The focal mechanism of the 2003 Tokachi-oki earthquake resembles a thrust-type event on the upper Pacific Plate boundary with strike, dip and rake of: 250^0, 20^0, 130^0, respectively [Yagi, 2004; Ito et al., 2004; Miyazaki et al., 2004]. The mechanism of the main shock is represented as a double couple source oriented to represent displacement on the subduction thrust fault. A hypocenter depth of ~23.5 km is adopted to match the iso-depth contours of the Kuril Trench. This depth is significantly less than the hypocenter depth of 42 km determined by the JMA, but it is comparable to the proposed U.S. Geological Survey (USGS) hypocenter depth of 27 km. The source is initiated by a Ricker time function with a dominant frequency of 1 Hz. The frequency of the source is comparable to the dominant frequency of 1 Hz observed in the data. The simulation results demonstrate the influence of crustal and upper mantle heterogeneity on seismic wave propagation while excluding the influence of complex source characteristics

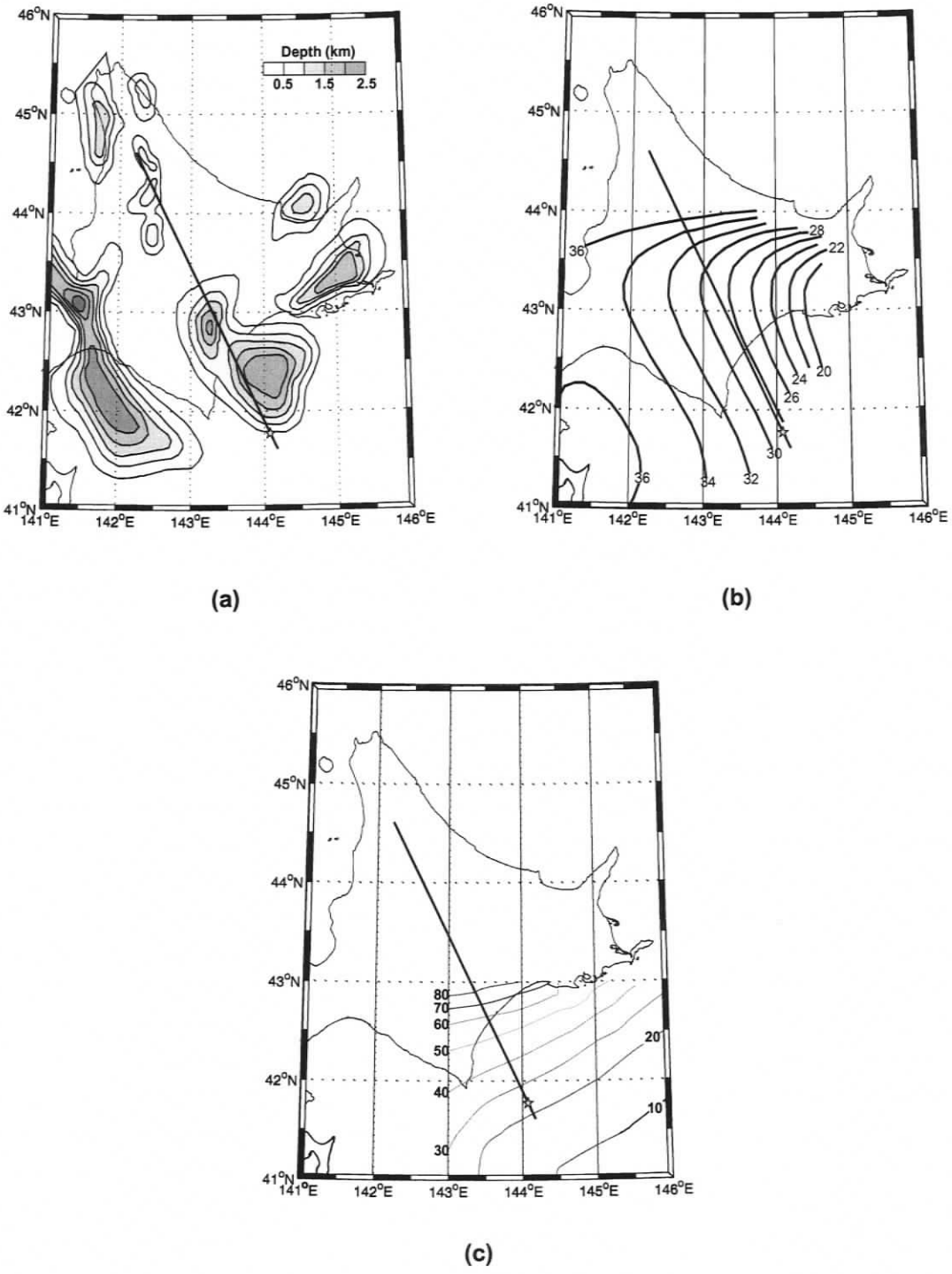

Figure 5.6 (a) Depth distribution of basement of basin (km) [adapted from Furumura & Furumura, 2001]. (b) Depth distribution of the continental Moho (km) [adapted from Miyamachi et al., 1994]. The standard error in depth for the Moho is $\pm$ 3 km. (c) Depth distribution of the upper boundary of the Pacific Plate (km) [adapted from Earthquake Research Committee, 2003]. (d) Velocity model along profile for numerical simulations.

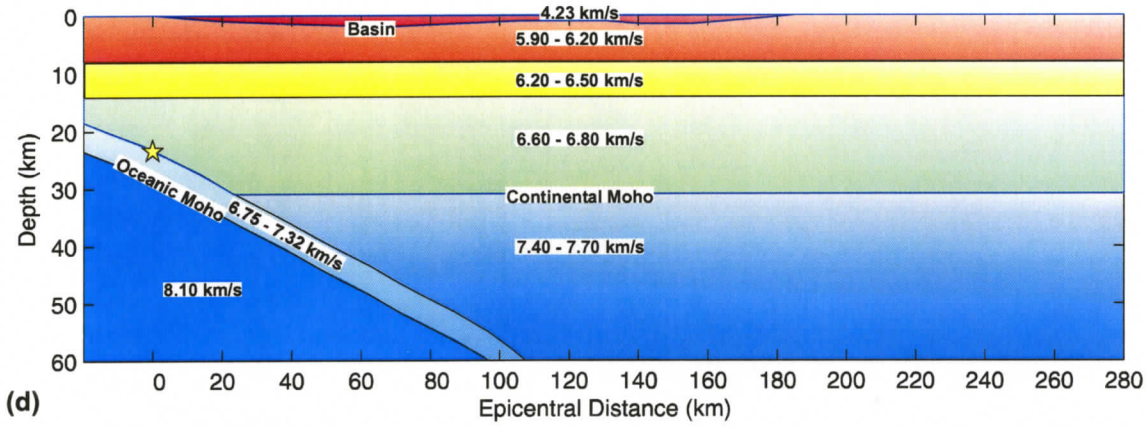

Figure 5.6 continued...

5.6 Data Analysis and Results

In order to examine the distance-dependence of the PGA across the network, PGA values are compared to the numerical modeling results for a profile across central Hokkaido (figure 5.7 & 5.8). PGA values were measured from a subset of the strong ground motion data, KiK-NET and K-NET stations within 25 km of the profile line (figure 5.2). Numerically simulated PGA values are scaled by a multiplier, which is defined by minimizing the least squares fit to the data in the epicentral range 140 – 270 km, in order to match relative amplitudes (figures 5.7 & 5.8). The horizontal component of the modeling results is compared to both the radial and transverse components of the data.

For each component, the measured PGA values consistently increase in the epicentral distance range 70 – 140 km beyond which values decay as a function of distance (figures 5.7 & 5.8). However, this relation is less distinct in the vertical component. In the radial and transverse components, maximum measured PGA values at 140 km are approximately 3 – 4 times larger than average PGA values in the epicentral range 50 – 70 km. For the vertical component, the maximum measured PGA value at 80 km is approximately 9 times larger than the average PGA values in the epicentral range 50 – 70 km. At 140 km, the measured PGA value is approximately 5 times greater. This is consistent with the radial and transverse components.

The base model results display the same character of the data for each component (figure 5.7). Relatively constant PGA values are evident in the 50 – 100 km range. In the 110 – 140 km range, a marked increase in PGA values is apparent. Beyond 140 km PGA values decay as a function of epicentral distance. The complete model displays a similar trend (figure 5.8). However, the increase and decrease in PGA values are more pronounced. In the 50 – 100 km range, PGA values decrease gradually. This is followed by a rapid decrease in PGA values in the 100 – 110 km range. In the 110 – 140 km range, an increase in PGA values is evident. Beyond 140 km PGA values decay.

To investigate the phases responsible for PGA values, the radial-component velocity waveforms for a profile across central Hokkaido are compared to simulation results based on travel times from ray tracing through the velocity model (figure 5.9 & 5.10). The velocity traces are obtained by numerical integration of the acceleration records. Each seismogram is normalized to a global scale factor and plotted as a function of epicentral distance. P-wave arrivals are not observed in the data due to the threshold criterion on the recording system. Therefore, a small time correction is applied to all traces such that the observed P-wave and S-wave arrivals measured from HI-NET stations on Hokkaido coincide with the theoretical arrival times. In figures 5.9 & 5.10, the seismograms are overlaid on the pseudo-spectral results. The scatter of measure P-wave arrival times about the numerical results is because the true velocity model and

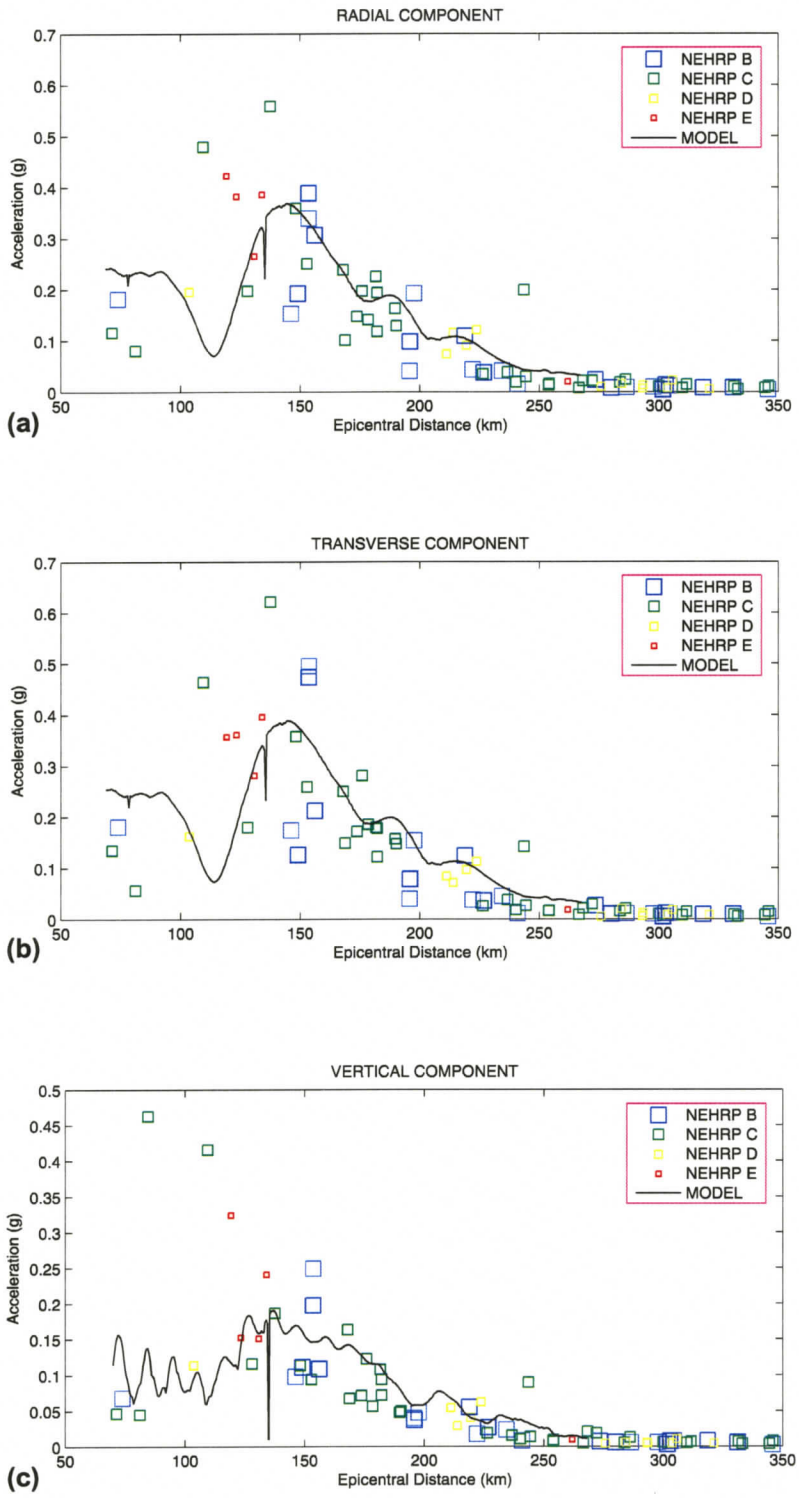

Figure 5.7 Comparison of base model (line) results to observed PGA, only data values from along the profile indicated in figure 5.2. Symbols denote NEHRP site class. (a) Radial component, (b) Transverse component, (c) Vertical component.

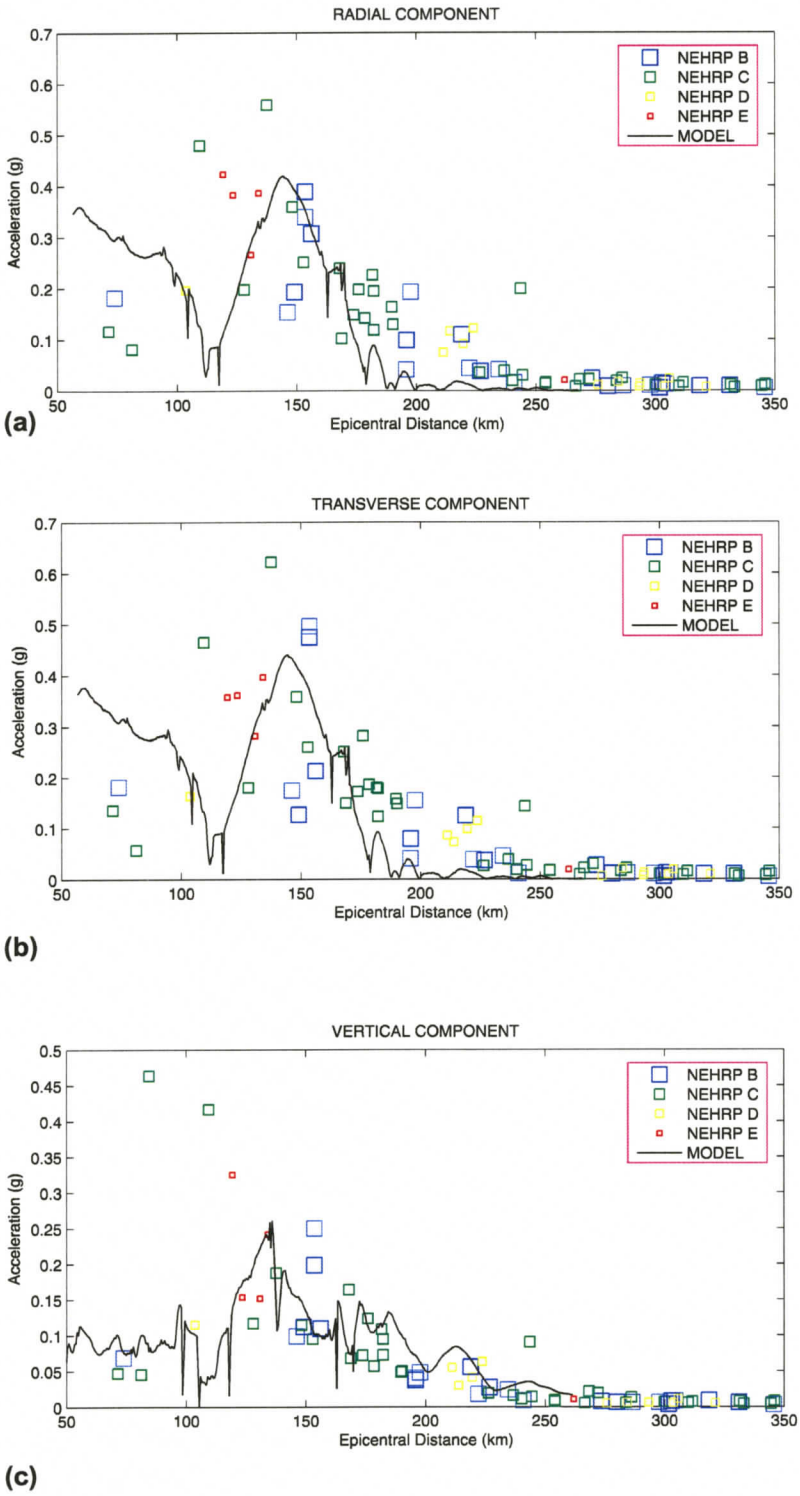

Figure 5.8. Comparison of complete model (line) results to observed PGA values, only data values from along the profile indicated in figure 5.2. Symbols denote NEHRP site class. (a) Radial component, (b) Transverse component, (c) Vertical component.

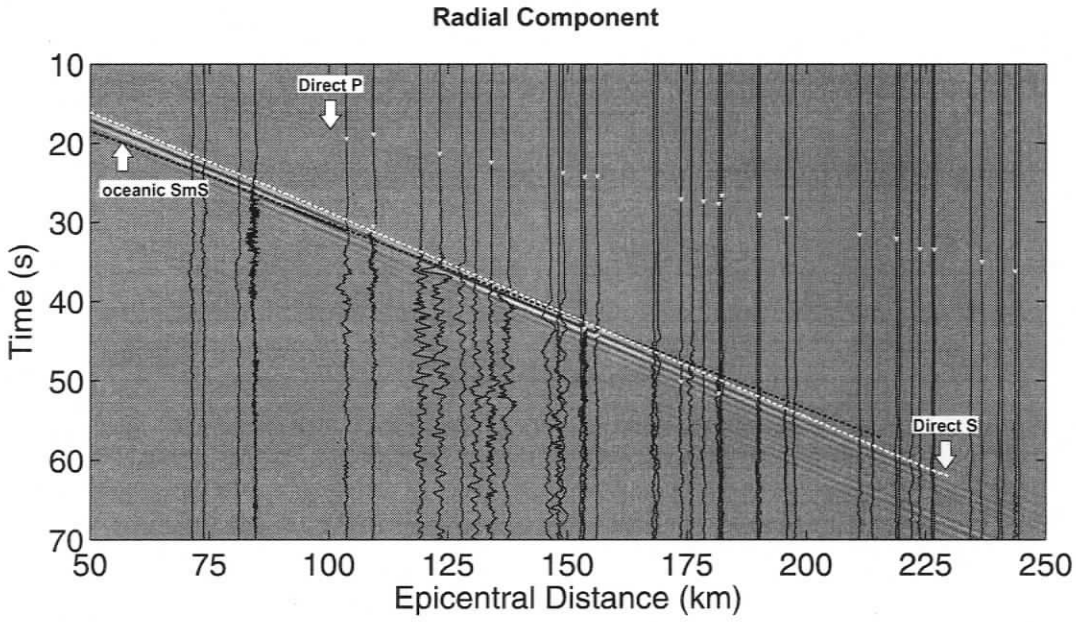

Figure 5.9 Radial-component velocity waveforms for a profile across central Hokkaido are compared to base model results. HI-NET P- and S-wave arrival time picks are represented as triangles. Theoretical travel times for the direct S-wave and the oceanic SmS wave are indicated.

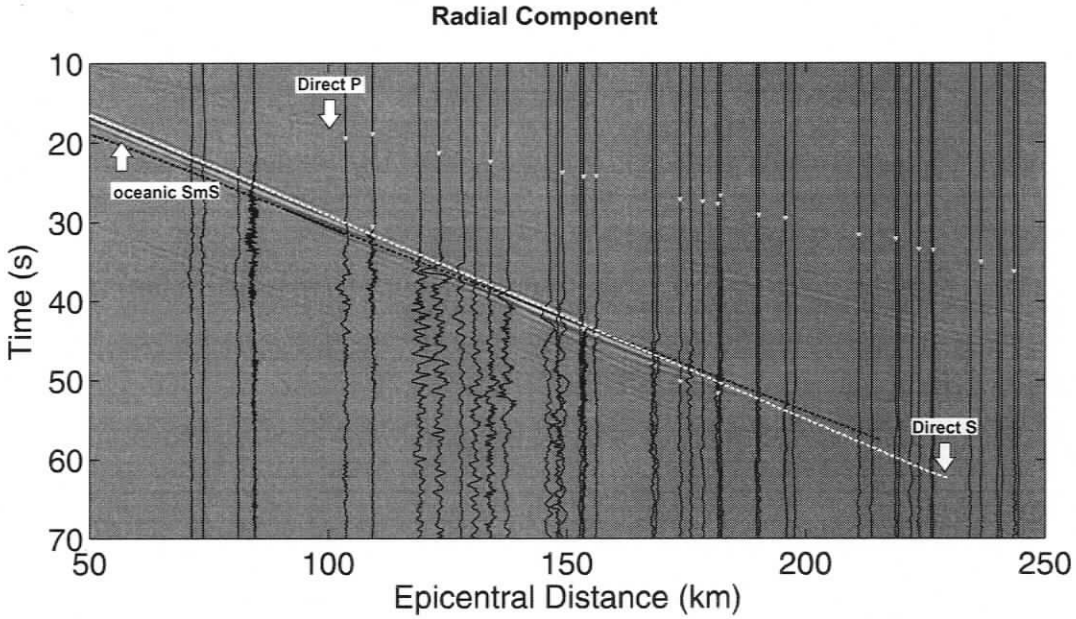

Figure 5.10 Radial-component velocity waveforms for a profile across central Hokkaido are compared to complete model results. HI-NET P- and S-wave arrival time picks are represented as triangles. Theoretical travel times for the direct S-wave and the oceanic SmS wave are indicated.

earthquake source are much more complex than the models assumed.

The velocity traces indicate the existence of large-amplitude phases specifically in the epicentral range of 120 – 160 km (figure 5.9 & 5.10). However, these phases are not apparent for stations with closer epicentral distances. Beyond the 150 km range, the amplitude of the velocity traces is smaller. In the 120 – 160 km epicentral range, simulation results display a region of enhanced amplitudes, which correlate with the large amplitudes on the velocity traces. In this enhanced region, theoretical arrival times indicate that the direct S-wave arrival is joined by the oceanic SmS-wave arrival, which is the S-wave critically-reflected off the oceanic Moho. Comparison between the observed and calculated arrival times suggest that the large amplitudes on the velocity traces in the range 120 – 160 km can be interpreted as the oceanic SmS phase.

5.7 Discussion

PGA values are influenced by a variety of effects, several of which may contribute together. Site conditions are known to effect PGA values. Furthermore, previous studies have indicated that the influence of structure can significantly impact the focusing and defocusing of seismic energy from an earthquake, with consequent enhanced PGA at the surface [Kennett & Furumura, 2002]. It is important to establish which of these different effects is the predominant cause of the widespread peak in recorded PGA amplitudes.

Post-critical reflections are expected to increase the PGA at all sites in the epicentral range 120 – 160 km regardless of site conditions, since they control the amplitude of motions arriving beneath the site. This is evident in figure 5.5 in which PGA values are elevated over a specific epicentral range independent of site conditions. The effect of site conditions is to locally amplify these critical reflections in a frequency dependent manner [Somerville & Yoshimura, 1990].

An effect that could potentially explain the distribution of PGA values is the trapping of seismic waves entering a sedimentary basin. Examining the simulation results from the base and complete models can assess the effect of the sedimentary basin structure. The largest amplitude phases of the base and complete model results coincide (figure 5.9 & 5.10). However, the complete model results are slightly more complicated in this region. PGA values along the profile exhibit similar characteristics for each model. However, the complete model displays a more prominent increase and decrease in PGA values. It is evident that the influence of the basin structure combines with the post-critical reflections. The underlying influence is the arrival of post-critical reflections from the oceanic Moho

5.8 Conclusions

Strong ground motion recordings from the September 25, 2003 Tokachi-oki earthquake show large amplitudes in the epicentral distance range of 110 – 160 km. In this range, the simulated maximum PGA values are due to the arrival of strong post-critical oceanic Moho reflections. It is inferred that this is also true of the recorded PGA based on a similarity in arrival times, phase velocity and amplitude. This study shows that the large-amplitude phases (oceanic SmS), site amplification effect and basin structure are responsible for the distribution of peak ground acceleration.

CHAPTER 6
CONCLUSIONS

In this thesis, the influence of post-critical reflections at the oceanic Moho on the pattern of peak ground motions from mega-thrust earthquakes in the Cascadia subduction zone was investigated. This was accomplished through the examination of synthetic seismograms for several source locations and source frequencies. The main conclusions of this thesis are below.

Synthetic seismograms indicate that the direct S-wave and reflections at the oceanic Moho are primarily responsible for the pattern of peak ground motions from a mega-thrust event. At close distances, peak ground motions are controlled by direct up-going S-waves. At greater distances the S-wave reflection off the oceanic Moho turns post-critical producing an arrival that is comparatively larger than the direct S-wave arrival and increasing peak ground motions. These reflections follow a path from the oceanic crust directly into the overlying continental crust. The behavior of peak ground motions becomes more complex with the interaction of multiple propagation paths, including propagation through the forearc mantle wedge.

The influence of post-critical reflections at the oceanic Moho may locally increase peak ground motions in the vicinity of populated areas in the Pacific Northwest. For rupture at the down-dip limit of the locked zone, the post-critically enhanced region is located on the coast (figure 4.5). Consequently, peak ground motions from source frequencies between 1 Hz and 3 Hz are a factor of up to 1.5 greater than amplitudes calculated for a model without oceanic Moho reflections. For rupture at the 15 km depth contour of the subducting oceanic crust, the post-critically enhanced region maps within the Pacific Northwest urban corridor locally increasing peak ground motions by a factor up to 1.5 (figure 4.6).

The low-velocity serpentinized forearc mantle wedge produces a second amplitude maximum by focusing post-critical reflections at the oceanic Moho into a narrow region just landward of the major population centers (centered at longitude $122^{0}30$'W). For rupture extending down-dip of the 15 km depth contour of the oceanic slab, the geographic location of this region does not change (figures 4.7 – 4.9). The primary control on the location of this region is the velocity structure of the forearc mantle wedge. These results indicate the importance of an accurate structural model for the forearc mantle wedge to predict ground motions from a mega-thrust event.

In the analysis of ground motions from mega-thrust events, dominant source frequencies of 1 Hz, 2 Hz and 3 Hz were tested to examine the effect of source frequency on the contribution of post-critical reflections to peak ground motions. The geographical region in which post-critical reflections at the oceanic Moho influence peak ground motions is similar for different source frequencies. However, for rupture extending

down-dip of the locked zone, higher source frequencies exhibited PGM amplitudes that decayed less rapidly than expected for two-dimensional geometric spreading. This observation combined with the effect of attenuation on the results indicates that the influence of post-critical reflections to peak ground motions is progressively less significant at higher source frequencies.

In conclusion, the influence of post-critical reflections at the oceanic Moho to peak ground motions from a mega-thrust event in the Cascadia subduction zone is significant. Two key factors define the geographical location of the post-critically enhanced region: the landward extent of coseismic rupture and the geometry of the subducting oceanic crust. For rupture extending into the transition zone, the post-critically enhanced region maps within the Pacific Northwest urban corridor. This result points to the importance of accurately estimating the landward extent of rupture. The influence of post-critical reflections may increase seismic hazard within the Pacific Northwest urban corridor.

REFERENCES

Adams, J., 1990, Cascadia subduction zone: evidence from turbidites off the Oregon-Washington margin, Tectonics, 9, 569-583.

Alford, R.M., Kelly, K.R., and Boore, D.M., 1974, Accuracy of finite difference modeling of acoustic wave equations, Geophysics, 39, 834-841.

Arita, K., Ikawa, T., Ito, T., Yamamoto, A., Saito, M., Nishida, Y., Satoh, H., Kimura, G., Watanabe, T., and Kuroda, T., 1998, Crustal structure and tectonics of the Hidaka Collision Zone, Hokkaido (Japan), revealed by vibroseis reflection and gravity surveys, Tectonophysics, 290, 197-210.

Atwater, T., 1970, Implications of plate tectonics for the Cenozoic tectonic evolution of western North America, Geological Society of America Bulletin, 81, 3513-3536.

Atwater, T., 1989, Plate tectonic history of the northeast Pacific and western North America, in The Geology of North America, vol. N, The Eastern Pacific Ocean and Hawaii, edited by E.L. Winterer, D.M. Hussong, and R.E. Decker, 21-71, Geological Society of America, Boulder, Colorado.

Atwater et al., 1995, Summary of coastal geological evidence for past great earthquakes on the Cascadia subduction zone, Earthquake Spectra, 11, 1-18.

Bakun, W.H., Haugerud, R.A., Hopper, M.G., and Ludwin, R.S., 2002, The December 1872 Washington State earthquake, Bulletin of the Seismological Society of America, 92(8), 3239-3258.

Bilek, S.L., Lay, T., and Ruff, L.J., 2004, Radiated seismic energy and earthquake source duration variations from teleseismic source time functions for shallow subduction zone thrust earthquakes, Journal of Geophysical Research, 109, B09308, doi:10.1029/2004JB003039.

Boore D., 2004, Estimating $\overline{V_S}$ (30) (or NEHRP site classes) from shallow velocity models (depth < 30 m), Bulletin of the Seismological Society of America, 94(2), 591-597.

Botros, M., and Johnson, H.P., 1988. Tectonic evolution of the Explorer – northern Juan de Fuca region from 8 Ma to the present. Journal of Geophysical Research, 93, 10421-10437.

Bostock, M.G., Hyndman, R.D., Rondenay, S., and Peacock, S.M., 2002, An inverted continental Moho and serpentinization of the forearc mantle, Nature, 417, 536-538.

Braunmiller, J., and Nabelek J., 2002, Seismotectonics of the Explorer Region, Journal of Geophysical Research, 107, B10, 2208, doi:10.1029/2001JB000220.

Brocher, T.M., Parson, T., Blakely, R.J., Christensen, N.I., Fisher, M.A., Wells, R.E., and the SHIPS Working Group, 2001, Upper crustal structure in Puget Lowland, Washington: Results from the 1998 Seismic Hazards Investigation in Puget Sound, Journal of Geophysical Research, 106, 13541-13564.

Brocher, T.M., Parsons, T., Trehu, A.M., Snelson, C.M., and Fisher, M.A., 2003, Geology, 31(3), 267-270.

Burger, R.W., Somerville, P.G., Barker, J.S., Herrmann, R.B., and Helmberger, D.V., 1987, The effect of crustal structure on strong ground motion attenuation relations in eastern North America, Bulletin of the Seismological Society of America, 77, 420-439.

Calvert, A.J., 1996, Seismic reflection constraints on imbrication and underplating of the northern Cascadia convergent margin, Canadian Journal of Earth Science., 33, 1295-1307.

Calvert, A., 2004, Seismic reflection imaging of two megathrust shear zones in the northern Cascadia subduction zone, Nature, 428, 163-167.

Cassidy, J.F., and Ellis, R.M., 1991, Shear wave constraints on a deep crustal reflective zone beneath Vancouver Island, Journal of Geophysical Research, 96, 19843-19851.

Cassidy, J.F., and Ellis, R.M., 1993, S-wave velocity structure of the Northern Cascadia subduction zone, Journal of Geophysical Research, 98, 4407-4421.

Cassidy, J.F., Ellis, R.M., Karavas, C., and Rogers, G.C., 1998, The northern limit of the subducted Juan de Fuca plate system, Journal of Geophysical Research, 103, 26949-26961.

Cerveny, V., Molotkov, I., and Psencik, I., 1997, Ray method in seismology, Charles University Press.

Clowes, R.M., Brandon, M.T., Green, A.G., Yorath, C.J., Sutherland Brown, A., Kanesewich, E.R., and Spencer, C., 1987, LITHOPROBE – southern Vancouver Island: Cenozoic subduction complex imaged by deep seismic reflections, Canadian Journal of Earth Sciences, 24, 31-51.

Cohee, B.P., Somerville, P.G., and Abrahamson, N.A., 1991, Simulated ground motions for hypothesized M_w 8 subduction earthquakes in Washington and Oregon, Bulletin of the Seismological Society of America, 81, 28-56.

Conder, J.A., 2005, A case for hot slab surface temperatures in numerical viscous flow models of subduction zones with an improved fault zone parameterization, Physics of the Earth and Planetary Interiors, 149 (1-2): 155-164

Crosson, R.S., and Owens, T.J., 1987, Slab geometry of the Cascadia subduction zone beneath Washington from earthquake hypocenters and teleseismic converted waves, Geophysical Research Letter, 14, 824-827.

Davis, E.E., and Riddihough R.P., 1982, The Winona Basin: structure and tectonis. Canadian Journal of Earth Sciences, 19, 767-788.

DeMets, C., Gordan, R.G., Argus, D.F., and Stein, S., 1990, Current plate tectonics, Geophysical Journal International, 101, 425-478.

Detrick, R., Collins, J., Stephen, R., and Swift, S., 1994, In situ evidence for the nature of the seismic layer 2/3 boundary in the oceanic crust, Nature, 370, 288-290.

Dragert, H., Hyndman, R.D., Rogers, G.C., and Wang, K., 1994, Current deformation and the width of the seismogenic zone of the northern Cascadia subduction thrust, Journal of Geophysical Research, 99, 653-668.

Dragert, H., and Hyndman, R.D., 1995, Continuous GPS monitoring of elastic strain in the northern Cascadia subduction zone, Geophysical Research Letter, 22, 755-758.

Drew, J.J. and Clowes, R.M., 1990, A re-interpretation of the seismic structure across the active subduction zone of western Canada; in Studies of Laterally Heterogeneous Structures Using Seismic Refraction and Reflection Data, ed. A.G. Green; Geological Survey of Canada, Paper 89-13, 115-132.

Engebretson, D.C., Gordon, R.G., and Cox, A., 1985, Relative motions between oceanic and continental plates in the Pacific basin, Geological Society of America, Special Paper 206.

Flueh, E.R., Fisher, M.A., Bialas, J., Childs, J.R., Klaeschen, D., Kukowski, N., Parson, T., Scholl, D.W., Brink, U, Trehu, A.M., and Vidal, N., 1998, New seismic images of the Cascadia subduction zone from cruise SO108 – Orwell, Tectonophysics, 293, 69-84.

Fluck, P., Hyndman, R.D., and Wang, K., 1997, Three-dimensional dislocation model for great earthquakes of the Cascadia subduction zone, Journal of Geophysical Research, 102, 20539-20550.

Furumura, M., and Furumura, T., 2001, Numerical simulations of strong ground motion during destructive earthquakes in Hokkaido, Japan, Journal of Computational Acoustics, 9(4), 1647-1657.

Gerdom, M., Trehu, A.M., Flueh, E.R., and Klaeschen, D., 2000, The continental margin off Oregon from seismic investigations, Tectonophysics, 329, 79-97.

Green, A.G., Clowes, R.M., Yorath, C.J., Spencer, C., Kanesewich, E.R., Brandon, M.T., and Sutherland Brown, A., 1986, Seismic reflection imaging of the subducting Juan de Fuca plate, Nature, 319, 210-213.

Hacker, B.R., Peacock, S.M., Abers, G.A., and Holloway, S.D., 2003, Subduction factory 2. Are intermediate depth earthquakes linked to metamorphic dehydration reactions? Journal of Geophysical Research, 108, doi: 10.1029/2001JB001129.

Hasegawa, A., Horiuchi, S., and Umino, N., 1994, Seismic structure of the northeastern Japan convergent margin: a synthesis, Journal of Geophysical Research, 99, 22295-22311.

Heaton, T.H., and Kanamori, H., 1984, Seismic potential associated with subduction in the northwestern United States, Bulletin of the Seismological Society of America, 74, 933-944.

Hudson, J.A., 1980, The excitation and propagation of elastic waves, Cambridge University Press, Great Britian.

Hyndman, R.D., Yorath, C.J., Clowes, R.M., and Davis E.E., 1990, The northern Cascadia subduction zone at Vancouver Island: seismic structure and tectonic history, Canadian Journal of Earth Science, 27, 313-329.

Hyndman, R.D., and Wang, K., 1993, Thermal constraints on the zone of major thrust earthquake failure: The Cascadia subduction zone, Journal of Geophysical Research, 98, 2039-2060.

Hyndman R.D., 1995, The lithoprobe corridor across the Vancouver Island continental margin: the structural and tectonic consequences of subduction, Canadian Journal of Earth Science, 32, 1777-1802.

Hyndman, R.D., and Wang, K., 1995, The rupture zone of Cascadia great earthquakes from current deformation, Journal of Geophysical Research, 100, 22133-22154.

Hyndman, R.D., and Peacock, S.M., 2003, Serpentization of the forearc mantle, Earth and Planetary Science Letters, 212, 417-432.

Ito, Y., Matsubayashi, H., Kimura, H., Matsumoto, T., Asano, Y., and Sekiguchi, S., 2004, Spatial distribution for moment tensor solution of the 2003 Tokach-oki earthquake and aftershocks, Earth Planets Space, 56, 301-306.

Iwasaki, T., Yoshii, T., Ito, T., Sato, S., and Hirata, N., 2002, Seismological features of island arc crust as inferred from recent seismic expeditions in Japan, Tectonophysics, 355, 53-66.

Iwasaki, T., Ozel, O., Moriya, T., Sakai, S., Suzuki, S., Aoki, G., Maeda, T., and Iidaka, T., 1998, Later structural variation across a collision zone in central Hokkaido, Japan, as revealed by wide-angle seismic experiments, Geophysical Journal International, 132, 435.

Johnston, S.T., and Acton, S., 2003, The Eocene of southern Vancouver Island orocline – a response to seamount accretion and the cause of fold-and-thrust belt and extensional basin formation, Tectonophysics, 365, 165-183.

Katsumata, K., Wada, N., and Kasahara, M., 2003, Newly imaged shape of the deep seismic zone within the subducting Pacific plate beneath the Hokkaido corner, Japan-Kurile arc-arc junction, Journal of Geophysical Research, 10.1029/2002JB002175.

Kennett, B., and Furumura, T., 2002, The influence of 3-D structure on the propagation of seismic waves away from earthquakes, Pure and Applied Geophysics, 159, 2113-2131.

Kern H., Liu, B., and Popp T., 1997, Relationship between anisotropy P and S wave velocities and anisotropy of attenuation in serpentinite and amphilbolite, Journal of Geophysical Research, 102, B2, 3051-3065.

Kosloff, D.D., and Baysal, E., 1982, Forward modeling by a Fourier method, Geophysics, 47(10), 1402-1412.

Kosloff, D.D., Reshef, M., and Loewenthal, D., 1994, Elastic wave calculations by the Fourier method, Bulletin of the Seismological Society of America, 74(3), 875-891.

Kosloff, D.D., and Baysal, E., 1982, Forward modeling by a Fourier method, Geophysics, 47(10), 1402-1412.

Malone, S.D, and Bor, S., 1979, Attenuation patterns in the Pacific Northwest based on intensity data and the location of the 1872 North Cascades earthquake, Bulletin of the Seismological Society of America, 679, 531-576.

McCrory, P.A., Blair, J.L., Oppenheimer, D.H., and Walter, S.R., 2004, Depth to the Juan de Fuca slab beneath the Cascadia subduction margin – A 3-D model for sorting earthquakes, U.S. Geological Survey Data Series 91.

McMechan, G.A., and Spence, G.D., 1983, P-wave velocity structure of the Earth's crust beneath Vancouver Island, Canadian Journal of Earth Science, 20, 742-752.

McNeill, A.F., Bostock, M.G., Rogers, G.C., and Shragge, J.C., 2004, The effect of forearc mantle serpentinization on ground motions from megathrust and intraslab events in the Cascadia subduction zone, Bulletin of the Seismological Society of America, 94(1), 147-154.

Miller, K.C., Keller, G.R., and Gridley, J.M., 1997, Crustal structure along the west flank of the Cascades, western Washington, Journal of Geophysical Research, 102, 17857-17873.

Miyamachi, H., Kasahara, M., Suzuki, S., Tanaka, K., and Hasegawa, A., 1994, Seismic velocity structure in the crust and upper mantle beneath northern Japan, Journal of the Physics of the Earth, 42, 269-301.

Miyazaki, S., Larson, K.M., Choi, K., Hikima, K., Koketsu, K., Bodin, P., Haase, J., Emore, G., and Yamagiwa, A., 2004, Modeling the rupture process of the 2003 September 25 Tokachi-oki (Hokkaido) earthquake using 1-Hz GPS data, Geophysical Research Letters, L21603, doi:10.1029/2004GL021457.

Nakanishi, A., Miura, S., Obana, K., Kodaira, S., Takahashi, N., Tsuru, T., Park, J., Kaneda, Y., Kurashimo, E., Hirata, N., and Iwasaki, T., 2001, Crustal structure across the coseismic rupture zone of the 1973 Nemuro-oki earthquake occurred in the Kuril trench, Abstracts for the Joint Meeting of Earth and Planetary Science, Sz-011.

Nakanishi, A., Smith, A.J., Miura, S., Tsuru, T., Kodaira, S., Obana, K., Takahashi, N., Cummins, P.R., and Kaneda, Y., 2004, Structural factors controlling the coseismic rupture zone of the 1973 Nemuro-Oki earthquake, the southern Kuril Trench seismogenic zone, Journal of Geophysical Research, 109 (B5): Art. No. B05305.

Nedimovic, M.R., Hyndman, R.D., Ramachandran, K., and Spence, G.D., 2003, Reflection signature of seismic and aseismic slip on the northern Cascadia subduction interface, Nature, 424, 416-420.

Nicholson, T., Bostock, M., and Cassidy, J.F., 2005, New constraints on subduction zone structure in northern Cascadia, Geophysical Journal International, 161, 849-859.

Oleskevich, D.A., Hyndman, R.D., and Wang, K., 1999, The updip and downdip limits of great subduction earthquakes: Thermal and structural models of Cascadia, south Alaska, SW Japan and Chile, Journal of Geophysical Research, 104, 14965-14991.

Parsons, T., Trehu, A.M., Luetgert, J.H., Miller, K., Killbride, F., Wells, R.E., Fisher, M.A., Flueh, E., ten Brink, U.S., and Christensen, N.I., 1998, A new view into the Cascadia subduction zone and volcanic arc: implications for earthquake hazards along the Washington margin, Geology, 26, 199-202.

Parsons, T., Wells, R.E., Fisher, A., Flueh, E., and ten Brink, U.S., 1999, Three-dimensional velocity structure of Siletzia and other accreted terranes in the Cascadia forearc of Washington, Journal of Geophysical Research, 104, 18015-18039.

Preston, L.A., Creager, K.C., Crosson, R.S., Brocher, T.M., and Trehu A.M., 2003, Intraslab earthquakes: Dehydration of the Cascadia slab, Science, 302, 1197-1200

Ramachandran, K., Dosso, S.E., Spence, G.D., Hyndman, R.D., and Brocher, T.M., 2005, Forearc structure beneath southwestern British Columbia: A three-dimensional tomographic velocity model, Journal of Geophysical Research, 110, B02303, doi:10.1029/2004JB003258.

Reshef, M., and Kosloff, D., 1985, Applications of elastic forward modeling to seismic interpretation, Geophysics, 50(8), 1266-1272.

Riddihough, R.P., 1982, One hundred million years of plate tectonics in western Canada, Geoscience Canada, volume 9, number 1, 28-34.

Riddihough, R.P., 1984. Recent movements of the Juan de Fuca plate system, Journal of Geophysical Research, 89, 6980-6994.

Ristau, J.P., 2004, Seismotectonics of western Canada from regional moment tensor analysis, Ph.D. Thesis, University of Victoria.

Rogers, G.C., and Hasegawa, H.S., 1978, A second look at the British Columbia earthquake of 23 June, 1946, Bulletin of the Seismological Society of America, 68, 653-676.

Rogers, G.C., 1988, An assessment of the megathrust earthquake potential of the Cascadia subduction zone, Canadian Journal of Earth Science, 25, 844-852.

Rogers, G.C., 1998, Earthquakes and earthquake hazard in the Vancouver area, In: Geology and Natural Hazards of the Fraser River Delta, British Columbia, Geological Survey of Canada, Bulletin, 525, 17-25.

Saffer, D.M. and Marone, C., 2003, Comparison of smectite- and illite-rich gouge frictional properties: application to the updip limit of the seismogenic zone along subduction megathrusts, Earth and Planetary Science Letters, 215 (1-2), 219-235.

Satake, K., Shimazaki, K., Tsuji, Y., and Ueda, K., 1996, Time and size of a giant earthquake in Cascadia inferred from Japanese tsunami records of January 1700, Nature, 246-249.

Savage, J.C., Lisowski, M., and Prescott, W.H., 1991, Strain accumulation in western Washington, Journal of Geophysical Research, 96, 14493-14507.

Scholtz, C.H., Mechanics of Earthquakes and Faulting, 439 pp., Cambridge Univ. Press, New York, 1990.

Simoes, M., Avouac, J.P., Cattin, R., and Henry, P., 2004, The Sumatra subduction zone: A case for a locked fault zone extending into the mantle, Journal of Geophysical Research, (B10), Art. N0. B10402.

Somerville, P., and Yoshimura, J., 1990, The influence of critical Moho reflections on strong ground motions recorder in San Francisco and Oakland during the 1989 Loma Preita earthquake, Geophys. Res. Letters, 17(8), 1203-1206.

Spence, G.D., Clowes, R.M., and Ellis, R.M., 1985, Seismic structure across the active subduction zone of western Canada, Journal of Geophysical Research, 90, 6754-6772.

Stachnik, J.C., and Abers, G.A., 2004, Seismic attenuation and mantle wedge temperatures in the Alaska subduction zone, Journal of Geophysical Research, 109, B10304, doi:10.1029/2004JB003018.

Spudich, P., and Orcutt, J., 1980, Peterology and porosity of an oceanic crustal site: results from wave form modeling of seismic refraction data, Journal of Geophysical Research, 85, B3, 1409-1433.

Takanami, T., Sacks, I.S., Hasegawa, A., 2000, Attenuation structure beneath the volcanic front in northwestern Japan from broad-band seismograms, Physics of Earth Planet International, 121, 339-357.

Trehu, A.M., Asudeh, I., Brocher, T.M., Luetgert, J.H., Mooney, W.D., Nabelek, J.L., and Nakamura, Y., 1994, Crustal architecture of the Cascadia forearc, Science, 266, 237-242.

Tsumura, N., Matsumoto, S., Horiuchi, S., and Hasegawa, A., 2000, Three-dimensional attenuation structure beneath the northeastern Japan arc estimated from spectra of small earthquakes, Tectonophysics, 319, 241-260.

Wang, K., Wells, R., Mazzotti, S., and Hyndman, R.D., 2003, A revised dislocation model of interseimic deformation of the Cascadia subduction zone, JGR, 108, doi:10.1029/2001JB001227.

White, R.S., McKenzie, D., and O'Nions, R.K., 1992, Oceanic crustal thickness form seismic measurements and rare earth element inversions, Journal of Geophysical Research, 97, 19638-19715.

Willoughby, E.C., and Hyndman, R.D., 2005, Earthquake rate, slip rate, and the effective seismic thickness for oceanic transform faults of the Juan de Fuca plate system, Geophysical Journal International, 160(3), 855-868.

Yagi, Y., 2004, Source rupture process of the 2003 Tokachi-oki earthquake determined by joint inversion of teleseismic body wave and strong ground motion data, Earth Planets Space, 56, 311-316.

Yamaguchi, D.K., Atwater, B.F., Bunker, D.E., Benson, B.E., and Reid, M.S., 1997, Tree-ring dating the 1700 Cascadia earthquake, Nature, 389, 922-923.

Zelt, C.A., and Ellis, R.M., 1988, Practical and efficient ray tracing in two-dimensional media for rapid traveltime and amplitude forward modeling, Canadian Journal of Exploration Geophysics, 24(1), 16-31.

Zelt B.C., Dotzev, N.T., Ellis, R.M., and Rogers, G.C., 1999, Coda Q in southwestern British Columbia, Canada, Bulletin of the Seismological Society of America, 89(4), 1083-1093.

Zhao, D., Hasegawa, A., and Horiuchi, S., 1992, Tomographic imaging of p and s wave velocity structure beneath northeastern Japan, Journal of Geophysical Research, 97, 19909-19928.

Zhao, D., Horiuchi, S., and Hasegawa, A., 1992, Seismic velocity structure of the crust beneath the Japan Islands, Tectonphysics, 212, 289-301.

APPENDIX A: Pseudo-spectral Method Algorithm

For an isotropic elastic medium undergoing infinitesimal deformation, the equations of momentum conservation are given by the following:

$$\rho \ddot{U}_x = \frac{\partial \sigma_{xx}}{\partial x} + \frac{\partial \sigma_{xy}}{\partial y} + f_x, \qquad [A.1]$$

$$\rho \ddot{U}_y = \frac{\partial \sigma_{xy}}{\partial x} + \frac{\partial \sigma_{yy}}{\partial y} + f_y, \qquad [A.2]$$

The stress components are σ_{xx}, σ_{yy} and σ_{xy}; f_x, and f_y are the body forces; the displacements are U_x, and U_y. Dots above a variable denote differentiations with respect to time and ρ denote density. Equations relating stress and strain components can be written as follows:

$$\sigma_{xx} = \lambda(e_{xx} + e_{yy}) + 2\mu e_{xx}, \qquad [A.3]$$

$$\sigma_{yy} = \lambda(e_{xx} + e_{yy}) + 2\mu e_{yy}, \qquad [A.4]$$

$$\sigma_{xy} = 2\mu e_{xy}, \qquad [A.5]$$

λ and μ denote the Lame constants and e_{xx}, e_{yy} and e_{xy} are the body strains. Strains can be expressed in terms of displacements as follows:

$$e_{xx} = \frac{\partial U_x}{\partial x}, \qquad [A.6]$$

$$e_{yy} = \frac{\partial U_y}{\partial y}, \qquad [A.7]$$

$$e_{xy} = \frac{1}{2}\left(\frac{\partial U_x}{\partial y} + \frac{\partial U_y}{\partial x}\right), \qquad [A.8]$$

In the solution algorithm of the pseudo-spectral method, the set of equations (1) to (8) are solved numerically after a discretization in space and time. The spatial derivates are calculated by means of the FFT. Second order difference operators approximate the time derivates.

Given the model parameters, the Lame constants and densities, and the initial condition of U_x,U_y, V_x and V_y a typical time step of the algorithm will consist of the following operations:

(1) Perform a two dimensional FFT on U_x and U_y and form the combinations:

$\underline{A3} = iK_x\underline{U_y}+iK_y\,\underline{U_x}$ [A.9]

$\underline{A2} = iK_x\underline{U_x}$ [A.10]

$\underline{A1}= iK_y\underline{U_y}$ [A.11]

where K_x and K_y are the spatial wave-numbers and an underline represents a two-dimensional spatial Fourier transform.

(2) Perform a two-dimensional inverse transformation to obtain e_{xx}, e_{yy} and e_{xy}. Use these values and the Lame parameters to form the right-hand sides of equation (3) to (5).

(3) Perform a two dimensional FFT on σ_{xx}, σ_{yy} and σ_{xy} and form the combinations:

$\underline{A4} = iK_x\sigma_{xx}$ [A.12]

$\underline{A3} = iK_y\sigma_{xx}$ [A.13]

$\underline{A2} = iK_x\sigma_{xy}$ [A.14]

$\underline{A1}= iK_y\sigma_{xy}.$ [A.15]

(4) Perform a two-dimensional inverse transformation to obtain $\frac{\partial \sigma_{xy}}{\partial x}, \frac{\partial \sigma_{yy}}{\partial y}, \frac{\partial \sigma_{xy}}{\partial y}$ *and* $\frac{\partial \sigma_{xx}}{\partial x}$. Use these values along with body force terms to form right-hand side of equation (1) and (2).

(5) Step the variables in time according to:

$V_x = V_x + B_1*dt/\rho$ [A.16]

$V_y = V_y + B_1*dt/\rho$ [A.17]

$U_x = U_x + V_x*dt/\rho$ [A.18]

$U_y = U_y + V_y*dt/\rho$ [A.19]

Where B_1 is the left-hand side of equation 1, B_2 is the left-hand side of equation 2, and dt is the time-step interval. The calculations in steps (1) to (5) are repeated for the desired number of time steps.

APPENDIX B: QUANTITATIVE COMPARISONS

The following figures are the quantitative comparisons for source frequencies, source locations and profiles not displayed in section 4.5.

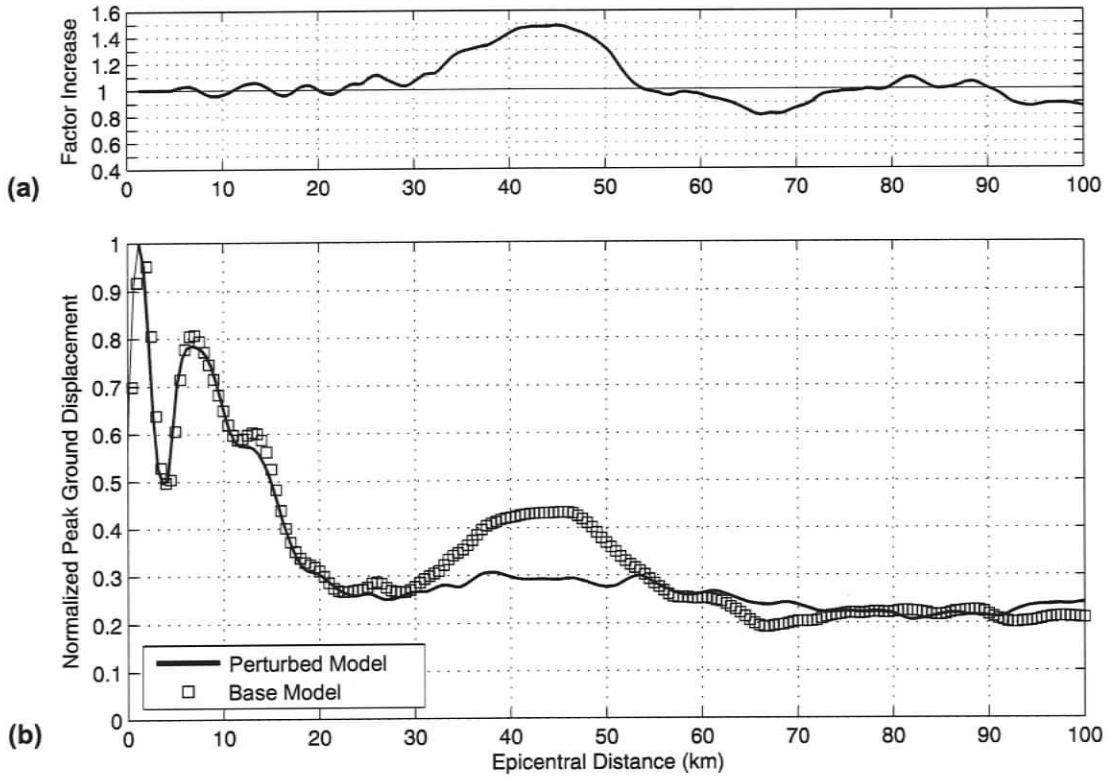

Figure B.1 Quantitative comparison for a 1 Hz source at the up-dip limit of the locked zone along a profile in the vicinity of Victoria. (a) Ratio between the base (square data points) and perturbed model results (solid line). (b) Peak ground motions for a 1 Hz source located at the up-dip limit of the locked zone for the base and perturbed models. Victoria is located at ~250 km epicentral distance.

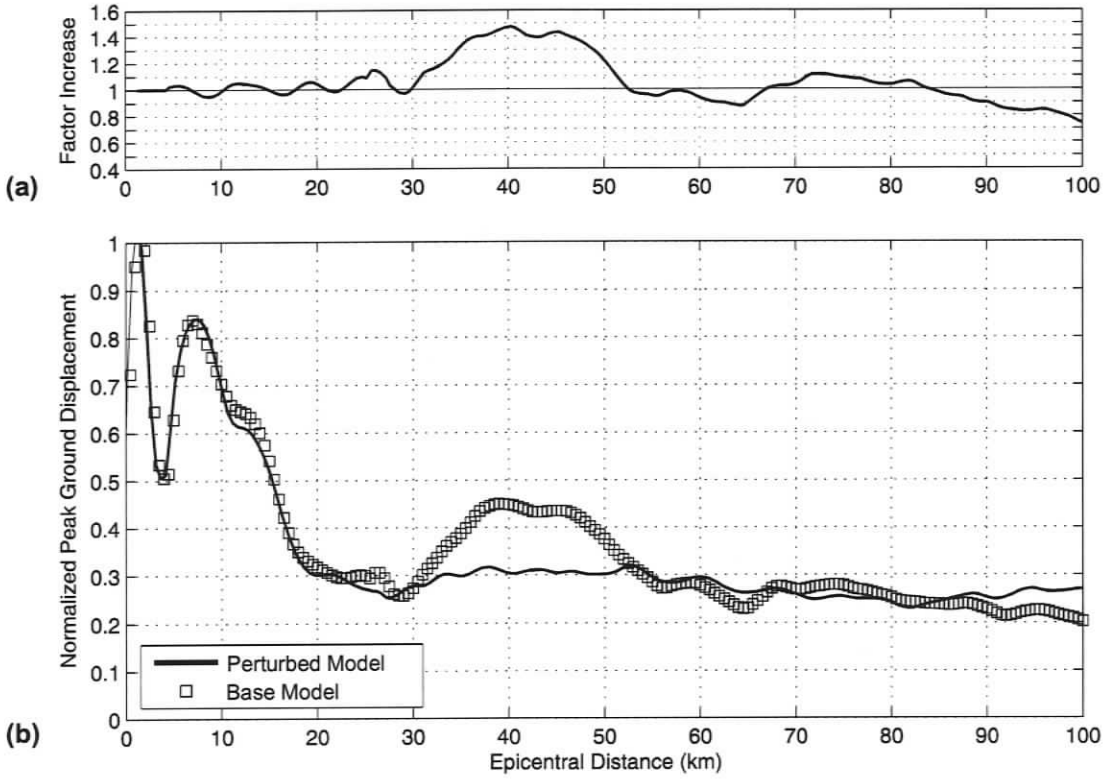

Figure B.2 Quantitative comparison for a 1 Hz source at the up-dip limit of the locked zone along a profile in the vicinity of Seattle. (a) Ratio between the base (square data points) and perturbed model results (solid line). (b) Peak ground motions for a 1 Hz source located at the up-dip limit of the locked zone for the base and perturbed models. Seattle is located at ~300 km epicentral distance.

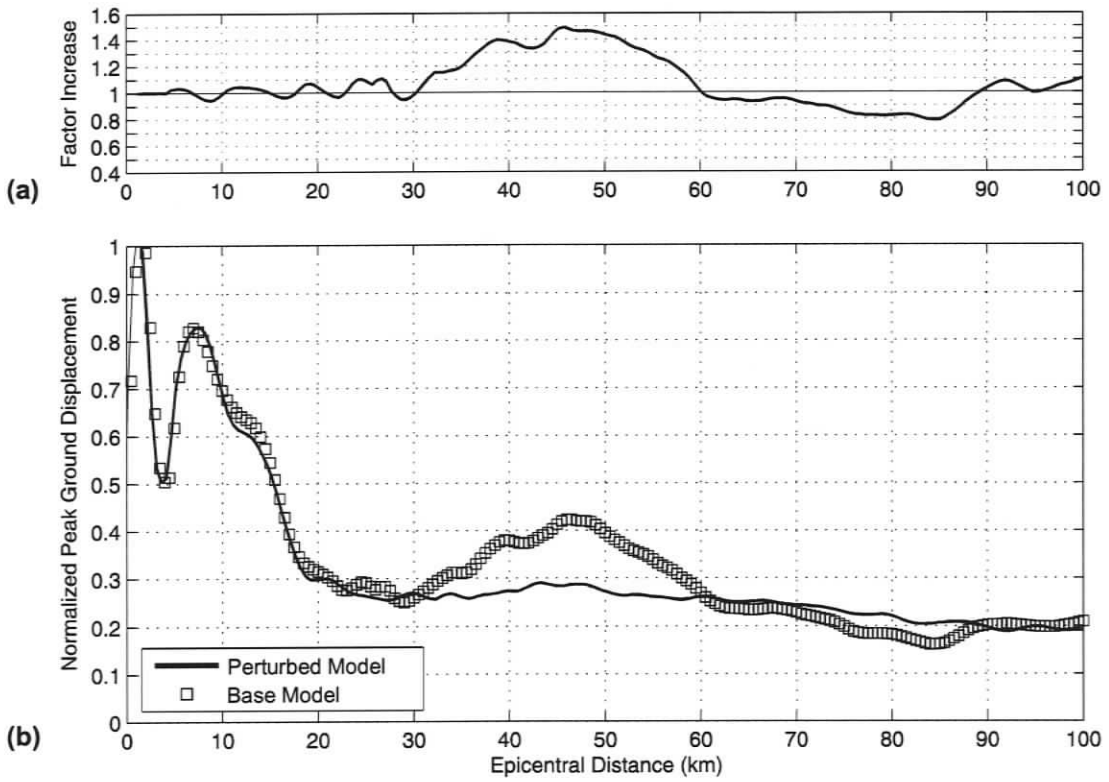

Figure B.3 Quantitative comparison for a 1 Hz source at the up-dip limit of the locked zone along a profile in the vicinity of Portland. (a) Ratio between the base (square data points) and perturbed model results (solid line). (b) Peak ground motions for a 1 Hz source located at the up-dip limit of the locked zone for the base and perturbed models. Portland is located at ~250 km epicentral distance.

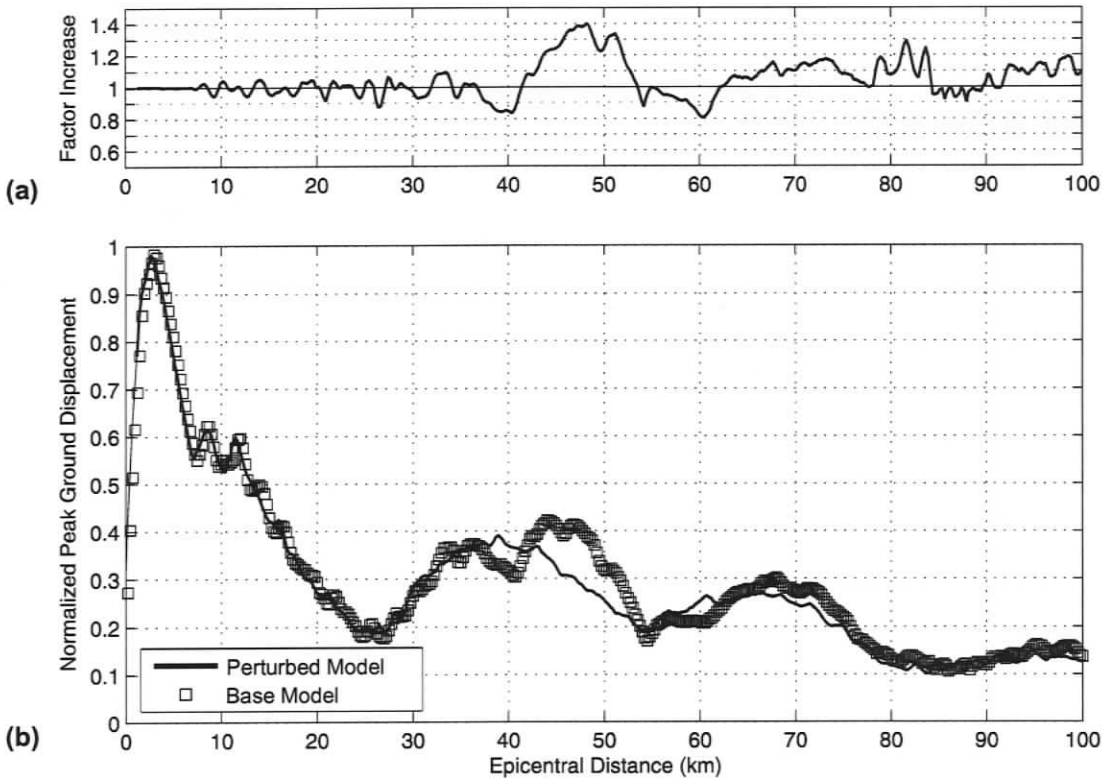

Figure B.4 Quantitative comparison for a 3 Hz source at the up-dip limit of the locked zone along a profile in the vicinity of Victoria. (a) Ratio between the base (square data points) and perturbed model results (solid line). (b) Peak ground motions for a 3 Hz source located at the up-dip limit of the locked zone for the base and perturbed models. Victoria is located at ~250 km epicentral distance.

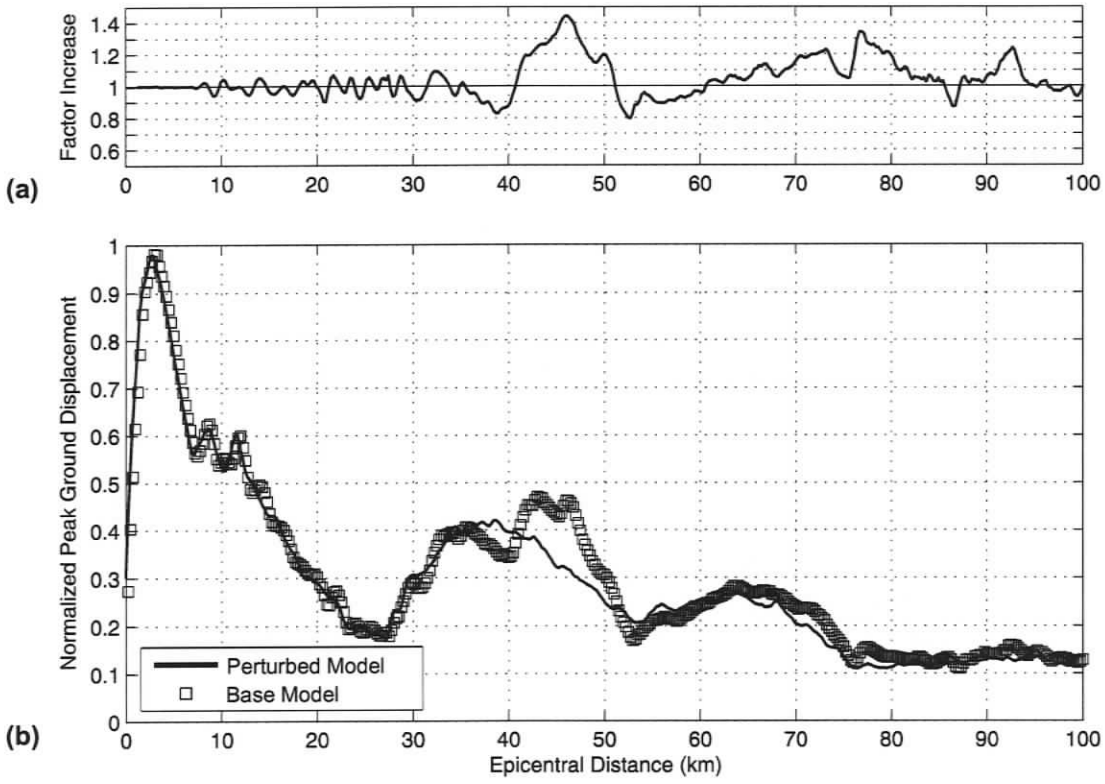

Figure B.5 Quantitative comparison for a 3 Hz source at the up-dip limit of the locked zone along a profile in the vicinity of Seattle. (a) Ratio between the base (square data points) and perturbed model results (solid line). (b) Peak ground motions for a 3 Hz source located at the up-dip limit of the locked zone for the base and perturbed models. Seattle is located at ~300 km epicentral distance.

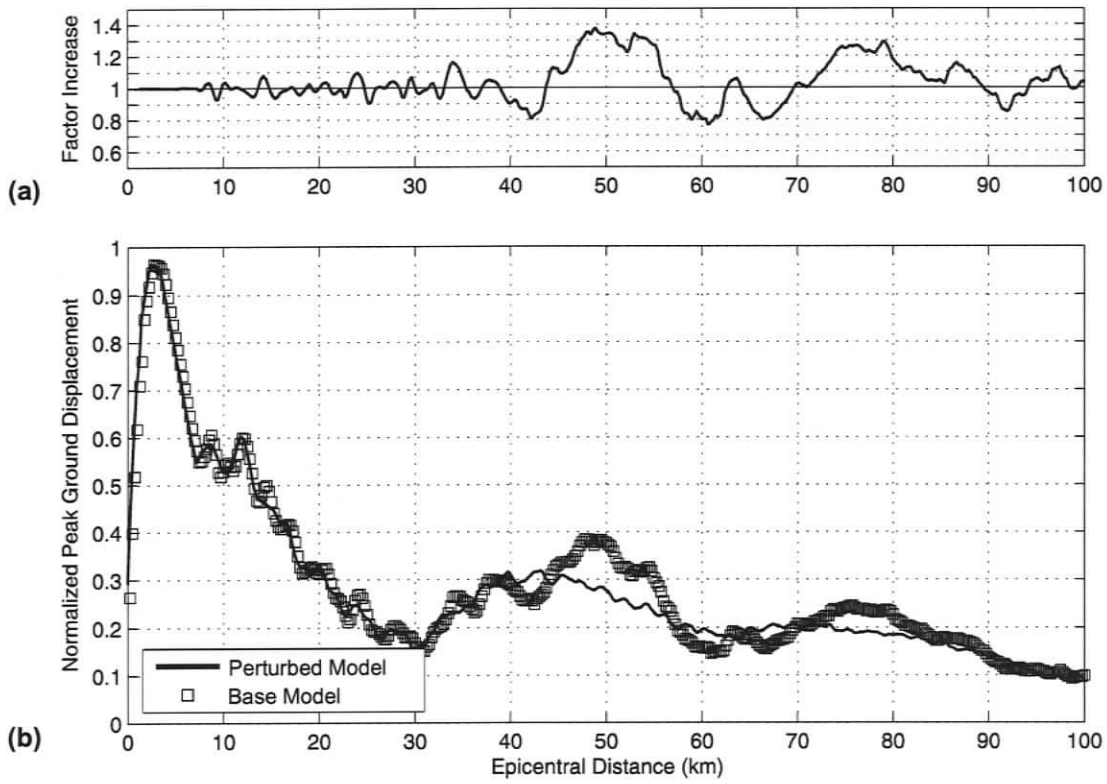

Figure B.6 Quantitative comparison for a 3 Hz source at the up-dip limit of the locked zone along a profile in the vicinity of Portland. (a) Ratio between the base (square data points) and perturbed model results (solid line). (b) Peak ground motions for a 3 Hz source located at the up-dip limit of the locked zone for the base and perturbed models. Portland is located at ~250 km epicentral distance.

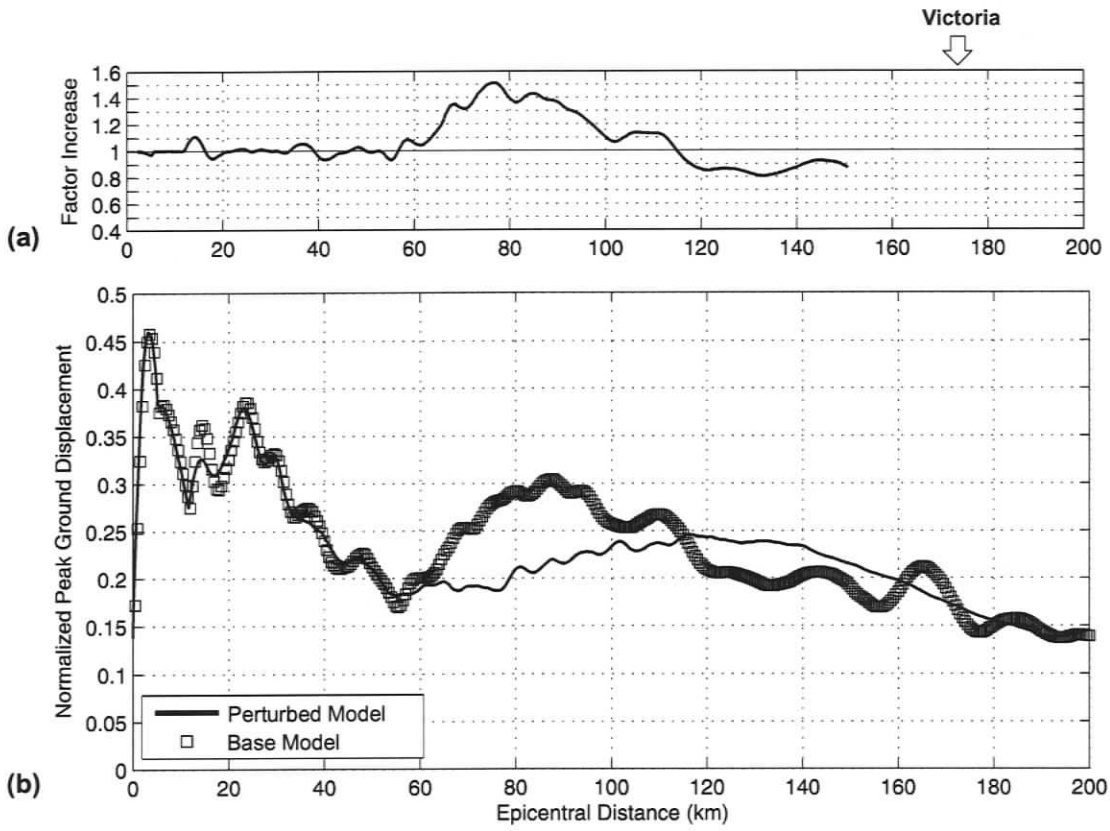

Figure B.7 Quantitative comparison for a 1 Hz source at the down-dip limit of the locked zone along a profile in the vicinity of Victoria. (a) Ratio between the base (square data points) and perturbed model results (solid line). (b) Peak ground motions for a 1 Hz source located at the up-dip limit of the locked zone for the base and perturbed models.

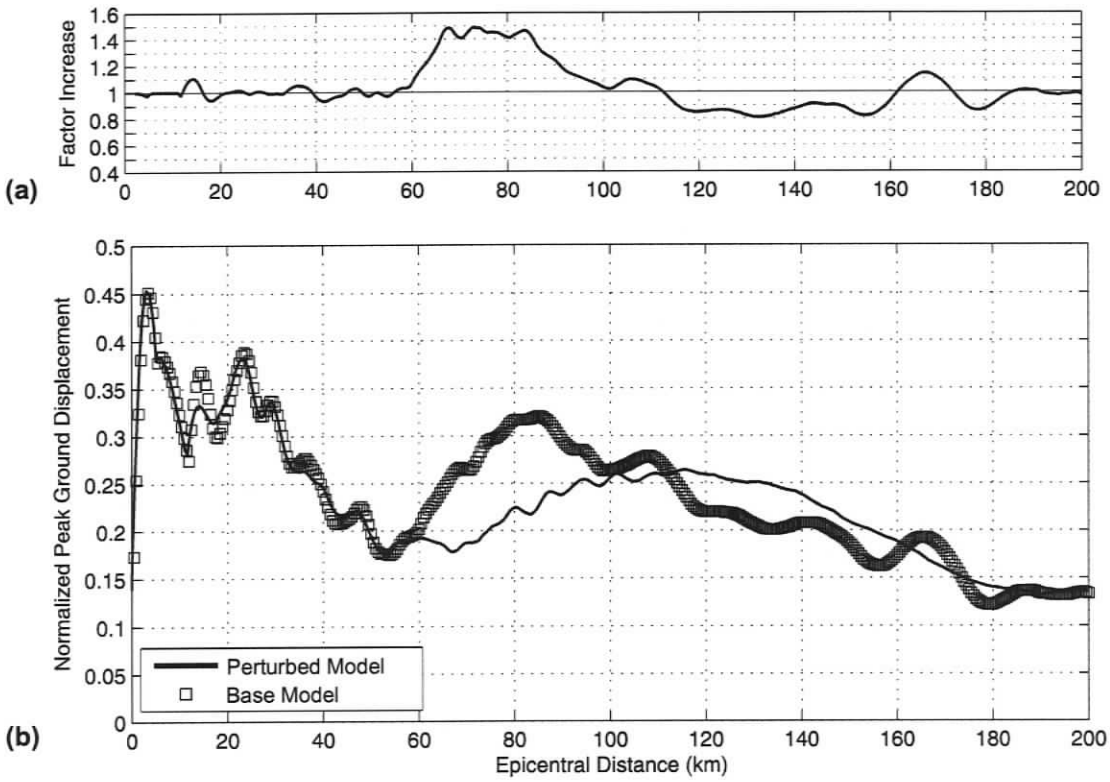

Figure B.8 Quantitative comparison for a 1 Hz source at the down-dip limit of the locked zone along a profile in the vicinity of Seattle. (a) Ratio between the base (square data points) and perturbed model results (solid line). (b) Peak ground motions for a 1 Hz source located at the up-dip limit of the locked zone for the base and perturbed models. Seattle is located at ~225 km epicentral distance.

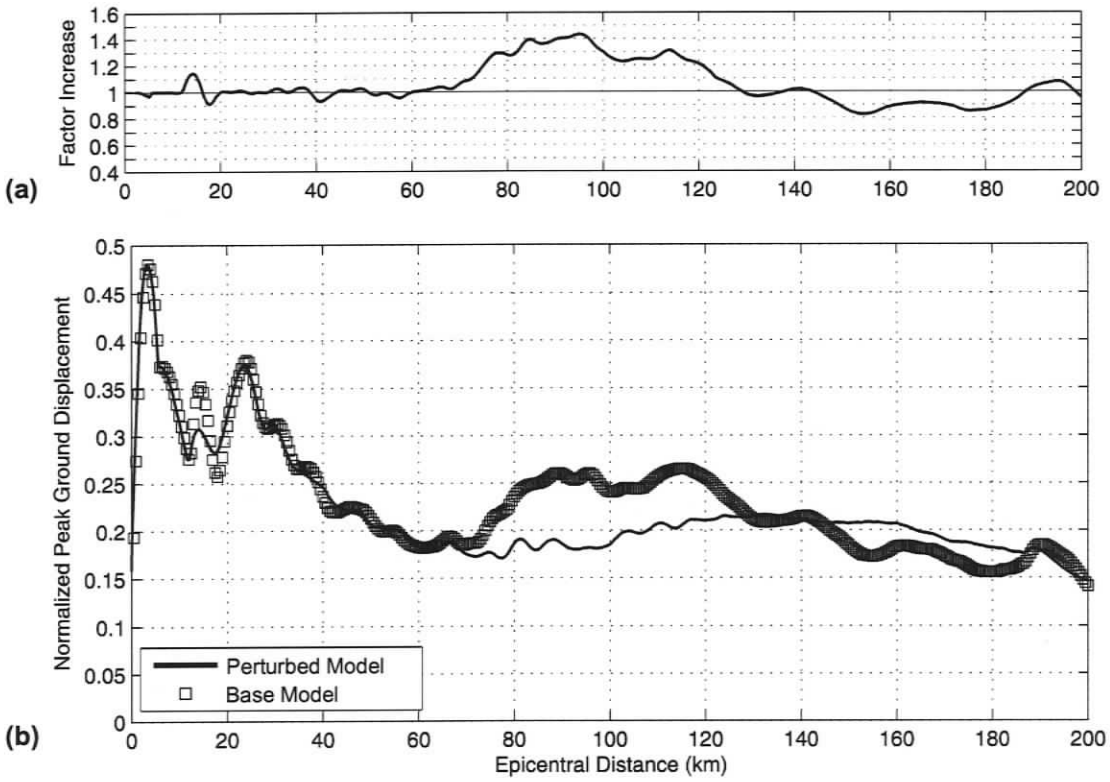

Figure B.9 Quantitative comparison for a 1 Hz source at the down-dip limit of the locked zone along a profile in the vicinity of Portland. (a) Ratio between the base (square data points) and perturbed model results (solid line). (b) Peak ground motions for a 1 Hz source located at the up-dip limit of the locked zone for the base and perturbed models. Portland is located at ~200 km epicentral distance.

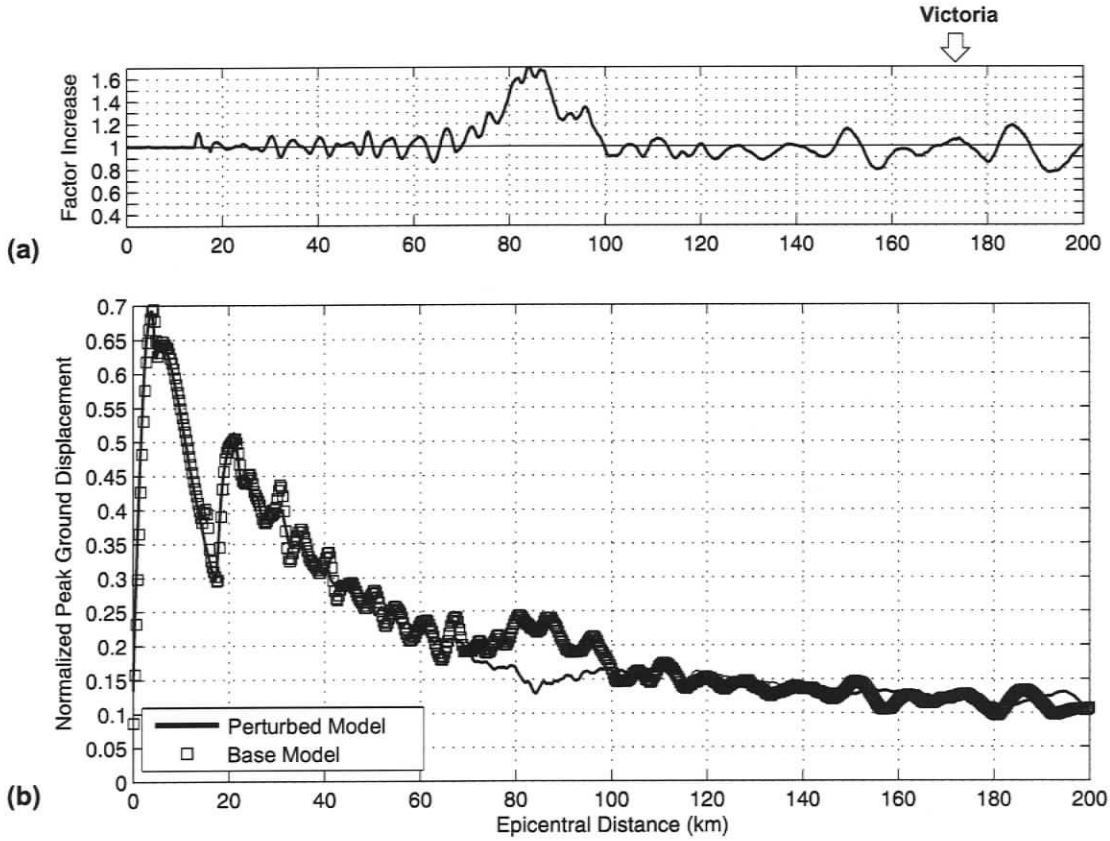

Figure B.10 Quantitative comparison for a 2 Hz source at the down-dip limit of the locked zone along a profile in the vicinity of Victoria. (a) Ratio between the base (square data points) and perturbed model results (solid line). (b) Peak ground motions for a 2 Hz source located at the up-dip limit of the locked zone for the base and perturbed models.

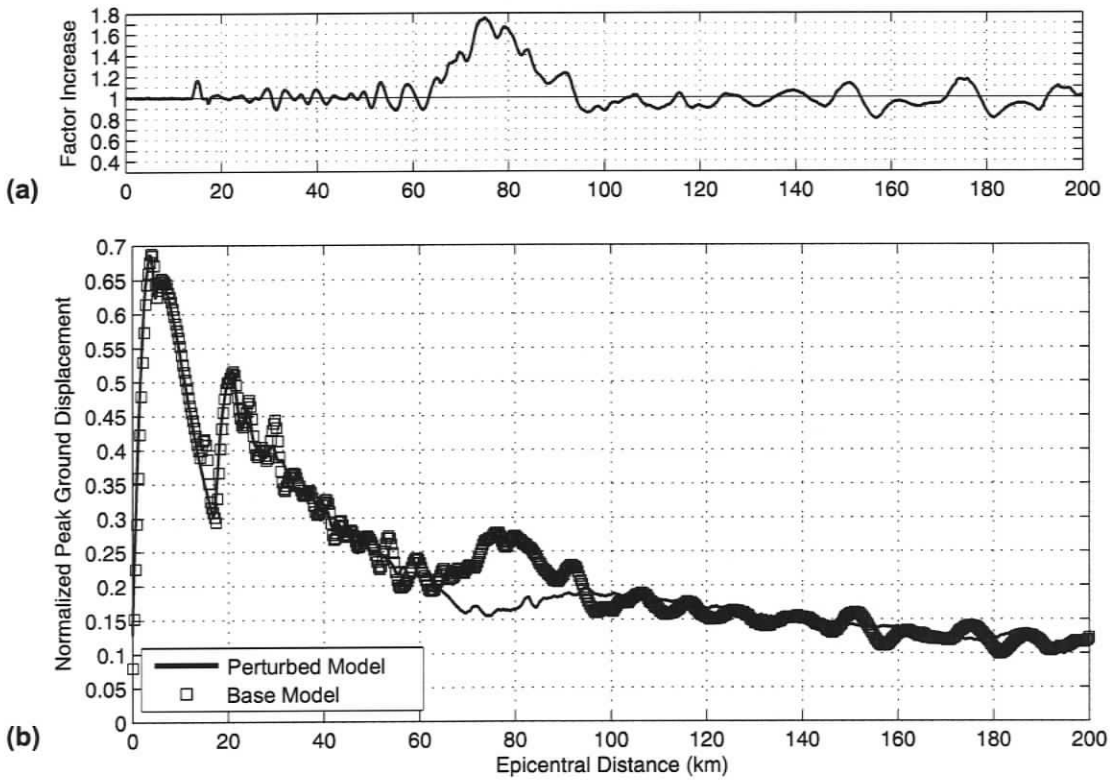

Figure B.11 Quantitative comparison for a 2 Hz source at the down-dip limit of the locked zone along a profile in the vicinity of Seattle. (a) Ratio between the base (square data points) and perturbed model results (solid line). (b) Peak ground motions for a 2 Hz source located at the up-dip limit of the locked zone for the base and perturbed models. Seattle is located at ~225 km epicentral distance.

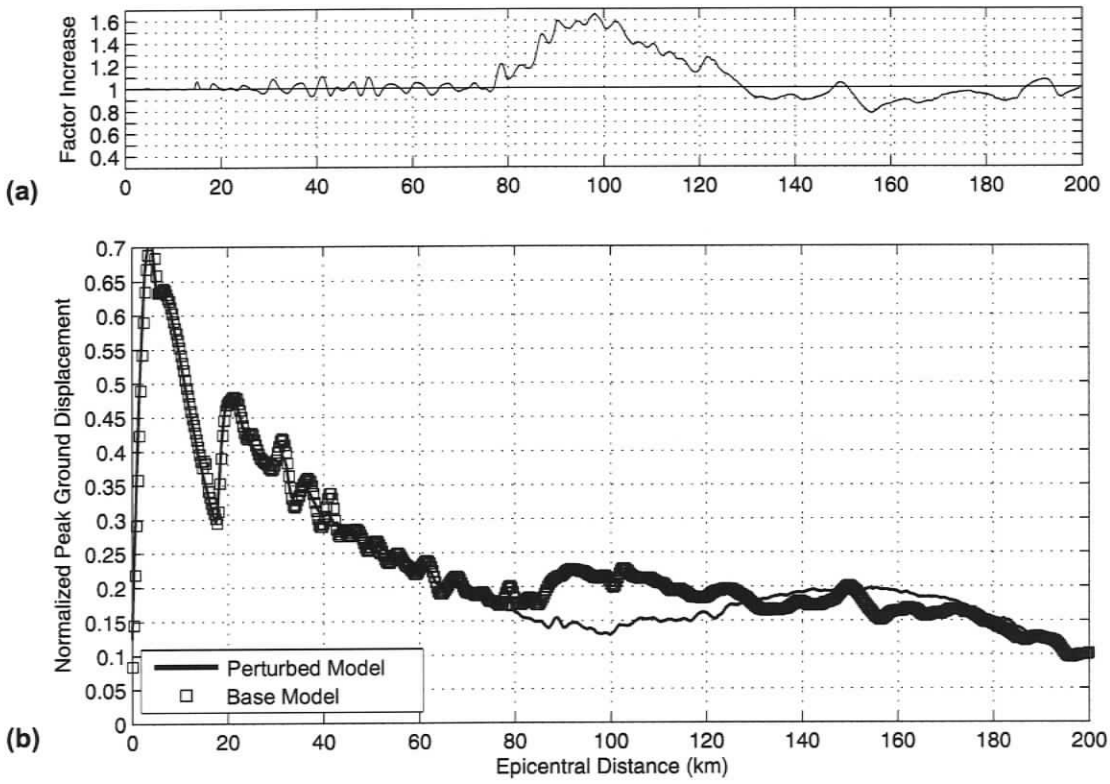

Figure B.12 Quantitative comparison for a 2 Hz source at the down-dip limit of the locked zone along a profile in the vicinity of Portland. (a) Ratio between the base (square data points) and perturbed model results (solid line). (b) Peak ground motions for a 2 Hz source located at the up-dip limit of the locked zone for the base and perturbed models. Portland is located at ~200 km epicentral distance.

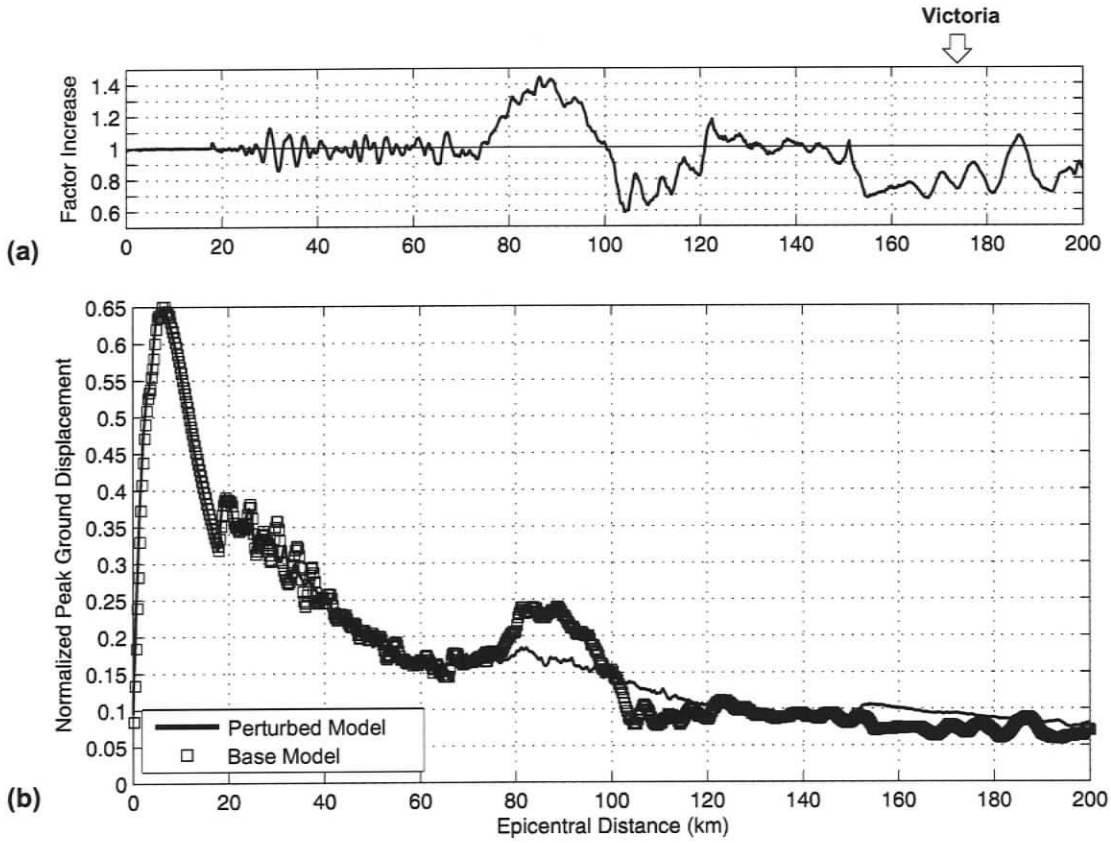

Figure B.13 Quantitative comparison for a 3 Hz source at the down-dip limit of the locked zone along a profile in the vicinity of Victoria. (a) Ratio between the base (square data points) and perturbed model results (solid line). (b) Peak ground motions for a 3 Hz source located at the up-dip limit of the locked zone for the base and perturbed models.

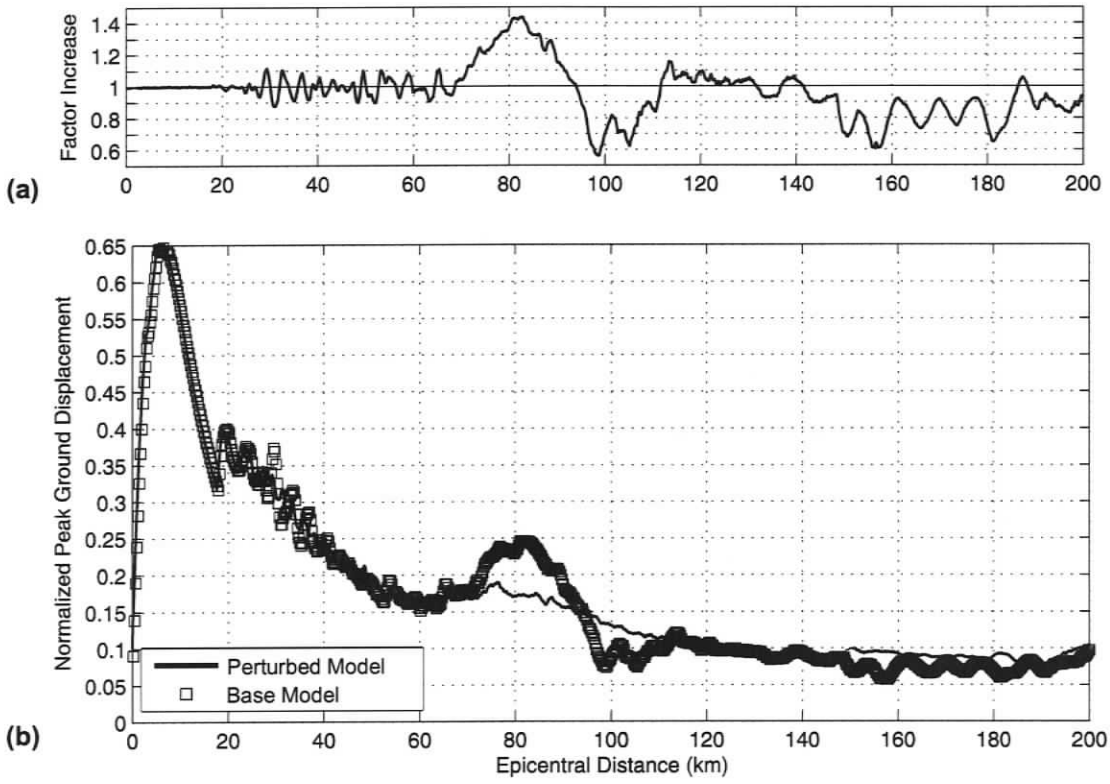

Figure B.14 Quantitative comparison for a 3 Hz source at the down-dip limit of the locked zone along a profile in the vicinity of Seattle. (a) Ratio between the base (square data points) and perturbed model results (solid line). (b) Peak ground motions for a 3 Hz source located at the up-dip limit of the locked zone for the base and perturbed models. Seattle is located at ~225 km epicentral distance.

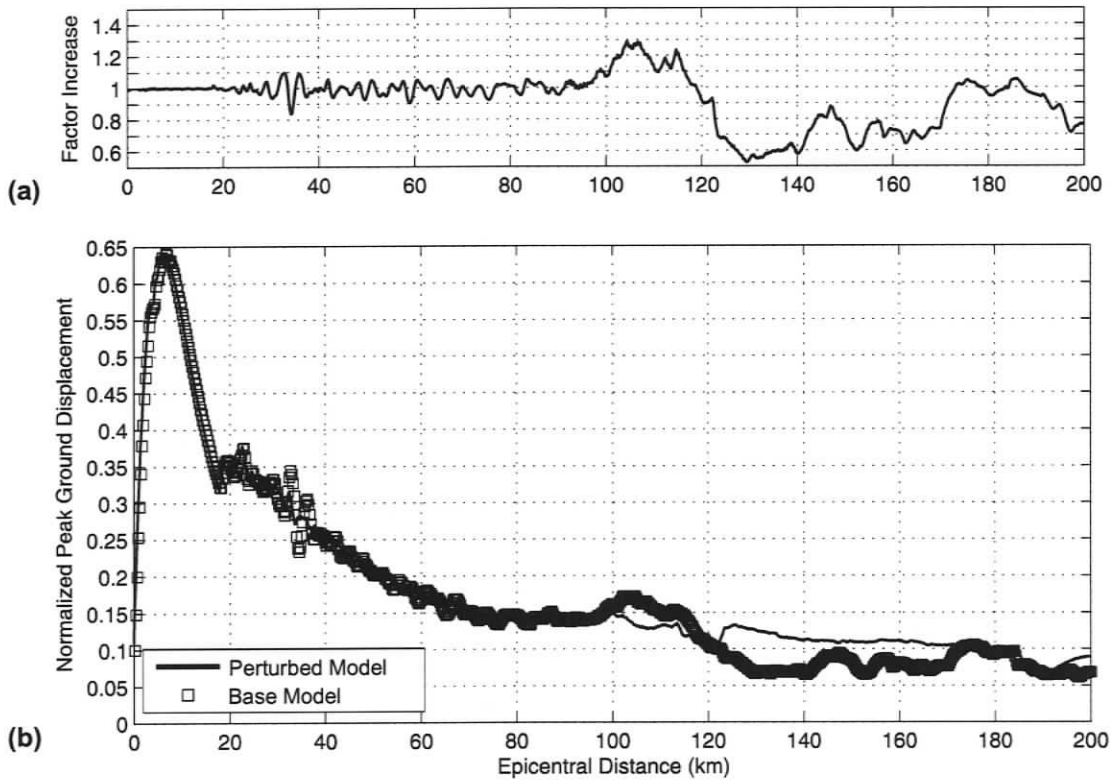

Figure B.15 Quantitative comparison for a 3 Hz source at the down-dip limit of the locked zone along a profile in the vicinity of Portland. (a) Ratio between the base (square data points) and perturbed model results (solid line). (b) Peak ground motions for a 3 Hz source located at the up-dip limit of the locked zone for the base and perturbed models. Portland is located at ~200 km epicentral distance.

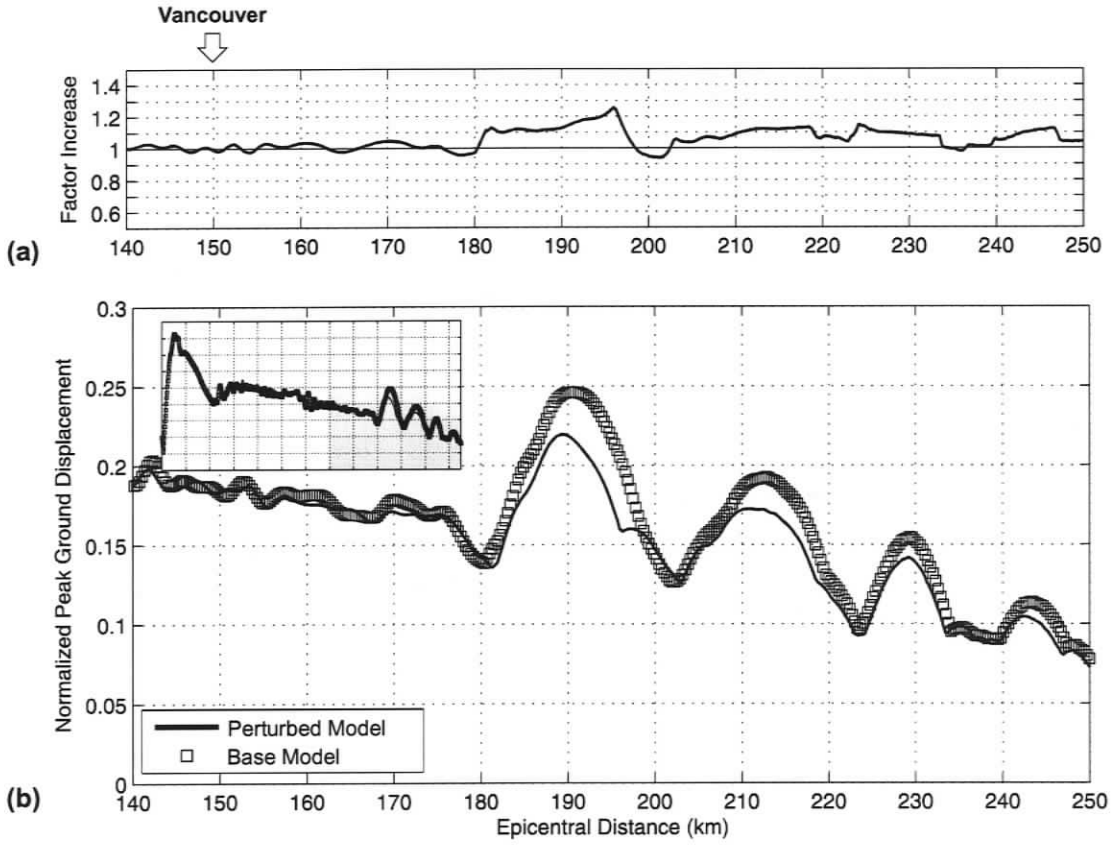

Figure B.16 Quantitative comparison for a 2 Hz source at the down-dip limit of the transition zone along a profile in the vicinity of Vancouver. (a) Ratio between the base (square data points) and perturbed model results (solid line). (b) Peak ground motions for a 2 Hz source located at the down-dip limit of the transition zone for the base and perturbed models. The inset shows peak ground motions in the range 0 - 250 km.

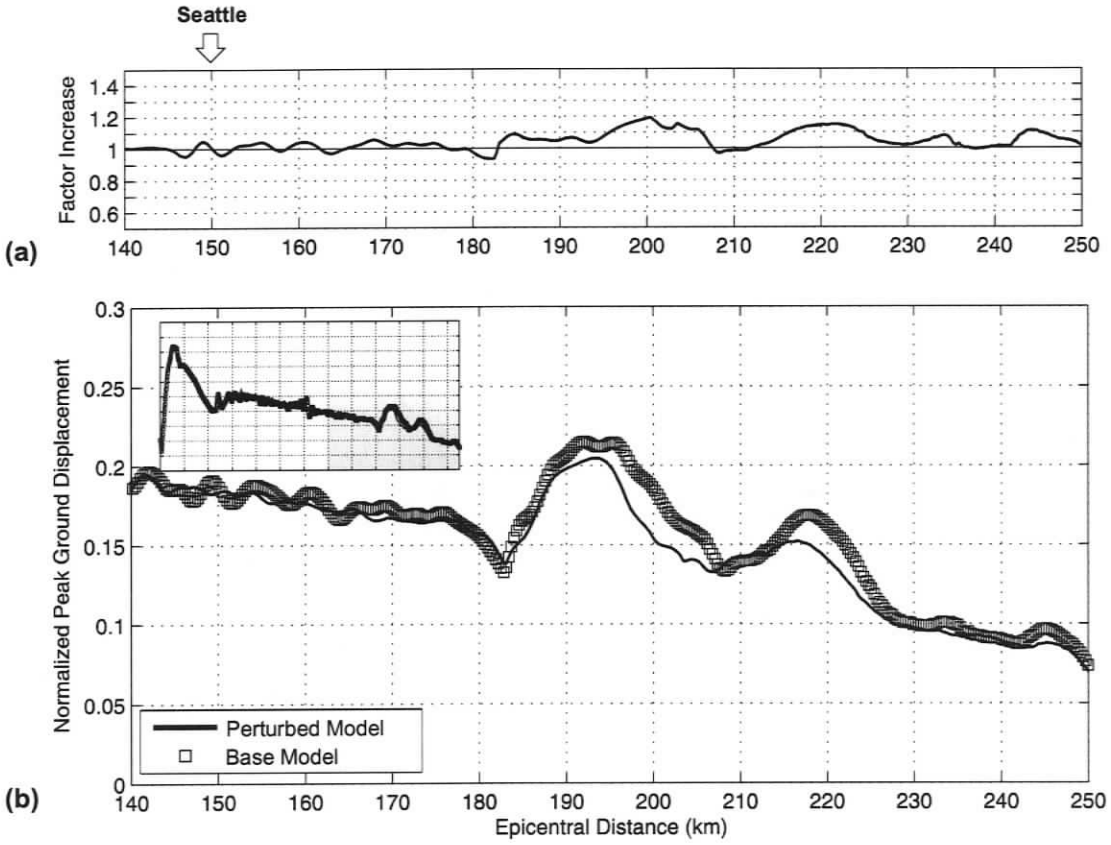

Figure B.17 Quantitative comparison for a 2 Hz source at the down-dip limit of the transition zone along a profile in the vicinity of Seattle. (a) Ratio between the base (square data points) and perturbed model results (solid line). (b) Peak ground motions for a 2 Hz source located at the down-dip limit of the transition zone for the base and perturbed models. The inset shows peak ground motions in the range 0 - 250 km.

APPENDIX C: 0.5 Hz SOURCE FREQUENCY

Figures C.1 - C.5 display the normalized peak ground motions within the post-critically enhanced region for source depths of 5 km, 10 km, 15 km, 20 km and 25 km, respectively. Figures C.6 - C.17 are the quantitative comparisons for the 0.5 Hz source frequency.

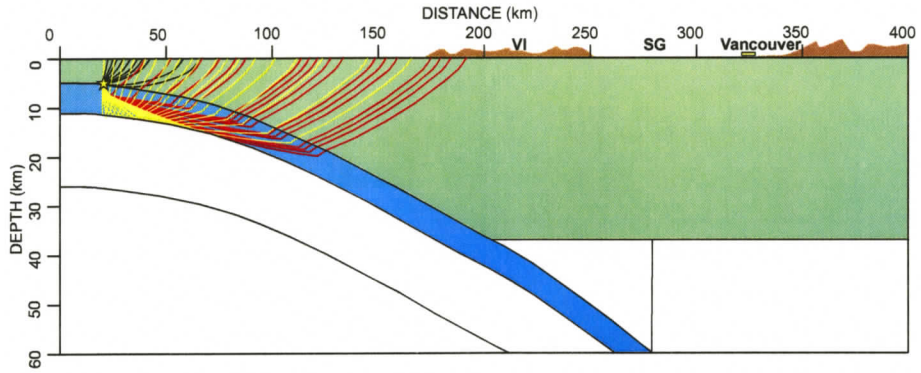

(a)

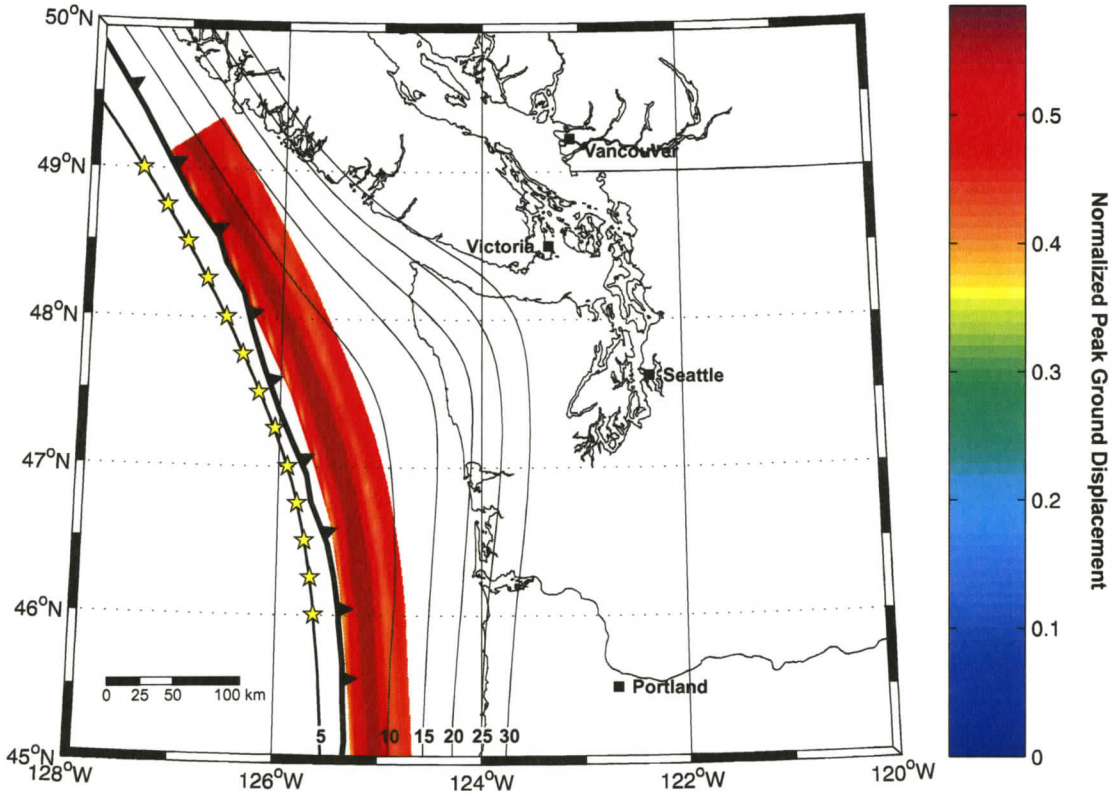

(b)

Figure C.1 Post-critically enhanced region for a 0.5 Hz source (yellow stars) at the up-dip limit of the locked zone. (a) Ray tracing diagram indicating propagation paths of direct waves (green), refractions in the oceanic crust (red) and reflections at the oceanic Moho (yellow). (b) Normalized peak ground motions within the post-critically enhanced region. Ray tracing profile indicated by dashed line. Abbreviations: VI-Vancouver Island; SG-Strait of Georgia.

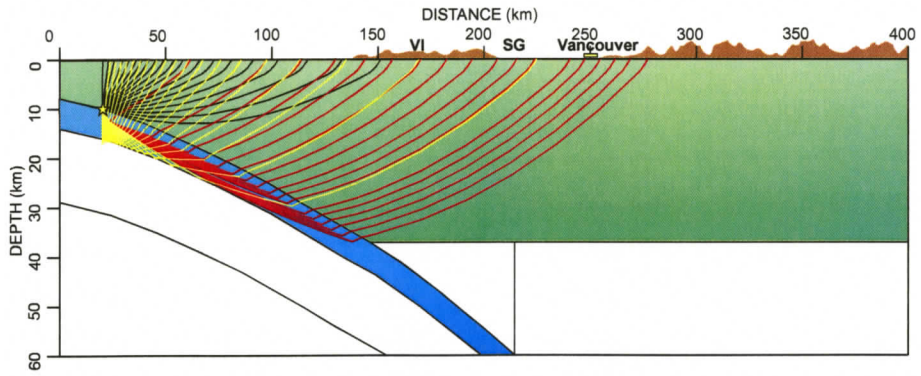

(a)

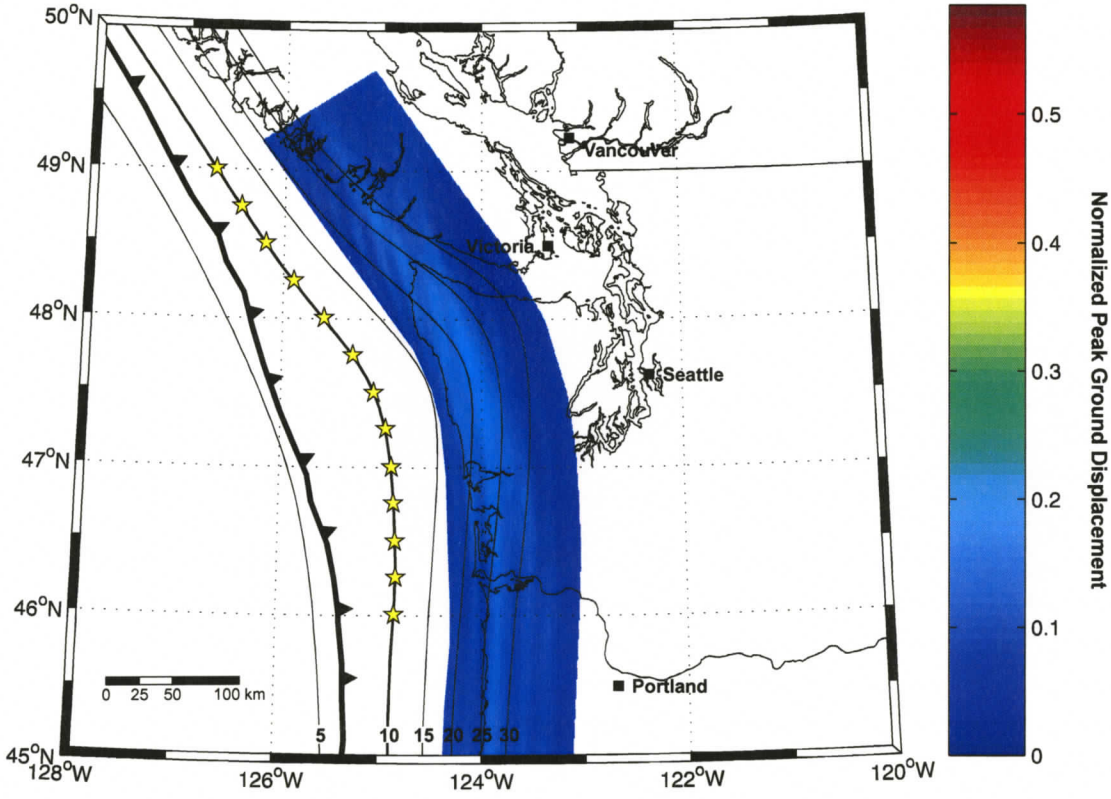

(b)

Figure C.2 Post-critically enhanced region for a 0.5 Hz source (yellow stars) at the down-dip limit of the locked zone. (a) Ray tracing diagram indicating propagation paths of direct waves (green), refractions in the oceanic crust (red) and reflections at the oceanic Moho (yellow). (b) Normalized peak ground motions within the post-critically enhanced region. Ray tracing profile indicated by dashed line. Abbreviations: VI-Vancouver Island; SG-Strait of Georgia.

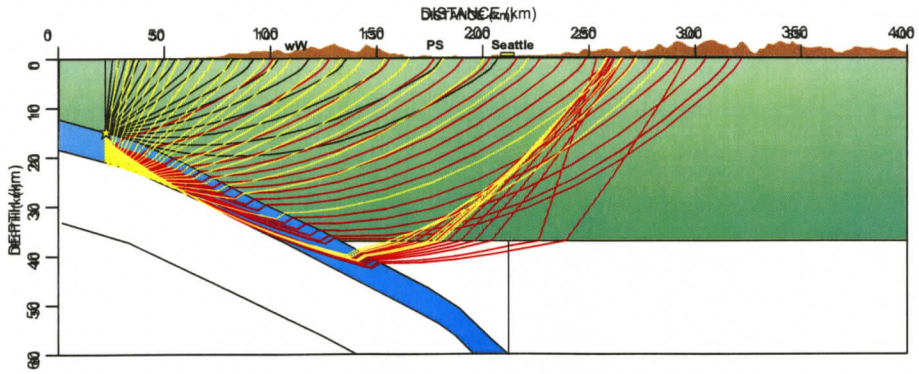

(a)

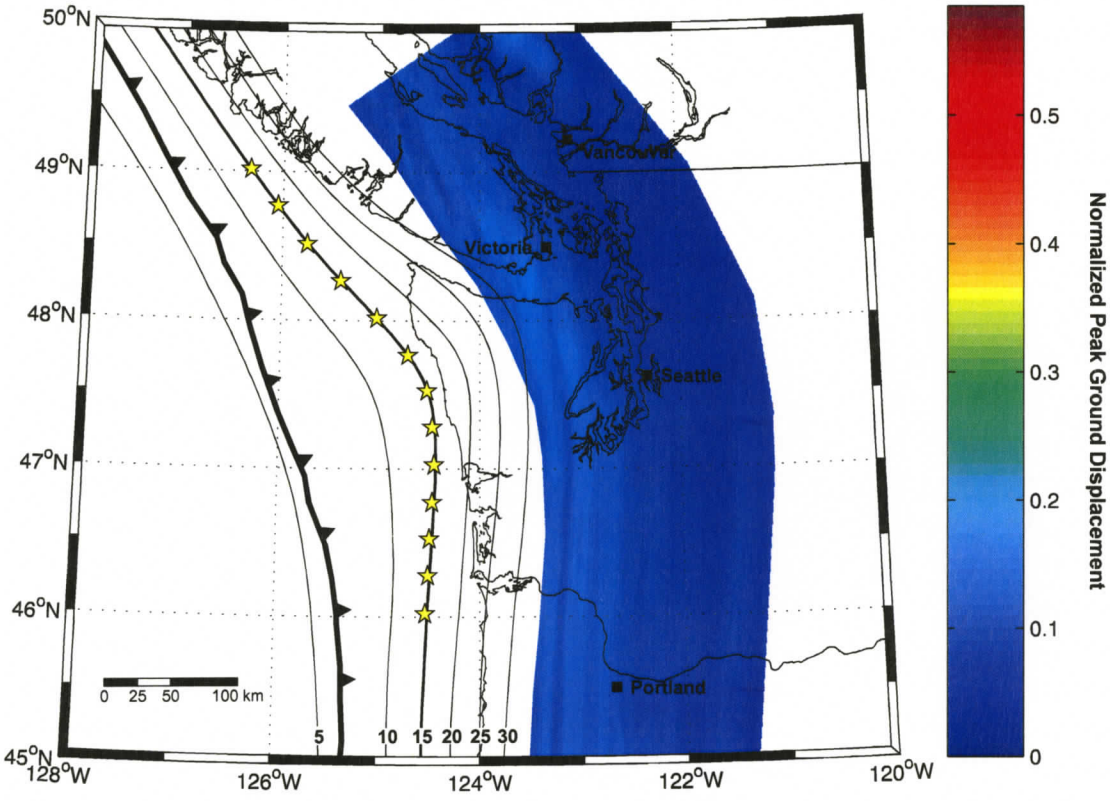

(b)

Figure C.3 Post-critically enhanced region for a 0.5 Hz source (yellow stars) located at the 15 km depth contour of the oceanic slab. (a) Ray tracing diagram indicating propagation paths of direct waves (green), refractions in the oceanic crust (red) and reflections at the oceanic Moho (yellow). (b) Normalized peak ground motions within the post-critically enhanced region. Ray tracing profile indicated by dashed line. Abbreviations: wW-Western Washington; PS-Puget Sound.

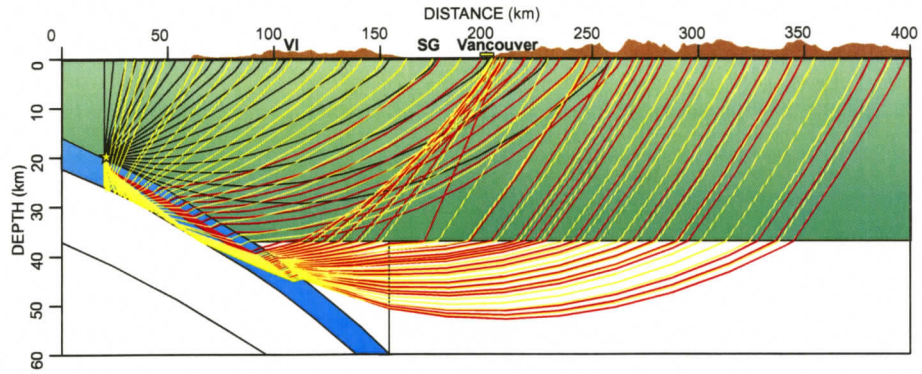

(a)

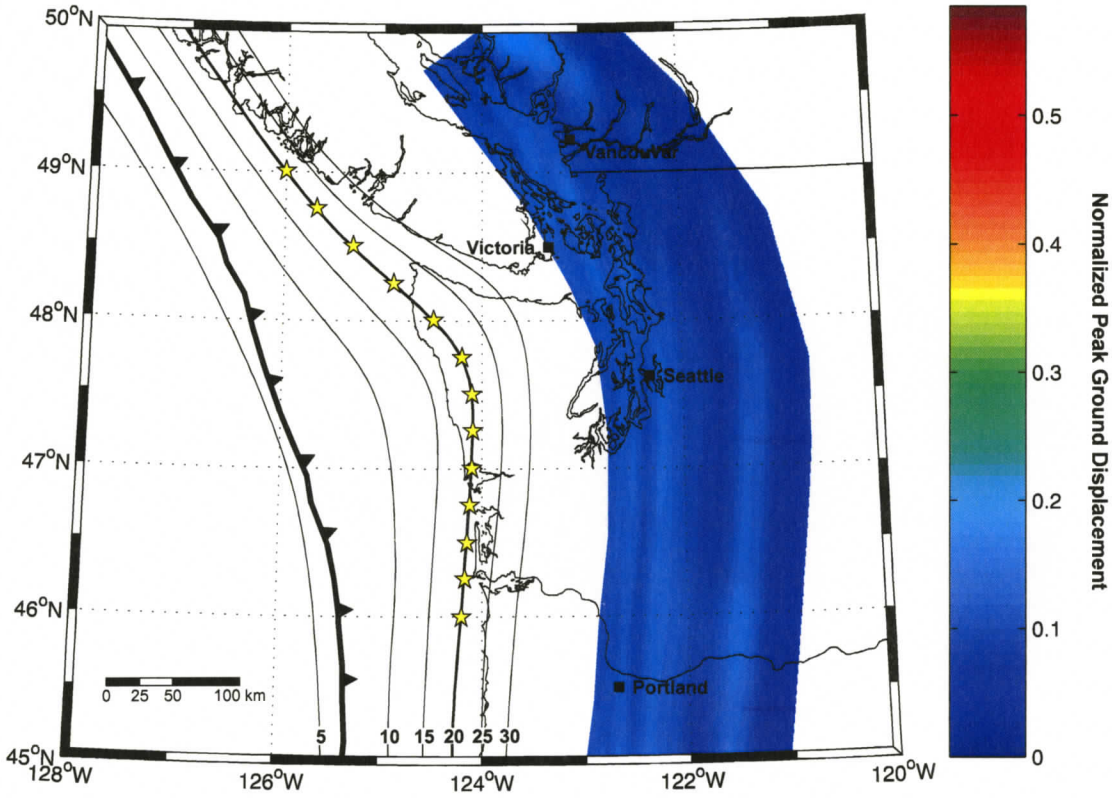

(b)

Figure C.4 Post-critically enhanced region for a 0.5 Hz source (yellow stars) located at the 20 km depth contour of the oceanic slab. (a) Ray tracing diagram indicating propagation paths of direct waves (green), refractions in the oceanic crust (red) and reflections at the oceanic Moho (yellow). (b) Normalized peak ground motions within the post-critically enhanced region. Ray tracing profile indicated by dashed line. Abbreviations: VI-Vancouver Island; SG-Strait of Georgia.

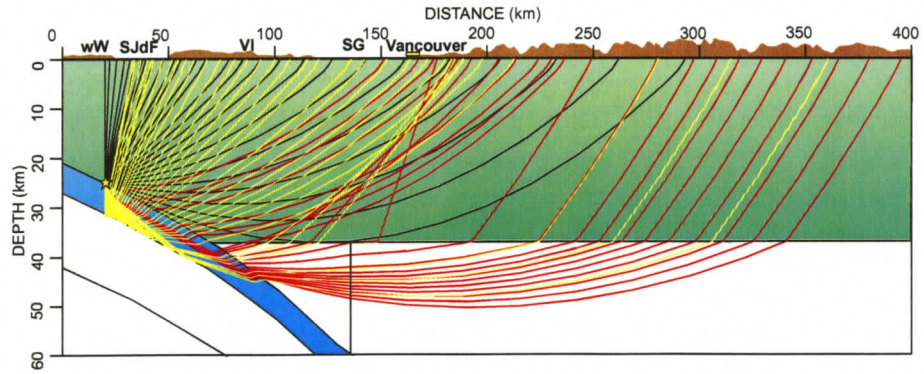

(a)

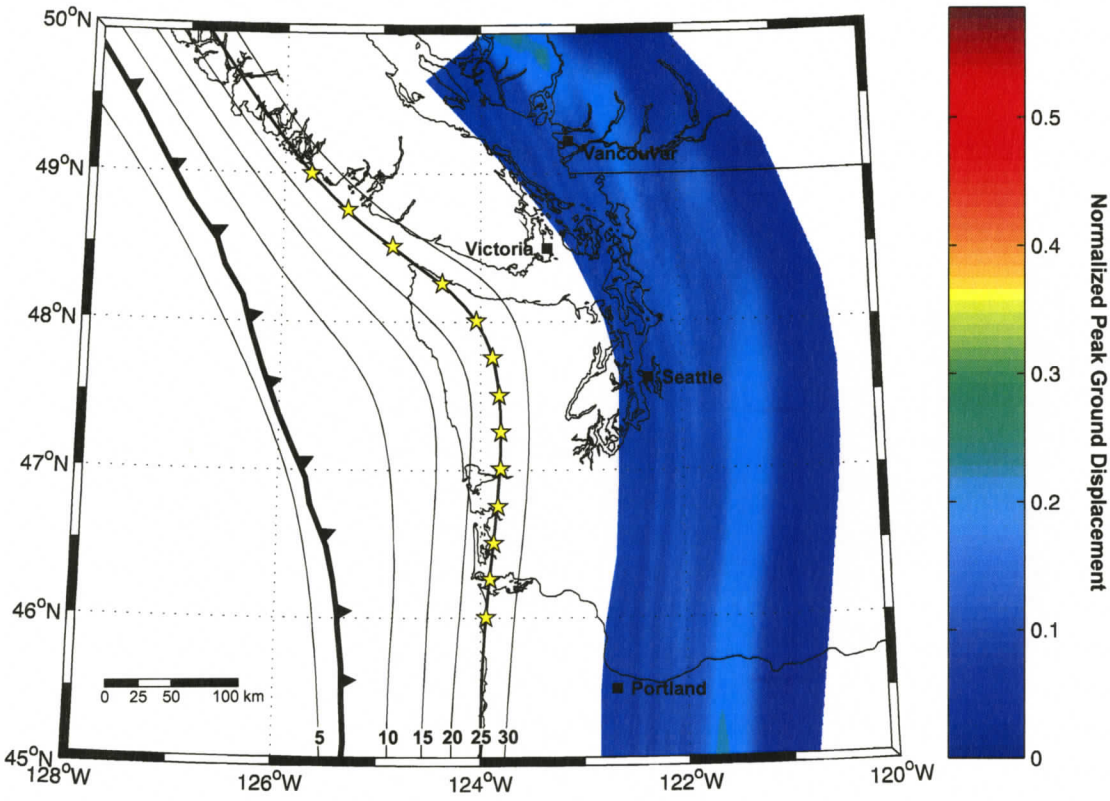

(b)

Figure C.5 Post-critically enhanced region for a 0.5 Hz source (yellow stars) at the down-dip limit of the transition zone. (a) Ray tracing diagram indicating propagation paths of direct waves (green), refractions in the oceanic crust (red) and reflections at the oceanic Moho (yellow). (b) Normalized peak ground motions within the post-critically enhanced region. Ray tracing profile indicated by dashed line. Abbreviations: wW-western Washington; SJdF-Strait of Juan de Fuca; VI-Vancouver Island; SG-Strait of Georgia.

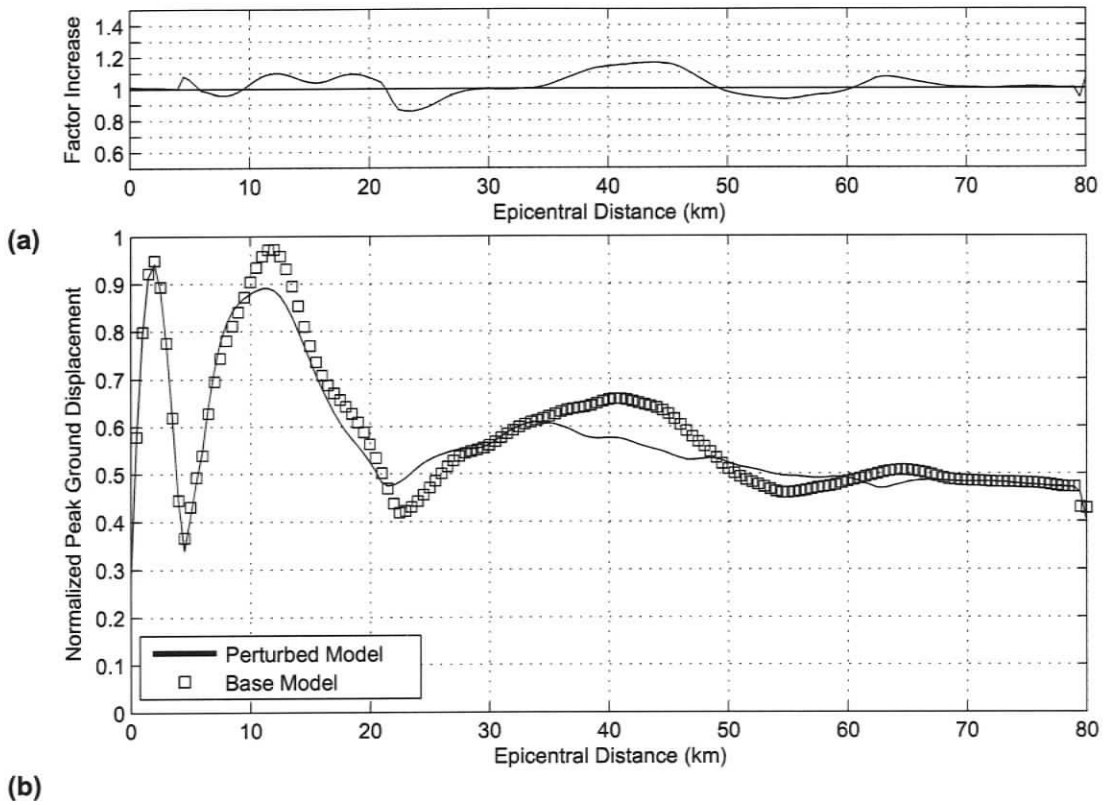

Figure C.6 Quantitative comparison for a 0.5 Hz source at the up-dip limit of the locked zone along a profile in the vicinity of Vancouver. (a) Ratio between the base (square data points) and perturbed model results (solid line). (b) Peak ground motions for a 0.5 Hz source located at the up-dip limit of the locked zone for the base and perturbed models. Vancouver is located at ~325 km epicentral distance.

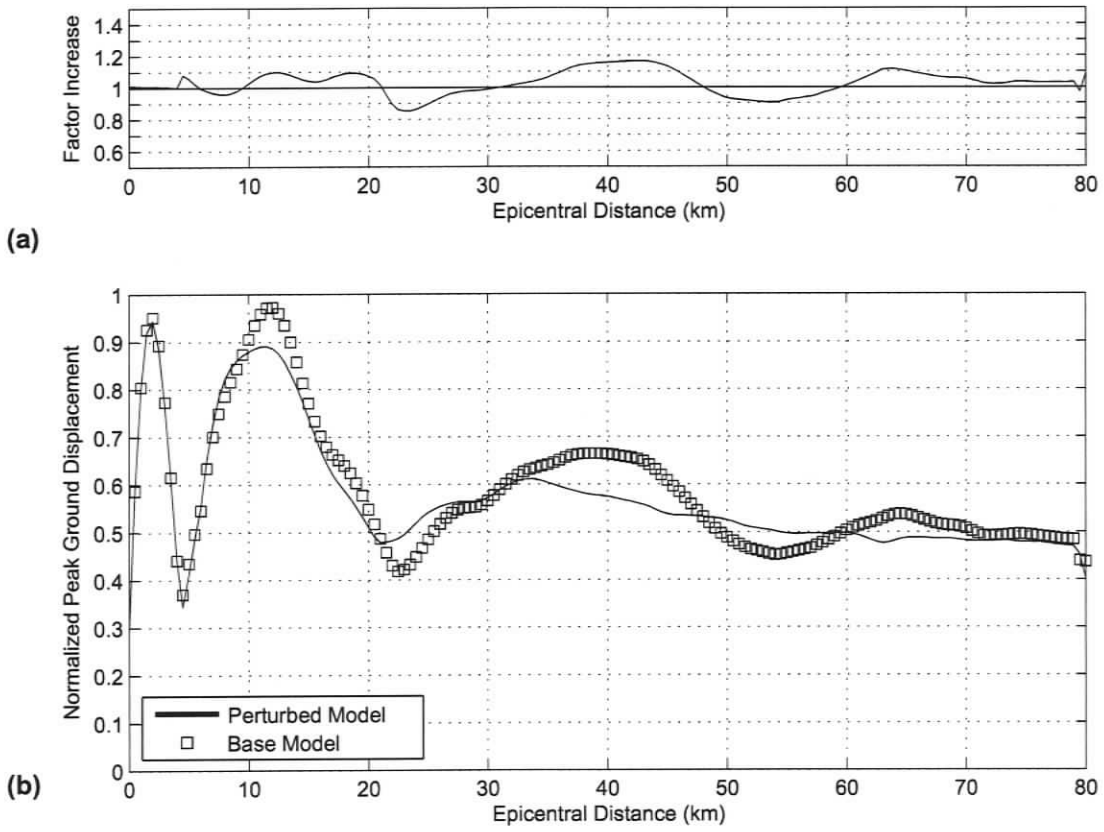

Figure C.7 Quantitative comparison for a 0.5 Hz source at the up-dip limit of the locked zone along a profile in the vicinity of Victoria. (a) Ratio between the base (square data points) and perturbed model results (solid line). (b) Peak ground motions for a 0.5 Hz source located at the up-dip limit of the locked zone for the base and perturbed models. Victoria is located at ~250 km epicentral distance.

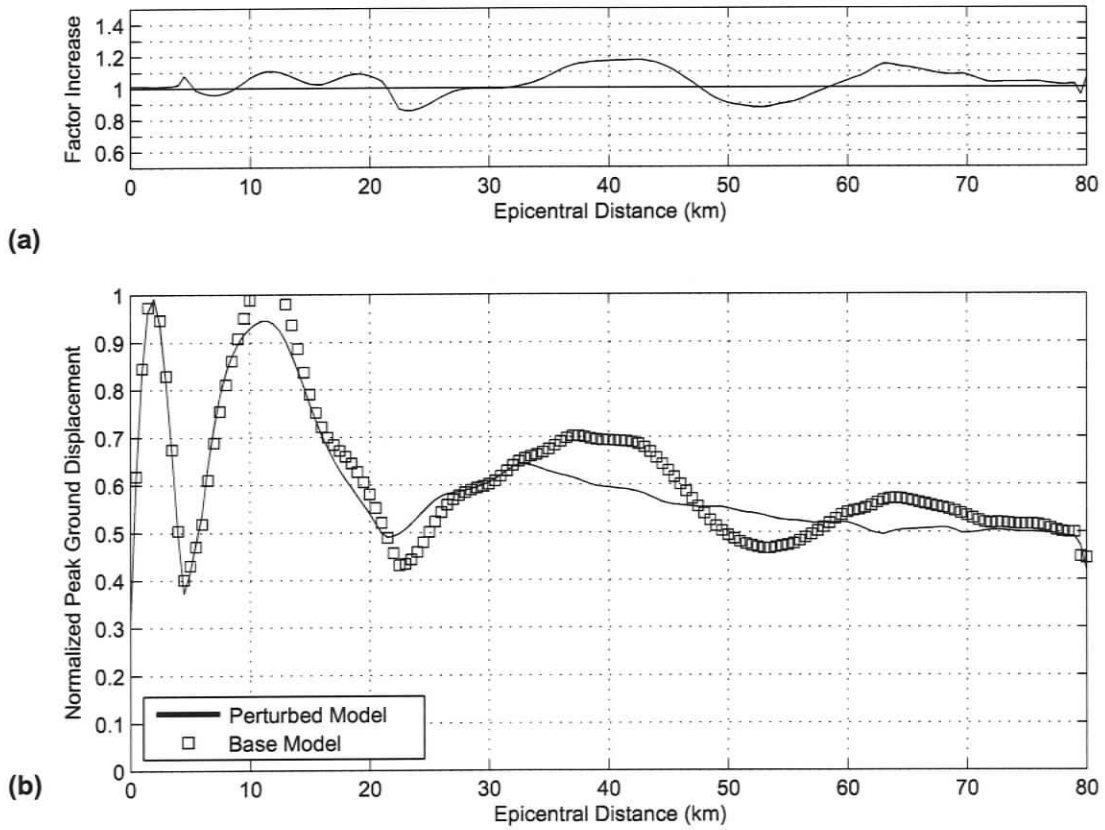

Figure C.8 Quantitative comparison for a 0.5 Hz source at the up-dip limit of the locked zone along a profile in the vicinity of Seattle. (a) Ratio between the base (square data points) and perturbed model results (solid line). (b) Peak ground motions for a 0.5 Hz source located at the up-dip limit of the locked zone for the base and perturbed models. Seattle is located at ~300 km epicentral distance.

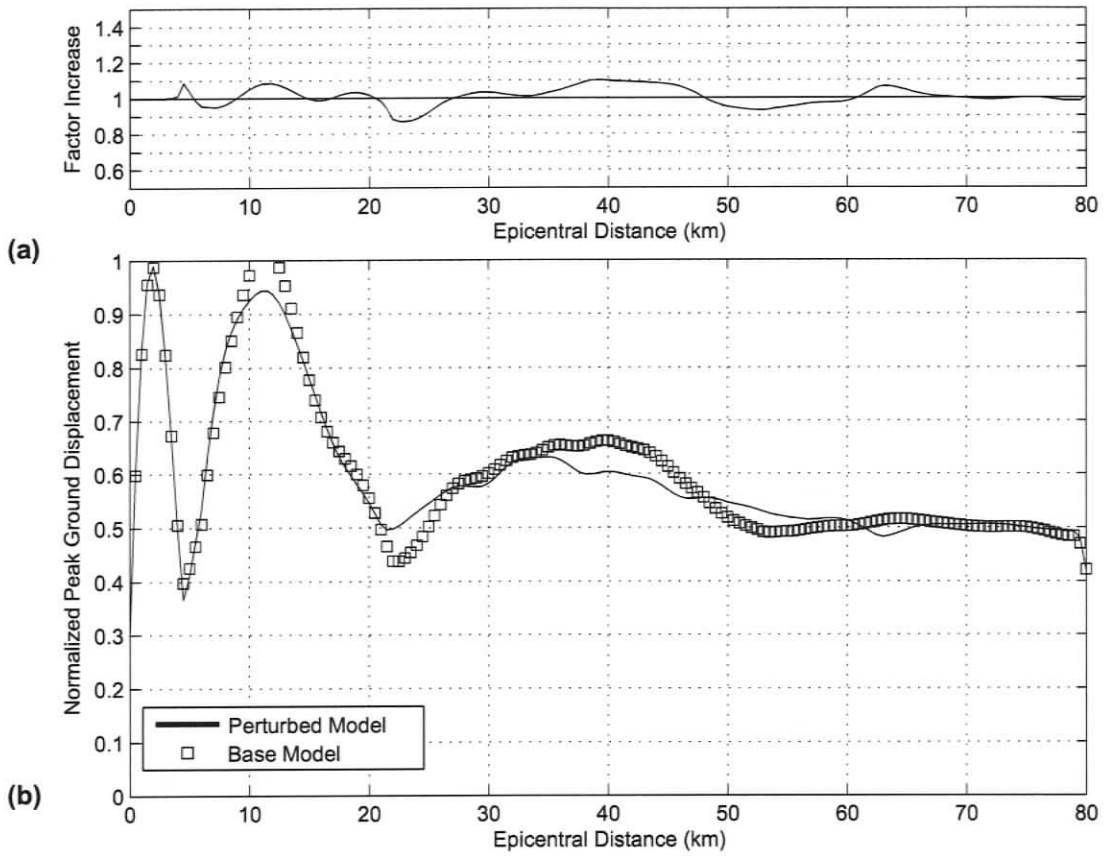

Figure C.9 Quantitative comparison for a 0.5 Hz source at the up-dip limit of the locked zone along a profile in the vicinity of Portland. (a) Ratio between the base (square data points) and perturbed model results (solid line). (b) Peak ground motions for a 0.5 Hz source located at the up-dip limit of the locked zone for the base and perturbed models. Portland is located at ~250 km epicentral distance.

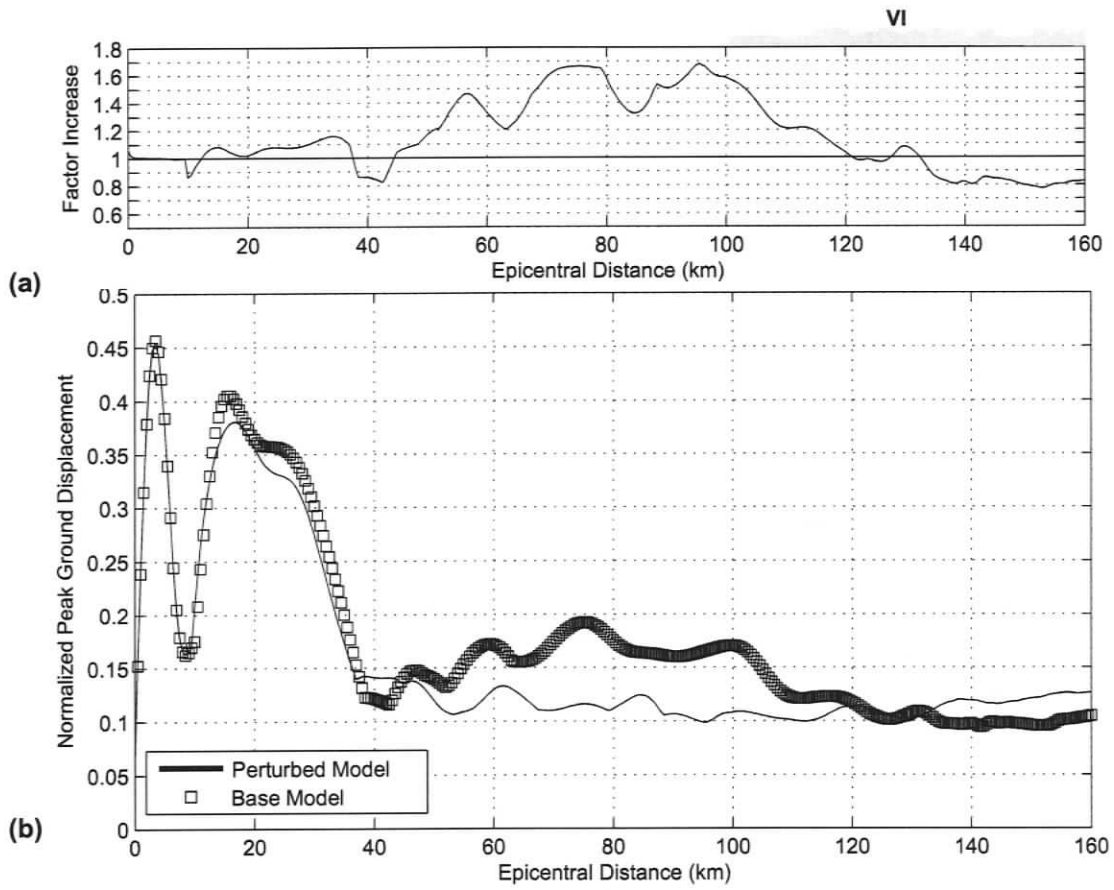

Figure C.10 Quantitative comparison for a 0.5 Hz source at the down-dip limit of the locked zone along a profile in the vicinity of Vancouver. (a) Ratio between the base (square data points) and perturbed model results (solid line). (b) Peak ground motions for a 0.5 Hz source located at the up-dip limit of the locked zone for the base and perturbed models. Vancouver is located at ~250 km epicentral distance. Abbreviations: VI-Vancouver Island.

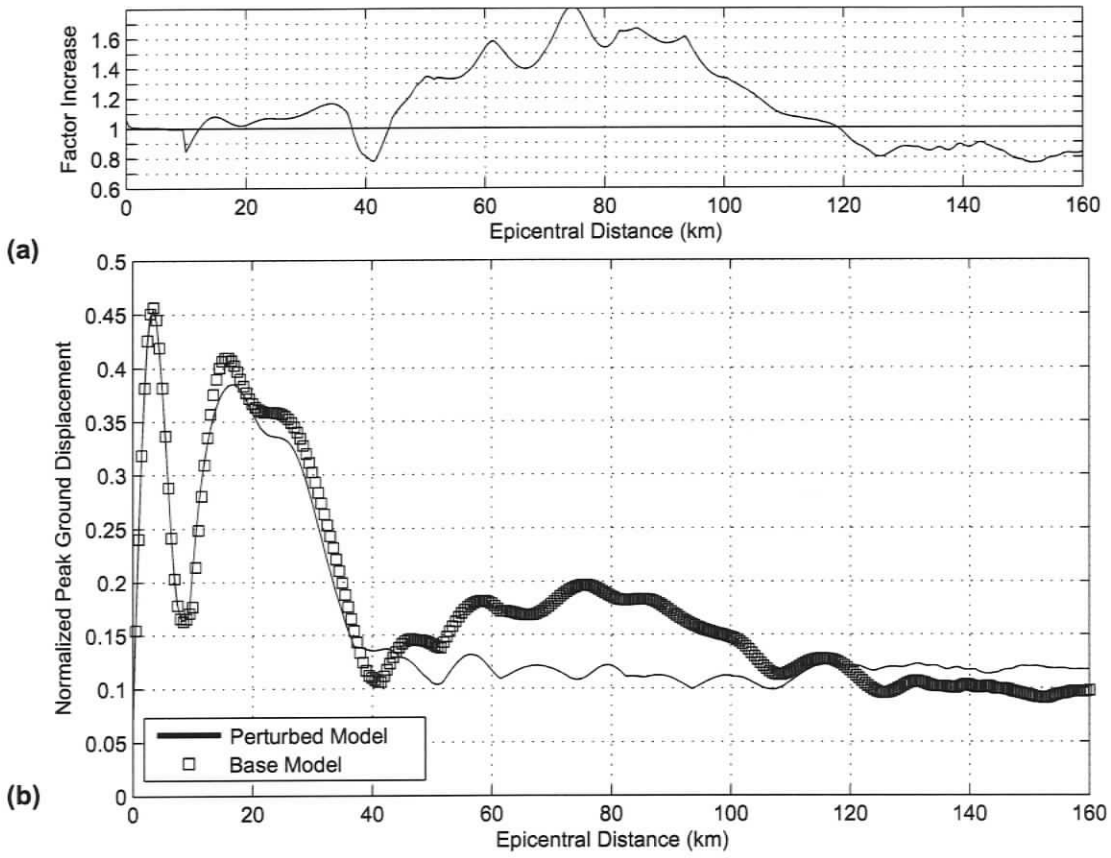

Figure C.11 Quantitative comparison for a 0.5 Hz source at the down-dip limit of the locked zone along a profile in the vicinity of Victoria. (a) Ratio between the base (square data points) and perturbed model results (solid line). (b) Peak ground motions for a 0.5 Hz source located at the up-dip limit of the locked zone for the base and perturbed models. Victoria is located at approximately 170 km epicentral distance.

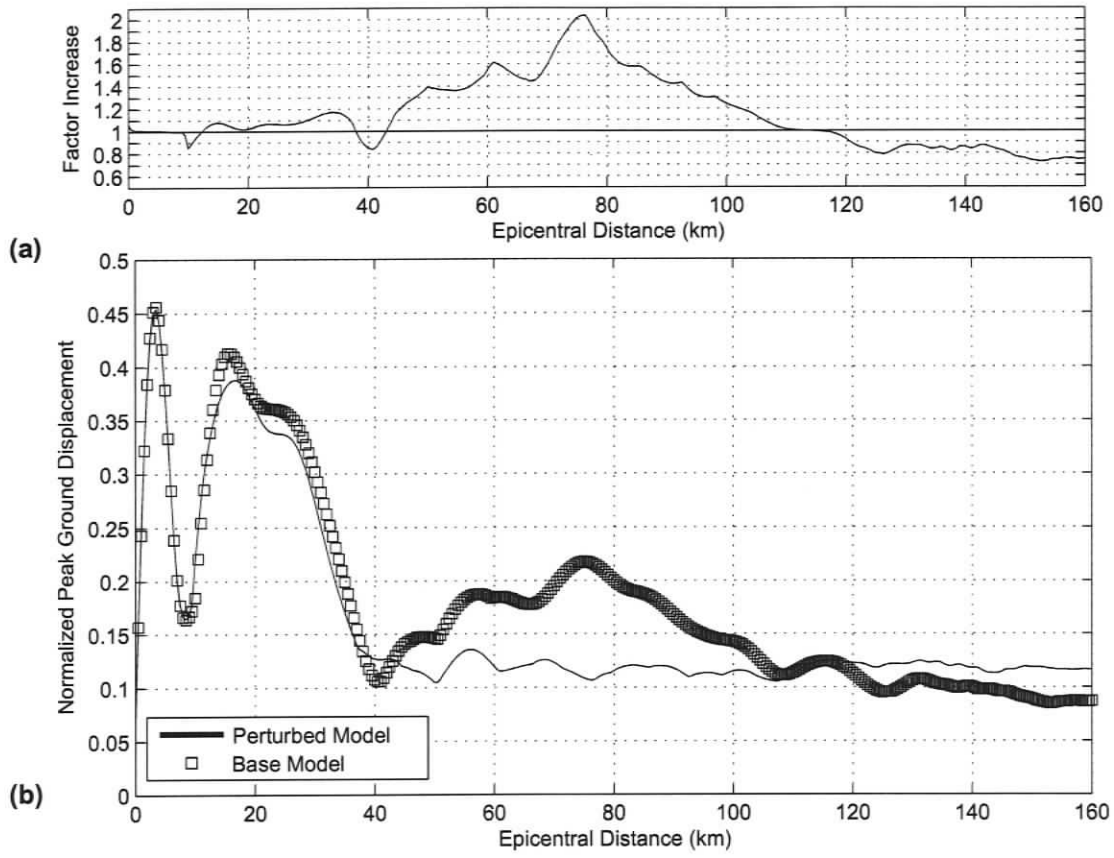

Figure C.12 Quantitative comparison for a 0.5 Hz source at the down-dip limit of the locked zone along a profile in the vicinity of Seattle. (a) Ratio between the base (square data points) and perturbed model results (solid line). (b) Peak ground motions for a 0.5 Hz source located at the up-dip limit of the locked zone for the base and perturbed models. Seattle is located at ~225 km epicentral distance.

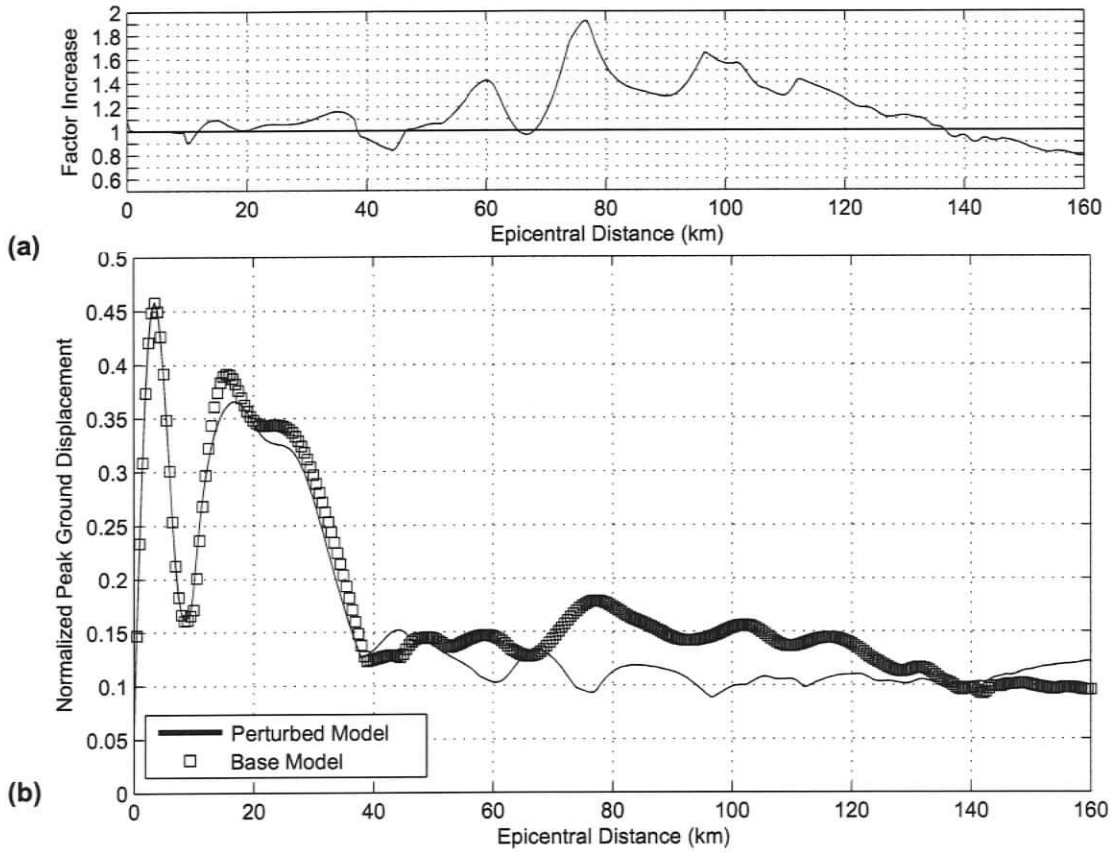

Figure C.13 Quantitative comparison for a 0.5 Hz source at the down-dip limit of the locked zone along a profile in the vicinity of Portland. (a) Ratio between the base (square data points) and perturbed model results (solid line). (b) Peak ground motions for a 0.5 Hz source located at the up-dip limit of the locked zone for the base and perturbed models. Portland is located at ~200 km epicentral distance.

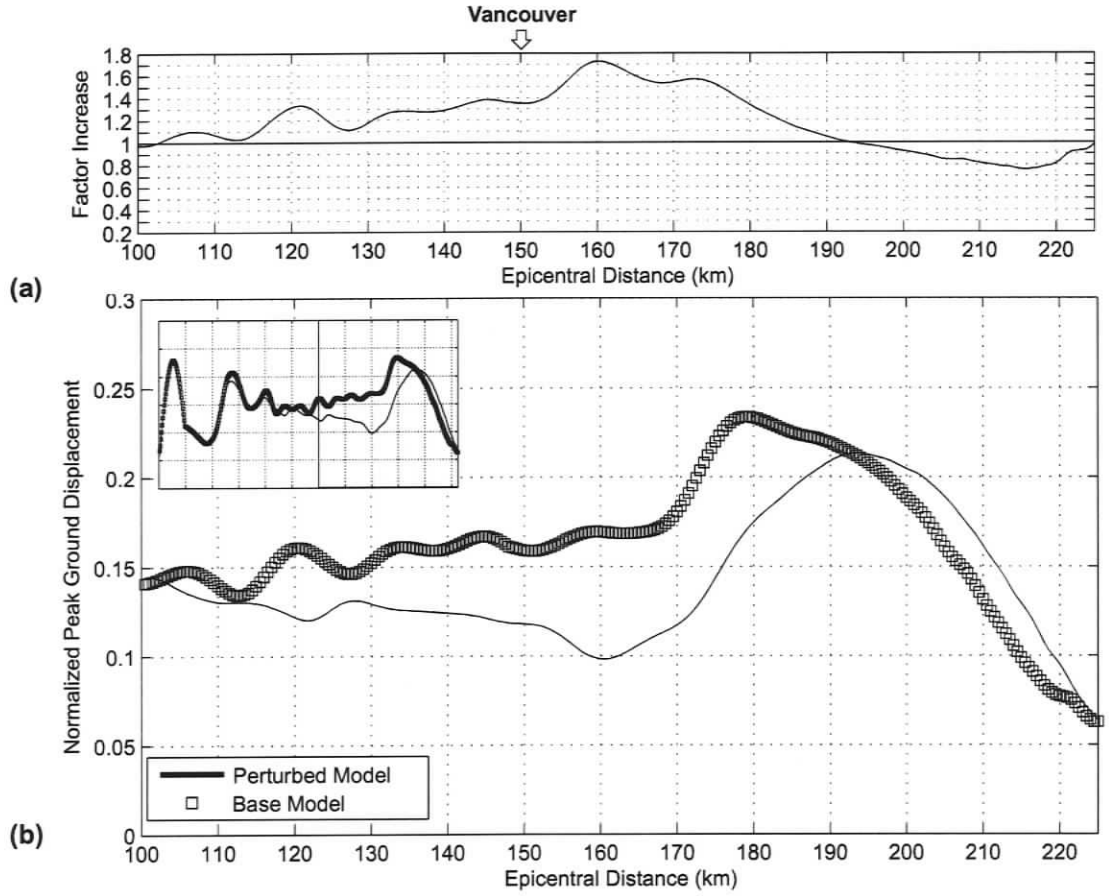

Figure C.14 Quantitative comparison for a 0.5 Hz source at the down-dip limit of the transition zone along a profile in the vicinity of Vancouver. (a) Ratio between the base (square data points) and perturbed model results (solid line). (b) Peak ground motions for a 0.5 Hz source located at the down-dip limit of the transition zone for the base and perturbed models. The inset shows peak ground motions in the range 0 - 225 km.

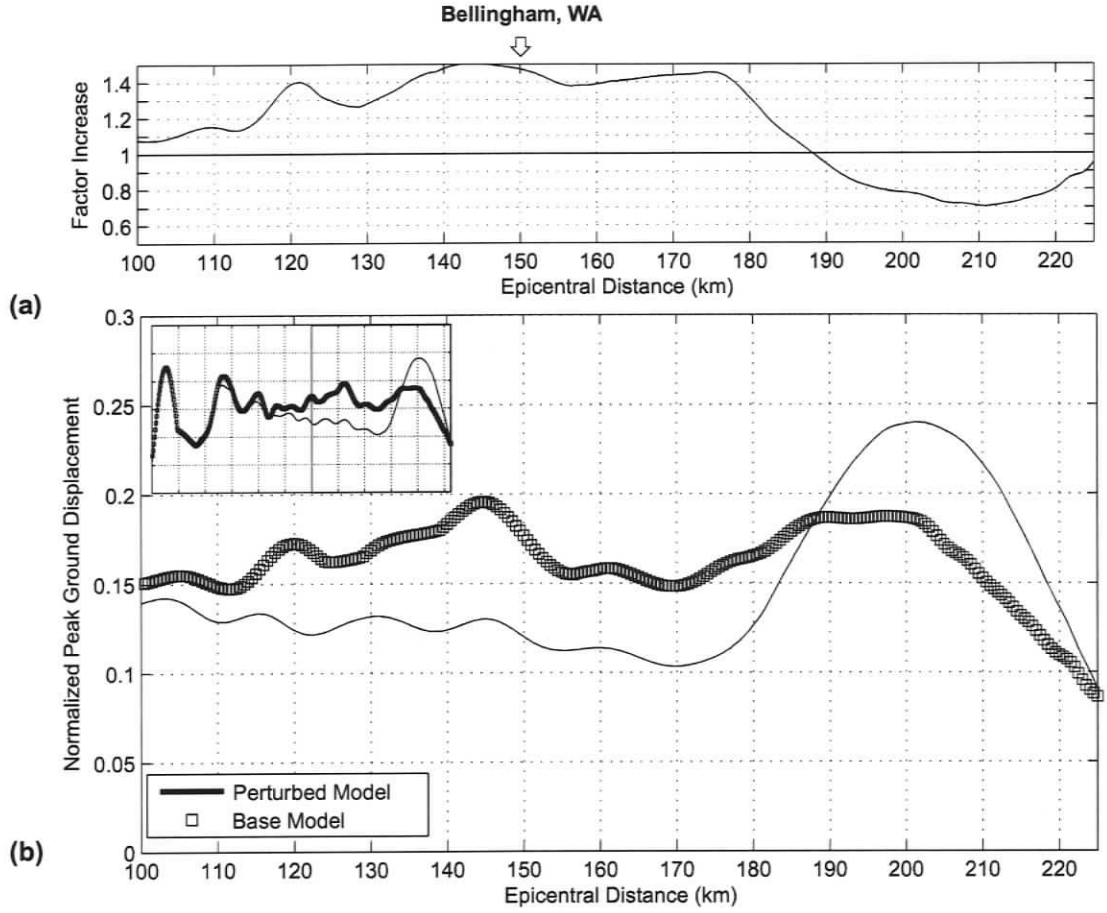

Figure C.15 Quantitative comparison for a 0.5 Hz source at the down-dip limit of the transition zone along a profile in the vicinity of Victoria. (a) Ratio between the base (square data points) and perturbed model results (solid line). (b) Peak ground motions for a 0.5 Hz source located at the down-dip limit of the transition zone for the base and perturbed models. The inset shows peak ground motions in the range 0 - 225 km. Victoria is located at ~100 km epicentral distance.

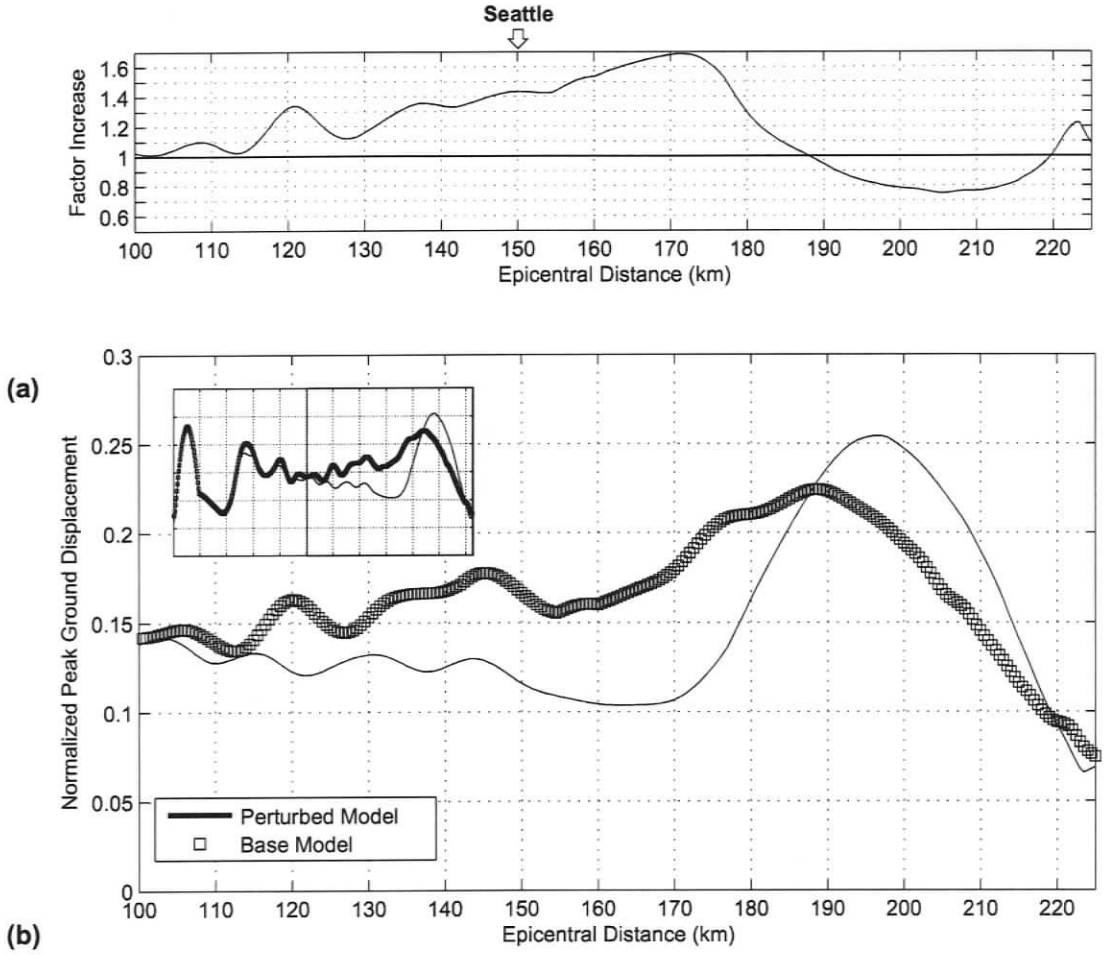

Figure C.16 Quantitative comparison for a 0.5 Hz source at the down-dip limit of the transition zone along a profile in the vicinity of Seattle. (a) Ratio between the base (square data points) and perturbed model results (solid line). (b) Peak ground motions for a 0.5 Hz source located at the down-dip limit of the transition zone for the base and perturbed models. The inset shows peak ground motions in the range 0 - 225 km.

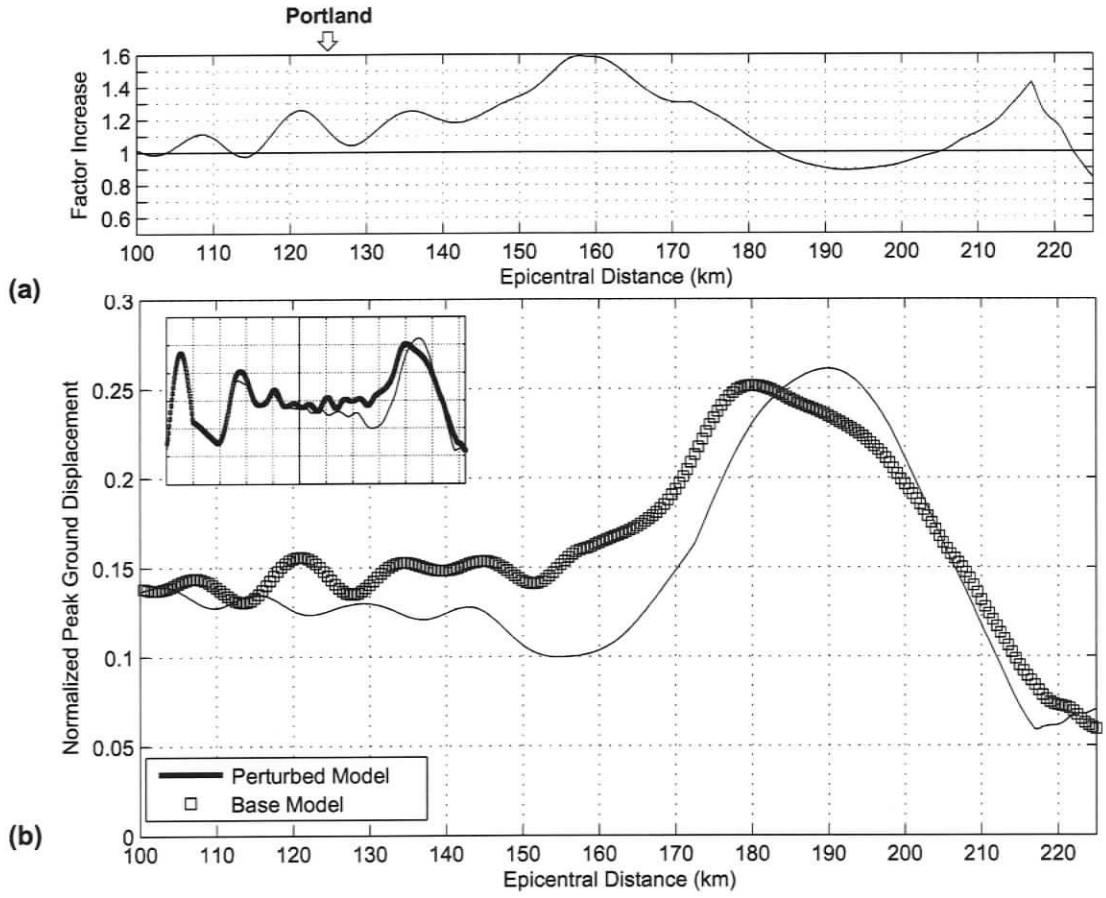

Figure C.17 Quantitative comparison for a 0.5 Hz source at the down-dip limit of the transition zone along a profile in the vicinity of Portland. (a) Ratio between the base (square data points) and perturbed model results (solid line). (b) Peak ground motions for a 0.5 Hz source located at the down-dip limit of the transition zone for the base and perturbed models. The inset shows peak ground motions in the range 0 - 225 km.

APPENDIX D: K-NET AND KiK-NET SITE CLASSIFICAITON

Table D.1 K-NET site classification. NEHRP site class is assigned according to $\overline{V_s}$ (30). $\overline{V_s}$ (30) is computed using shear-wave velocities extrapolated to 30 m depth using method 1 and 2 (see section 5.2 for description).

K-NET Station Code	$\overline{V_s}$ (30) Method 1 (m/s)	NEHRP Site Class Method 1	$\overline{V_s}$ (30) Method 2 (m/s)	NEHRP Site Class Method 2
HKD001	536	C	758	C
HKD002	495	C	654	C
HKD003	174	E	272	D
HKD004	86	E	103	E
HKD005	390	C	637	C
HKD006	188	D	190	D
HKD007	400	C	583	C
HKD008	272	D	383	C
HKD009	285	D	397	C
HKD010	657	C	989	B
HKD011	433	C	610	C
HKD012	388	C	530	C
HKD013	582	C	826	B
HKD014	268	D	367	C
HKD015	234	D	283	D
HKD016	325	D	501	C
HKD017	422	C	583	C
HKD018	561	C	785	B
HKD019	409	C	593	C
HKD020	636	C	935	B
HKD021	424	C	652	C
HKD022	468	C	490	C
HKD023	310	D	457	C
HKD024	428	C	637	C
HKD025	275	D	381	C
HKD026	349	D	503	C
HKD027	532	C	632	C
HKD028	526	C	747	C
HKD029	515	C	799	B

Table D.1 continued…

K-NET Station Code	$\overline{V}_S$ (30) Method 1 (m/s)	NEHRP Site Class Method 1	$\overline{V}_S$ (30) Method 2 (m/s)	NEHRP Site Class Method 2
HKD030	504	C	753	C
HKD031	667	C	1057	B
HKD032	354	D	523	C
HKD033	562	C	698	C
HKD034	286	D	370	C
HKD035	719	C	1015	B
HKD036	143	E	180	E
HKD037	353	D	435	C
HKD038	679	C	808	B
HKD039	546	C	779	B
HKD040	338	D	476	C
HKD041	627	C	786	B
HKD042	543	C	812	B
HKD043	226	D	291	D
HKD044	167	E	184	D
HKD045	658	C	921	B
HKD046	711	C	975	B
HKD047	427	C	623	C
HKD048	290	D	414	C
HKD049	316	D	293	D
HKD050	304	D	423	C
HKD051	303	D	416	C
HKD052	224	D	261	D
HKD053	312	D	410	C
HKD054	489	C	643	C
HKD055	290	D	349	D
HKD056	267	D	357	D
HKD057	305	D	361	C
HKD058	386	C	569	C
HKD059	276	D	403	C
HKD060	251	D	315	D
HKD061	228	D	304	D
HKD062	153	E	200	D

Table D.1 continued…

K-NET Station Code	$\overline{V}_S$ (30) Method 1 (m/s)	NEHRP Site Class Method 1	$\overline{V}_S$ (30) Method 2 (m/s)	NEHRP Site Class Method 2
HKD063	507	C	823	B
HKD064	354	D	490	C
HKD065	565	C	687	C
HKD066	137	E	163	E
HKD067	236	D	318	D
HKD068	278	D	370	C
HKD069	187	D	228	D
HKD070	151	E	168	E
HKD071	262	D	294	D
HKD072	368	C	543	C
HKD073	266	D	357	D
HKD074	325	D	468	C
HKD075	310	D	436	C
HKD076	146	E	169	E
HKD077	233	D	316	D
HKD078	269	D	370	C
HKD079	184	D	252	D
HKD080	327	D	435	C
HKD081	427	C	643	C
HKD082	156	E	163	E
HKD083	744	C	928	B
HKD084	513	C	731	C
HKD085	150	E	163	E
HKD086	270	D	435	C
HKD087	404	C	583	C
HKD088	511	C	718	C
HKD089	425	C	623	C
HKD090	731	C	1036	B
HKD091	120	E	179	E
HKD092	286	D	391	C
HKD093	368	C	530	C
HKD094	330	D	381	C
HKD095	532	C	896	B

Table D.1 continued…

K-NET Station Code	$\overline{V}_S$ (30) Method 1 (m/s)	NEHRP Site Class Method 1	$\overline{V}_S$ (30) Method 2 (m/s)	NEHRP Site Class Method 2
HKD096	477	C	632	C
HKD097	238	D	331	D
HKD098	480	C	677	C
HKD099	303	D	435	C
HKD100	275	D	410	C
HKD101	655	C	935	B
HKD102	379	C	492	C
HKD103	406	C	623	C
HKD104	298	D	397	C
HKD105	533	C	687	C
HKD106	245	D	304	D
HKD107	408	C	575	C
HKD108	244	D	331	D
HKD109	251	D	353	D
HKD110	197	D	233	D
HKD111	353	D	476	C
HKD112	338	D	516	C
HKD113	763	B	1194	B
HKD114	482	C	826	B
HKD115	303	D	272	D
HKD116	385	C	457	C
HKD117	536	C	687	C
HKD118	427	C	556	C
HKD119	393	C	535	C
HKD120	238	D	228	D
HKD121	397	C	589	C
HKD122	231	D	283	D
HKD123	923	B	1359	B
HKD124	589	C	907	B
HKD125	271	D	393	C
HKD126	206	D	304	D
HKD127	403	C	623	C
HKD128	181	D	239	D

Table D.1 continued…

K-NET Station Code	$\overline{V}_S(30)$ Method 1 (m/s)	NEHRP Site Class Method 1	$\overline{V}_S(30)$ Method 2 (m/s)	NEHRP Site Class Method 2
HKD129	419	C	468	C
HKD130	466	C	621	C
HKD131	498	C	640	C
HKD132	235	D	304	D
HKD133	399	C	501	C
HKD134	459	C	611	C
HKD135	233	D	272	D
HKD136	321	D	435	C
HKD137	694	C	1016	B
HKD138	463	C	735	C
HKD139	542	C	819	B
HKD140	451	C	711	C
HKD141	669	C	948	B
HKD142	236	D	283	D
HKD143	360	D	446	C
HKD144	268	D	370	C
HKD145	339	D	523	C
HKD146	431	C	512	C
HKD147	300	D	348	D
HKD148	426	C	589	C
HKD149	562	C	826	B
HKD150	333	D	435	C
HKD151	243	D	359	D
HKD152	521	C	687	C
HKD153	495	C	799	B
HKD154	483	C	788	B
HKD155	261	D	337	D
HKD156	450	C	643	C
HKD157	554	C	880	B
HKD158	128	E	163	E
HKD159	472	C	788	B
HKD160	283	D	381	C
HKD161	282	D	540	C

Table D.1 continued…

K-NET Station Code	$\overline{V_s}$ (30) Method 1 (m/s)	NEHRP Site Class Method 1	$\overline{V_s}$ (30) Method 2 (m/s)	NEHRP Site Class Method 2
HKD162	347	D	530	C
HKD163	523	C	758	C
HKD164	485	C	673	C
HKD165	295	D	490	C
HKD166	666	C	975	B
HKD167	446	C	693	C
HKD168	383	C	543	C
HKD169	477	C	664	C
HKD170	818	B	1263	B
HKD171	697	C	1030	B
HKD172	391	C	570	C
HKD173	225	D	250	D
HKD174	449	C	677	C
HKD175	440	C	623	C
HKD176	516	C	826	B
HKD177	452	C	664	C
HKD178	264	D	425	C
HKD179	185	D	217	D
HKD180	137	E	195	D
HKD181	219	D	261	D
HKD182	403	C	611	C
HKD183	559	C	826	B
HKD184	328	D	468	C
HKD185	410	C	545	C

Table D.2 KiK-NET site classification. NEHRP site class is assigned according to $\overline{V}_S(30)$. $\overline{V}_S(30)$ is computed using shear-wave velocities extrapolated to 30 m depth using method 1 and 2. KiK-NET stations on Hokkaido are assigned a NEHRP site class based on the nearest K-NET station.

KiK-NET Station Code	Nearest K-NET Station Code	$\overline{V}_S(30)$ Method 1 (m/s)	NEHRP Site Class Method 1	$\overline{V}_S(30)$ Method 2 (m/s)	NEHRP Site Class Method 2
ABSH01	HKD043	226	D	291	D
ABSH02	HKD044	167	E	184	D
ABSH03	HKD047	427	C	623	C
ABSH04	HKD046	711	C	975	B
ABSH05	HKD046	711	C	975	B
ABSH06	HKD048	290	D	414	C
ABSH07	HKD050	304	D	423	C
ABSH08	HKD061	304	D	423	C
ABSH10	HKD052	224	D	261	D
ABSH11	HKD055	290	D	349	D
ABSH12	HKD059	276	D	403	C
ABSH13	HKD062	153	E	200	D
ABSH14	HKD057	305	D	361	C
ABSH15	HKD056	267	D	357	D
HDKH01	HKD103	406	C	623	C
HDKH02	HKD103	406	C	623	C
HDKH04	HKD105	533	C	687	C
HDKH05	HKD104	298	D	397	C
HDKH06	HKD106	245	D	304	D
HDKH07	HKD110	197	D	233	D
IBUH01	HKD127	403	C	623	C
IBUH02	HKD127	403	C	623	C
IBUH03	HKD126	206	D	304	D
IBUH05	HKD130	466	C	621	C
IBUH06	HKD131	498	C	640	C
IBUH07	HKD134	459	C	611	C
IKRH01	HKD177	452	C	664	C
IKRH02	HKD179	185	D	217	D
IKRH03	HKD184	328	D	468	C
KKWH01	HKD027	532	C	632	C
KKWH02	HKD042	236	D	283	D
KKWH03	HKD027	532	C	632	C
KKWH05	HKD029	532	C	632	C
KKWH06	HKD029	532	C	632	C
KKWH07	HKD039	546	C	779	B
KKWH08	HKD040	338	D	476	C
KKWH09	HKD026	349	D	503	C
KKWH10	HKD018	561	C	785	B
KKWH11	HKD115	303	D	272	D
KKWH12	HKD037	353	D	435	C

Table D.2 continued…

KiK-NET Station Code	Nearest K-NET Station Code	$\overline{V}_S(30)$ Method 1 (m/s)	NEHRP Site Class Method 1	$\overline{V}_S(30)$ Method 2 (m/s)	NEHRP Site Class Method 2
KKWH13	HKD037	353	D	435	C
KKWH14	HKD039	546	C	779	B
KKWH15	HKD034	286	D	370	C
KSRH01	HKD082	156	E	163	E
KSRH02	HKD084	513	C	731	C
KSRH03	HKD079	184	D	252	D
KSRH04	HKD079	184	D	252	D
KSRH05	HKD083	744	C	928	B
KSRH06	HKD083	744	C	928	B
KSRH07	HKD078	269	D	370	C
KSRH09	HKD085	150	E	163	E
KSRH10	HKD071	262	D	294	D
NMRH02	HKD066	137	E	163	E
NMRH04	HKD069	187	D	228	D
NMRH05	HKD068	278	D	370	C
RMIH01	HKD007	400	C	583	C
RMIH02	HKD015	234	D	283	D
RMIH03	HKD016	325	D	501	C
RMIH04	HKD024	428	C	637	C
RMIH05	HKD024	428	C	637	C
SOYH01	HKD005	390	C	637	C
SOYH02	HKD004	86	E	103	E
SOYH03	HKD001	536	C	758	C
SOYH04	HKD014	268	D	367	C
SOYH05	HKD002	495	C	654	C
SOYH06	HKD003	174	E	272	D
SOYH07	HKD006	188	D	190	D
SOYH08	HKD007	400	C	583	C
SOYH09	HKD009	285	D	397	C
SOYH10	HKD010	197	D	233	D
SRCH01	HKD114	482	C	826	B
SRCH02	HKD115	303	D	272	D
SRCH03	HKD115	303	D	272	D
SRCH04	HKD116	385	C	457	C
SRCH05	HKD115	303	D	272	D
SRCH06	HKD117	536	C	687	C
SRCH07	HKD122	231	D	283	D
SRCH08	HKD118	427	C	556	C
SRCH09	HKD124	589	C	907	B
SRCH10	HKD123	923	B	1359	B
TKCH01	HKD088	511	C	718	C
TKCH02	HKD088	511	C	718	C

Table D.2 continued…

KiK-NET Station Code	Nearest K-NET Station Code	$\overline{V_s}(30)$ Method 1 (m/s)	NEHRP Site Class Method 1	$\overline{V_s}(30)$ Method 2 (m/s)	NEHRP Site Class Method 2
TKCH03	HKD089	425	C	623	C
TKCH04	HKD099	303	D	435	C
TKCH05	HKD090	731	C	1036	B
TKCH06	HKD095	532	C	896	B
TKCH07	HKD091	120	E	179	E
TKCH08	HKD098	480	C	677	C
TKCH10	HKD101	655	C	935	B
TKCH11	HKD095	532	C	896	B